



Delft University of Technology

## On Doppler Processing for Fast Scanning Weather Radars

Dash, T.K.

**DOI**

[10.4233/uuid:ee3b682f-75e3-4210-83c3-a71dc44d1b4d](https://doi.org/10.4233/uuid:ee3b682f-75e3-4210-83c3-a71dc44d1b4d)

**Publication date**

2025

**Document Version**

Final published version

**Citation (APA)**

Dash, T. K. (2025). *On Doppler Processing for Fast Scanning Weather Radars*. [Dissertation (TU Delft), Delft University of Technology]. <https://doi.org/10.4233/uuid:ee3b682f-75e3-4210-83c3-a71dc44d1b4d>

**Important note**

To cite this publication, please use the final published version (if applicable).  
Please check the document version above.

**Copyright**

Other than for strictly personal use, it is not permitted to download, forward or distribute the text or part of it, without the consent of the author(s) and/or copyright holder(s), unless the work is under an open content license such as Creative Commons.

**Takedown policy**

Please contact us and provide details if you believe this document breaches copyrights.  
We will remove access to the work immediately and investigate your claim.

# **ON DOPPLER PROCESSING FOR FAST SCANNING WEATHER RADARS**



# **ON DOPPLER PROCESSING FOR FAST SCANNING WEATHER RADARS**

## **Dissertation**

for the purpose of obtaining the degree of doctor  
at Delft University of Technology  
by the authority of the Rector Magnificus, Prof. dr. ir. T.H.J.J. van der Hagen,  
chair of the Board for Doctorates  
to be defended publicly on  
Monday 24 February 2025 at 12:30

by

**Tworit Kumar DASH**

Master of Science in Electrical Engineering,  
Delft University of Technology  
born in Nayagarh, India

This dissertation has been approved by the promotor.

Composition of the doctoral committee:

Rector Magnificus,	chairperson
Prof. dr. A. Yarovoy	Delft University of Technology, promotor
Dr. O.A. Krasnov	Delft University of Technology, copromotor
Dr. ir. J.N. Driessen	Delft University of Technology, copromotor

Independent members:

Prof. dr. ir. H.W.J. Russchenberg	Delft University of Technology
Prof. dr. ir. B. De Schutter	Delft University of Technology
Prof. dr. ir. R. Uijlenhoet	Delft University of Technology
Prof. dr. D. Moiseev	University of Helsinki
Prof. dr. ir. F.M.J. Willems	Eindhoven University of Technology



This research was supported by “European Regional Development Fund (ERDF) via the Kansen voor West II Program” under the project “Airport Technology Lab and the Delft University of Technology in the Microwave Sensing, Signals and Systems (MS3) group.

**Keywords:** Weather Radars, Doppler Processing, Precipitation, Wind Fields, Drop Size Distribution.

**Printed by:** Proefschriftspecialist, 1506RZ Zaandam, The Netherlands.

**Front & Back:** Design by Tworit Kumar Dash.

Copyright © 2025 by T.K. Dash

All rights reserved. No parts of this publication may be reproduced or transmitted in any form or by any means, electronic or mechanical, including photocopy, recording, or any information storage and retrieval system, without permission in writing from the author.

ISBN/EAN 978-94-6384-731-5 (Paperback/softback)

ISBN/EAN 978-94-6518-011-3 (E-book, PDF)

An electronic version of this dissertation is available at

<http://repository.tudelft.nl/>.

Author e-mail: [tworitdash@gmail.com](mailto:tworitdash@gmail.com)

To my mother, Smt Sasmita Tripathy



# LIST OF FIGURES

2.1	Scattering phenomena. . . . .	10
2.2	Scattering illustration with vectors. Adapted from [1, Fig.1]. . . . .	11
2.3	Max3D phased array X-band radar. . . . .	18
3.1	Estimation and performance of the Doppler moments for $L = 1$ with respect to the number of coherent samples $N$ . a Mean normalized Doppler frequency $\hat{\mu}_{fn}$ . b normalized Doppler frequency width $\hat{\sigma}_{fn}$ . c Standard deviation in estimating the normalized Mean Doppler frequency $\hat{\mu}_{fn}$ . d Standard deviation in estimating the normalized Doppler spectrum width $\hat{\sigma}_{fn}$ . . . . .	31
3.2	Estimation and performance of the Doppler moments for $L = 1$ with respect to $\sigma_{fn}$ at $\mu_{fn} = 0$ . a Biases in the estimates of the mean Doppler frequency normalized $\hat{\mu}_{fn}$ . b Doppler frequency width normalized $\hat{\sigma}_{fn}$ . c Standard deviation in estimating the mean Doppler frequency normalized $\hat{\mu}_{fn}$ . d Standard deviation in estimating the Doppler spectrum width normalized $\hat{\sigma}_{fn}$ . . . . .	33
3.3	Estimation and performance of the Doppler moments for $L = 1$ with respect to $\mu_f$ at $\sigma_f = 0.05$ . a Biases in the estimates of the mean Doppler frequency normalized $\hat{\mu}_{fn}$ . b Doppler frequency width normalized $\hat{\sigma}_{fn}$ . c Standard deviation in estimating the mean Doppler frequency normalized $\hat{\mu}_{fn}$ . d Standard deviation in estimating the Doppler spectrum width normalized $\hat{\sigma}_{fn}$ . . . . .	34
3.4	Estimation and performance of the Doppler moments for $N = 64$ with respect to $L$ . $\mu_{fn} = 0$ and $\sigma_{fn} = 0.033$ a Standard deviation in estimating the mean Doppler frequency normalized $\hat{\mu}_{fn}$ . b Standard deviation in estimating the Doppler spectrum width normalized $\hat{\sigma}_{fn}$ . . . . .	35
3.5	a PPI plot of reflectivity using the DFT approach. b log-likelihood (3.14) of PSE. . . . .	37
3.6	PPI plots showing Mean Doppler velocity and Doppler spectrum width with all the approaches discussed in the chapter. The first row shows the results of the mean Doppler velocity, and the second row shows the results of the Doppler spectrum width. a e, DFT, b f, PP, c g, Levin, d h, PSE. . . .	37
3.7	PSE derived mean Doppler velocity. The Doppler spectrum is analyzed in the highlighted areas of this figure. . . . .	39
3.8	Doppler spectrum reconstruction at cell (1) a 512 total samples b 64 total samples . . . . .	40
3.9	Doppler spectrum reconstruction at cell (2) a 512 total samples b 64 total samples . . . . .	40



3.10 Doppler spectrum reconstruction at cell (3) a 512 total samples b 64 total samples . . . . .	41
3.11 PSE derived mean Doppler velocity. The Doppler spectrum is analyzed in the highlighted areas of this figure. . . . .	42
3.12 Doppler moments estimation on real radar data with respect to number of observations $L$ at resolution cell (1). a Mean Doppler velocity $\hat{\mu}_v$ m/s b Doppler spectrum width $\hat{\sigma}_v$ m/s . . . . .	43
3.13 Doppler spectrum reconstruction with $L = 10$ . Incoherent processing of 5 scans of the radar at cell (1) . . . . .	43
3.14 Doppler moments estimation on real radar data with respect to the number of observations $L$ at resolution cell (2). a Mean Doppler velocity $\mu_v$ m/s b Doppler spectrum width $\sigma_v$ m/s . . . . .	43
3.15 Doppler spectrum reconstruction with $L = 10$ . Incoherent processing of 5 scans of the radar at cell (2). . . . .	44
3.16 PPI plots at $L = 10$ . Incoherent processing of 5 scans of the radar a Mean Doppler velocity $\mu_v$ m/s with Levin's ML approach. b Mean Doppler velocity $\mu_v$ m/s with PSE. c Doppler spectrum width $\sigma_v$ m/s with Levin's ML approach. d Doppler spectrum width $\sigma_v$ m/s with PSE. . . . .	45
3.17 Estimation performance with $\sigma_{fn}$ with an input SNR of 12dB, $N = 64$ , $L = 16$ a Bias of $\hat{\mu}_{fn}$ b Standard deviation of $\hat{\mu}_{fn}$ c Bias of $\hat{\sigma}_{fn}$ d Standard deviation of $\hat{\sigma}_{fn}$ e Bias of $\hat{\sigma}_n$ f Standard deviation of $\hat{\sigma}_n$ . The legend with "Theo" refers to theoretical plots. . . . .	46
3.18 Parameter estimation and Doppler PSD reconstruction with real radar data collected from five consecutive scans of a fast scanning radar from the voxel located at range $R = 1.24$ km, azimuth $\phi = 264^\circ$ from the north in a clockwise direction, and an elevation of $\theta = 30^\circ$ . a $\hat{\mu}_v$ m/s b $\hat{\sigma}_v$ m/s c $\hat{\sigma}_n$ (linear scale) d Reconstruction of the PSD. The abbreviation "GT" stands for "ground truth" PSD measurements. . . . .	47
4.1 Performance of the hyper-parameter estimation for with respect to $\sigma_{fn}$ at $\mu_{fn} = 0$ . a Biases in the estimates of the mean Doppler frequency normalized $\hat{\mu}_{fn}$ , b Doppler frequency width normalized $\hat{\sigma}_{fn}$ . c Standard deviation of the estimates of the Mean Doppler frequency normalized $\hat{\mu}_{fn}$ , d the Doppler spectrum width normalized $\hat{\sigma}_{fn}$ , e legends for the figures. "Theor" refers to the theoretical plots. . . . .	57
4.2 Time domain reconstruction for real part of the signal a 12.5% data, b 25% data, c legend for the figures. . . . .	59
4.3 Real part of the frequency domain reconstruction a 12.5% data, b 25% data, c legend for the figures. "Meas" stands for measurements. . . . .	60
4.4 PSD reconstruction a 12.5% data, b 25% data, c legend for the figures. "Meas" stands for measurements. . . . .	61
4.5 PSD reconstruction a rRMSE error in the full mean reconstruction, b rRMSE error in the mean reconstruction only at the observation points. . . . .	62
4.6 Time domain reconstruction for real part of the signal a 12.5% data, b 25% data, c legend for the figures. . . . .	63

4.7	Real part of the frequency domain reconstruction a 12.5% data, b 25% data, c legend for the figures. “Meas” stands for measurements. . . . .	64
4.8	PSD reconstruction a 12.5% data, b 25% data, c legend for the figures. “Meas” stands for measurements. . . . .	65
5.1	Sampling sequences; periodic and aperiodic cases. . . . .	80
5.2	Estimation and performance of the Doppler moments with respect to $\sigma_{fn}$ . For the periodic case, the number of samples is 82, whereas for the aperiodic case, it is 64. Bias in estimating a the mean normalized Doppler frequency $\hat{\mu}_{fn}$ . b normalized Doppler frequency width $\hat{\sigma}_{fn}$ . Standard deviation in estimating c the normalized mean Doppler frequency $\hat{\mu}_{fn}$ . d the normalized Doppler spectrum width normalized $\hat{\sigma}_{fn}$ . The abbreviation “per” refers to the periodic sampling, “aper” refers to the aperiodic one, “ST” refers to staggered sampling (“ST” for velocity difference transfer function and “ST CGP” for CGP applied to staggered sequence), “LP” for the log-periodic sampling, and “Theor” refers to the theoretical plots. e Legend for the plots. . . . .	83
5.3	Histogram of parameter estimates $\hat{\mu}_{fn}$ for staggered (“ST” for velocity difference transfer function and “ST CGP” for CGP applied to staggered sequence) and the proposed CGP (“LP” stands for the log-periodic sequence) approach at a $\sigma_{fn} = 0.01$ , and b $\sigma_{fn} = 0.2$ . True mean Doppler velocity is $\mu_{fn} = -1.2$ . . . . .	84
5.4	Estimation and performance of the normalized mean Doppler frequency $\hat{\mu}_{fn}$ with respect to $\sigma_{fn}$ and $d_2$ . The number of samples is 33. Bias in estimating the mean normalized Doppler frequency $\hat{\mu}_{fn}$ . a CGP, b DFT aperiodic. Standard deviation in estimating the mean normalized Doppler frequency $\hat{\mu}_{fn}$ . c CGP, d DFT aperiodic. . . . .	85
5.5	The spectral width at which $ \mathbb{B}[\hat{\mu}_{fn}]  = 0.2 \mu_{fn} $ as a function of the non-linearity in the sampling ( $d_2$ ). . . . .	86
5.6	Estimation and performance of the normalized Doppler spectrum width $\hat{\mu}_{fn}$ with respect to $\sigma_{fn}$ and $d_2$ . The number of samples is 33. Bias in estimating the normalized Doppler spectrum width $\hat{\sigma}_{fn}$ . a CGP, b DFT aperiodic. Standard deviation in estimating the normalized Doppler spectrum width $\hat{\sigma}_{fn}$ . c CGP, d DFT aperiodic. . . . .	87
5.7	Estimation probability of $\hat{\mu}_f$ with true $\mu_f$ : a for $\mu_{fn} \in [-500, 500]$ b for $\mu_{fn} \in [-100, -20]$ (zoomed in). “GT”, “ST”, and “LP” stand for “Ground Truth”, “Staggered” and “Log-Periodic”, respectively. . . . .	88
5.8	Estimation probability of $p(\hat{\mu}_{fn} \in [\mu_{fn} - 2\epsilon, \mu_{fn} + 2\epsilon])$ (given in (5.18)). “ST”, and “LP” stand for “Staggered” and “Log-Periodic”, respectively. The approach “DFT aper” is applied on the log-periodic sampling sequence. . . .	89
5.9	Spectrum Reconstruction: a Power spectrum b Power spectrum zoomed in c Legend for the plots. The posterior spectrum contains five realizations of the power spectrum. . . . .	91

6.1	Bias in the estimation of: a $\hat{\mu}_v$ m/s b $\hat{\sigma}_v$ m/s c $\hat{\eta}$ d $\hat{\Lambda}$ mm <sup>-1</sup> at $\mu_v = 3.53$ m/s, $\sigma_v = 0.6$ m/s, $\eta = 2.07$ , $\Lambda = 3.48$ mm <sup>-1</sup> , and $L = 32$ with the number of coherent echo samples $N$ . e Legend for the figures. . . . .	106
6.2	Standard deviation in the estimation of: a $\hat{\mu}_v$ m/s b $\hat{\sigma}_v$ m/s c $\hat{\eta}$ d $\hat{\Lambda}$ mm <sup>-1</sup> at $\mu_v = 3.53$ m/s, $\sigma_v = 0.6$ m/s, $\eta = 2.07$ , $\Lambda = 3.48$ mm <sup>-1</sup> , and $L = 32$ with the number of coherent echo samples $N$ . The expression "Theor" refers to theoretical plots, e Legend for the figures. . . . .	107
6.3	Bias in the estimation of: a $\hat{\mu}_v$ m/s b $\hat{\sigma}_v$ m/s c $\hat{\eta}$ d $\hat{\Lambda}$ mm <sup>-1</sup> , with the radial wind spectral width $\sigma_v$ at $N = 64$ , and $L = 32$ . e Legend for the figures. . .	108
6.4	Standard deviation in the estimation of: a $\hat{\mu}_v$ m/s b $\hat{\sigma}_v$ m/s c $\hat{\eta}$ d $\hat{\Lambda}$ mm <sup>-1</sup> , with the radial wind spectral width $\sigma_v$ at $N = 64$ , and $L = 32$ . The expression "Theor" refers to theoretical plots e Legend for the figures. . . . .	109
6.5	Bias in the estimation of: a $\hat{\mu}_v$ m/s b $\hat{\sigma}_v$ m/s c $\hat{\eta}$ d $\hat{\Lambda}$ mm <sup>-1</sup> with the DSD parameters at $\sigma_v = 0.6$ m/s, $N = 64$ , and $L = 32$ . e Legend for the figures. .	110
6.6	Standard deviation in the estimation of: a $\hat{\mu}_v$ m/s b $\hat{\sigma}_v$ m/s c $\hat{\eta}$ d $\hat{\Lambda}$ mm <sup>-1</sup> with the DSD parameters at $\sigma_v = 0.6$ m/s, $N = 64$ , and $L = 32$ . The expression "Theor" refers to theoretical plots, e Legend for the figures. . . . .	111
6.7	Bias in the estimation of: a $\hat{\mu}_v$ m/s b $\hat{\sigma}_v$ m/s c $\hat{\eta}$ d $\hat{\Lambda}$ mm <sup>-1</sup> with $L$ at $\sigma_v = 0.6$ m/s, $N = 64$ , $\eta = 2.07$ , $\Lambda = 3.48$ mm <sup>-1</sup> . The expression "Theor" refers to theoretical plots, e Legend for the figures. . . . .	112
6.8	Standard deviation in the estimation of: a $\hat{\mu}_v$ m/s b $\hat{\sigma}_v$ m/s c $\hat{\eta}$ d $\hat{\Lambda}$ mm <sup>-1</sup> with $L$ at $\sigma_v = 0.6$ m/s, $N = 64$ , $\eta = 2.07$ , $\Lambda = 3.48$ mm <sup>-1</sup> . The expression "Theor" refers to theoretical plots, e Legend for the figures. . . . .	113
6.9	Log-likelihood (6.19) $\log(p(Z \Theta))$ with $\eta$ , and $\Lambda$ at $N = 64$ , $L = 32$ at fixed values of $\mu_v$ and $\sigma_v$ . True values of $\eta$ and $\Lambda$ are 1.2 and 3 respectively. . . .	114
6.10	Doppler spectrum reconstruction at three sets of estimated parameters. "GT" stands for Ground Truth. In the legend, the $\mathbb{E}[\Theta]$ , $\mathbb{V}[\Theta]$ are expected value and variance of the radial wind and the DSD parameters. The Doppler spectrum is then computed using (6.11) with the parameter values mentioned in the legend. . . . .	115
6.11	a Terminal fall velocity retrieval $\hat{V}_T$ m/s. "GT" stands for Ground Truth. In the legend, the $\mathbb{E}[\Theta]$ , $\mathbb{V}[\Theta]$ are expected value and variance of the DSD parameters. The terminal fall velocity is then computed using [2, Eq. (4)] with the parameter values mentioned in the legend, b Median volume diameter $\hat{D}_0$ mm. In the legend, the $\mathbb{E}[\Theta]$ , $\mathbb{V}[\Theta]$ are expected value and variance of the DSD parameters. The median volume drop diameter is then computed using [3, Eq. (5)] with the parameter values mentioned in the legend. . . .	115
6.12	a Average reflectivity (dbZ) using $L = 64$ PSDs, b Average mean Doppler velocity (m/s) using $L = 64$ different mean Doppler velocities computed in each resolution volume using the PP approach. . . . .	117
6.13	Plan Position Indicator (PPI) plots after applying WiDSE algorithm, a mean radial wind velocity $\hat{\mu}_v$ m/s, b mean radial velocity width $\hat{\sigma}_v$ m/s, c DSD shape parameter $\hat{\eta}$ , d DSD rate parameter $\hat{\Lambda}$ mm <sup>-1</sup> , and derived parameters, e mean terminal fall velocity $\hat{V}_{T\psi}/\sin(\psi)$ m/s, f median diameter $\hat{D}_0 = (3.67 + \hat{\eta})/\hat{\Lambda}$ mm. . . . .	118

6.14	Scatter plot of the estimated DSD parameters $\hat{\eta}$ and $\hat{\Lambda}$ $\text{mm}^{-1}$ . "HM" stands for the higher order method of moments, "LM" stands for the lower order method of moments [4], and "Disdro" stands for disdrometer. . . . .	119
6.15	Doppler spectrum reconstruction at specific resolution volumes, a at the Green Village; $r = 472$ m, $\phi = 128^\circ$ , b at a radar volume where the mean Doppler velocity is aliased (Fig. 6.12b), $r = 1.829$ km, $\phi = 257^\circ$ , c at the melting layer, $r = 4.662$ km, $\phi = 73^\circ$ . . . . .	119
6.16	Optimal log-likelihood using (6.19) at the estimated parameter values $\hat{\Theta}$ . The melting layer (around $r = 4.5$ km) is adequately filtered out because it has very small log-likelihood values than the other regions. . . . .	120
C.1	Decay study for $G(q)$ with $\eta$ , and $\Lambda$ a Lifetime computed numerically b Analytical lifetime based on [2] c Difference of halftimes between the numerical and the analytical methods. d Difference of lifetimes between the numerical and the analytical methods. The times are converted to dB scale for better visualization. . . . .	137
C.2	$G(q)$ . "Int form" is the original integral of (6.16), and "Approx" is the approximation of (6.17). . . . .	137



# LIST OF TABLES

3.1	MESEWI radar specifications . . . . .	36
3.2	Highlighted resolution cells' coordinates . . . . .	39
3.3	Highlighted resolution cells' coordinates . . . . .	42
4.1	Hyper-parameter (Doppler moments) estimation . . . . .	58
4.2	Hyper-parameter (Doppler moments) estimation . . . . .	62
5.1	Hyper-parameter estimation for the three-extended-targets scenario of §5.5.6	90
6.1	Parameters for the analysis . . . . .	104
6.2	MESEWI radar specifications . . . . .	114



# CONTENTS

<b>List of Figures</b>	<b>vii</b>
<b>List of Tables</b>	<b>xiii</b>
<b>Symbols and Conventions</b>	<b>xix</b>
<b>Summary</b>	<b>xxiii</b>
<b>Samenvatting</b>	<b>xxv</b>
<b>Preface</b>	<b>xxvii</b>
<b>1 Introduction</b>	<b>1</b>
1.1 Role of Doppler Radars in Weather Monitoring . . . . .	2
1.2 What is the Need for New Doppler Processing Techniques for Weather Radar? Why Doppler Processing for Fast Scanning Weather Radars? . . . .	2
1.3 Research Questions Addressed in the Thesis . . . . .	3
1.4 Research Approaches and Outline of the Thesis. . . . .	4
<b>2 A Brief Overview of Atmospheric Weather Radar Remote Sensing</b>	<b>7</b>
2.1 History of Weather Radar Systems . . . . .	8
2.1.1 Early Developments (1940s-1960s). . . . .	8
2.1.2 Doppler Radar in the Late 1960s . . . . .	8
2.1.3 Dual Polarization Radars. . . . .	9
2.1.4 Phased Array Radars . . . . .	9
2.2 Electromagnetic Aspects and Rayleigh Scattering. . . . .	9
2.2.1 Scattering Principles and Regimes . . . . .	9
2.2.2 Raindrop Backscattering. . . . .	12
2.3 Doppler Velocity and Wind Field Estimation with Weather Radars . . . . .	13
2.3.1 Doppler Shift. . . . .	13
2.3.2 Wind Field Estimation . . . . .	16
2.4 Advancements in Radar Remote Sensing: Advent of Multifaceted Radars with Phased Array Technology . . . . .	18
2.5 Conclusions. . . . .	19
<b>3 Doppler Spectrum Moments Estimation for Precipitation</b>	<b>21</b>
3.1 Introduction . . . . .	22
3.2 Classical Doppler Moment Estimators and the Rationale behind the Proposed Approach. . . . .	23
3.3 Signal Model . . . . .	25
3.4 Semi-analytical Form of the PSD . . . . .	26
3.5 Optimization Goals . . . . .	27



3.6	Numerical Simulation. . . . .	29
3.6.1	Parameter Estimation with $L = 1$ . . . . .	31
3.6.2	Performance Analysis With Respect to $L$ . . . . .	33
3.6.3	Discussion on the Simulation Results . . . . .	34
3.7	Application to Real Data . . . . .	35
3.7.1	Experiment 1: Slow Scan of One Rotation Per Minute . . . . .	36
3.7.2	Application to Fast Scanning Radar Data. . . . .	41
3.8	Joint Estimation of Noise Variance and the Doppler Moments . . . . .	44
3.8.1	Numerical Simulation . . . . .	44
3.8.2	Application to Real Radar Data. . . . .	45
3.9	Conclusions. . . . .	47
<b>4</b>	<b>Gaussian Process Regression for Doppler Spectrum Reconstruction</b>	<b>51</b>
4.1	Introduction . . . . .	52
4.2	Rationale Behind the Approach, A Bayesian Perspective . . . . .	53
4.3	Hyper-parameter Estimation (Training the CGP) . . . . .	54
4.4	Local Signal and Spectrum Reconstruction . . . . .	54
4.4.1	Posterior in the Time Domain . . . . .	54
4.4.2	Posterior in the Frequency Domain . . . . .	55
4.5	Covariance Model for Weather Echoes . . . . .	55
4.6	Performance of Hyper-parameter Estimation. . . . .	56
4.7	Spectrum Reconstruction on Simulated Radar Echoes . . . . .	57
4.8	Application to Real Radar Data . . . . .	60
4.9	Conclusions. . . . .	64
<b>5</b>	<b>Counter-aliasing of Doppler Spectrum</b>	<b>67</b>
5.1	Introduction . . . . .	68
5.2	State of the Art and the Rationale Behind the Proposed Approach . . . . .	70
5.2.1	The Nyquist Limit for Aperiodically Sampled Signals. . . . .	70
5.2.2	Radar Signal Processing Approaches to Deal with Aperiodically Sampled Signals in the Frequency Domain . . . . .	71
5.2.3	Frequency Domain Conversion Techniques Specifically Designed for Aperiodic Sampled Signals. . . . .	73
5.2.4	Model-based Parameter Estimation and Reconstruction of Doppler Frequency Spectrum. . . . .	74
5.2.5	Rationale Behind the Proposed Approach . . . . .	75
5.3	Signal and Covariance Model . . . . .	76
5.4	Hyper-parameter Estimation and Spectrum Reconstruction . . . . .	77
5.5	Numerical Simulation. . . . .	78
5.5.1	Sampling Strategy . . . . .	78
5.5.2	Performance Analysis of Hyper-parameter Estimation with $\sigma_{fn}$ . . . . .	80
5.5.3	Performance Analysis of Hyper-parameter Estimation with $d_2$ for the Aperiodically Sampled Sequence. . . . .	84
5.5.4	Recommendation for Minimum Pulse Repetition Interval . . . . .	86
5.5.5	Performance Analysis with Varying $\mu_{fn}$ . . . . .	88
5.5.6	Simulation Study of the Spectrum Reconstruction . . . . .	90

5.5.7	Recommendations for Real Radar Application . . . . .	90
5.6	Conclusions. . . . .	92
<b>6</b>	<b>Fitting of Precipitation Doppler spectrum with Wind and Rain DSD Parameters</b>	<b>95</b>
6.1	Introduction . . . . .	96
6.2	Classical DSD and Wind Parameter Estimations and the Rationale Behind the Proposed Approach . . . . .	97
6.3	Signal Model . . . . .	99
6.4	Semi-analytical form of the expected PSD and Formulation of the Covariance related to Vertical Fall . . . . .	101
6.5	Optimization Goals . . . . .	103
6.6	Numerical Simulation. . . . .	103
6.6.1	Dependence on the Number of Coherent Echo Samples $N$ . . . . .	106
6.6.2	Dependence on the Radial Wind Spectral Width ( $\sigma_\nu$ ) . . . . .	106
6.6.3	Dependence on the DSD Parameters . . . . .	107
6.6.4	Dependence on $L$ with Known and Unknown Concentration . . . . .	108
6.6.5	Discussion on DSD-Derived Quantities . . . . .	110
6.6.6	Computational Resource Considerations . . . . .	113
6.7	Application to Real Radar Observations. . . . .	114
6.7.1	Description of the Experiment . . . . .	114
6.7.2	Application of WiDSE on Real Radar Data . . . . .	117
6.8	Conclusions. . . . .	121
<b>7</b>	<b>Conclusions and Recommendations</b>	<b>125</b>
<b>A</b>	<b>Expected Value of the Power Spectrum</b>	<b>129</b>
<b>B</b>	<b>Theoretical Variance and the CRB of PSE and CGP</b>	<b>133</b>
B.1	PSE . . . . .	133
B.2	CGP. . . . .	134
<b>C</b>	<b>Decay Study of <math>G(q)</math>: Auto-correlation Function Related to the Vertical Fall Velocity</b>	<b>135</b>
<b>D</b>	<b>Theoretical Variance and the Cramer Rao Lower Bound (CRB) of WiDSE</b>	<b>139</b>
	<b>Bibliography</b>	<b>142</b>
	<b>Epilogue</b>	<b>157</b>
	<b>Acknowledgements</b>	<b>159</b>
	<b>Curriculum Vitæ</b>	<b>161</b>
	<b>List of Publications</b>	<b>163</b>



# SYMBOLS AND CONVENTIONS

This thesis incorporates terminologies from estimation theory, radar signal processing, electromagnetics, and atmospheric physics. Therefore, it is necessary to use discernible terminologies to avoid confusion.

## SYMBOLS:

- $j = \sqrt{-1}$ : The imaginary unit,
- $\sigma_n$ : Noise standard deviation,
- $\mathbb{I}_N$ : Identity matrix of size  $N \times N$ ,
- $\mathbb{B}$ : Bias,
- $\mathbb{E}$ : Expected value,
- $\mathbb{V}$ : Variance,
- $\mathcal{CGP}$ : Complex Gaussian Process,
- $\mathcal{FT}$ : Fourier Transform,
- $\mathcal{N}$ : Normal distribution,
- $A$ : Amplitude,
- $C$ : Covariance. Specific sub-scripted  $C$  (like  $C_{CN}$ ) are explained in the chapters where those are defined,
- $D$ : Diameter,
- $d$ : Number of decimal places,
- $F$ : Model of the expected PSD,
- $f$ : Frequency,
- $f_c$ : Central frequency,
- $f_s$ : ADC sampling frequency,
- $G$ : Covariance of signal with vertical fall of raindrops,
- $I$ : Fisher Information,
- $J$ : Cost function,

- $L$ : Number of measurements,
- $N$ : Number of echo samples. Specific sub-scripted  $N$  (like  $N_{\text{per}}$ ) are explained in the chapters where those are defined,
- $N(D)$ : Drop Size Distribution,
- $R$ : Reflectivity,
- $r$ : Range, Radius
- $S$ : Complex Fourier transform (has real and imaginary parts) of the signal model,
- $s$ : Signal model,
- $T$ : Pulse repetition interval (PRT). Specific sub-scripted  $T$  (like  $T_{\text{ap,min}}$ ) are explained in the chapters where those are defined,
- $t$ : Time,
- $v$ : Radial velocity,
- $V_a$ : Maximum unambiguous velocity,
- $\mathcal{V}$ : Volume,
- $V_T$ : Terminal fall velocity,
- $Y$ : Covariance of signal from wind only,
- $Z$ : Power Spectral Density (PSD) of the measurements,
- $\beta$ : Phase. Specific sub-scripted  $\beta$  (like  $\beta_s$ ) are explained in the chapters where those are defined,
- $\epsilon$ : Used for threshold computation in (5.18) (in chapter 5), and attenuation of weather echoes (in chapter 6).
- $\in$ : Belongs to,
- $\eta, \Lambda$ : Shape and scale DSD parameters,
- $\Gamma$ : Gamma function,
- $\lambda$ : Wavelength,
- $\mu$ : Mean of a quantity. Specific sub-scripted  $\mu$  (like  $\mu_{fn}$ ) are explained in the chapters where those are defined,
- $\phi$ : Azimuthal angle,
- $\psi$ : Elevation angle,
- $\sigma$ : Standard deviation of a quantity. Specific sub-scripted  $\sigma$  (like  $\sigma_{fn}$ ) are explained in the chapters where those are defined,
- $\Theta$ : Parameter vector,  $\theta$  refers to any parameter

## ACRONYMS:

- BW: Bandwidth,
- CGP: Complex Gaussian Process,
- CGP-R: Complex Gaussian Process Regression,
- CRB: Crámer Rao Lower Bound,
- dB: Decibel,
- dBZ: Decibel relative to reflectivity factor,
- DFT: Discrete Fourier Transform,
- DSD: Drop Size Distribution,
- FMCW: Frequency Modulated Continuous Wave,
- ML: Maximum Likelihood,
- PP: Pulse Pair,
- PRT, PRI, PRF: Pulse Repetition Time, Pulse Repetition Interval, Pulse Repetition Frequency,
- PSD: Power Spectral Density,
- PSE: Parametric Spectrum Estimator,
- rRMSE: relative Root Mean Square Error,
- WiDSE: Wind and DSD Estimator.

## CONVENTIONS

- A diacritic mark of a hat ( $\hat{\cdot}$ ) is used on top of the variables to refer to their estimated quantity. Sometimes, a diacritic mark of a hat ( $\hat{\cdot}$ ) also refers to a unit vector in space, and they are specified wherever unit vectors are mentioned.
- Regular lowercase mathematical symbols are variables, such as  $s$ ,  $z$ , etc.
- Bold lowercase mathematical symbols are vectors, such as  $\mathbf{s}$ ,  $\mathbf{z}$ , etc.
- Bold uppercase mathematical symbols are matrices, such as  $\mathbf{S}$ ,  $\mathbf{Z}$ , etc.
- $\mathbf{0}$ : Zero vector,
- $\mathbf{0}$ : Zero Matrix,
- A superscript ( $^*$ ) is used for complex conjugate,
- A superscript ( $^T$ ) is used for transpose,
- A superscript ( $^H$ ) is used for Hermitian.



# SUMMARY

Modern, multifunctional ground-based weather radar systems deployed at the airports are designed to detect and track point-like targets, such as birds and drones. Therefore, these radars scan the field of view in azimuth very fast to get quick updates on the whereabouts of these targets. The fast scanning nature of these radars limits their capacity to accurately estimate parameters for weather applications, such as the precipitation intensity and velocity distribution parameters of the raindrops during rainy conditions. This thesis aims to develop novel techniques to estimate the parameters related to the precipitation Doppler spectrum with limited time on target. In addition to estimating the parameters, this thesis extensively discusses the trade-offs and recommends application-specific measurement techniques.

Chapter 2 discusses the historical development of weather radars, the scattering mechanisms of electromagnetic waves, and a brief literature review on the Doppler effect and processing. The chapter also contains a short review of the application affected by the Doppler processing: the 3D wind field estimation. In addition to that, it includes the modern challenges faced by the phased array weather radars deployed at the airports.

Chapter 3 formulates the estimation of statistical Doppler spectrum moments as a parametric estimation problem (parametric spectrum estimator - PSE). The power spectral density (PSD) of the Doppler spectrum is modeled with the Doppler moments but also the limited observation interval. Modeling the PSD with the limited observation interval significantly improved the statistical performance of the parameter estimation. The proposed approach can also accommodate the PSD measurements from incoherent radar scans, typically realized in fast scanning radars.

Chapter 4 formulates the local Doppler spectrum reconstruction with a more generic scenario where the pulse train doesn't necessarily have to be periodic. Contrary to the previous chapter, the Doppler moments estimation problem is formulated in the time domain with a parametric form of the covariance of the echo sequence. It is shown that the performance of the parameter estimation matches that of the PSE but requires more computational resources as it involves an inverse matrix operation. The advantage of this approach is that it can process aperiodically spaced echoes in time, which can be realized when some of the samples are corrupted or for applications where aperiodic pulse trains are purposefully desired for resolving ambiguities. With the proposed approach, the local Doppler spectrum can be reconstructed directly in the frequency domain with the Gaussian process posterior with high resolution.

In chapter 5, the problem of aliasing in the Doppler spectrum is discussed, and an integrative approach is proposed to mitigate the issues in the estimation of the mean Doppler velocity. A comprehensive literature review has been presented where the advantages and limitations of various research disciplines that address the aliasing/ ambiguity are delineated. The integrative approach proposed in this chapter makes use of an appropriate aperiodic pulse train and the complex Gaussian process (CGP) regres-



sion introduced in the chapter 4 to estimate the mean Doppler velocity unambiguously and reconstruct the Doppler spectrum directly in the frequency domain. The proposed approach outperforms the state-of-the-art methods in resolving ambiguity, like the approach involving multiple alternating periodic sequences.

In chapter 6, the formulation of chapter 3 is extended, and a novel generic model of the Doppler PSD is proposed that contains the raindrop size distribution (DSD) and the wind velocity parameters, such as mean wind and turbulence. These parameters are then retrieved with a similar procedure as explained in chapter 3. The proposed technique is effective in fitting the Doppler spectrum with DSD and wind parameters. However, the estimation of DSD parameters from the Doppler PSD is a challenging problem, and these estimated parameters can be heavily biased because the radars are not very sensitive to the smaller raindrops. Despite the biased results, the statistical performance of the DSD-derived parameters, such as the vertical fall speed and the mean diameter, is adequate enough with the proposed approach. As it is a joint estimation of the wind speed and vertical fall speed of raindrops designed for each resolution volume, it can play a pivotal role in the estimation of a 3D wind field with high spatial resolution.

This thesis presents a deeper insight into the Doppler parameters and spectrum estimation for precipitation with scanning radar echoes. It shows that with the proposed signal processing approaches, the statistical performance of the atmospheric Doppler parameter estimation can be significantly improved. Although the core application is precipitation Doppler parameter and spectrum estimation, the techniques developed in the thesis can be easily tuned for other applications involving any form of spectral estimation. In addition, it also presents future research avenues based on the limitations presented in the current research.

# SAMENVATTING

Moderne, multifunctionele grondgebaseerde weerradarsystemen die op luchthavens worden ingezet, zijn ontworpen om puntdoelen, zoals vogels en drones, te detecteren en te volgen. Daarom scannen deze radars het gezichtsveld in azimut zeer snel om snel updates te krijgen over de locaties van deze doelen. De snelle scanmethode van deze radars beperkt echter hun capaciteit om nauwkeurig parameters voor weersvoorspellingsdoeleinden te schatten, zoals de neerslagintensiteit en de snelheidsverdelingsparameters van regendruppels tijdens regenachtige omstandigheden. Dit proefschrift heeft als doel nieuwe technieken te ontwikkelen om de parameters met betrekking tot het Dopplerspectrum van neerslag te schatten met beperkte tijd op het doel. Naast het schatten van de parameters, bespreekt dit proefschrift uitgebreid de afwegingen en geeft het aanbevelingen voor toepassingsspecifieke meetmethoden.

Hoofdstuk 2 bespreekt de historische ontwikkeling van weerradars, de verstrooiingsmechanismen van elektromagnetische golven, en een beknopte literatuurstudie met betrekking tot het Dopplereffect en de verwerking ervan. Het hoofdstuk bevat ook een kort overzicht van de toepassing die door de Dopplerverwerking wordt beïnvloed: de schatting van het 3D-windveld. Daarnaast komen de moderne uitdagingen aan bod waarmee de fasegestuurde antennes op luchthavens worden geconfronteerd.

Hoofdstuk 3 formuleert de schatting van statistische Dopplerspectrummomenten als een parametrisch schattingsprobleem (parametrische spectrumschatter - PSE). De spectrale vermogensdichtheid (PSD) van het Dopplerspectrum wordt gemodelleerd met zowel de Dopplermomenten als het beperkte observatie-interval. Door de PSD te modelleren met het beperkte observatie-interval werd de statistische prestatie van de parameterschatting significant verbeterd. De voorgestelde aanpak kan ook de PSD-metingen van incoherente radarscans verwerken, welke typisch zijn voor snel scannende radars.

Hoofdstuk 4 formuleert de lokale reconstructie van het Dopplerspectrum in een meer generiek scenario waarbij de pulsreeks niet per se periodiek hoeft te zijn. In tegenstelling tot het vorige hoofdstuk wordt het Dopplermomentenschattingsprobleem in dit hoofdstuk geformuleerd in het tijddomein met een parametrische vorm van de covariantie van de echoreeks. Het wordt aangetoond dat de prestatie van de parameterschatting overeenkomt met die van de PSE, maar meer rekenkracht vereist vanwege de betrokken matrixinversieberekening. Het voordeel van deze benadering is dat het aperiodiek gespreide echo's in de tijd kan verwerken, wat nuttig is wanneer sommige monsters beschadigd zijn of voor toepassingen waarbij aperiodieke pulsreeksen opzettelijk worden gebruikt om ambiguïteiten op te lossen. Met de voorgestelde aanpak kan het lokale Dopplerspectrum direct in het frequentiedomein worden gereconstrueerd met de Gaussiaanse procesposterior in hoge resolutie.

In hoofdstuk 5 wordt het probleem van aliasing in het Dopplerspectrum besproken en wordt een integratieve aanpak voorgesteld om de problemen bij het schatten van de gemiddelde Dopplersnelheid te verlichten. Een uitgebreide literatuurstudie toont de

voordelen en beperkingen van verschillende onderzoeksdisciplines die zich richten op aliasing/ambigüiteit. De in dit hoofdstuk voorgestelde integratieve aanpak maakt gebruik van een geschikte aperiodieke pulsreeks en de complexe Gaussiaanse procesregressie (CGP) die in hoofdstuk 4 werd geïntroduceerd, om de gemiddelde Dopplersnelheid eenduidig te schatten en het Dopplerspectrum direct in het frequentiedomein te reconstrueren. De voorgestelde aanpak overtreft de state-of-the-art methoden voor het oplossen van ambigüiteit, zoals de aanpak gebaseerd op meerdere, afwisselende, periodieke reeksen.

In hoofdstuk 6 wordt de formulering uit hoofdstuk 3 uitgebreid en wordt een nieuw generiek model van de Doppler PSD voorgesteld dat de regendruppelgrootteverdeling (DSD) en windsnelheidsparameters, zoals gemiddelde wind en turbulentie, bevat. Deze parameters worden vervolgens teruggevonden met een procedure vergelijkbaar met die in hoofdstuk 3. De voorgestelde techniek is effectief in het modelleren van het Dopplerspectrum met DSD- en windparameters. Het schatten van DSD-parameters uit de Doppler PSD blijft echter een uitdagend probleem, aangezien radars minder gevoelig zijn voor kleinere regendruppels, wat kan leiden tot vertekening in de resultaten. Ondanks deze vertekening is de statistische prestatie van de DSD-afgeleide parameters, zoals de verticale valsnelheid en de gemiddelde diameter, voldoende met de voorgestelde aanpak. Omdat het een gezamenlijke schatting van de windsnelheid en de verticale valsnelheid van regendruppels betreft, die is ontworpen voor elk resolutievolume, kan het een cruciale rol spelen bij het schatten van een 3D-windveld met hoge ruimtelijke resolutie.

Dit proefschrift biedt diepere inzichten in Dopplerparameters en spectrumschatting voor neerslag met behulp van scannende radarecho's. Het toont aan dat met de voorgestelde signaalverwerkingsbenaderingen de statistische prestatie van de atmosferische Dopplerparameterschatting aanzienlijk kan worden verbeterd. Hoewel de kern van de toepassing ligt bij de schatting van Dopplerparameters en -spectrum van neerslag, kunnen de in dit proefschrift ontwikkelde technieken eenvoudig worden aangepast voor andere toepassingen waarbij enige vorm van spectrumschatting betrokken is. Daarnaast biedt het proefschrift toekomstig onderzoek aan op basis van de beperkingen die in het huidige onderzoek zijn gepresenteerd.

# PREFACE

Throughout my Ph.D. journey, I've come to realize that true success transcends mere academic achievements; it encompasses personal growth and self-discovery. This transformative expedition has deepened my understanding of both myself and my role within the broader context of our world. It is my earnest aspiration that this thesis not only contributes to the scholarly discourse but also serves as an inspiration for others to embrace the profound journey of self-discovery inherent in the pursuit of knowledge.

*Tworit Kumar Dash*  
*Delft, June 2024*



# 1

## INTRODUCTION

द्वयं विसृष्टिर्यत आबभूव यदि वा दधे यदि वा न ।  
यो अस्याध्यक्षः परमे व्योमन्सो अङ्ग वेद यदि वा न वेद ॥  
ऋग्वेदः १०.१२९.०७

*iyam visṛṣṭir yata ābabhūva yadi vā dadhe yadi vā na  
yo asyādhyakṣaḥ parame vyoman so aṅga veda yadi vā na veda ॥*

ṛgvedaḥ 10.129.7 International Alphabet of Sanskrit Transliteration - IAST

*This creation, whence it has arisen— whether it was made or not— that which  
surveys it in the highest heaven, it alone knows, or perhaps it does not know.*

Rig Veda 10.129.7 (Translated to English)

## 1.1. ROLE OF DOPPLER RADARS IN WEATHER MONITORING

Weather forecasting has always been a pressing issue, and researchers across various domains work together to create tools, both theoretical and experimental, to tackle the challenge of predicting the weather. As we improve our ability to forecast weather, we enhance our capacity to mitigate the impacts of extreme weather events and adapt to the evolving climate, ultimately contributing to global efforts in climate change adaptation and resilience. Predicting weather accurately is a very broad topic, and it goes outside the scope of the thesis.

However, all disciplines of study that address this issue, whether directly or indirectly, contribute significantly and are essential. The thesis looks at one such discipline, which is dedicated to the precise measurement of specific weather phenomena. Without appropriate instruments and theoretical tools to measure the weather, addressing global challenges like climate change and local issues such as aviation safety becomes implausible.

Many different wireless instruments and systems are used for this purpose. These instruments, such as radiometers, radars, and lidars, study the hydrometeors at a distance without physically interacting with them. The whole process of measuring wirelessly, retrieving critical parameters, and interpreting them is often called remote sensing. These instruments work under the principles of electromagnetic (EM) wave scattering (more on that later in §2.2).

The sub-discipline of atmospheric remote sensing that this thesis focuses on is the accurate estimation of velocity parameters of hydrometeors, particularly raindrops, during precipitation events. The instruments of focus are ground-based weather Doppler radars. The following section explains the difference between the operating principles of traditional and modern radar systems to motivate the need for novel Doppler processing techniques.

## 1.2. WHAT IS THE NEED FOR NEW DOPPLER PROCESSING TECHNIQUES FOR WEATHER RADAR? WHY DOPPLER PROCESSING FOR FAST SCANNING WEATHER RADARS?

In traditional weather radar systems, the radars typically scan the whole field of view mechanically at a fixed elevation angle. Due to the mechanical scan of the radar beam, the time that it spends at each radar resolution volume is limited. As the time on target for each resolution volume determines the velocity resolution (for Doppler processing), scan strategies are carefully designed. This scan rate, while effective for detailed weather observations, is sometimes inadequate for rapidly updating information on pointed targets like birds and drones. Modern phased array radars, designed to scan and track these fast-moving objects quickly, highlight the limitations of conventional methods when applied to weather-related signal processing. Therefore, to enhance radar capabilities for both rapid target detection and accurate weather monitoring, novel Doppler processing approaches are essential. These advanced techniques must reconcile the need for fast scanning with the requirement for precise weather data, enabling radars to provide timely

updates across the entire field of view while maintaining the accuracy needed for comprehensive meteorological analysis.

It is crucial to understand that the notions of "fast" and "slow" are relative and context-dependent, varying significantly with the specific demands of the radar application (more on it in §3.2). In weather radar systems, a scan rate considered fast enough to capture rapid meteorological changes might still be insufficient compared to the demands of other applications that require more immediate updates. Therefore, a comprehensive scientific investigation into the trade-offs involved in Doppler processing is necessary. The development of novel Doppler processing techniques and their performance estimation under a range of diverse weather conditions, considering factors such as precipitation intensity, storm dynamics, and turbulence, has become a necessity.

Furthermore, the importance of these advancements is underscored by their deployment in critical environments like airports, where weather radars play a pivotal role in aviation safety. The ability to rapidly and accurately monitor weather conditions is essential for ensuring safe aircraft operations and preventing adverse weather-related incidents. Additionally, incorporating statistical performance metrics is essential to this analysis. Evaluating the accuracy, reliability, and overall effectiveness of different processing methods through rigorous statistical assessments will provide deeper insights into their practical applicability. By systematically studying these trade-offs and performance statistics, one can better understand how to balance scan speed with the precision of weather information. This approach will help optimize Doppler processing methods to ensure that weather radars can deliver timely, accurate, and reliable data, ultimately enhancing the effectiveness of weather monitoring systems and improving our ability to respond to dynamic weather events.

### 1.3. RESEARCH QUESTIONS ADDRESSED IN THE THESIS

The following research questions are addressed in the thesis:

1. How to accurately estimate the Doppler spectral moments with limited time on target? How do we make use of the radar-backscattered echoes from several fast scans of the radar (coherent echo sequences from individual radar scans that are mutually incoherent across scans) to estimate the Doppler moments?
2. How do we accurately estimate the Doppler spectral moments for aperiodically sampled echo sequences? How do we reconstruct the local spectrum with a few echo samples aperiodically spaced?
3. Which probing pulse sequences should be used for unambiguous estimation of the Doppler spectrum, and how to reconstruct the local spectrum with a few echo samples from such a sequence? How the Doppler moments of precipitation can be estimated unambiguously? How to mitigate aliasing effects in the Doppler spectrum? How do we unambiguously estimate the mean Doppler velocity of precipitation?
4. How to simultaneously estimate the contribution of the radial wind and vertical fall velocities of raindrops on the Doppler spectrum with limited time



on target? Can we accurately and effectively fit the Doppler spectrum with a generic model involving the raindrop size distribution (DSD) parameters?

## 1.4. RESEARCH APPROACHES AND OUTLINE OF THE THESIS

To address these questions, the main body of the thesis is organized as follows:

### CHAPTER 2

In this chapter, a broad overview of weather radar signal processing is presented, starting with a brief history of the development of meteorological radar systems, followed by the physical principles with which meteorological radars operate (electromagnetic scattering of microwaves), to the mathematical frameworks that have paved the way for processing radar signals to get valuable insights about the weather. The chapter explains the Doppler effect and the Doppler shift observed in the radar echo sequence, which the radar systems take advantage of to deduce the motion of hydrometeors. Finally, it presents state-of-the-art 3D wind field estimation using weather radars and advancements/ challenges associated with modern fast-scanning phased array radars deployed typically at airports. In each sub-section of the chapter, the added value and novelty of the thesis have been highlighted.

### CHAPTER 3

This chapter addresses the first research question mentioned in §1.3. It underscores the importance of estimation accuracy for Doppler moments. It has a detailed state-of-the-art section (§3.2) explaining the current methods to estimate the Doppler moments for precipitation. The chapter presents further enhancements to the Doppler moment estimation by proposing a novel model of the Power Spectral Density (PSD) as a function of the Doppler moments, but also the dwell time (total time of observation). By adding the dwell time into the model, it has been shown that the statistical performance of the Doppler moment estimation has significantly improved. Furthermore, the proposed parametric maximum likelihood estimation approach (also called as the Parametric Spectrum Estimator - PSE) can incorporate PSD measurements from several scans of the radar, assuming the stationarity condition of the atmosphere. Its limitation at higher spectral widths (a measure of the turbulence present in precipitation), formulae for theoretical variance, and Crámer Rao Lower Bound (CRB), along with a scanning strategy for smaller spectral widths (for accurate estimation), have been presented in this chapter. An experimental validation has been carried out to show the applicability of the proposed approach. This chapter is successful in addressing the research question but also shows the limitations of the approach for weather conditions that are rapidly changing, like the melting layer of the atmosphere.

## CHAPTER 4

This chapter introduces a different technique to estimate the Doppler moments and reconstruct the echo sequence and the local Doppler spectrum with a few echo samples in one sequence, which are not necessarily placed periodically. A practical application of aperiodically sampled sequence can be realized when some of the samples are corrupted or interfered with or in cases where it is purposefully made aperiodic to mitigate aliasing in the spectrum. A complex Gaussian process regression (CGP-R) approach (leveraging a known form of the covariance of the echo sequence) is proposed with which the Doppler moments can be estimated, and the local Doppler spectrum can be reconstructed. The proposed approach has been implemented on simulated and real radar echo sequences. This chapter is successful in addressing the second research question mentioned in §1.3. This approach can be used directly and accurately for each scan of a fast-scanning radar.

## CHAPTER 5

This chapter addresses the issue of aliasing observed in the Doppler spectrum. A detailed inquiry about aliasing/ ambiguity is presented in §5.2 from several research areas. An integrative approach has been presented where an aperiodic sampling of the radar echo sequence is proposed along with a suitable inverse technique (with CGP-R proposed in chapter 4) to reconstruct the Doppler spectrum. It is concluded that with this integrative methodology, the mean Doppler velocity of precipitation can be unambiguously estimated. Furthermore, it has been shown with simulated radar echoes that this approach is applicable for applications involving multiple extended targets (multi-layered precipitation or with the presence of vortices inside precipitation). Although this approach is effective and accurate in estimating the Doppler parameters and local Doppler spectrum, its limitations are presented. A trade-off between the applicability of this approach in terms of the spectral widths and the non-linearity in the sampling sequence has been presented. The superiority of this approach is shown by comparing it with state-of-the-art techniques along with the well-known staggered sequence approach. This chapter adequately addresses the third research question presented in §1.3.

## CHAPTER 6

In this chapter, the challenge of jointly estimating the parameters of rain Drop Size Distribution (DSD) and radial wind velocities with a very fast scanning weather radar is addressed. The approach is named as Wind and DSD Estimation (WiDSE). A novel semi-analytical expected Doppler PSD model has been proposed as a function of the above-mentioned parameters and the dwell time. A maximum likelihood estimation is proposed where the measurements are the stochastic Doppler PSD realizations. The proposed approach has been compared with one state-of-the-art estimator that uses the Doppler PSD as the measurement. Furthermore, the proposed technique can use incoherent PSD measurements from several fast radar scans. The estimator's performance has been assessed by the theoretical variance in the estimates, and it is shown that this variance converges to the CRB when the number of echo samples

reaches infinity. An unprecedented analysis with parameter sweeps with respect to the number of echo samples  $N$ , wind spectral width  $\sigma_v$ , the DSD parameters ( $\eta$  and  $\Lambda$ ), and the number of incoherent PSD measurements  $L$  is presented. Although the proposed approach performs better than the existing approximate approaches, it is shown that the estimation of DSD parameters, in general, is very challenging because the log-likelihood (cost function with radar retrieved measurements) is not very sensitive to the DSD parameters. Nonetheless, even though estimates of DSD parameters are biased, the Doppler spectrum's fitting is sufficient for determining derived parameters such as the terminal fall velocity and median volume diameter of the raindrops. The proposed approach is implemented on simulated and real weather radar echoes. This approach can effectively be used on echo sequences gathered from several scans for each radar resolution cell. Furthermore, this approach can help decompose the radial Doppler velocity into a sum of the estimated terminal fall velocity and the radial wind velocity (with turbulence).

## CHAPTER 7

This chapter contains the conclusions drawn from the thesis and presents several ideas for future research.

## APPENDICES

### APPENDIX A

This appendix contains the expected value of the power spectrum used in chapter 3.

### APPENDIX B

This appendix contains the derivation of the theoretical variance and the CRB for PSE and CGP approach used in chapters 3, 4, 5.

### APPENDIX C

This appendix contains the study of the covariance of the signal related to the vertical fall of raindrops  $G(q)$  used in chapter 6.

### APPENDIX D

This appendix contains the derivation of the theoretical variance and the CRB of the WiDSE approach used in chapters 6.

# 2

## A BRIEF OVERVIEW OF ATMOSPHERIC WEATHER RADAR REMOTE SENSING

*This chapter provides an overview of the historical development and current state of research in weather radar remote sensing applications. An introductory section sets the stage for understanding the broader context within which this thesis is situated, highlighting the specific issues it addresses. Additionally, this chapter elucidates the applications directly impacted by the research outcomes presented herein. Furthermore, it introduces the terminologies and conventions employed throughout the thesis.*

*The laws governing the motion of air molecules, and also of the other physical quantities that might be relevant to computing the weather, all are perfectly well known. However, the weather patterns that may actually emerge, after only a few days, depend so subtly on the precise initial conditions that there is no possibility of measuring the conditions accurately enough for reliable prediction.*

§1.7, (Chaos)

R. Penrose, *Shadows of the Mind: A Search for the Missing Science of Consciousness*.  
Oxford University Press, 1994

---

Parts of this chapter have been published in:

T. Dash, O. A. Krasnov, and A. G. Yarovoy, "Performance Analysis of the Wind Field Estimation for a Very Fast Scanning Weather Radar," in *2022 23rd International Radar Symposium (IRS)*, pp. 420–425, IEEE, 9 2022

The following sections dive deep into the historical development, state-of-the-art weather radar systems, principles of EM scattering in the atmosphere, wind field estimation with Doppler radars, advancements and challenges in modern weather radar technologies, and the terminology adopted in the thesis.

## 2.1. HISTORY OF WEATHER RADAR SYSTEMS

Weather radar remote sensing has evolved significantly since its inception and has become an essential tool in meteorology. This section outlines the historical development of weather radar systems and their current state.

### 2.1.1. EARLY DEVELOPMENTS (1940s-1960s)

Initial weather radars were developed for defense during World War II. These radars were S-band frequency range ( $2 \rightarrow 4\text{GHz}$ ). This band of frequencies was chosen to have a balance between good range resolution and its ability to penetrate heavy precipitation without significant attenuation.

The scattering in the S-band for hydrometeors like raindrops, snowflakes, and hailstones primarily follows the Rayleigh scattering principles. The radar wavelengths in this band ( $15 \rightarrow 7.5\text{cm}$ ) are much higher than the sizes of the raindrops ( $0.1\text{mm} \rightarrow 6\text{mm}$  [7]). The radar received power from these hydrometeors is proportional to the sixth power of the diameter. Therefore, these radars are sensitive to the larger hydrometeors and not sensitive to the smaller ones, like light drizzles and cloud droplets [8].

### 2.1.2. DOPPLER RADAR IN THE LATE 1960s

In addition to detecting precipitation, the technology in the late 1960s allowed radar systems to deduce the radial velocity of the ensemble of raindrops (in large volumes) using the principles of the Doppler effect. This capability provided critical information about wind patterns within storms, significantly enhancing the detection and prediction of severe weather events such as tornadoes and hurricanes.

The C-band radars ( $4 \rightarrow 8\text{GHz}$ ) operate in a scattering regime that is still largely governed by Rayleigh scattering for typical hydrometeors but with slightly higher resolution and sensitivity to smaller particles compared to S-band radars. These advancements allowed meteorologists to identify features like wind shear and tornado signatures with greater accuracy [9] (more on it in §2.3).

Before the advent of dual-polarization technology, conventional Doppler radars were only capable of measuring (estimating) the first three Doppler moments. The zeroth moment is the reflectivity, which in the Rayleigh regime is proportional to the sixth moment of the particle size distribution (more on that in §2.2). The first moment is the mean Doppler velocity of the scatterers, and the second moment is the square of the Doppler spectrum width. For each radar resolution volume, these three spectral moments are computed.

### 2.1.3. DUAL POLARIZATION RADARS

The introduction of dual-polarization (in the late 20<sup>th</sup> and early 21<sup>st</sup> century) radars paved the way to acquire unprecedented information about the atmosphere by exploiting two different polarizations of the EM waves. As these radars use two different orthogonal polarizations, identifying different precipitation types and estimating more accurate rainfall rates became possible [10].

The dual-polarization radar systems compute derived quantities like the differential reflectivity  $Z_{dr}$ , the linear depolarization ratio ( $L_{dr}$ ), differential phase ( $\beta_{dp}$ ), and its derivative with respect to range ( $k_{dp}$ ). These quantities help discern different kinds of hydrometeors and their phases (rain, hail, snow), enhancing the understanding of complex precipitation processes [11, Ch. 19a], [8, Ch. 8, §8.5.3].

### 2.1.4. PHASED ARRAY RADARS

The phased array radars operate under the principles of superposition of the signals received at several antennas placed in space according to some specific rules. These radars can steer the antenna beam in directions of interest based on the phase difference between the antennas. Unlike conventional radars, these radars can provide precipitation profiles in elevation instantaneously. Thus, in addition to radar range and Doppler, angular information can also be provided [12].

These phased array radars usually operate in the X-band ( $8 \rightarrow 12\text{GHz}$ ), offering higher resolution and better sensitivity to small-scale precipitation features, making them ideal for studying rapidly evolving weather systems.

## 2.2. ELECTROMAGNETIC ASPECTS AND RAYLEIGH SCATTERING

### 2.2.1. SCATTERING PRINCIPLES AND REGIMES

To understand the signals received from hydrometeors in weather radar, one needs to understand the scattering phenomena. As the phenomena occur in space when the EM waves interact with the hydrometeors, it can be safely assumed that these waves are plane waves. Plane waves are the general solution to Maxwell's equations in space. The electric and magnetic fields for plane waves can be represented as follows:

$$\begin{aligned}\mathbf{E}(\mathbf{r}, t) &= E_0 \exp(j(\mathbf{k} \cdot \mathbf{r} - \omega t + \beta)), \\ \mathbf{B}(\mathbf{r}, t) &= B_0 \exp(j(\mathbf{k} \cdot \mathbf{r} - \omega t + \beta)),\end{aligned}\tag{2.1}$$

where  $E_0$  and  $B_0$  are the amplitudes of the electric and magnetic fields respectively,  $j = \sqrt{-1}$ ,  $\mathbf{k}$  is the wave number vector:

$$\mathbf{k} = k_x \hat{\mathbf{x}} + k_y \hat{\mathbf{y}} + k_z \hat{\mathbf{z}},\tag{2.2}$$

where  $\hat{\mathbf{x}}$ ,  $\hat{\mathbf{y}}$ ,  $\hat{\mathbf{z}}$  are the unit vectors in  $x$ ,  $y$  and  $z$  directions respectively. The amplitude of  $\mathbf{k}$  vector is  $k_0$ , which is the wavenumber  $k_0 = 2\pi/\lambda$ , where  $\lambda$  is the EM wave's

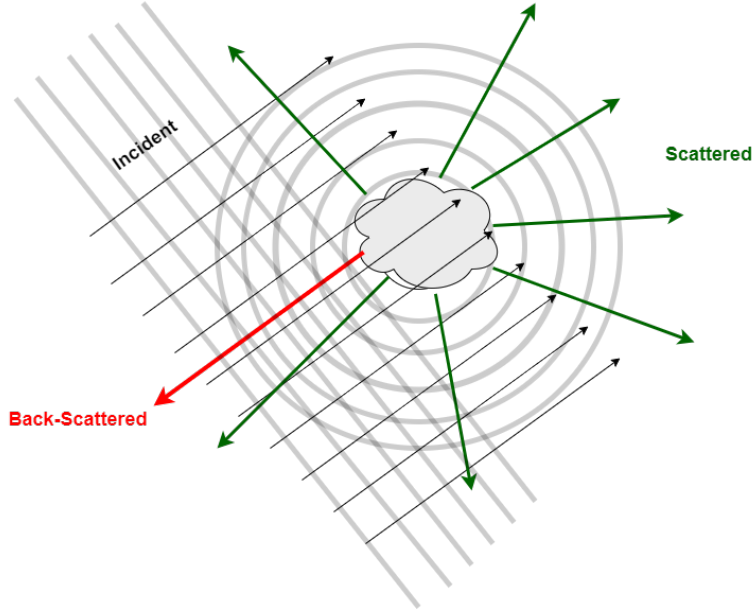


Figure 2.1: Scattering phenomena.

wavelength. The  $\mathbf{r}$  is the position vector  $\mathbf{r} = x\hat{\mathbf{x}} + y\hat{\mathbf{y}} + z\hat{\mathbf{z}}$ ,  $\omega$  is the angular frequency of the EM wave ( $\omega = 2\pi f = 2\pi c/\lambda$ , where  $c$  is the speed of light,  $f$  is the frequency of the EM wave),  $t$  and  $\beta^1$  are time and the initial phase of the EM wave. Thus, the term  $\mathbf{k} \cdot \mathbf{r}$  encapsulates the spatial variation of the wave's phase in the direction of the wave vector  $\mathbf{k}$  and  $\omega t$  represents the evolution of the temporal phase of the wave.

When the EM wave is incident on a target/ object, the object scatters the energy in different directions based on its geometry. For radars, the back-scattered fields are important as these are the only scattered fields that arrive at the radar. A back-scattered field is a field that is scattered exactly in the direction from where they arrived in the first place (Fig. 2.1).

If the incident field is denoted as  $\mathbf{E}^i = \mathbf{E}_0^i \exp(j(\mathbf{k}_1 \cdot \mathbf{r} - \omega t))$ , the scattered field  $\mathbf{E}^s$  is given by <sup>2</sup>:

$$\mathbf{E}^s = f(\mathbf{K}_1, \mathbf{K}_2) r^{-1} \exp(-jkr), \quad (2.3)$$

where  $\mathbf{K}_1$  is the unit vector along the incident wave, and  $\mathbf{K}_2$  is a unit vector directed from the origin to the observation point. The function  $f(\mathbf{K}_1, \mathbf{K}_2)$  is a vector function denoting scattering amplitude and the polarization state of the scattered wave [1]. An illustration of the scattering mechanism with vectors is presented in 2.2.

The size parameter  $\chi$  defines the scattering regimes. The size parameter is given

<sup>1</sup>The notation  $\beta$  is chosen for phase unlike popular literature because  $\psi$ ,  $\phi$ , and  $\theta$  are reserved in this thesis for elevation, azimuth, and parameters (for estimation problems).

<sup>2</sup>In this chapter, the notation  $r$  for electric field equations (like in (2.3)) represents the range. However, for the size parameter (like in (2.4)),  $r$  represents the radius of the scatterers.

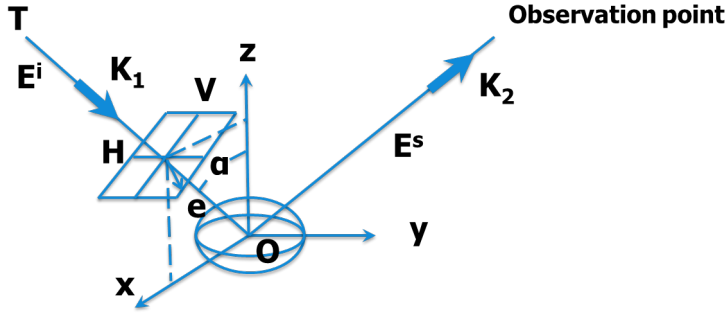


Figure 2.2: Scattering illustration with vectors. Adapted from [1, Fig.1].

by:

$$\chi = \frac{2\pi r}{\lambda}. \quad (2.4)$$

Another parameter that affects the scattering is the relative refractive index  $m$ , which is given by:

$$m = \frac{n_2}{n_1}, \quad (2.5)$$

where  $n_2$  and  $n_1$  are the refractive indices of the object and the surrounding medium, respectively.

The different kinds of scattering regimes are explained below:

1. **Rayleigh Scattering:** Rayleigh Scattering occurs when the size (denoted with radius  $r$ ) of the scatterers is much smaller than the wavelength of the incident wave:

$$\chi \ll 1, r \ll \lambda. \quad (2.6)$$

2. **Mie Scattering:** Mie Scattering occurs when the size of the scatterers is similar to the wavelength of the incident wave:

$$\chi \approx 1, r \approx \lambda. \quad (2.7)$$

3. **Geometrical Optics:** In this regime, the wavelength is much smaller than the size:

$$\chi \gg 1, r \gg \lambda. \quad (2.8)$$

This chapter focuses on the Rayleigh scattering only, as it is relevant for the chapter 6 of the thesis. However, the real radar data used in this thesis are from an X-band radar at a center frequency of 9.5 GHz. The size parameter  $\chi$  is approximately equals to  $0.2r$  ( $r$  in mm) at this center frequency. Typical raindrop diameters are less than 4mm ( $r = 2$  mm), and they rarely exceed 6 mm ( $r = 3$  mm). If we consider a maximum diameter of 6 mm ( $r = 3$  mm), the size parameter becomes  $\chi_{\max} \approx 0.6$ , which is not small enough to be considered in the Rayleigh regime. The Rayleigh



scattering regime can safely be assumed for a radius less than  $\lambda/20$ . At 9.5 GHz, this maximum radius is  $r_{\max}^{(\text{Rayleigh})} = 1.6$  mm (e.g, in [13, Tab. 5.1] it says that Rayleigh regime can be applied for  $r_{\max}^{(\text{Rayleigh})} = 1.15$  mm). For raindrops exceeding this radius experience a mix of Rayleigh and Mie scattering instead of purely Rayleigh scattering. There is a gradual introduction of Mie scattering for  $r > 1.6$  mm. It implies that the Rayleigh approximation completely holds for light rain events, but as the sizes of the raindrops increase, Mie scattering plays a role.

However, modeling the scattered power with a Mie scattering model is mathematically very involved and is out of the scope of this thesis. For the Doppler parameter estimation in chapters 3, 4 and 5 do not consider any explicit model of the reflectivity as the focus is on retrieving the Doppler moments/ spectrum. The reflectivity is considered a nuisance parameter and is estimated with the total power contained in the signal (more on it in chapter 3). However, in the simulations of chapter 6, the reflectivity in the PSD is modeled with the Rayleigh approximation in X-band frequencies to avoid mathematical complexity (similarly as in [14], [15]). A complete scattering model considering Rayleigh and Mie scattering can be considered in the future.

The scattered intensity in the Rayleigh regime is proportional to the sixth power of the particle diameter and inversely proportional to the fourth power of the wavelength. The following §2.2.2 explains the scattering from rain in the Rayleigh regime.

### 2.2.2. RAINDROP BACKSCATTERING

If we consider a volume of raindrops (and not one isolated raindrop) because the wavelengths in the Rayleigh regime are much larger than the size of the raindrops, the backscattering cross-section per volume  $\Sigma_{\text{Vol}}$  [16, Eq. (66)] can be given as (assuming spherical raindrops) <sup>3</sup>:

$$\Sigma_{\text{Vol}} = \frac{\pi^5}{\lambda^4} \left| \frac{m-1}{m+2} \right|^2 R, \quad (2.9)$$

where  $R$  is the radar reflectivity factor, which is given by [16, Eq. (67)]:

$$R = \int_{D_{\min}}^{D_{\max}} N(D) D^6 dD, \quad (2.10)$$

where  $D$  is the diameter of the raindrops and  $N(D)$  is the drop-size distribution. There are many models explaining the drop size distribution of raindrops inside a volume (more on this in chapter 6).

<sup>3</sup>A change of notation is adopted in this thesis, which is not typically present in popular literature. Radar reflectivity factor  $Z$  is changed to  $R$ , as  $Z$  is used in later chapters for measurements of power spectral density (more on it in chapter 3). The backscattering cross-section  $\sigma$  is changed to  $\Sigma$ , as  $\sigma$  is reserved later for the standard deviation. These changes are adopted as the thesis also uses terminologies of estimation theory, which might create confusion if not discernible from the scattering-related physical quantities.

## 2.3. DOPPLER VELOCITY AND WIND FIELD ESTIMATION WITH WEATHER RADARS

With the introduction of weather Doppler radars, which are capable of Doppler processing, the estimation of wind fields became an interesting problem to tackle. Let's first discuss the Doppler shift observed by the radars in general before discussing the estimation of wind fields.

### 2.3.1. DOPPLER SHIFT

The Doppler shift is the change in frequency observed due to the relative motion between the source and observer. Let's consider a radar that generates a train of microwave pulses spaced with an interval of  $T_s$  in time (Pulse Repetition Interval or PRT); each pulse has a duration  $\tau$ . if the radar is stationary, and a point scatterer at a range  $r$  is moving with a velocity  $v$ ; the signal received in time for this one object can be expressed as [8, Eq. (3.25)]:

$$x(t, r) = A \exp \left( j 2 \pi f \left( t - \frac{2r}{c} \right) + j \beta \right) U \left( t - \frac{2r}{c} \right), \quad (2.11)$$

where  $U \left( t - \frac{2r}{c} \right)$  is:

$$U \left( t - \frac{2r}{c} \right) = \begin{cases} 1 & , \quad \frac{r}{c} \leq t \leq \left( \frac{r}{c} + \tau \right) \\ 0 & , \quad \text{otherwise.} \end{cases} \quad (2.12)$$

The amplitude of the scatterer is  $A$  (proportional to the electric field in the direction of the backscattered field). This complex amplitude  $A = |A| \exp(j\beta_s)$  encompasses all the effects, such as the scattering and attenuation. The  $\beta_s$  is the phased shift caused by the scatterer. The total echo phase  $\beta_e$  is therefore given as [8, Eq. (3.26)]:

$$\beta_e = -\frac{4\pi r}{\lambda} + \beta_t + \beta_s, \quad (2.13)$$

where  $\beta_s$  is the phase shift caused by scattering,  $\beta_t$  is the transmitter phase shift ( $\omega t$  is not included in this expression).

The angular Doppler frequency shift is nothing but the change of the phase  $\beta_e$ . The quantities that change over time are  $r$  and  $\beta_s$ .

$$\omega_d = \frac{\partial \beta_e}{\partial t} \quad (2.14)$$

If  $\beta_s$  is not changing over time, (2.14) can be rewritten as [8, Eq. (3.30)]:

$$\omega_d = \frac{\partial \beta_e}{\partial t} = -\frac{4\pi}{\lambda} \frac{\partial r}{\partial t} = -\frac{4\pi}{\lambda} v_r, \quad (2.15)$$

where  $v_r$  is the Doppler velocity. It is worth noting that the Doppler velocity is the estimate of only one component of the target's resultant velocity in space. The resultant velocity is the total velocity vector of the target in 3D space. The component that is observable by the radar when transmitting to one direction in space is the radial component (the subscript  $r$  represents the radial component).

The expression and discussion of  $\nu_r$  as a function of the other components are given in further chapters 3 and 6.

A physical explanation for the Doppler shift is as follows: A pulse of radiation striking a hydrometeor induces molecular vibrations that synchronize with the time-varying electric and magnetic fields. If the hydrometeor is moving toward the transmitter at a velocity  $\nu_r$ , its vibrational frequency increases by  $\nu_r/\lambda$  because the scatterer molecules experience more rapid fluctuations of electric and magnetic forces. These vibrating molecules then generate electromagnetic fields that radiate outward from the scatterer. The Doppler frequency shift is  $f_d = 2\nu_r/\lambda$ ; the factor of 2 comes from the fact that the frequency of the radiation field in the direction of the receiver is increased by a further  $\nu_r/\lambda$  [8, §3.4.3].

The objective of any Doppler processing algorithm is to retrieve the information  $f_d$  and, by extension,  $\nu_r$  given a set of echo samples in time (an echo sequence). It is a usual practice to change the domain of the signal, e.g., frequency or correlation domain, to estimate the Doppler frequency shift (more on it in chapter 3).

Transforming the signal to a different domain is beneficial because it can enhance certain features of the signal, making the Doppler frequency shift more discernible. For example, in the frequency domain, periodic components of the signal become more apparent, which is crucial for identifying and measuring the frequency shift caused by the Doppler effect. This approach leverages the Fourier transform, which is widely used due to its ability to decompose a signal into its constituent frequencies.

Notable studies have underscored the advantages of such transformations. In [8], the authors discuss how Fourier-based methods facilitate the separation of different velocity components in meteorological radar signals, thereby improving the accuracy of velocity measurements.

The above-mentioned explanations for the Doppler effect are for pointed targets. However, when we consider many scatterers inside a big resolution volume (like in the case of weather radars), the echo sample signal in time can be written as (detailed expressions in §3.3):

$$s(t, r) = \sum_{m=1}^M x_m(t, r), \quad (2.16)$$

where  $M$  is the number of scatterers and  $x_m(t, r)$  are the echo sequence of  $m$ th scatterer. The objective of Doppler processing algorithms for signals from hydrometeors is, therefore, should be to detect all the frequencies present in the signal (2.16). However, as  $M$  can be a very large number, the signal becomes stochastic in nature, and estimating all frequencies in the signal becomes uninformative. The frequency domain response of stochastic signals is continuous. Therefore, it is sufficient to retrieve only some parameters that can describe the whole Doppler spectrum (the frequency response of echo sequence is denoted as the Doppler spectrum) instead of retrieving each and every frequency present in the signal. The motion of scatterers can be very random in the resolution volume. However, the signal can still remain stationary. A signal is classified as “stationary” when the statistical properties of the signal are independent of time, although the

signal samples themselves can be a random variable in time. A completely stationary process does not exist, especially in weather where the atmospheric parameters are constantly changing. However, given a short observation interval<sup>4</sup>, and the signal can be considered stationary. There are different kinds of stationary random processes, and the echo samples from hydrometeors are often considered wide-sense stationary (WSS) for a short time period. The following conditions have to be met for a random process  $X$  to become WSS:

1.  $\mathbb{E}[X] = \mu_X$ ,
2.  $\mathbb{V}[X] = \sigma_X^2$ ,
3.  $\mathbb{E}[X(t_p)X^*(t_q)] = C(t_p - t_q) = C(\tau)$ ,

where  $C$  is the covariance, which is a function of the difference of times only ( $t_p - t_q$ ) (more on it in §4.2). It has a constant mean ( $\mu_X$ ) and a constant variance ( $\sigma_X^2$ ) as well. The symbols  $\mathbb{E}$  and  $\mathbb{V}$  denote expected value and variance, respectively. The superscript  $*$  denotes the complex conjugate. The power spectrum of the WSS is the Fourier transform ( $\mathcal{FT}$ ) of its autocorrelation (autocovariance) (Wiener–Khinchin theorem)<sup>5</sup>.

$$S_{(\text{PSD})}(f) = \mathcal{FT}[C(\tau)](f) = \int_{-\infty}^{+\infty} C(\tau) \exp(-j2\pi f\tau) d\tau \quad (2.17)$$

For stationary random processes, the parameters controlling  $S(f)$  and  $C(\tau)$  do not change in time. The parameters that affect these quantities are estimated to provide an informative quantification of the processes. The usual process followed in the case of echoes from hydrometeors in precipitation events is to estimate the statistical Doppler moments. The details of these are presented in chapter 3. In this thesis, the estimation of the Doppler moments is extensively studied, and new approaches are presented (chapter 3, chapter 4). The chapters 3 and 4 discuss the Doppler moments estimation with short echo sequences with multiple periodic sequences (typically realized from multiple scans of radar) and aperiodic sequences with missing echo samples, respectively. Furthermore, given a short echo sequence, a full reconstruction of the local spectrum is presented (chapter 4).

Chapter 5 discusses the problem of Doppler spectrum aliasing when the scatterers' velocities fall outside the radar's unambiguous velocity interval. Aliasing is a very well-known issue not only in the field of radar but in other domains as well, where the signal of interest has a sampling interval (in this case, it is the PRT) that is not small enough to capture the fast-moving phenomena in the signal (in this case, it is the Doppler frequency/ velocity). Due to aliasing, the Doppler moment estimations can be wrong (especially the mean Doppler velocity  $\mu_v$ ; more on it in

<sup>4</sup>The use of "short" in this context does not mean there is a universal observation interval that applies to all weather applications to realize a stationary random echo sequence (process). For stratiform rain events with weaker wind fields, the observation time (to realize stationarity in the signal) can be longer than storms that are affected by variable background wind fields, convective storms, etc.

<sup>5</sup>Only continuous Fourier transforms are shown in this chapter. In later chapters, discrete Fourier transforms are demonstrated.

the next subsection 2.3.2), causing issues in decision-making under adverse weather conditions (e.g., aviation).

Earlier attempts at mitigating the aliasing issue in Doppler by simply decreasing the PRT resulted in the well-known range-Doppler dilemma. The maximum unambiguous range ( $r_a$ ) is directly proportional to the pulse repetition interval, but the maximum unambiguous velocity ( $V_a$ ) is inversely proportional to it.

$$\begin{aligned} r_a &= \frac{cT_s}{2}, \\ V_a &= \frac{\lambda}{4T_s}, \\ r_a V_a &= \frac{c\lambda}{8}. \end{aligned} \tag{2.18}$$

The product of  $r_a$  and  $V_a$  is a constant indicating that one has to make a compromise in either range or velocity unambiguous interval. Due to this dilemma, radar waveform design becomes a crucial task. With approaches dealing with aperiodically sampled sequences for Doppler processing, a maximum range (for Doppler-related computations) is chosen using the minimum PRT present in the sequence of echoes. For example, for a two-pulse repetition time-based staggered sampling scenario, the reliable Doppler velocity estimates are drawn from ranges with a maximum range associated with the shorter PRT [17], [18], [19]. There are other techniques [20], [21] to deal with overlaid signals and improve the unambiguous range, but this is outside the scope of the thesis.

An aperiodically sampled echo sequence is proposed in chapter 5 to mitigate the aliasing issue and enhance the unambiguous velocity interval. The sampling sequence proposed in this thesis is a log-periodic one, which is parametrized in a way that the minimum PRT can be fixed. This parameter can be tuned based on the maximum range requirements (to perform Doppler processing). Doppler spectrum moments play a crucial role in further interpreting the storm dynamics. For example, a spatio-temporal distribution of the mean Doppler velocity can be used to reconstruct the wind fields in space and in time. The following sub-section explains the trends followed for the wind field estimation.

### 2.3.2. WIND FIELD ESTIMATION

In the context of weather radar signal processing, the notion of "wind" is different than in other fields. Here, the wind field is the velocity with which the ensemble of scatterers (e.g., raindrops) move in space. The actual wind field is the motion of the aerosols (even smaller particles than the hydrometeors that are not sensitive to weather radars). There is a difference between the actual wind field (aerosol motion) and the motion of the ensemble of the hydrometeors, and it can be explained by the inertia effect [22, Ch. 2]. However, we do not consider the inertia effect in the thesis and only consider the motion of the hydrometeors.

As pointed out in the previous sub-section, the Doppler velocity is the radial velocity of the scatterers only; to deduce the wind fields (resultant velocity), one

needs more information. Apart from the wind, Doppler velocity also includes the vertical fall velocity of the hydrometeors (more on this in chapter 6) if the radar beam's elevation direction is greater than 0 ( $\psi > 0$ ). To retrieve the wind field only, one needs to estimate and eliminate the terminal fall velocity of the raindrops from the Doppler velocity.

The traditional weather radars scan the atmosphere (in azimuth  $\phi$  at a fixed elevation  $\psi$ ) and retrieve the mean Doppler velocities from several different directions. The azimuthal variation of the mean Doppler velocity can give some ideas about the wind fields and was discussed first in [9] and applies to the observations. In [9], it is assumed that the resultant wind field as a function of azimuth can be decomposed with a Fourier series with a few components. The zeroth harmonic explains the pure divergence; the first harmonic explains pure translation, and the second harmonic explains pure deformation. The order of the Fourier series can be higher than two, but for simplicity, it is considered to be 2. This approach is called the Velocity Azimuthal Display (VAD).

$$\mu_v(\phi) = a_0 + \sum_{k=1}^2 a_k \cos(k\phi) + b_k \sin(k\phi). \quad (2.19)$$

The objective is to estimate the coefficients  $a_k$ ,  $k = 0, 1, 2$ . If there is no vertical wind effect, the quantity  $a_0$  explains an averaged estimate of the projection of the vertical fall speed of hydrometeors onto the radial direction. In this approach, it is assumed that the wind field is homogeneous, i.e.,  $a_k$ ,  $k = 0, 1, 2$  are constants and are not functions of space. However, in realistic scenarios, local wind fields can exist.

To estimate the local wind fields, more information is needed, and approaches such as the simple adjoint (SA) and least squares (LS) method [22–28] in 3-D and 4-D use the continuity of the reflectivity field in time (with the assumption that the reflectivity field is conserved) and Doppler information to deduce local wind fields. The terminal fall velocity of the scatterers is separately estimated with external inputs (vertically pointed radars or non-radar inputs computed from retrieved rainfall rates). The studies mentioned above are called single Doppler velocity retrieval techniques (SDVR). There are approaches that involve the data from two Doppler radars (dual-Doppler approach) [29] as well. In all these techniques, the assumption of reflectivity conservation (with the continuity equation) can be inadequate as the concepts of the incompressible flow of fluids can not directly be applied to the reflectivity images of weather radars.

There are other approaches [30] that try to compute the contribution of the terminal fall velocity and the wind velocity jointly by modeling the Doppler spectrum with parameters related to the DSD of the hydrometeors. The terminal fall velocity is a function of the DSD [2, Eq. (4)]. If the wind and DSD parameters are computed jointly for each resolution cell, the 3D wind field can easily be deduced. However, these approaches are computationally very expensive. In this thesis, a novel model of the Doppler spectrum is presented with the wind and DSD parameters in chapter 6.

There are other approaches to estimating DSD parameters using polarimetric variables, but these are not in the scope of this thesis. The details about the

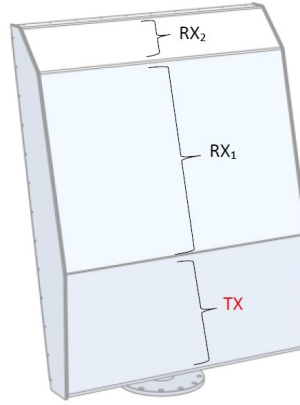


Figure 2.3: Max3D phased array X-band radar.

challenges in estimating the DSD parameters with Doppler techniques are presented in the chapter 6.

## 2.4. ADVANCEMENTS IN RADAR REMOTE SENSING: ADVENT OF MULTIFACETED RADARS WITH PHASED ARRAY TECHNOLOGY

The phased array radars deployed at the airports are designed to detect and track point-like targets like birds and drones. The phased array radars provide an extra feature where multiple beams can be formed in elevation, and the echo sequences from several elevations can be acquired simultaneously. These X-band ( $8 \rightarrow 12\text{GHz}$ ) radars have very high range resolution and are short-range, unlike the traditional S or C-band weather radars. Although these radars have a phased array in the elevation, they scan the azimuthal direction very quickly, limiting the time on target. An example of such a radar is discussed in [31]. Such X-band radars are of Frequency Modulated Continuous Wave (FMCW) type, improving the range resolution. A picture of the Max3D radar [31] is shown in Fig. 2.3.

Modern demands for improving the situation awareness in airports and urban regions formulated the interest to extend the capabilities of such radars' with new functions - to observe and estimate the intensity of precipitations to retrieve the 3D wind field with high temporal and spatial resolution. This task requires coherent Doppler signal processing for the estimation of the Doppler velocity spectrum of the meteorological objects. The performance of such processing is limited by the negative effect of fast radar antenna rotation, limiting the radar's dwell time ( $T_{\text{Dwell}}$ ) - the time the radar spends in one specific azimuthal sector of space. This time on target is directly proportional to the radar's beamwidth and inversely proportional to the scanning speed of the radar. The applicability of Doppler processing becomes questionable with such dependency between the dwell time and the radar scan

speed because the existing techniques for Doppler processing require long echo sequences to be coherently integrated for Doppler velocity spectrum estimation for weather applications.

The errors in the Doppler parameters (in this case, the moments) due to the fast scanning nature of such radars affect the retrievals of the other derived parameters that are dependent on the Doppler moments.

The phased array radars offer new opportunities, such as effectively and instantaneously estimating the profile of Doppler moments in 3D. This thesis addresses research questions on effective Doppler processing, assuming a fixed radar beam in the elevation. However, the Doppler processing approaches developed here are designed for fast scans in azimuth, augmenting the capabilities of phased array radars. For instance, the techniques introduced in Chapters 3 and 5 can be applied across multiple elevations simultaneously (leveraging the phased array nature) to estimate 3D Doppler information. Additionally, using the technique from Chapter 6 across various elevations enables instantaneous estimation of the 3D motion of the precipitation field.

Although this thesis focuses only on the Doppler/ wind velocity parameters for raindrops, the methodologies presented can be scaled for other hydrometeors using several models of terminal fall velocity (e.g., for snow, hail and ice) provided there are instruments sensitive to their sizes and equipped with Doppler processing capabilities (e.g., polarimetric Doppler radars). Such DSD and terminal fall velocity models are developed in the past by using basic principles such as Reynold's and Davies numbers [32–52]. The use of these models in inverse problems requires the estimation of many more physical parameters. Similarly, for turbulence estimation, novel models can be formulated by considering parameters such as the Eddy current Dissipation Rate (EDR) [8, 53–55].

## 2.5. CONCLUSIONS

In this chapter, a broad overview of weather radar remote sensing has been presented. A brief history of the evolution of such radars is put forward with details, including their frequency of operation and dual-polarization abilities. As weather radars operate with the principles of electromagnetic (EM) wave propagation, several aspects of the EM wave interaction with the extended atmospheric targets (e.g., precipitation fields) are explained. First, the fundamentals of the scattering regimes are presented in terms of the relative sizes of the targets with respect to the wavelength of the radar. Then, the principles of the Doppler effect are presented, which helps in determining the radial motion of the targets of interest. Then, general practices followed for the modeling of the radar echo signals from atmospheric targets, the parameters of interest, and the retrieval practices of these parameters are presented. Furthermore, the state-of-the-art approaches to estimating the wind fields in space and time are presented. Moreover, in each section, the contributions of this thesis are delineated, wherever applicable, to underscore the novelties.





# 3

## DOPPLER SPECTRUM MOMENTS ESTIMATION FOR PRECIPITATION

*This chapter proposes a novel approach that is apposite for mitigating the challenges related to the estimation of the Doppler moment estimation for fast scanning radars. The results indicate the superiority of the proposed approach, especially for short observation intervals (in each radar scan). The proposed approach is also capable of fusing the echo sequences from multiple scans. Furthermore, a scanning strategy to accurately estimate the Doppler moments based on the true velocity dispersion of the scatterers is provided with the help of the proposed approach.*

---

Parts of this chapter have been published in:

T. Dash, H. Driessen, O. Krasnov, and A. Yarovoy, "Doppler Spectrum Parameter Estimation for Weather Radar Echoes Using a Parametric Semi-analytical Model," *IEEE Transactions on Geoscience and Remote Sensing*, vol. 62, pp. 1–18, 2024,

T. Dash, H. Driessen, O. A. Krasnov, and A. Yarovoy, "Incoherent Doppler Processing for Doppler Moment and Noise Estimation for Precipitation," in *Proceedings of the 4th URSI Atlantic RadioScience Conference – AT-RASC 2024*, no. May, (Meloneras, Spain), pp. 1–4, URSI – International Union of Radio Science, 2024

### 3.1. INTRODUCTION

Traditionally, three Doppler parameters (also known as the Doppler moments) are retrieved from the echoes received by the radar to characterize the intensity and the motion of the raindrops. The first parameter is the total power contained in the backscattered radar signal (also known as the Zeroth Doppler moment), and it is used to detect the presence of precipitation.

The other two parameters help determine the motion of the raindrops, which are derived from the phase change of these echoes over time. The mean Doppler velocity (also known as the first Doppler moment) is a measure of the mean radial velocity of the raindrops. The spatial and temporal variability of the mean Doppler velocity helps determine the horizontal wind field (speed and direction of the wind as a function of space and time) and the mean vertical fall velocity of the raindrops [9, 23–28].

The Doppler spectrum width (the square root of the second spectral Doppler moment about the mean velocity, i.e., the second central moment) is a measure of velocity dispersion associated with several statistical effects such as wind shear, turbulence, as well as antenna beam shape. The Doppler spectrum width is used mainly to estimate the turbulence intensity field in the atmosphere [22, 54, 58–60], and the drop size distribution (DSD) of the raindrops [61–65]. The use of Doppler moments can also be found in fields of study other than weather radars, such as ultrasonic Doppler blood flow sensing [66] and radar astronomy [67], [68].

The classical Doppler moment estimators need long records of the echo samples to estimate the moments accurately (especially for the Doppler spectrum width), for which it is assumed that the spectral content is constant for a long observation time (stationarity condition). However, the stationarity condition is often not realized in practice due to, e.g., instability of the physical atmospheric conditions and rapid radar scans. A changing atmosphere is disadvantageous for slowly scanning traditional weather radars that can accumulate long records of echo samples. On the other hand, classical estimators give biased results in the case of rapidly scanning radars because of limited time on target [69].

In this chapter, the focus is on the fast azimuthal scanning radars. Therefore, considering the stationarity condition of the atmosphere only for a short period, a desired moment estimator should have the feature to estimate the moments with a small observation time accurately. Another feature of this desired estimator is the ability to process the data from multiple radar scans. A maximum likelihood estimator that has both the features mentioned above is proposed. In addition, a quantitative guide to how fast the radar should scan as a function of the true velocity dispersion is proposed.

The main body of the chapter is organized as follows. The §3.2 discusses the classical estimators and the rationale behind the proposed approach. The §3.3 explains the simplified time domain echo signal model for precipitation-like weather targets. The §3.4 contains the proposed semi-analytical model of the power spectrum. The §3.5 discusses the optimization goals of the approach and the formulation of the likelihood function for the parameter estimation. The §3.6 contains some examples of the estimation using simulated weather echoes, the

comparison with the existing approaches, and the performance analysis. The §3.7 presents the application to real radar observations. The §3.8 presents a joint Doppler moment and noise variance estimation strategy. The conclusions are mentioned in the §3.9. The Appendix A contains the derivation of the expected semi-analytical model of the PSD. The Appendix B contains the derivation of the theoretical variances (for any number of echo samples) and the unbiased CRB for the proposed approach (for an infinite number of echo samples).

### 3.2. CLASSICAL DOPPLER MOMENT ESTIMATORS AND THE RATIONALE BEHIND THE PROPOSED APPROACH

Before diving deep into the classical Doppler spectrum moment estimation algorithms, it is important to understand the requirements for the bias and standard deviation for various radar variables, including the Doppler moments. The requirements vary with respect to the type of storm. An example of such practical requirements on the bias and the standard deviations for radar variables can be found in [70] for the Weather Surveillance Doppler Radar (WSR 88D) in the absence of clutter filtering. Based on the requirements and the capability of the estimation technique, a suitable scan strategy and pulse repetition interval can be adopted. A balance must be maintained between the radar's scan time and pulse repetition time to ensure accurate retrievals within each resolution volume, while also providing timely updates across the full field of view with acceptable temporal resolution. Therefore, the extent to which a scan can be called "slow" or "fast" depends on the storm dynamics and the pulse repetition time.

In this chapter, the Doppler moments under investigation (mean Doppler and Doppler spectral width) are normalized with the maximum unambiguous velocity, which is a function of the pulse repetition time. This chapter does not explicitly study the estimation of the reflectivity (zeroth Doppler moment). The type of the storm is characterized by the normalized spectral width. As this chapter evaluates the classical Doppler moment estimators with a proposed one, the study is made very generic by considering normalized quantities. The pulse repetition times are the same for all the estimators under study, and then the performance is evaluated as a function of the coherent processing interval (per radar scan), the normalized spectral width, and the normalized mean Doppler velocity. The bias and variance studies in this chapter the bias and variance studies can directly be used for practical applications based on the requirements by scaling the pulse repetition time and normalized spectral width accordingly. Let's dive deep into the classical Doppler moment estimators and their advantages and disadvantages.

The Doppler moments estimation techniques can be categorized into parametric and non-parametric approaches. The most common and classical non-parametric techniques used to estimate these moments are the periodogram-based (also called the power spectrum-based approach, which is referred to as DFT in this chapter) and the Auto-Co-Variance (ACV) based approach (also called the pulse pair method, and referred as PP approach in this chapter). The performance analysis of such methods, along with some other classical non-parametric estimators, such as the

Vector Phase Change (VPC) and the scalar phase change (SPC), has been studied in existing literature [69, 71–73]. The DFT-based moment estimation is carried out after the reconstruction of the spectrum shape in the frequency domain and is sensitive to the Doppler spectrum resolution due to limited observation time. The moment estimates are asymptotically unbiased, meaning that the estimates converge to the true value when the number of coherent echo samples in time approaches infinity. The PP approach on the other hand, is an unbiased estimator of the first moment provided the Doppler spectrum is symmetric around the mean Doppler velocity. Different versions of the PP approach exist for the spectrum width estimation that benefit from various combinations of the auto-covariance of the echo samples with various numbers of sample lags [74], [75], [76, Ch. 6, p. 136-138]. The different PP approaches are denoted as PP Rm/Rn, where Ri is the auto-correlation of the echo samples in the time domain with 'i' number of sample lags. It has been shown in [74] and [75] that the PP approaches with higher lags perform superior for smaller spectrum widths and vice versa. A hybrid estimator is proposed in [75], where the estimator chooses one of the PP versions heuristically based on an initial estimate of the spectrum width. Moreover, a different version of the PP algorithm exists in the literature as Poly Pulse Pair (PPP) [77] method for the first Doppler moment, but its discussion goes beyond the scope of this chapter. Another non-parametric approach [78] assumes the band-limited nature of the Doppler spectrum. Although its accuracy is better than the DFT and PP approaches, it is based on estimating interpolation-filter coefficients. The choice of the impulse transfer function of the filter is empirical and due to the need to estimate many filter coefficients, the approach becomes computationally expensive. Another non-parametric moment estimator class uses auto-regressive moving average (ARMA) models [79]. However, fitting ARMA models also consumes considerable computational resources. Even though many non-parametric approaches for Doppler spectrum estimation exist in the literature, the DFT and PP approaches are the most popular because of their computational efficiency and non-parametric nature.

The parametric approaches assume a model for the echo samples' PSD or auto-covariance (ACV). The maximum likelihood estimation using a power spectrum model of the weather echoes is studied in [80], [81] and a maximum entropy-based approach is studied in [82]. These methods have the advantage of processing finite sequences of echo samples and gapped records (like that of a scanning radar). Although these techniques provide accurate results for the mean Doppler velocity, they give biased results when estimating the Doppler spectrum width due to the limited observation time. These estimators use a closed-form shape of the Doppler spectrum and do not consider the Doppler resolution. In [83], a Gaussian spectrum convolved with a rectangular window has been considered as a model of the PSD to remove the effect of the limited resolution. However, the de-convolution is performed manually after studying the bias in a tabular form, and analytical expressions are not known for the variance of the estimator.

In this chapter, a novel approach, referred to later as a *parametric spectrum estimator* (PSE), is proposed to estimate Doppler spectrum moments accurately by processing several mutually incoherent finite sequences of echo samples. The

method is based on a novel semi-analytical model of the PSD, which is derived using a limited observation time and thus incorporates the Doppler resolution in the model. The PSD model is derived using a simplified physical model of the time domain signal similar to [84] with some changes in the model of the velocities of the raindrops.

In the signal model, the velocities of the scatterers are considered to be independent and identically distributed (*i.i.d.*) random variables. As the shape of the majority of the weather Doppler spectrum is Gaussian in nature [76, Ch. 5, p. 112-115][71][72][85], the velocities of the raindrops are assumed to be normally distributed having parameters  $\mu_v$  as the mean of the distribution (true mean Doppler velocity) and  $\sigma_v$  as the standard deviation (true Doppler spectrum width). The model of the PSD is derived by taking the expectation of the power of the Discrete Fourier Transform of the time domain signal model. The resulting expression for the PSD is semi-analytical with a numerical sum across the finite time interval with steps equal to the pulse repetition time of the radar. A maximum likelihood approach is used to obtain the spectrum parameters similar to [80]. The formulation of the signal model, along with the derivation of the PSD is presented in the following sections.

The performance of this estimator is evaluated by comparing its variance with the other approaches, such as DFT, PP and Levin's ML approach [80]. In addition, a quantitative guide to how fast a radar should scan the atmosphere as a function of the true velocity dispersion is proposed. The approach is successfully applied to multiple scans of experimental data acquired by a fast-scanning atmospheric radar.

### 3.3. SIGNAL MODEL

This chapter focuses on the echo sample modeling of weather radar in the context of precipitation-like events only. Consider a radar resolution volume filled with  $M$  raindrops during a rain event. The radar echo at time  $k$  is a superposition of the echoes received from all the raindrops [76, Ch. 4, p. 67]. It is given by:

$$s(t_k) = \sum_{m=1}^M A_m \exp \left( j \frac{4\pi}{\lambda} r_m(t_k) \right). \quad (3.1)$$

In (3.1),  $A_m$  is the amplitude caused by the reflection from the  $m$ th scatterer. It is usually a function of the geometry of the scatterers (size, shape, orientation, and composition), the range weighting function due to the effect of the radar waveform, and the antenna weighting function based on the antenna beam shape [76, Ch. 5, p. 112-115], [84]. The quantity  $\lambda$  is the wavelength of the radar signal,  $r_m$  is the distance to the  $m$ th scatterer, and  $j$  is the imaginary unit  $\sqrt{-1}$ . The change in a scatterer's radial distance depends on its radial velocity. If one considers the radial velocity of the  $m$ 'th scatterer to be  $v_{m,r}$  at the time instant  $t_{k-1}$ , the radial distance of the  $m$ th scatterer at time  $t_k$  becomes  $r_m(t_k) = r_m(t_{k-1}) + v_{m,r} T$ , where  $T = t_k - t_{k-1}$  is the pulse repetition time for the radar. If the radial velocity of each scatterer is constant throughout the observation time, and if the initial position of the  $m$ 'th scatterer is denoted as  $r_{m,0}$ , the expression in (3.1) could be rewritten as

the following:

$$s(t_k) = \sum_{m=1}^M A_m \exp \left( j \frac{4\pi}{\lambda} (r_{m,0} + v_{m,r}(t_k - t_0)) \right). \quad (3.2)$$

If one considers the initial time instant to be  $t_0 = 0$  and by using  $\beta_m = (4\pi/\lambda)r_{m,0}$ , (3.2) could be rewritten as the following:

$$s(t_k) = \sum_{m=1}^M A_m \exp(j\beta_m) \exp \left( j \frac{4\pi}{\lambda} v_{m,r} t_k \right), \quad (3.3)$$

where the term  $\exp(j\beta_m)$  is the initial phase caused by the incident phase of the electromagnetic wave (related to the transmit phase, range to resolution volume, and atmospheric affects) and the position of the  $m$ th scatterer relative to the center of the resolution volume. In this chapter, several assumptions have been considered for mathematical simplicity. The first assumption is that the sizes of the scatterers (raindrops) are assumed to be the same ( $A_m = A, \forall m$ ). The initial positions of the scatterers are *i.i.d.* random variables with a uniform distribution.

$$\{\beta_m\}_{m=1}^M \stackrel{i.i.d.}{\sim} \mathcal{U}[-\pi, \pi]. \quad (3.4)$$

It is assumed that the Gaussian shape of the Doppler spectrum around the mean Doppler velocity is caused purely by the scatterers' motion and not by other statistical effects explained in the introduction for mathematical convenience. The radial velocities of the scatterers are considered *i.i.d.* random variables with a Gaussian probability density.

$$\{v_{m,r}\}_{m=1}^M \stackrel{i.i.d.}{\sim} \mathcal{N}(\mu_v, \sigma_v^2). \quad (3.5)$$

The time domain measurement model considered in this chapter includes the signal (3.3) with added zero mean complex white Gaussian noise with variance  $\sigma_n^2$  and is given by:

$$\mathbf{z} = \mathbf{s} + \mathbf{n}, \quad \{n_k\}_{k=0}^{N-1} \stackrel{i.i.d.}{\sim} \mathcal{CN}(0, \sigma_n^2). \quad (3.6)$$

### 3.4. SEMI-ANALYTICAL FORM OF THE PSD

The signal model of (3.3) is used to derive the semi-analytical form of the PSD. Considering uniform sampling with pulse repetition interval of  $T$ , the DFT at a velocity point  $v$  can be represented as:

$$S(v) = A \sum_{k=0}^{N-1} \sum_{m=1}^M \exp \left[ j \left( \frac{4\pi T}{\lambda} (v_{m,r} - v) k + \beta_m \right) \right]. \quad (3.7)$$

Performing the sum with respect to the time (summing a geometric progression) results in the following expression:

$$S(v) = A \sum_{m=1}^M \frac{\sin \left( \frac{2\pi T}{\lambda} N (v_{m,r} - v) \right)}{\sin \left( \frac{2\pi T}{\lambda} (v_{m,r} - v) \right)} \times \exp \left[ j(N-1)(v_{m,r} - v) \frac{2\pi T}{\lambda} + j\beta_m \right], \quad (3.8)$$

where  $\sin((2\pi T/\lambda)N(v_{m,r}-v))/\sin((2\pi T/\lambda)(v_{m,r}-v))$  (3.8) is a result of the finite observation time. This function is also called the Dirichlet kernel [86, Ch. 8, p. 189]. As it is assumed that the  $\beta$  are uniformly distributed phase, the expectations of the real and imaginary parts of (3.8) are 0 when  $M \rightarrow \infty$ . However, the PSD of the spectrum function of (3.8) does have a positive expectation. The PSD using (3.8) can be represented as follows:

$$\begin{aligned} |S(v)|^2/N &= A^2/N \left( \sum_{m=1}^M \frac{\sin^2((2\pi T/\lambda)N(v_{m,r}-v))}{\sin^2((2\pi T/\lambda)(v_{m,r}-v))} \right. \\ &\quad + \sum_{p \neq q}^M \frac{\sin((2\pi T/\lambda)N(v_{p,r}-v))}{\sin((2\pi T/\lambda)(v_{p,r}-v))} \frac{\sin((2\pi T/\lambda)N(v_{q,r}-v))}{\sin((2\pi T/\lambda)(v_{q,r}-v))} \\ &\quad \left. \times \cos[(N-1)(v_{p,r}-v_{q,r})(2\pi T/\lambda) + (\beta_p - \beta_q)] \right), \end{aligned} \quad (3.9)$$

where the expectation of the second term is 0 because of the uniformly distributed  $\beta$  inside the cosine term. A detailed explanation of these two terms and their contribution to receiver power can be found in [76, Ch. 4, p. 67-68]. Finally, the following expression gives the expectation of the first term, and the detailed derivation is presented in Appendix A.

$$\begin{aligned} F(v) &= \mathbb{E} \left[ \frac{1}{N} |S(v)|^2 \right] \\ &= A^2 M \left[ 1 + 2 \sum_{q=1}^{N-1} \left( 1 - \frac{q}{N} \right) \exp \left( - \left( \frac{4\pi T}{\lambda} \right)^2 \frac{\sigma_v^2 q^2}{2} \right) \times \cos \left( \frac{4\pi T}{\lambda} q(\mu_v - v) \right) \right] \end{aligned} \quad (3.10)$$

The dependence on  $N$  in the model is advantageous, especially for estimating the Doppler spectrum width, because that parameter is heavily affected by the limited resolution of the spectrum. This makes it different from the existing maximum likelihood estimators, where a complete closed form of the PSD is used without the dependence of  $N$ .

### 3.5. OPTIMIZATION GOALS

The expression of (3.10) suggests that the PSD is a function of the spectrum parameters (the mean frequency (velocity,  $\mu_v$ ), the spectrum width  $\sigma_v$ ), the finite number of coherent samples  $N$ , and the multiplicative factor  $A^2 \times M$ . As the multiplicative factor is a measure of the signal power, it can be estimated by taking the average of the signal power in the time domain.

$$\hat{A}'^2 \approx \overline{|\mathbf{z}|^2} \quad (3.11)$$

Here, a change of parametrization is used for  $A^2 M$  and is indicated as  $A'^2$ . The notation  $\hat{A}'$  is used to suggest that it is an estimated quantity. In the following analysis, however, the value of  $A'$  is assumed to be known beforehand. The objective of the optimization here is to estimate the parameters  $\Theta = [\mu_v, \sigma_v]$  based on the given PSD (the PSD of  $\mathbf{z}$  is referred to as  $\mathbf{Z}$ ).

Let us denote the number of observations (measurements) of the PSD as  $L$ . Each of the  $L$  observations contains the PSD of  $N$  coherent radar echoes.



However, the observations themselves need not be coherent.  $L$  can be interpreted as the number of measurements with similar statistical properties (similar mean Doppler velocity and Doppler spectrum width, for example). There are several practical ways to gather such measurements. For example, measurements from several neighboring range cells or high temporal updates can be used to increase  $L$  [87]. Similarly, the measurements after whitening in the range can be considered [88], [89]. In this case, the received signal is sampled at a rate several times larger than the reciprocal of the transmitted pulse length. In this chapter, however, these incoherent measurements are interpreted as the echo sequences acquired from several fast scans of the radar corresponding to the same resolution volume. For a radar with a constant scan rate, the number of samples  $N$  in each of the  $L$  observations (measurements) at a specific resolution volume remains the same. Therefore, unlike in [88], [89], each of the  $L$  measurements is considered in the temporal domain (scan-to-scan) instead of in the range (spatial domain).

If the power spectrum is denoted by  $Z_l(v)$  for  $l$ th observation, at a velocity point  $v$ , the likelihood probability is given by the following expression [80] [81]:

$$p(\mathbf{Z}|\Theta) = \prod_{i=1}^N \prod_{l=1}^L \frac{1}{\pi(F(v_i, \Theta) + \sigma_n^2)} \exp\left(-\frac{Z_l(v_i)}{F(v_i, \Theta) + \sigma_n^2}\right), \quad (3.12)$$

where  $p(\mathbf{Z}|\Theta)$  is the likelihood probability of  $\mathbf{Z}$  given the parameters  $\Theta$ . Here,  $\mathbf{Z}$  is a matrix of size  $L \times N$ . This likelihood function is inspired by the fact that the probability density function of the PSD at a particular frequency (velocity) is exponential, indicating that the mean of the PSD is equal to its standard deviation [90].

$$Z(v_i) \sim \text{Exp}\left[\frac{1}{F(v_i) + \sigma_n^2}\right] \quad (3.13)$$

The following expression gives the logarithm of this likelihood function. In this formulation, the noise variance  $\sigma_n^2$  is considered to be known.

$$\log(p(\mathbf{Z}|\Theta)) = -\sum_{i=1}^N \left[ L \log(\pi(F(v_i, \Theta) + \sigma_n^2)) + \frac{\sum_{l=1}^L Z_l(v_i)}{F(v_i, \Theta) + \sigma_n^2} \right] \quad (3.14)$$

The optimization aims at maximizing this log-likelihood (3.14) function to estimate the parameters  $\Theta$ .

$$\hat{\Theta} = \max_{\Theta} \log(p(\mathbf{Z}|\Theta)) \quad (3.15)$$

The theoretical variances are computed for PSE and Levin's ML approaches by following [80, eq. (4)]. The derivation of these variances is given in Appendix B. These can be computed for a finite number of samples. The theoretical variance (also can be referred to as the dispersion  $((1/\text{sensitivity})^2)$  as explained in [80, eq. (4)]), and should not be confused with the unbiased CRB because to get the unbiased CRB, one should consider unbiased estimators. However, the estimators here are not unbiased in all conditions, so there can be a difference between the theoretical and the numerical standard deviations. A biased CRB can also be computed by considering the biased gradients of the parameters [91, eq. (2)], [80, eq. (2)]:

$$\text{CRB}(\theta) = \text{diag}\{[\mathbf{1} + \nabla_{\theta} \mathbb{B}(\theta)] \mathbf{I}^{-1}(\theta) [\mathbf{1} + \nabla_{\theta} \mathbb{B}(\theta)]^T\}, \quad (3.16)$$

where  $\mathbb{B}[\theta]$  are the bias vectors, and  $\nabla_{\theta}\mathbb{B}(\theta)$  is the bias-gradient matrix. However, the biases of these estimators are not known in closed form, making it challenging to obtain the biased CRB for a finite number of samples or with constraints for the parameter space (as considered in this and later chapters of the thesis). Nevertheless, it is essential to note that the theoretical variances for the infinite number of echo samples ( $N \rightarrow \infty$ , and for a fixed  $L$ ) reach the unbiased-CRB (also referred to as CRB) as the estimators are asymptotically unbiased.

In (3.14), it can be noticed that the likelihood function can integrate multiple observations ( $L$  in the expressions) of the stationary stochastic signal PSD. However, the existing classical non-parametric techniques only process one observation for the Doppler moment estimation, except for the DFT approach when periodogram smoothing is applied. The moment estimation with the DFT approach can be carried out after applying a periodogram smoothing technique on several realizations of the PSD (e.g., the periodogram of Bartlett and Welch [92, Ch. 4, p. 49-52]) at the expense of poor Doppler resolution and hence is out of the scope of this chapter. In the simulation study, to have comparable results with DFT and PP,  $L$  is kept as 1, suggesting that only one observation (3.6) is processed in the proposed method and the classical methods. The optimization is performed using the active-set and the Limited Memory Broyden–Fletcher–Goldfarb–Shanno (L-BFGS) algorithms [93] [94]. This method is chosen because of its faster computation time.

The optimization is performed several times with random starting points (following a uniform distribution) inside the parameter space to avoid getting stuck at local minima if any. The algorithm is explained in 1. In algorithm 1,  $\Theta_i^{(0)}$  are the starting points of the parameters in iteration  $i$ ,  $\Theta_l$ ,  $\Theta_u$  are the lower and upper limits of the parameter space, and  $U$  is the number of iterations. In all the examples in this chapter, the optimization is performed  $U = 32$  times.

---

**Algorithm 1** Optimization Algorithm
 

---

- 1: **for**  $i = 1$  to  $U$  **do**
    - Initialize parameters  $\Theta_i^{(0)} \sim \mathcal{U}(\Theta_l, \Theta_u)$
    - $\hat{\Theta}_i = \max_{\Theta} \log(p(\mathbf{Z}|\Theta))$
    - $J_i = \log(p(\mathbf{Z}|\hat{\Theta}_i))$
  - 2: **end for**
  - 3:  $i_{\max} = \max_i J_i$
  - 4:  $\hat{\Theta} = \hat{\Theta}_{i_{\max}}$ .
- 

### 3.6. NUMERICAL SIMULATION

This section applies the Doppler moment estimation on simulated radar echo samples. First, the noise-free echo samples are simulated using (3.3). A complex white Gaussian noise is added to the samples as shown in (3.6). The input noise variance for the measurement model is computed with a user-defined input SNR [90]. The PSE parameter estimation is compared with the DFT, PP, and Levin's ML

approach. For all these approaches, the noise variance is assumed to be known to allow for a fair comparison. The expressions for moment estimation with the DFT approach using known noise variance are from [71, eq. (9)] (The equation is for the mean Doppler, but similarly, the Doppler spectrum width is computed by using the second moment). The mean Doppler estimation with the PP approach is taken from [71, eq. (16)]. For the Doppler spectrum width (PP R0/R1; also denoted as PP in this chapter, and PP R1/R2), the formulae [95, eq. (6.17), eq. (6.32)] are used as these estimators are asymptotically unbiased. The formula [75, eq. (3)] is used for the R1/R3 spectrum width estimator.

For Levin's approach, the parameters are estimated jointly, like the PSE. The implementation of Levin's approach in this chapter differs from [80] in the sense that the continuous integrals are replaced with numerical sums along the frequencies, to include the effect of the limited frequency resolution. However, the implementation proposed in [80] assumes that the resolution is enough to contain the detailed structure of the spectrum, and also, it is assumed that the PSD is slowly varying (after applying some smoothing operation). Hence, in [80], continuous integrals along the frequencies are justified. However, to have a fair comparison of the PSE with Levin's approach, no smoothing operation has been performed on the PSD. Comparing the results of PSE with Levin's ML approach allows us to observe the differences between the estimates when using a model of the PSD has a semi-analytical form (PSE) that includes the Doppler resolution as a sum over time as compared to a model with a complete closed form (Levin).

The quantitative performance is assessed with Monte Carlo simulations. The evaluation metric used in this chapter is the bias and variance of the estimators. The Doppler frequencies in the following examples are normalized ( $\lambda/(2T) = 2V_a$ ), where  $V_a$  is the unambiguous Doppler velocity of the radar. Therefore, the range of frequencies is from  $-0.5$  to  $0.5$ . The parameters are denoted as  $\mu_{fn} = \mu_v/(2V_a) = 2T\mu_v/\lambda$  (normalized mean Doppler velocity), and  $\sigma_{fn} = \sigma_v/(2V_a) = 2T\sigma_v/\lambda$  (normalized Doppler spectrum width). The upper and lower bounds of the parameters for the optimization (explained in algorithm 1) are  $[\mu_{fn,l}, \mu_{fn,u}] = [-0.5, 0.5]$ , and  $[\sigma_{fn,l}, \sigma_{fn,u}] = [0, 0.5]$ .

The bias is the difference between the expected value of the estimated quantity and the true value.

$$\mathbb{B}[\hat{\Theta}] = \mathbb{E}[\hat{\Theta}] - \Theta. \quad (3.17)$$

Here, the expectation of the estimated quantity ( $\mathbb{E}[\hat{\Theta}]$ ) is approximated by doing a Monte Carlo simulation and taking the average. Therefore, a positive bias refers to an overestimation, and a negative bias refers to an underestimation. The following expression computes the numerical variance in the parameters:

$$\mathbb{V}[\hat{\Theta}] = \mathbb{E}\left[(\hat{\Theta} - \mathbb{E}[\hat{\Theta}])^2\right]. \quad (3.18)$$

The standard deviation in the estimates is computed by taking the square root of  $\mathbb{V}[\hat{\Theta}]$ .

In the following sections, "GT" refers to the Ground Truth. The normalized quantities are denoted with a subscript  $n$ . The theoretical variances are denoted as "Theor" on the plots.

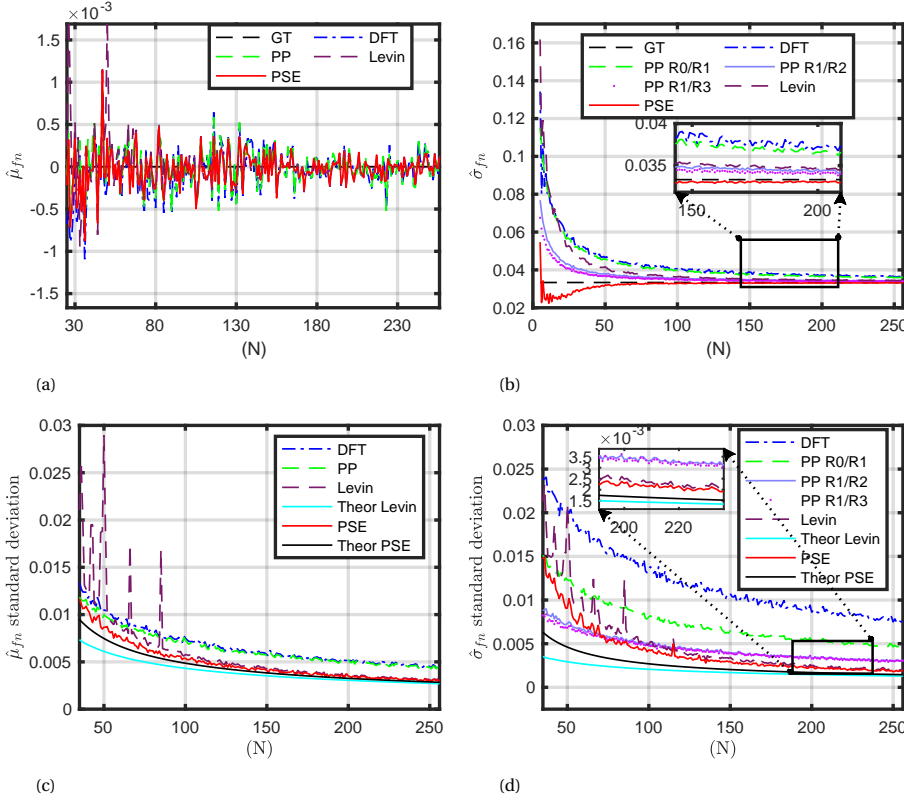


Figure 3.1: Estimation and performance of the Doppler moments for  $L=1$  with respect to the number of coherent samples  $N$ . **a** Mean normalized Doppler frequency  $\hat{\mu}_{f_n}$ . **b** normalized Doppler frequency width  $\hat{\sigma}_{f_n}$ . **c** Standard deviation in estimating the normalized Mean Doppler frequency  $\hat{\mu}_{f_n}$ . **d** Standard deviation in estimating the normalized Doppler spectrum width  $\hat{\sigma}_{f_n}$ .

### 3.6.1. PARAMETER ESTIMATION WITH $L = 1$

In this example, the simulated signal has parameters (also referred to as the ground truth)  $\mu_{f_n} = 0$  and  $\sigma_{f_n} = 0.033$ . The number of scatterers in the model is kept as  $M = 10000$ . The SNR input for the model (3.6) is 12dB. The number of iterations used in the Monte Carlo simulation is 1024 for this analysis. The mean retrieval (using the Monte Carlo simulations) of the normalized mean Doppler frequency and the Doppler frequency width is shown in Fig. 3.1a and Fig. 3.1b, respectively. According to Fig. 3.1a, all approaches perform similarly when the number of coherent samples is large for estimating the first moment. For a lower number of coherent samples (especially below  $N = 30$ ), PSE and PP approaches have lower bias than the DFT and Levin's ML approaches. From 3.1b, it can also be observed that the biases of the higher lag versions of PP PP R2/R1 and PP R3/R1 are lower than PP R0/R1, because the spectrum width considered for this example is relatively narrow. According to Fig. 3.1b, PSE achieves convergence at a lower number of coherent

samples (at  $N > 30$ ) than the other approaches. The bias is  $-0.004$  and percentage error is  $13.34\%$  at  $N = 30$  for  $\sigma_{fn}$ .

The variances of the estimates in  $\mu_{fn}$  and  $\sigma_{fn}$  are computed numerically as a function of the number of coherent samples ( $N$ ). The standard deviation is plotted in Fig. 3.1c and Fig. 3.1d for  $\mu_{fn}$  and  $\sigma_{fn}$ , respectively. The standard deviations of the approaches are plotted for  $N > 30$ , which is the reciprocal of the true normalized frequency spectrum width ( $1/\sigma_{fn}$ ). The minimum number of coherent samples for the performance analysis is greater than  $1/\sigma_{fn}$  (the normalized frequency resolution  $\Delta f_{fn}$  should be  $0 < \Delta f_{fn} < 1/[\sigma_{fn}^{-1} - 1]$ ) to have sufficient resolution for the PSD and a low bias in the estimates.

According to Fig. 3.1c and Fig. 3.1d, the variance of the PSE goes lower than the other techniques with an increase in the number of samples.

Performance is also evaluated as a function of the normalized Doppler spectrum width  $\sigma_{fn}$ , with a fixed normalized mean Doppler frequency ( $\mu_{fn} = 0$ ) and a fixed number of coherent samples ( $N = 64$ ). The biases in the estimation results are shown in Fig. 3.2a and Fig. 3.2b for the mean Doppler frequency and Doppler spectrum width, respectively. The performance analyses of both parameters are shown in Fig. 3.2c and Fig. 3.2d with the other approaches.

All the approaches perform similarly for the mean Doppler velocity  $\sigma_{fn} = 0.2$ . The PP and PSE approaches have large biases and oscillate around the true normalized mean Doppler. The variance of the PSE approach is lower as compared to the other approaches for the mean Doppler till  $\sigma_{fn} < 0.2$ . The DFT and Levin's approach have an increasing negative bias with increasing spectral width for  $\sigma_{fn} > 0.2$ .

It can be observed that the different versions of the PP approach give lower bias than the PSE approach for specific intervals of the spectrum width. It is well known from the literature that the PP approaches with larger lags give lower bias for smaller spectral widths and vice versa [74], [75]. However, to construct an adaptive lag estimator, some prior information has to be known for the spectral width such that one of the PP versions can be chosen. It is evident from Fig. 3.2b that the PSE approach performs reliably across all ranges of spectral widths. The bias increases for very large spectral widths  $\sigma_{fn} > 0.25$ .

For very low spectral widths  $\sigma_{fn} < 0.04$ , the PP versions R2/R1 and R3/R1 perform better and have lower variances than the PSE. For spectrum widths  $0.04 < \sigma_{fn} < 0.25$ , PSE has the lowest variance amongst all the approaches. For higher spectrum widths, PP R1/R0 and PSE approaches give similar variances. The PP R3/R1 and DFT show very low variances at very high spectrum widths  $\sigma_{fn} > 0.25$  due to their significant biases.

The performance is further evaluated as a function of the normalized mean Doppler frequency  $\mu_{fn}$  with a fixed normalized Doppler spectrum width ( $\sigma_{fn} = 0.05$ ) and a fixed number of coherent samples ( $N = 64$ ). The biases in the estimation results are shown in Fig. 3.3a and Fig. 3.3b for the mean Doppler frequency and Doppler spectrum width, respectively. The performance analyses of both parameters are shown in Fig. 3.3c and Fig. 3.3d. The estimated mean Doppler frequency suffers from the aliasing near the unambiguous limit for all methods. The aliasing effect is observed at a lower mean Doppler frequency for the positive frequencies and higher

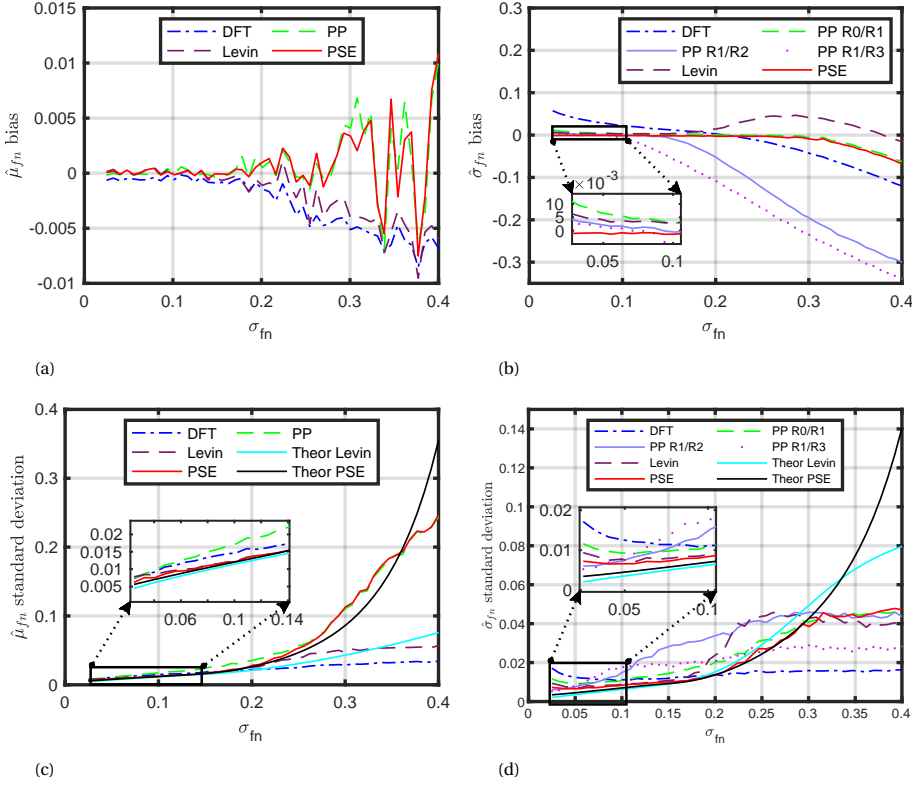


Figure 3.2: Estimation and performance of the Doppler moments for  $L=1$  with respect to  $\sigma_{fn}$  at  $\mu_{fn}=0$ . **a** Biases in the estimates of the mean Doppler frequency normalized  $\hat{\mu}_{fn}$ . **b** Doppler frequency width normalized  $\hat{\sigma}_{fn}$ . **c** Standard deviation in estimating the mean Doppler frequency normalized  $\hat{\mu}_{fn}$ . **d** Standard deviation in estimating the Doppler spectrum width normalized  $\hat{\sigma}_{fn}$ .

mean Doppler frequency for the negative frequencies with the DFT and Levin's ML approaches than the PP and PSE. The Doppler spectrum width estimated with PP and PSE approaches is not affected by the aliasing, whereas the other approaches suffer from the aliasing effect. The bias and variance of PSE are superior to the other approaches for the Doppler spectrum width estimate.

### 3.6.2. PERFORMANCE ANALYSIS WITH RESPECT TO $L$

The performance analysis of PSE has been compared with Levin's ML approach with a different number of observations  $L$ , keeping the number of coherent samples constant  $N=64$ . The performances are shown in figure 3.4a and 3.4b. It can be observed that with an increase in  $L$ , the variance decreases and converges for both techniques. The variance of PSE is lower than Levin's ML approach.

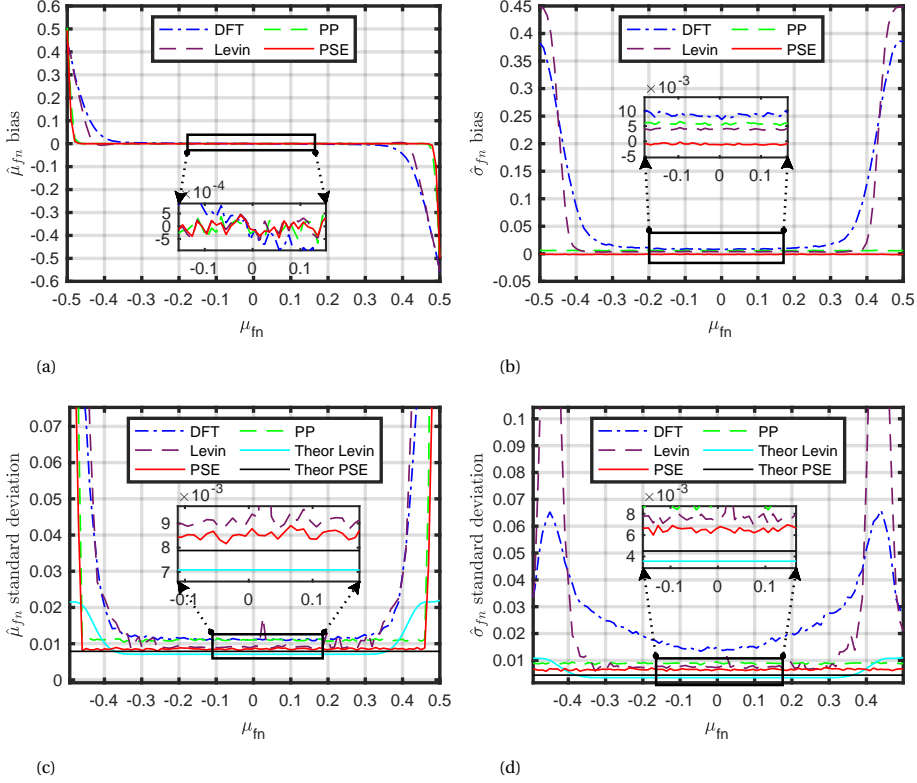


Figure 3.3: Estimation and performance of the Doppler moments for  $L=1$  with respect to  $\mu_f$  at  $\sigma_f=0.05$ . **a** Biases in the estimates of the mean Doppler frequency normalized  $\hat{\mu}_{fn}$ . **b** Doppler frequency width normalized  $\hat{\sigma}_{fn}$ . **c** Standard deviation in estimating the mean Doppler frequency normalized  $\hat{\mu}_{fn}$ . **d** Standard deviation in estimating the Doppler spectrum width normalized  $\hat{\sigma}_{fn}$ .

### 3.6.3. DISCUSSION ON THE SIMULATION RESULTS

The following conclusions can be made from the performance analysis of the proposed estimator in the previous sub-sections. The minimum observation time duration required for an accurate estimation of the Doppler spectrum width for PSE is inversely proportional to the true velocity dispersion of the scatterers (for normalized spectrum widths of  $\sigma_{fn} < 0.2$ ). For example, for a velocity dispersion of one-fortieth of the unambiguous velocity interval ( $2V_a$ ) in one resolution cell ( $\sigma_v = 2V_a/40$ ), the number of slow time samples needed with PSE should be at least more than 40 (or, the Doppler resolution of  $\Delta\nu < 2V_a/39$ ) to measure the Doppler spectrum width accurately. The minimum number of slow-time samples per resolution cell can be used to decide the scanning rate of the radar in azimuth. For the case mentioned above, if one uses 64 samples at least for one resolution cell with  $813.2\mu s$  pulse repetition time, the radar needs to spend only 26ms per resolution cell in azimuth. Suppose the azimuthal resolution cell is  $2.5^\circ$ ; the scanning speed of

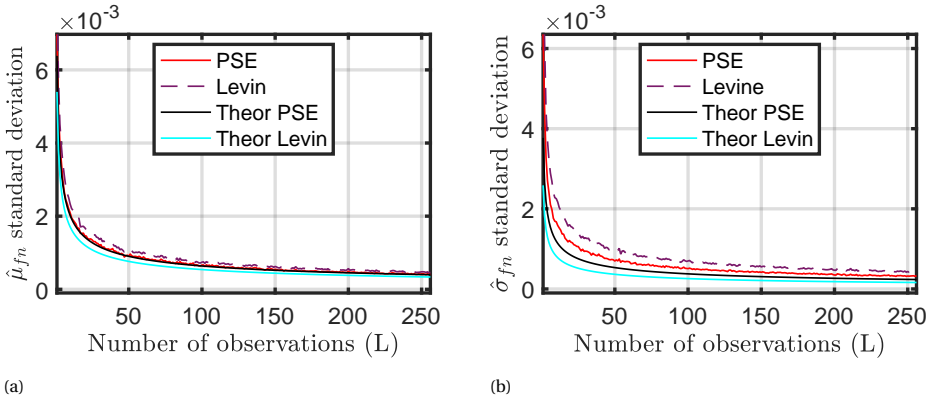


Figure 3.4: Estimation and performance of the Doppler moments for  $N=64$  with respect to  $L$ .  $\mu_{fn}=0$  and  $\sigma_{fn}=0.033$  **a** Standard deviation in estimating the mean Doppler frequency normalized  $\mu_{fn}$ . **b** Standard deviation in estimating the Doppler spectrum width normalized  $\sigma_{fn}$ .

the radar can be fixed to 16rpm. If the rain is turbulent with velocity dispersion of ( $\sigma_v = 2V_a/10$ ), and if one wants to use only 15 samples in one resolution cell, they can set the scanning rate to 68rpm with the configuration mentioned above.

As the model and algorithm explained in the chapter are developed to solve the estimation of Doppler moments considering the Doppler resolution, a practical accuracy needed for such weather conditions is not specified. Based on the analysis of the bias of the PSE, necessary scan strategies can be applied to meet the accuracy demanded by the applications.

As PSE uses a maximum likelihood technique performed numerically with an optimization algorithm (L-BFGS), it is challenging to provide a quantitative idea about the computational cost, unlike the non-parametric approaches. However, PSE has a lower computational cost than the ACV-based parametric approaches as it does not involve any matrix inverse operation.

### 3.7. APPLICATION TO REAL DATA

The proposed approach has been applied to real radar data recorded from the MESEWI radar at the Delft University of Technology in the Netherlands. In these experiments, only the signals from the HH channel is used. The MESEWI radar system is a fully polarimetric X-band (9.4 GHz) FMCW radar system. The PRI for each polarization is  $406.6\mu s$ . For one polarization, the PRI is  $813.2\mu s$  resulting in an maximal unambiguous Doppler velocity of  $V_a = (\lambda)/(4 \times \text{PRT}) = 9.8 \text{ m/s}$  ( $\lambda$  is the central wavelength of the radar). The radar specifications are shown in Table 3.1. The raw radar data is stored in a 3D format with fast time, slow time, and azimuthal angles as the three dimensions. The data discussed below was collected when the radar was pointed to a fixed elevation angle of  $30^\circ$ . Two experiments were performed with an interval of 26 minutes (the second experiment was performed 26 minutes after completing the first). In the first experiment, the azimuthal rotation speed



Table 3.1: MESEWI radar specifications

Parameter	Value
Center Frequency ( $f_c$ ) (Hz)	$9.4 \times 10^9$
PRI ( $T$ )	813.2 $\mu$ s
Beamwidth in Azimuth ( $d\phi$ )	2.5°
Elevation Angle ( $\psi$ )	30°
ADC Sampling $f_s$ (Hz)	$4.92 \times 10^6$

3

was one rotation per minute (1rpm), while in the second one, it was five rotations per minute (5rpm). The date of observation was May 9, 2023. It was a rainy day surrounding the area of Delft, Netherlands, which allowed us to observe clouds, the melting layer, and rain.

The pre-processing of sampled intermediate frequency data was performed along the following steps. After DC compensation, an FFT is applied on the fast time domain to ascertain the range dependence as it is an FMCW radar system. The mean is subtracted from each slow time sequence to remove the effects of the clutter. The Doppler processing is carried out on the slow time sequence for each range-azimuth resolution cell of the radar.

### 3.7.1. EXPERIMENT 1: SLOW SCAN OF ONE ROTATION PER MINUTE

The bandwidth of operation is  $BW = 50$  MHz for this experiment. The maximum range of the radar in this operational mode is six kilometers  $R_{max} = (f_s \times c) / (4BW \times PRF) = 6$  km ( $c$  is the speed of the electromagnetic wave), while the range resolution is three meters ( $\Delta R = c / (2 \times BW) = 3$  m). After the range processing across the fast time, 512 echo samples for Doppler processing for each range-azimuth cell are available. For the DFT approach, several cells around the zero Doppler are chosen as the clutter region and are interpolated with a chosen noise level. The noise spectrum level ( $\sigma_n^2$ ) is decided by taking the 15th percentile of the data contained in the PSD for each range-azimuth resolution cell because it is safe to assume that 15% of the data in the PSD are not from hydrometeors. The clutter region is not part of the observations for the PSE and Levin's ML approaches. The power scaling factor is determined from (3.11) for both Levin's ML approach and PSE. With the DFT approach, the total power estimate (reflectivity) of the Doppler spectrum in each resolution cell is shown in Fig. 3.5a. The reflectivity is shown here to explain some aspects of the mean Doppler and Doppler spectrum width estimated later in the chapter.

The Fig. of 3.5a shows a bright band ring of strong reflection around a range of 4km. It could be attributed to the melting layer in the atmosphere where the precipitation forms [96]. The azimuth is considered clockwise (0° is towards the north) in this figure and the successive figures in the chapter. It can be observed that the reflectivity is considerably higher in ranges below 4km, which corresponds to reflections from rain and in almost all azimuth sectors.

For the Plan Position Indicator (PPI) plots for the mean Doppler and Doppler spectrum width, the 512 echo samples are separated into eight observations ( $L = 8$ ),

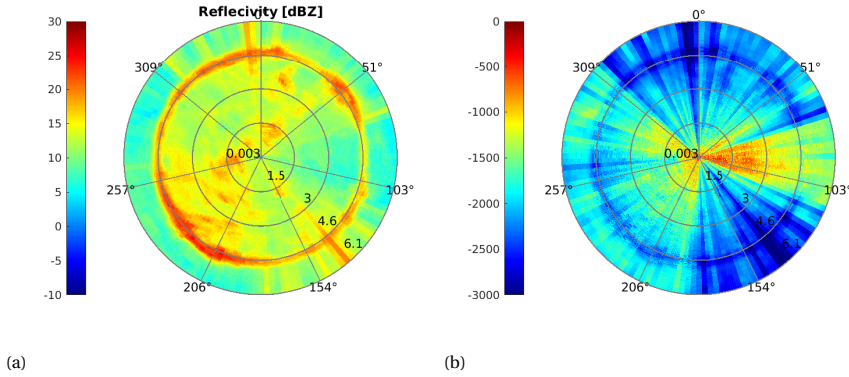


Figure 3.5: **a** PPI plot of reflectivity using the DFT approach. **b** log-likelihood (3.14) of PSE.

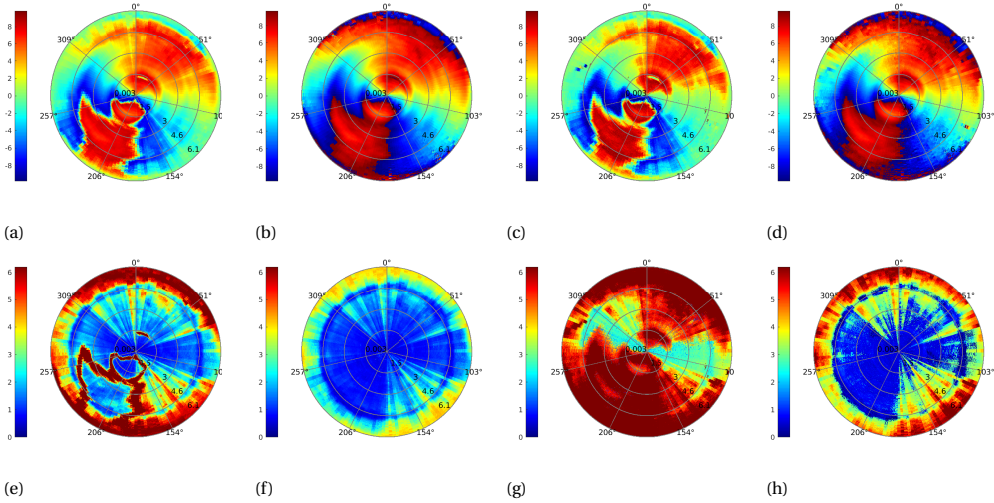


Figure 3.6: PPI plots showing Mean Doppler velocity and Doppler spectrum width with all the approaches discussed in the chapter. The first row shows the results of the mean Doppler velocity, and the second row shows the results of the Doppler spectrum width. **a** e, DFT, **b** f, PP, **c** g, Levin, **d** h, PSE.

with each observation containing 64 coherent samples ( $N = 64$ ) for the PSE and Levin's ML approach. The mean Doppler velocity and the spectrum width estimated with all the approaches considered in this chapter are shown in Fig. 3.6.

It is observed from the first row of Fig. 3.6 that the mean Doppler velocity estimates from all the approaches look similar except for some regions. The differences can be observed in the case of the DFT and Levin's ML approaches towards the edges of the figures (at more considerable distances from the radar). Although these approaches show near zero mean Doppler velocity, the PP and PSE approaches show a large deviation from zero. It is because the Doppler spectrum is nearly flat (having almost the same power in all velocity bins). Although the

spectrum is nearly flat due to minor asymmetry around the zero Doppler, the other approaches are sensitive and estimate the mean Doppler velocity on either side of the zero Doppler. The existing literature [71], [90] shows that the PP approach is an unbiased estimator of the mean Doppler velocity and very robust at low signal-to-noise ratios. According to the results of the mean Doppler velocity, it is observed that the estimate of the proposed approach (PSE) is very close to that of the PP. In the directions around from  $175^\circ$  till  $225^\circ$  azimuth, there is aliasing of the mean Doppler velocity. It has been captured by all the moment estimates. In the processing chain, it is logical first to perform de-aliasing based on the mean Doppler velocity and use an appropriate window of velocities to estimate the moments. However, the focus is not on the problem of de-aliasing the mean Doppler velocity in this chapter but rather on the moment estimation only. The next chapter in the thesis explores a new approach to avoiding aliasing to improve the mean Doppler estimates. Several observations are made based on the second row of Fig. 3.6. The borders of the aliased region are prominently visible on the Doppler spectrum width estimates of DFT and Levin's ML approaches having large values (till 9m/s). This can be explained by the theoretical simulations in the previous §(Fig. 3.3a, and Fig. 3.3b). As the mean Doppler velocity approaches the unambiguous limit, the estimation of mean Doppler velocity becomes increasingly negatively biased. As the Doppler spectrum width is the square root of the second central moment and the DFT and Levin's ML approaches use PSD measurements, the spectrum width also becomes increasingly biased at the borders of this folded region. However, these high-spectrum width borders are not visible in the case of the PP and the PSE estimates because the PP estimator uses measurements in the time domain directly, and the PSE approach takes care of the aliasing (the semi-analytical model takes the finite observation window into account). A visual inspection of the mean Doppler velocity estimate suggests that the wind direction (the direction the precipitation field is moving) is towards  $\phi = 15^\circ$ . The radial velocity observed by the radar is a scalar sum of projections of the horizontal wind ( $V$ ) speed and the vertical speed ( $V_T$ ) of the raindrops in the radial direction and is given by:

$$\mu_v = V \cos \psi \cos(\phi - \phi_{\text{wind}}) + \tilde{V}_T \sin \psi, \quad (3.19)$$

where the  $\psi$  is the elevation angle from the ground, and  $\phi_{\text{wind}}$  is the horizontal wind direction in azimuth. The mean vertical velocity  $\tilde{V}_T$  is usually associated with the diameters of the hydrometeors [49] [50] [43] (more on it in §6.3). That is why the Mean Doppler velocity estimates are closer to zero towards  $\phi = 135^\circ$ , and  $\phi = 315^\circ$  because these directions are perpendicular to the wind direction ( $\phi - \phi_{\text{wind}} \approx 90^\circ$ ).

In all the approaches discussed in this chapter, it has been assumed that the echo samples in the slow time domain are stationary and the spectrum is Gaussian shaped. Therefore, it is important to study not only the estimation performance but also the profile of the log-likelihood (3.14) as a function of the space because it gives a quantitative understanding of how well the real data fit the semi-parametric model discussed in the chapter. The log-likelihood (3.14) has been plotted and shown in Fig. 3.5b to access the performance of the PSE approach on the real radar data. It can be observed that at high reflectivity regions below the melting layer shown in

Fig. 3.5a, the likelihood is larger than in the melting layer. It can be concluded that the model considered in the PSE approach fits the observations better in the case of the rain Doppler spectrum than in the melting layer.

The Doppler spectrum reconstruction is performed on specific resolution cells using all the approaches discussed in the chapter to validate the abovementioned test cases. The PSD of the echo samples is used as a reference (Ground Truth). The reconstruction is performed using the theoretical expected PSD of (3.10). Their estimated counterparts replace the parameters  $\mu_v$  and  $\sigma_v$  in (3.10). To highlight the range-azimuth cells discussed in the next sub-sub-sections, Fig. 3.6d is shown again in Fig. 3.7. Table 3.2 shows the coordinates of the chosen resolution cells for the analysis.

Table 3.2: Highlighted resolution cells' coordinates

Cell Number	$R(\text{km})$	$\phi^\circ$
(1)	1.26	277
(2)	2.39	234
(3)	4.7	166

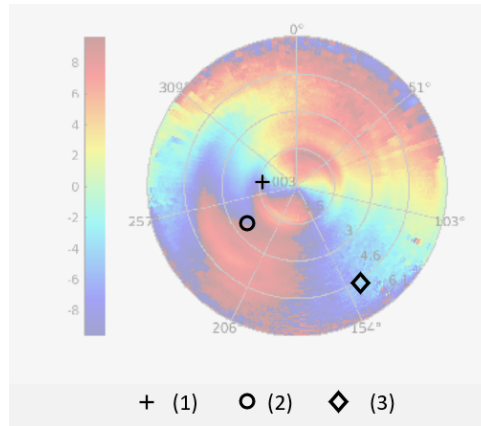


Figure 3.7: PSE derived mean Doppler velocity. The Doppler spectrum is analyzed in the highlighted areas of this figure.

#### HIGH REFLECTIVITY REGION (PRECIPITATION REGION)

Fig. 3.8a shows the Doppler spectrum at the cell (1). The Doppler spectrum reconstruction for the same resolution cell is shown in figure 3.8b for  $N = 64$  and  $L = 1$  case.

According to Fig. 3.8b, it is observed that with only one observation  $L = 1$  of 64 coherent samples, the PSE approach converges and reconstructs the spectrum better than the other approaches. The other approaches overestimate the Doppler spectrum width. This shows the superiority of the PSE approach with a low number of samples over the other approaches discussed in this chapter.

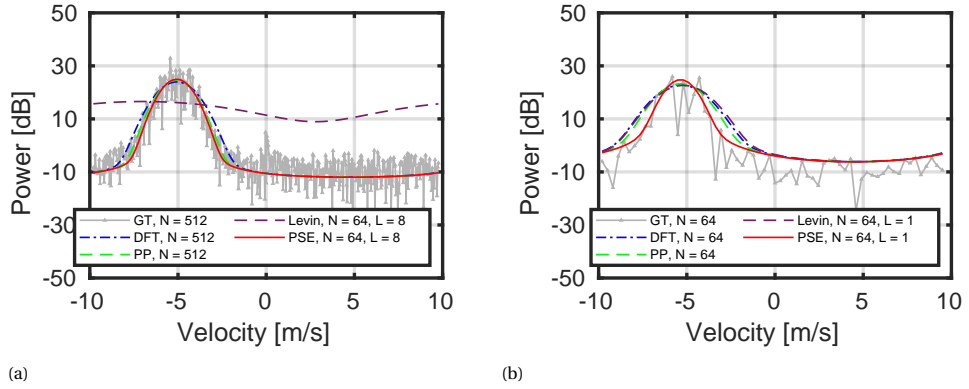


Figure 3.8: Doppler spectrum reconstruction at cell (1) **a** 512 total samples **b** 64 total samples

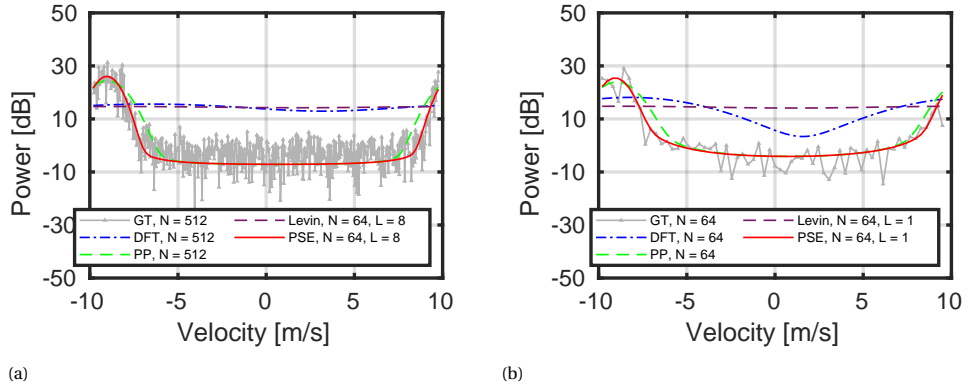


Figure 3.9: Doppler spectrum reconstruction at cell (2) **a** 512 total samples **b** 64 total samples

#### HIGH REFLECTIVITY REGION WITH DOPPLER ALIASING

Fig. 3.9a shows the Doppler spectrum at cell (2). The Doppler spectrum reconstruction for the same resolution cell is shown in Fig. 3.9b for  $N = 64$  and  $L = 1$  case.

It is observed from Fig. 3.9b that the PSE approach converges only with one observation  $L = 1$  of 64 coherent samples. In addition to that, the results of Fig. 3.9a and 3.9b validate the theoretical conclusions made on the Fig. 3.3b. The PP and PSE approaches are immune to the Doppler aliasing in the Doppler spectrum width estimate case. On the other hand, the other approaches overestimate the Doppler spectrum width.

#### MELTING LAYER REGION (LOW PSE LIKELIHOOD REGION)

Fig. 3.10a shows the Doppler spectrum at the cell (3). The Doppler spectrum reconstruction for the same resolution cell is shown in figure 3.10b for  $N = 64$  and  $L = 1$  case.

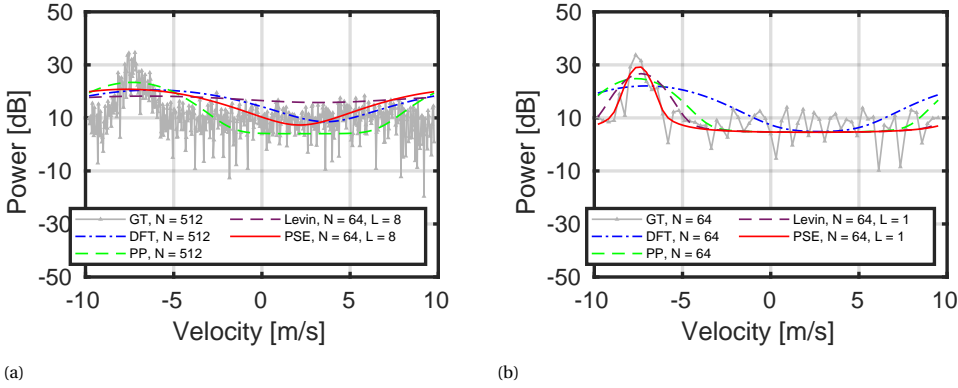


Figure 3.10: Doppler spectrum reconstruction at cell (3) **a** 512 total samples **b** 64 total samples

According to Fig. 3.10a, all moment estimators cannot reconstruct the spectrum with a large number of samples. The Gaussian spectrum shape assumption is violated for a long record of samples at the melting layer. It is confirmed by lower log-likelihood (3.14) values at the melting layer compared to the precipitation area, as shown in Fig. 3.5b. The log-likelihood (3.14) at this range-resolution cell for  $N=64$ , and  $L=8$  is  $-2891$ . However, according to Fig. 3.10b, PSE fitting is superior to the other approaches when a short record of only 64 echo samples is used. The log-likelihood (3.14) for  $N=64$ , and  $L=1$  is  $-334$ . From this analysis, it can be concluded that the Doppler spectrum at the melting layer can only assume stationarity for a short period.

### 3.7.2. APPLICATION TO FAST SCANNING RADAR DATA

Under the assumption that the spectral content (in terms of the spectral width) of the echo signals received from the multiple scans (from the precipitation regions) remains unchanged over this period, the PSE has been applied to real data acquired from multiple scans of the MESEWI radar with a fast scan in azimuth. In this experiment (mentioned as the second measurement at the beginning of the section), the bandwidth of operation was 20 MHz, and consequently, the range resolution was  $\Delta R = c/(2 \times BW) = 7.5$  m. The maximum range in this example was  $R_{max} = (f_s \times c)/(4BW \times PRF) = 15$  km. However, in all the PPI plots, the range is shown till 6 km to avoid the region above the melting layer. The number of echo samples was 100 per resolution cell per scan. The 100 echo samples were grouped into two 50 coherent samples. Five azimuthal scans are processed, resulting in 10 PSD observations per resolution cell ( $L=10$ ). The real data discussed in this section were acquired on the same day as the data discussed in the previous §3.6. As the data was acquired after 26 minutes of the first experiment, the spatial variability of reflection differs from the case shown in Fig. 3.6. The moment estimation uses both PSE and Levin's ML techniques. The performance is evaluated by reconstructing the spectrum with the moments derived similarly to the previous §3.6 for a few resolution cells.

The reconstruction is compared with the PSD of all the observations ( $1 \leq L \leq 10$  in this case). The noise variance estimate here is determined only from the first scan of the radar. The resolution cells chosen for the analysis of the reconstruction are highlighted on top of the Fig. 3.11, which shows the PPI plot of the mean Doppler velocity retrieved from PSE after incoherently processing five scans of the radar data. Table 3.3 shows the coordinates of the chosen resolution cells for the analysis.

Table 3.3: Highlighted resolution cells' coordinates

Cell Number	$R(\text{km})$	$\phi^\circ$
(1)	2.89	48
(2)	1.34	264

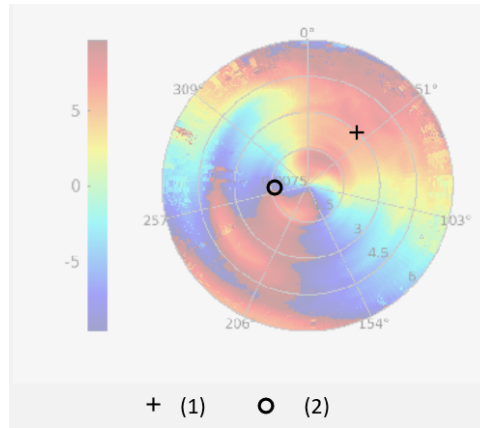


Figure 3.11: PSE derived mean Doppler velocity. The Doppler spectrum is analyzed in the highlighted areas of this figure.

The estimation of the first and second Doppler moments are shown in Fig. 3.12a and Fig. 3.12b with respect to  $L$  at the resolution cell (1). It can be observed that both the PSE and Levin's ML approaches converge to the same estimates with an increasing number of scans, but the rate of convergence of PSE is better than that of Levin's ML approach. As the resolution cell is inside the precipitation region, the approximation of the PSD with a Gaussian spectrum is adequate. The spectrum reconstruction with PSE and Levin is shown in Fig. 3.13 at  $L = 10$ . In the resolution cell (2), the mean Doppler velocity exceeds the maximum unambiguous velocity and Doppler spectrum aliasing takes place. The estimation of the first and second Doppler moments for this situation are shown in Fig. 3.14a and Fig. 3.14b with respect to  $L$ . It can be observed that the spectrum width estimate of the PSE approach is not affected by the aliasing of the Doppler spectrum, while Levin's ML approach gives completely wrong results. The spectrum reconstruction with both approaches is shown in Fig. 3.15 at  $L = 10$ . The PPI plots of the mean Doppler velocity and spectrum width are shown in figure 3.16 with five scans ( $L = 10$ )

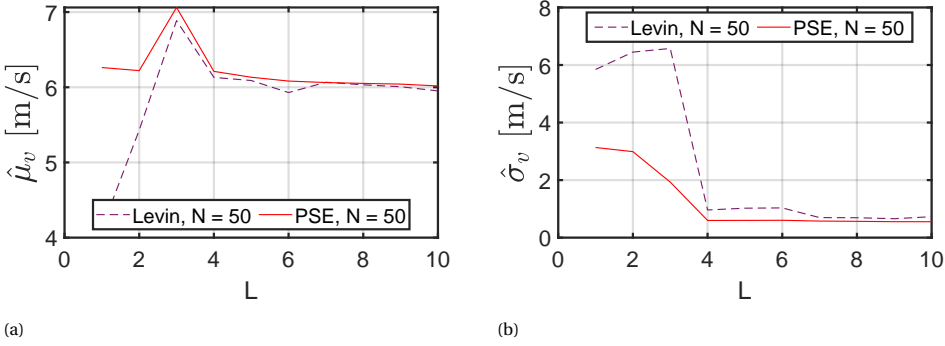


Figure 3.12: Doppler moments estimation on real radar data with respect to number of observations  $L$  at resolution cell (1). **a** Mean Doppler velocity  $\hat{\mu}_v$  m/s **b** Doppler spectrum width  $\hat{\sigma}_v$  m/s

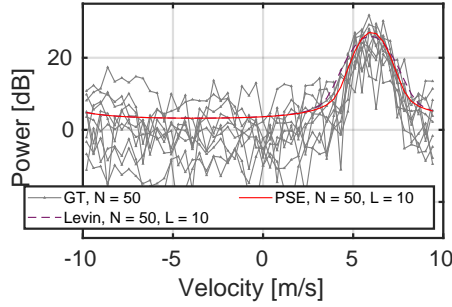


Figure 3.13: Doppler spectrum reconstruction with  $L=10$ . Incoherent processing of 5 scans of the radar at cell (1)

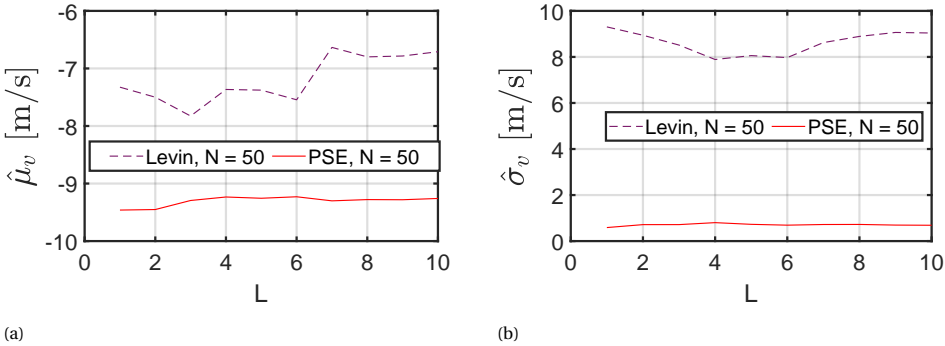


Figure 3.14: Doppler moments estimation on real radar data with respect to the number of observations  $L$  at resolution cell (2). **a** Mean Doppler velocity  $\hat{\mu}_v$  m/s **b** Doppler spectrum width  $\hat{\sigma}_v$  m/s

integrated into the estimation until the melting layer. It can be observed that the PSE approach is not affected by the Doppler aliasing when it comes to estimating



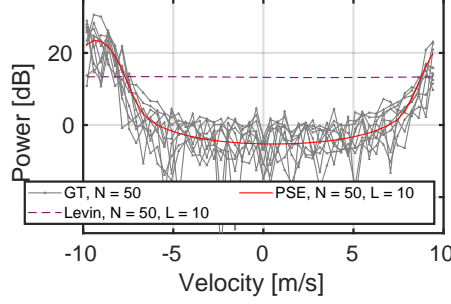


Figure 3.15: Doppler spectrum reconstruction with  $L = 10$ . Incoherent processing of 5 scans of the radar at cell (2).

the Doppler spectrum width.

### 3.8. JOINT ESTIMATION OF NOISE VARIANCE AND THE DOPPLER MOMENTS

In the previous sections of the chapter, the noise variance is considered known. This assumption is usually valid for radar applications because there are heuristic ways to estimate the noise variance. One such way to estimate it is to take the 15th percentile of the power in the PSD measurement (considered in the Subsection 3.7.1 for the real data analysis). In estimation problems, if the noise is of white Gaussian, the noise is often treated as a nuisance parameter [97]. In this section, the noise standard deviation  $\sigma_n$  is considered unknown, and it is estimated jointly with the Doppler moments. The parameters to be estimated here are  $\Theta = [\mu_{fn}, \sigma_{fn}, \sigma_n]$ . The noise standard deviation is automatically estimated without making any assumptions using the PSD model (3.10).

#### 3.8.1. NUMERICAL SIMULATION

The simulated signals are generated similarly to those in the previous subsection 3.6. The SNR with which the signals are generated is 12 dB. The number of coherent echoes  $N = 64$ , and the number of measurements  $L = 16$ . The performance is studied with respect to the normalized spectral width  $\sigma_{fn}$ . The bias and standard deviations in the estimates are shown in Fig. 3.17. The results of the PSE are compared with Levin's approach.

It can be observed that the bias in the estimates of normalized spectrum width  $\hat{\sigma}_{fn}$  and noise standard deviation  $\hat{\sigma}_n$  for PSE is lower than that of Levin's approach lower than a normalized spectral width of around  $\sigma_{fn} = 0.16$ . Doppler PSDs having a normalized spectral width of  $\sigma_{fn} = 0.2$ , or more can be considered "flat," and therefore, the estimates are increasingly biased. Therefore, typically, weather radars should be designed with a suitable PRT to have a sufficient maximum unambiguous velocity that can contain the useful spectrum from a wide range of atmospheric events (such that the  $\sigma_{fn}$  remains lower than 0.1).

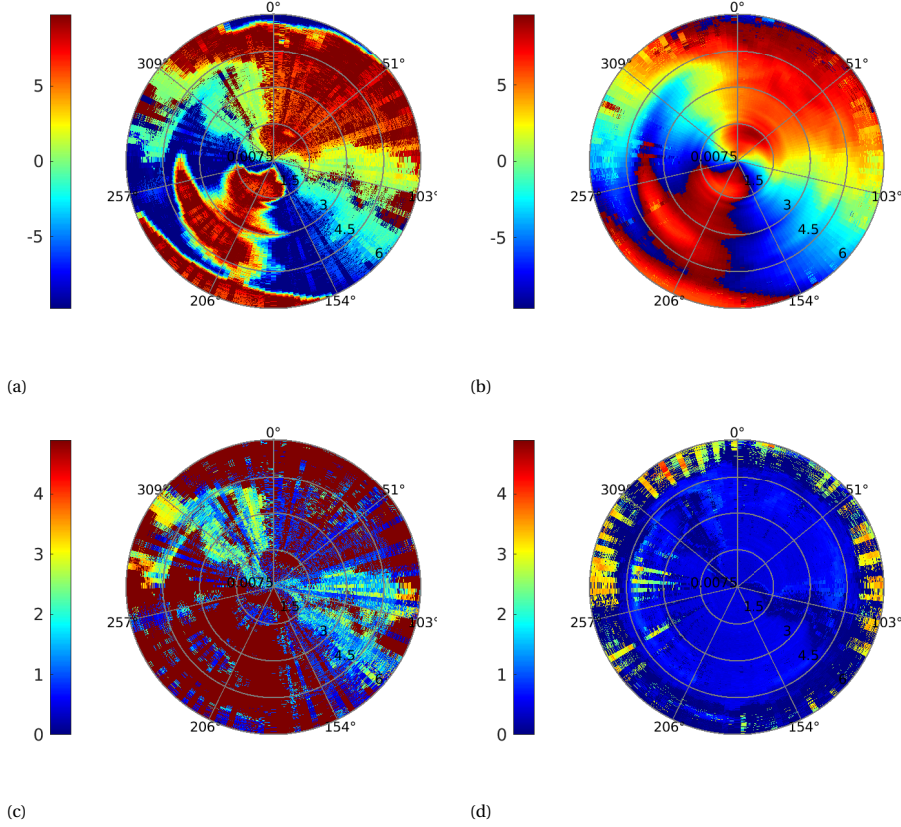


Figure 3.16: PPI plots at  $L=10$ . Incoherent processing of 5 scans of the radar **a** Mean Doppler velocity  $\mu_v$  m/s with Levin's ML approach. **b** Mean Doppler velocity  $\mu_v$  m/s with PSE. **c** Doppler spectrum width  $\sigma_v$  m/s with Levin's ML approach. **d** Doppler spectrum width  $\sigma_v$  m/s with PSE.

The theoretical standard deviations are derived by taking the diagonal elements of the inverse of the Fisher information matrix. The formulation of the Fisher information matrix of (B.1) is extended for three parameters instead of two ( $3 \times 3$  matrix).

It can be concluded that as the observation interval reaches infinite  $N \rightarrow \infty$ , the estimator achieves unbiasedness, and the derived theoretical variance converges to the unbiased CRB. The theoretical standard deviations deviate from the numerical results for higher  $\sigma_{fn}$  due to the increasing biases.

### 3.8.2. APPLICATION TO REAL RADAR DATA

The proposed approach is applied to the same data mentioned in the §3.7. The specification of this particular measurement set-up can be found in Table 3.1. The scan speed of the radar was five rotations per minute (rpm) in the azimuthal direction. The number of echo samples for each resolution cell was 100 (with a

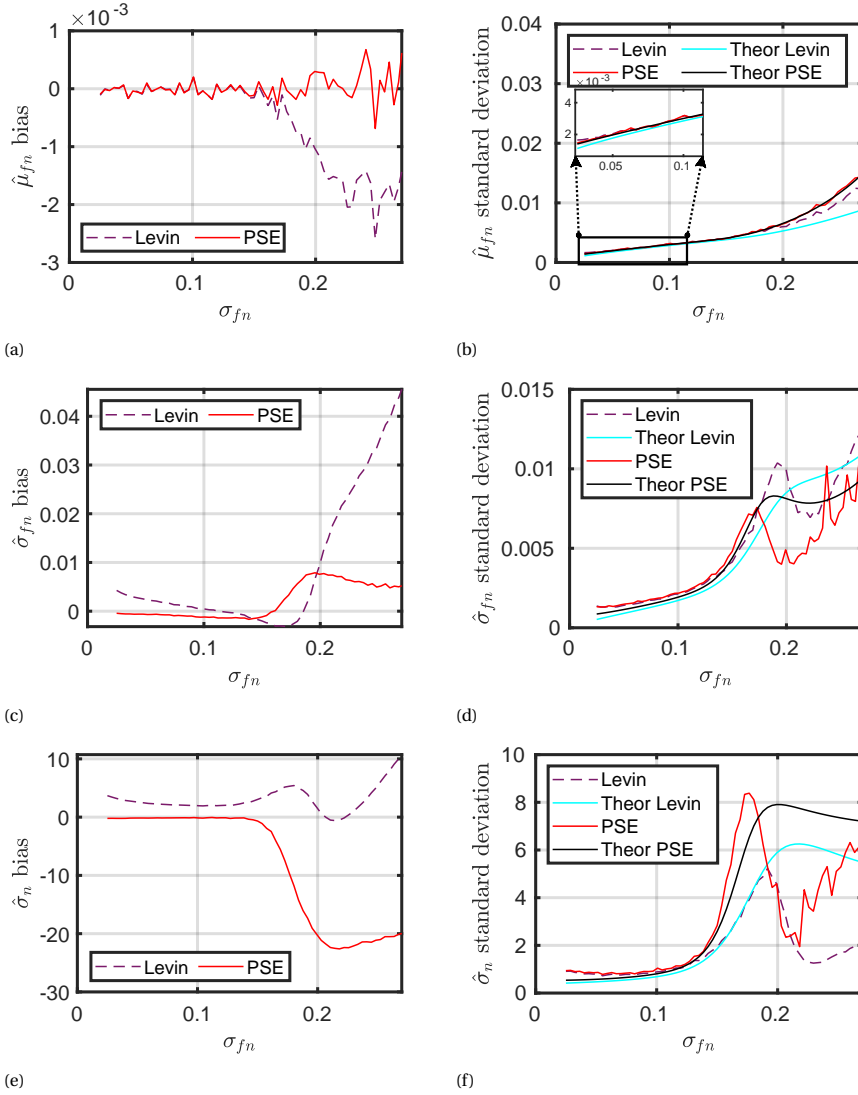


Figure 3.17: Estimation performance with  $\sigma_{fn}$  with an input SNR of 12dB,  $N = 64$ ,  $L = 16$  a Bias of  $\hat{\mu}_{fn}$  b Standard deviation of  $\hat{\mu}_{fn}$  c Bias of  $\hat{\sigma}_{fn}$  d Standard deviation of  $\hat{\sigma}_{fn}$  e Bias of  $\hat{\sigma}_n$  f Standard deviation of  $\hat{\sigma}_n$ . The legend with “Theo” refers to theoretical plots.

PRT of  $813.2\mu\text{s}$ , the time on target per scan was 81.32ms). The pre-processing, including the range Fast Fourier Transform (FFT) and the clutter removal processes, is explained in 3.7. The maximum unambiguous velocity for this radar is  $V_a = 9.8\text{m/s}$ . The number of radar scans used in this experiment is five, and the number of PSD measurements is  $L = 10$  (with two PSDs obtained from one radar scan using 50 echo samples each).

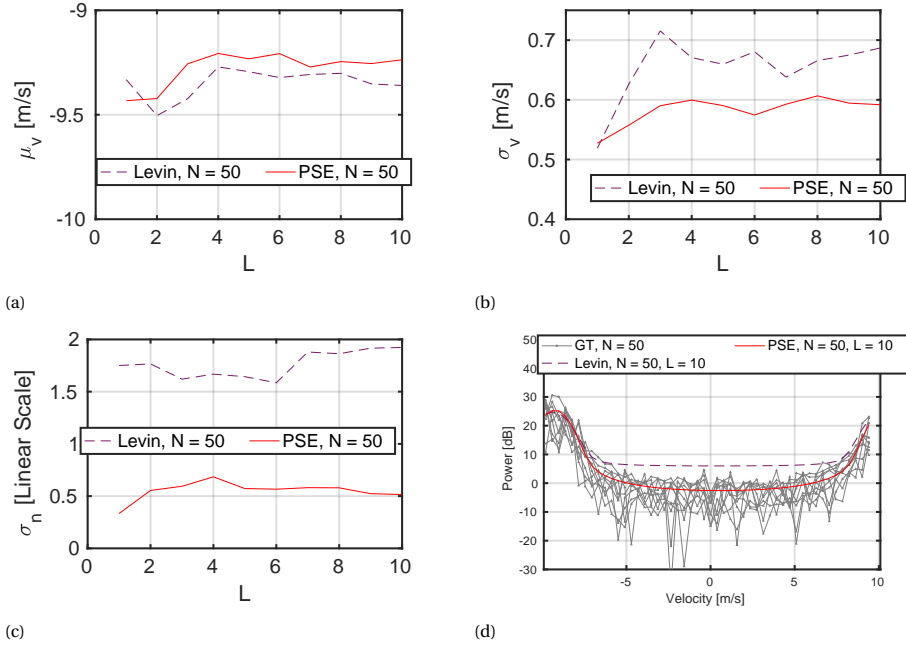


Figure 3.18: Parameter estimation and Doppler PSD reconstruction with real radar data collected from five consecutive scans of a fast scanning radar from the voxel located at range  $R = 1.24$  km, azimuth  $\phi = 264^\circ$  from the north in a clockwise direction, and an elevation of  $\theta = 30^\circ$ . **a**  $\hat{\mu}_v$  m/s **b**  $\hat{\sigma}_v$  m/s **c**  $\hat{\sigma}_n$  (linear scale) **d** Reconstruction of the PSD. The abbreviation “GT” stands for “ground truth” PSD measurements.

One resolution volume is chosen to show the variation in the estimated parameters as a function of  $L$ . The results are shown in Fig. 3.18. The location of this resolution cell can be referred from Fig. 3.11 and Table 3.3 (It is marked with a label (2)). This region was chosen because the useful Doppler spectrum from the precipitation is aliased at this resolution volume, making it challenging for typical Doppler moment estimators that use PSD measurements.

### 3.9. CONCLUSIONS

In this work, a model of the Doppler power spectral density (PSD) for the precipitation-like target is proposed as a function of the Doppler moments and the observation interval. A log-likelihood is then formulated by assuming that the spectral power is distributed exponentially at each velocity/ frequency. This log-likelihood function can deal with multiple such PSDs. Multiple PSDs can be acquired from several radar scans for a typical scanning radar. A maximum likelihood estimation is performed on the log-likelihood to estimate the Doppler moments. The proposed novel approach is named the Parametric Spectrum Estimator (PSE). The statistical bias and variance are presented with Monte Carlo simulation (to have enough realizations of the simulated signal in the time domain). Several parameter

sweeps are performed to show the performance.

The parameters considered in these sweeps are the normalized coherent processing interval (number of coherent echo samples in the time domain  $N$ ), the normalized spectral width  $\sigma_{fn}$  (the square root of the normalized second central Doppler moment), the normalized mean Doppler velocity  $\mu_{fn}$ , and the number of incoherent realizations of the PSDs  $L$  (the number of radar scans assuming a stationarity condition of the atmosphere). Normalized quantities are studied instead of the raw physical quantities to make an impartial and scalable performance analysis, meaning that the measurement device (in this case, it is the measurement strategy in terms of the pulse repetition interval  $T$  and the dwell time  $T_{\text{Dwell}}$ ) can be scaled following the real physical velocity parameters such as the raw Doppler parameters  $\mu_v \text{ ms}^{-1}$  and  $\sigma_v \text{ ms}^{-1}$ .

From the performance analysis, it is concluded that the desired number of samples required to have a good bias should be larger than the reciprocal of the normalized spectral width ( $N > 1/\sigma_{fn}$ ) for normalized spectral widths below 0.25, i.e.,  $\sigma_{fn} < 0.25$ , whereas the other Doppler moments estimators need an even larger number of echo samples to achieve a similar bias in the estimates. For higher normalized spectral widths  $\sigma_{fn} > 0.25$ , all approaches, including the proposed PSE approach, become increasingly biased.

The theoretical variances of the parameters are derived and compared with the numerical ones computed with Monte Carlo simulation. The estimates' theoretical variance converges to the Crámer Rao Lower Bound (CRB) when the number of echo samples approaches infinity  $N \rightarrow \infty$ .

The performance analysis with the number of incoherent PSD realizations  $L$  suggests that the variance in the estimates decreases with an increase in  $L$ . Based on theoretical analysis (B.1), (B.4), and (B.8), it can be observed that the theoretical variance in the estimates approaches 0 for  $L \rightarrow \infty$ .

The proposed PSE approach is applied to real scanning radar data acquired from the MESEWI radar at TU Delft. It has been shown that the PSE approach is superior to the other methods. The spectrum reconstruction is also presented with all the methods, and the fitting with PSE outperforms. The PSE approach needs comparatively smaller dwell time than the other methods, which shows its applicability for fast scanning radars.

The proposed approach has also been extended to accommodate the noise standard deviation as a parameter to be estimated. The joint estimation of Doppler moments and the noise standard deviation is presented in this chapter. The proposed PSE is compared with Levin's approach with simulated radar echoes. The PSE outperforms Levin's approach regarding the bias for Doppler spectrum width and the noise standard deviation.

The PSE is applied to real radar observations collected from the MESEWI radar at TU Delft. For resolution volumes with rain having high reflectivity, it is shown that an accurate estimation of the parameters with PSE is achieved with a relatively small number of samples. In some resolution volumes, especially in the melting layer, the echo samples in time do not follow the assumption that the PSD is Gaussian and stationary for a long period. For these cases, the estimation of the

Doppler moments is erroneous. However, using a short data record, the Doppler spectrum can be reconstructed accurately with the PSE approach. A comparison of the Doppler moments estimation using the techniques discussed in this chapter is shown for all range-azimuth radar cells.

A similar approach also could be developed using a semi-analytical form of the ACV function of the time series instead of the PSD. The next chapter in the thesis explores the approach in detail.



# 4

## GAUSSIAN PROCESS REGRESSION FOR DOPPLER SPECTRUM RECONSTRUCTION

*This chapter introduces a Complex Gaussian Process regression (CGP-R) technique for Doppler spectrum reconstruction with aperiodically sampled data. In addition to estimating the Doppler moments with a few samples in the sequence, the proposed approach can directly reconstruct the Doppler spectrum in the frequency domain by using the measurement in the time domain. The CGP-R is an advanced Bayesian inference technique that can estimate a high-resolution Doppler spectrum in the frequency domain along with providing uncertainty bounds for the estimates.*

---

Parts of this chapter have been published in:

T. K. Dash, H. Driessen, O. A. Krasnov, and A. Yarovoy, "Precipitation Doppler Spectrum Reconstruction with Gaussian Process Prior," *2023 IEEE Conference on Antenna Measurements and Applications (CAMA)*, pp. 909–914, 2023



## 4.1. INTRODUCTION

The Parametric Spectrum Estimator (PSE) for Doppler moment estimation proposed in the previous chapter 3 uses a model of the expectation of the PSD for the echo sequences sampled periodically. However, one can not use PSE for echo sequences that are acquired/ sampled aperiodically over time. An aperiodically sampled signal can be realized in cases where 1) periodic data acquisition is not possible, such as in radio astronomy applications; 2) some samples in the sequence are corrupted with interference; or 3) the sampling sequence is deliberately chosen to be aperiodic to address ambiguity or aliasing (more on this in chapter 5).

Given the short records of the echo samples in time and retrieved Doppler moments, the traditional approaches do not attempt to reconstruct the local Doppler spectrum, which could help study the microphysics of such events. In this case, the local spectrum of a stochastic signal refers to the spectrum of a finite-length (windowed) version of the signal. The stochastic signal sequence is considered stationary in that the covariance structure of the sequence remains constant no matter which local part of the signal is considered. However, the signal's spectrum can be different from realization to realization. The unavailability of local Doppler spectrum reconstruction techniques comes from the fact that only the Doppler moments are usually stored for further use rather than the raw echo samples due to memory limitations.

Due to the abovementioned limitations, a desired signal processing chain should have the following features for fast scanning radars:

1. Accurate estimation of Doppler moments with aperiodically sampled short echo records.
2. Reconstruct the local Doppler spectrum with the help of a few echo samples.

In this chapter, a novel signal processing pipeline is proposed that has several features such as accurate moment estimation with a few echo samples in time, the ability to process the echo samples that are not necessarily coherent (usually realized in a very fast scanning radar with the stationarity assumption of the atmosphere assumed for a short period) and reconstruct the high-resolution local stochastic signal and its spectrum directly using a few echo samples in the time domain. Therefore, by introducing the proposed processing chain, one can store a few echo samples from regions of interest in space for later investigations. Real radar data application is shown in §4.8.

The main body of the chapter is organized as follows. The §4.2 presents the rationale behind the proposed approach. The §4.3 presents the training of the complex Gaussian process (hyper-parameter estimation). The §4.4 presents the reconstruction of the local Doppler spectrum (complex Gaussian process posterior). The covariance models used in this chapter are presented in the §4.5. The performance of the hyper-parameter estimation is shown in the §4.6. The §4.7 presents the spectrum reconstruction using simulated radar echoes. The §4.9 concludes the chapter. The appendix B presents the formulae to compute the theoretical variances of the hyper-parameter estimation.

## 4.2. RATIONALE BEHIND THE APPROACH, A BAYESIAN PERSPECTIVE

As this chapter proposes an estimation of the Doppler moments and the reconstruction of the Doppler spectrum with a few echo samples stored in time, a new perspective is put forward. A Bayesian approach has been followed. The complex weather radar echoes are received from an ensemble of many raindrops in a certain volume in space [69], [76, Ch. 4, eq.(4.1), p. 67], the sequence of echo samples can be considered a complex Gaussian process (CGP) with zero mean, covariance function  $C$  and pseudo-covariance  $P$ . The PSD of the same process can be determined by taking the Fourier transform ( $\mathcal{FT}$ ) of the covariance. A stationarity condition is considered for the rainy events for a short period; therefore, it can be assumed that the covariance is a function of only the time difference between the echo samples and not the absolute time instances  $C(t_p, t_q) = C(t_p - t_q)$ . A parametric form of the covariance function with parameters denoted as  $\Theta$  is considered. From a Bayesian perspective, the model is assumed for the time domain sequence itself (as a CGP); the parameters of its covariance are usually referred to as hyper-parameters. The CGP of the echo samples in time can be expressed as the following [99].

$$\mathbf{z} \sim \mathcal{CGP}(\mathbf{0}, \mathbf{C}(\Theta), \mathbf{P}(\Theta)) \quad (4.1)$$

The covariance and pseudo-covariance are given as:

$$C(t_p, t_q) = \mathbb{E}[z(t_p)z^*(t_q)] \quad (4.2)$$

$$P(t_p, t_q) = \mathbb{E}[z(t_p)z(t_q)] \quad (4.3)$$

In some special cases, such as typical weather radar echoes, the Gaussian process is circularly symmetric, meaning that the pseudo-covariance is zero (the process is also called proper CGP). This can be easily derived if we consider the signal model of (3.3). The complex covariance function can be written as:

$$\mathbf{C} = \mathbf{C}_{rr} + \mathbf{C}_{ii} + j(\mathbf{C}_{ir} - \mathbf{C}_{ri}), \quad (4.4)$$

where  $\mathbf{C}_{rr}$ , and  $\mathbf{C}_{ii}$  are the covariances of the real and imaginary parts only. The covariances  $\mathbf{C}_{ri}$ , and  $\mathbf{C}_{ir}$  are the cross-covariances of the real and imaginary parts, and  $j = \sqrt{-1}$ . For a proper CGP, the following identities hold:

$$\mathbf{C}_{rr} = \mathbf{C}_{ii} \quad (4.5)$$

$$\mathbf{C}_{ir} = \mathbf{C}_{ri}^T = -\mathbf{C}_{ri} \quad (4.6)$$

The complex covariance function can be expressed in a matrix form with only real entries as follows:

$$\mathbf{C}_R = \begin{bmatrix} \mathbf{C}_{rr} & \mathbf{C}_{ri} \\ -\mathbf{C}_{ri} & \mathbf{C}_{ii} \end{bmatrix} \quad (4.7)$$

This real-valued covariance matrix formulation of (4.7) is advantageous when dealing with complex-valued observations. The complex-valued observations can be stacked up as one column vector with real and imaginary parts.

$$\mathbf{z}_{r,i} = [\Re(\mathbf{z}), \Im(\mathbf{z})]^T \quad (4.8)$$

Gaussian process regression has two steps. Firstly, the hyper-parameters are estimated by maximizing the marginal log-likelihood. The second step is sampling from a posterior distribution. These steps are explained in detail in the following sections.

### 4.3. HYPER-PARAMETER ESTIMATION (TRAINING THE CGP)

Modeling the signal sequence as a proper CGP gives us the advantage of using the well-defined marginal log-likelihood to estimate the hyper-parameters  $\Theta$ . The log-likelihood is given by (derived from the probability density function of [100, eq. (5.8)]):

$$\log(p(\mathbf{z}|\Theta)) = -\frac{1}{2}\mathbf{z}^H(\mathbf{C} + \sigma_n^2\mathbb{1}_N)^{-1}\mathbf{z} - \frac{1}{2}\log|\mathbf{C} + \sigma_n^2\mathbb{1}_N| - \frac{N}{2}\log(2\pi), \quad (4.9)$$

where  $^H$  is the Hermitian operator,  $||$  is the determinant operator, and  $\sigma_n^2\mathbb{1}_N$  is the covariance matrix of a zero mean white Gaussian noise ( $N$  is the number of data points). The hyper-parameters can be estimated by maximum likelihood estimation. It is worth noting that in (4.9), the covariance matrix used is the complex one (4.4), and the observations are also directly the complex observations  $\mathbf{z}$ . The hyper-parameters are the Doppler moments in this case.

$$\hat{\Theta} = \max_{\Theta} \log(p(\mathbf{z}|\Theta)). \quad (4.10)$$

The algorithm adopted for optimization is presented in algorithm 1.

## 4.4. LOCAL SIGNAL AND SPECTRUM RECONSTRUCTION

### 4.4.1. POSTERIOR IN THE TIME DOMAIN

After obtaining the estimates of the Doppler moments, the posterior can be obtained both in time and frequency domains directly using the time domain observations. The posterior outputs are jointly proper with the training data (observed data). The mean and covariance of the posterior outputs are given below.

$$\hat{\mathbf{z}}_{t,i}(\mathbf{t}^*) = \mathbf{C}^T(\mathbf{t}, \mathbf{t}^*) \mathbf{C}_{\text{CN}}^{-1}(\mathbf{t}, \mathbf{t}) \mathbf{z}_{t,i}, \quad (4.11)$$

$$\hat{\mathbf{C}}(\mathbf{t}^*, \mathbf{t}^*) = \mathbf{C}^T(\mathbf{t}^*, \mathbf{t}^*) - \mathbf{C}^T(\mathbf{t}, \mathbf{t}^*) \mathbf{C}_{\text{CN}}^{-1}(\mathbf{t}, \mathbf{t}) \mathbf{C}(\mathbf{t}, \mathbf{t}^*), \quad (4.12)$$

where  $\mathbf{t}$  are the time instances of the observations and  $\mathbf{t}^*$  are the desired time instances for the posterior. The observations  $\mathbf{z}$  have the same dimension as  $\mathbf{t}$ . The lower case letters in bold represent vectors, whereas the bold upper case letters represent matrices. The  $\hat{\phantom{x}}$  superscript refers to an estimated/ posterior quantity. The covariance with the subscript  $\text{CN}$  refers to the covariance of the data with added covariance of a white Gaussian noise sequence.

$$\mathbf{C}_{\text{CN}} = \mathbf{C}_{\text{R}} + \sigma_n^2 \mathbb{1}_{2N} \quad (4.13)$$

#### 4.4.2. POSTERIOR IN THE FREQUENCY DOMAIN

The frequency domain posterior can be sampled directly from a Gaussian process having the following mean and covariance [101] (because the time domain signal and the spectrum functions are jointly proper):

$$\hat{\mathbf{z}}_{F(r,i)}(\mathbf{f}) = \mathbf{C}_{tF}^T(\mathbf{t}, \mathbf{f}) \mathbf{C}_{CN}^{-1}(\mathbf{t}, \mathbf{t}) \mathbf{z}_{r,i}, \quad (4.14)$$

$$\hat{\mathbf{C}}_{FF}(\mathbf{f}, \mathbf{f}) = \mathbf{C}_{FF}^T(\mathbf{f}, \mathbf{f}) - \mathbf{C}_{tF}^T(\mathbf{t}, \mathbf{f}) \mathbf{C}_{CN}^{-1}(\mathbf{t}, \mathbf{t}) \mathbf{C}_{tF}(\mathbf{t}, \mathbf{f}), \quad (4.15)$$

where  $\mathbf{f}$  are the desired frequency points where the posterior needs to be sampled. In (4.14) and (4.15), there are two extra covariance matrices used along with  $\mathbf{C}_{CN}$ . The covariance matrix  $\mathbf{C}_{FF}$  is nothing but the covariance of the local spectrum  $C_F(f)$  [101] and is the  $\mathcal{FT}$  of the covariance matrix in the time domain  $\mathbf{C}$ .

$$\mathbf{C}_{FF} = \begin{pmatrix} \mathbf{C}_{FFr} & \mathbf{0} \\ \mathbf{0} & \mathbf{C}_{FFr} \end{pmatrix} \quad (4.16)$$

The entries of the  $\mathbf{C}_{FFr}$  are given by:

$$C_{FFr}(f_p, f_q) = \frac{1}{2} \mathcal{FT}(C(\tau)) \left( \frac{f_p + f_q}{2} \right) \times \delta(f_p - f_q) \quad (4.17)$$

The cross-diagonal terms are 0 because the Fourier transform of the time covariance is a real-valued function. It is also the PSD. The formulation of this covariance matrix is the same as given in [101] but without consideration of the window function. The cross-covariance between the local spectrum and the time series can be expressed as:

$$\mathbf{C}_{tF} = \begin{pmatrix} \mathbf{C}_{tFFr} & \mathbf{C}_{tFri} \\ -\mathbf{C}_{tFri} & \mathbf{C}_{tFFr} \end{pmatrix} \quad (4.18)$$

The entries of  $\mathbf{C}_{tFFr}$ , and  $\mathbf{C}_{tFri}$  are:

$$C_{tFFr}(t, f) = \mathcal{FT}(C(\tau))(f) \cos(2\pi f t) \quad (4.19)$$

$$C_{tFri}(t, f) = -\mathcal{FT}(C(\tau))(f) \sin(2\pi f t) \quad (4.20)$$

The covariance functions of typical weather, like Doppler time sequences, are explained in the following §4.5.

### 4.5. COVARIANCE MODEL FOR WEATHER ECHOES

The signal model with the Doppler moments as parameters are referred from [69] (also (3.3)). Using the same signal model and by using (4.2), it can be shown that the covariance function has the following expression:

$$C_{CN}(t_p, t_q) = R \exp \left( -8\pi^2 T^2 \sigma_v^2 (t_p - t_q)^2 / \lambda \right) \times \exp \left( j \frac{4\pi T}{\lambda} \mu_v (t_p - t_q) \right) + \sigma_n^2 \delta(t_p - t_q), \quad (4.21)$$

where  $\nu$  is the radial velocity,  $R$  is the total power of the signal PSD,  $\mu_v$  and  $\sigma_v$  are the mean Doppler velocity and the Doppler spectrum width,  $\lambda$  is the central

wavelength,  $T$  is the pulse repetition time of the radar. For simplicity, normalized frequency quantities (normalized with the maximum unambiguous frequency) are used instead of velocities for the parameters, and the normalized parameters are denoted with a subscript  $n$ . Therefore, using  $\mu_{fn} = 2\mu_v T/\lambda$ , and  $\sigma_{fn} = 2\sigma_v T/\lambda$ , the covariance can be rewritten as:

$$C_{CN}(t_p, t_q) = R \exp\left(-2\pi^2 \sigma_{fn}^2 (t_p - t_q)^2\right) \times \exp\left(j2\pi \mu_{fn} (t_p - t_q)\right) + \sigma_n^2 \delta(t_p - t_q). \quad (4.22)$$

The model of the  $C_{FR}$  therefore can be given by the  $\mathcal{FT}$  of the covariance function.

$$C_{FR}(f) = \frac{R}{2\sqrt{2\pi}\sigma_{fn}^2} \exp\left(-\frac{(\mu_{fn} - f)^2}{2\sigma_{fn}^2}\right) \quad (4.23)$$

The covariance  $C_{TF}$  can therefore be expressed in closed forms based on (4.19), and (4.20). In practice, for radar applications, obtaining an estimate of noise variance is possible experimentally. Moreover, in estimation problems, the power/ amplitude is often considered a nuisance parameter. An estimate of  $R$  can be obtained by taking the average power of the signal in the time domain. Therefore, in this chapter, it is assumed that the power  $R$  and the noise variance  $\sigma_n^2$  are known quantities.

## 4.6. PERFORMANCE OF HYPER-PARAMETER ESTIMATION

The signal model of (3.3) is used to simulate the weather echoes in time with various normalized spectrum widths and a fixed normalized mean Doppler  $\mu_{fn} = 0$  (the number of echo samples  $N = 64$ ). The samples are coherent in time, making a fair comparison with the non-parametric techniques. The number of iterations in the optimization process explained in the algorithm 1 is  $U = 256$ . A Monte-Carlo simulation is performed for each spectral width at a fixed noise level with 12 dB input SNR [90]. The hyper-parameters (Doppler moments) are computed by maximizing the log-likelihood (4.9). The optimization is performed using the active-set and the Limited Memory Broyden–Fletcher–Goldfarb–Shanno (L-BFGS) algorithms [93]. This method is preferred for its shorter computation time. Both moment estimates' bias and standard deviation ((3.17), (3.18)) with 1024 Monte-Carlo runs are shown in Fig. 4.1 with two other non-parametric techniques (DFT and PP) and PSE. The theoretical variances are computed similarly to those in PSE. The entries to the Fisher information matrix for CGP is presented in Appendix B.

It can be observed that the bias and standard deviations obtained by the proposed approach CGP and PSE are better than DFT and PP for ( $\sigma_{fn} < 0.2$ ). However, especially for very high spectrum widths ( $\sigma_{fn} > 0.2$ ), PP has a lower bias. The DFT approach has a smaller standard deviation for ( $\sigma_{fn} > 0.2$ ) than other approaches due to its considerable bias. The estimation performance of CGP is very similar to that of PSE. PSE does not involve inverse matrix operation, so it remains computationally more efficient. The advantage of CGP over PSE in moment estimation is that CGP can handle aperiodically sampled echoes.

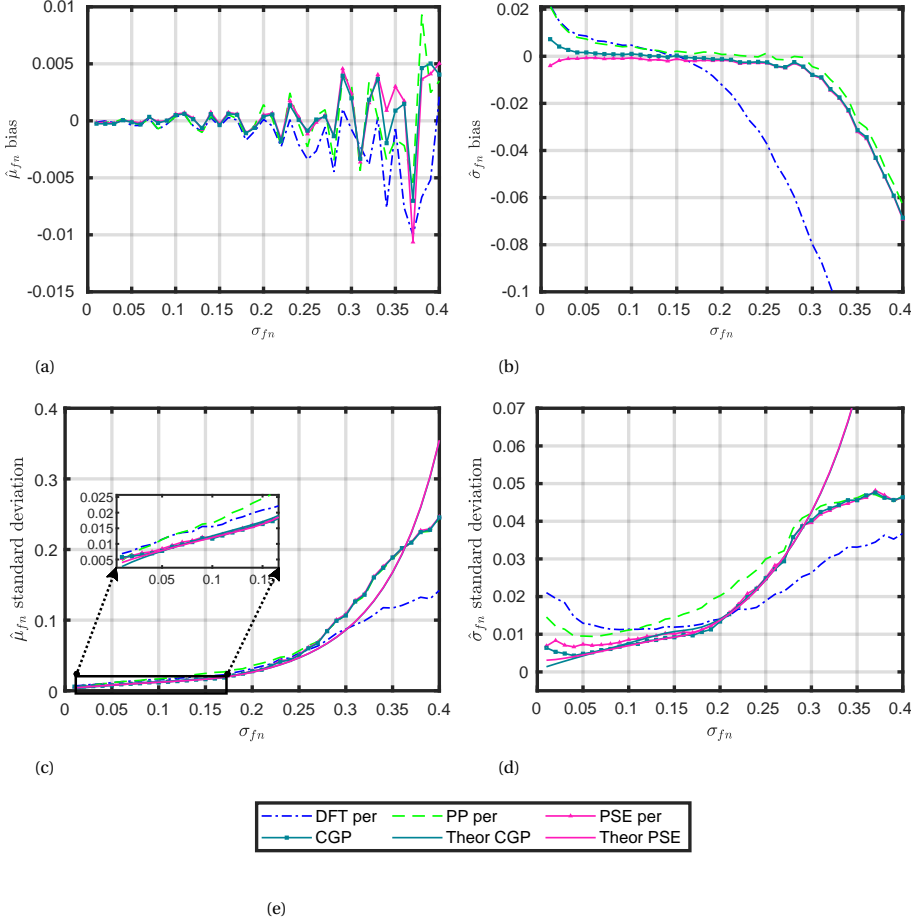


Figure 4.1: Performance of the hyper-parameter estimation for with respect to  $\sigma_{fn}$  at  $\mu_{fn} = 0$ . **a** Biases in the estimates of the mean Doppler frequency normalized  $\hat{\mu}_{fn}$ , **b** Doppler frequency width normalized  $\hat{\sigma}_{fn}$ . **c** Standard deviation of the estimates of the Mean Doppler frequency normalized  $\hat{\mu}_{fn}$ , **d** the Doppler spectrum width normalized  $\hat{\sigma}_{fn}$ , **e** legends for the figures. “Theor” refers to the theoretical plots.

## 4.7. SPECTRUM RECONSTRUCTION ON SIMULATED RADAR ECHOES

The spectrum reconstruction is applied to simulated radar echoes generated using the signal model given in (3.6) in chapter 3. The true normalized mean is  $\mu_{fn} = 0.1$ , and the normalized spectral width is  $\sigma_{fn} = 0.04$ . The signal is generated with  $N = 128$  coherent samples. Two cases are shown for reconstruction: one with 16 (12.5% data) echo samples randomly chosen from the original 128, and the second with 32 (25% of the data). Table 4.1 shows the hyper-parameter estimation results for one

realization of the measurement.

The real part of the posterior (posterior mean with some realizations sampled from the posterior distribution) with the observations and ground truth (the original signal) is shown in Fig. 4.2. It can be observed that with an increasing number of samples, the reconstruction is better. The uncertainty bounds in the estimates increase in regions without measurements. There are some large regions where there are no measurements, e.g., in Fig. 4.2a from  $t = 90$  till  $t = 110$ , the predicted mean in the reconstruction converges to 0, which is the prior distribution assumed by the Gaussian process model.

Table 4.1: Hyper-parameter (Doppler moments) estimation

Parameter	Percentage of data	True	Estimated
$\mu_{fn}$	12.5	0.1	0.1174
$\sigma_{fn}$	12.5	0.04	0.0402
$\mu_{fn}$	25	0.1	0.0905
$\sigma_{fn}$	25	0.04	0.0418

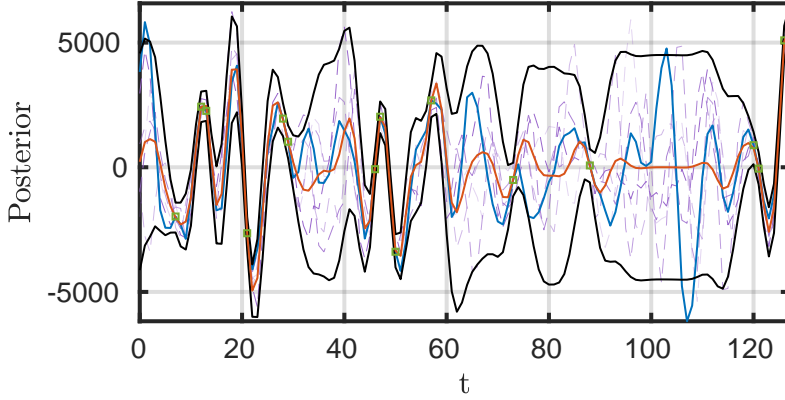
The real parts of the reconstructed posterior spectrum (posterior mean and some realizations sampled from the posterior distribution) are shown in Fig. 4.3. The plots are zoomed in to show the useful part of the spectrum. The reconstruction is compared with the DFT spectrum of the full signal and with zero-padded measurements. It can be observed that with just a fraction of the full signal as measurements, the CGP approach reconstructs the local spectrum, which agrees with the full DFT spectrum.

The power spectrum is shown in Fig. 4.4. The PSD reconstruction with CGP improves with an increasing number of samples. The posterior mean estimate only with 12.5% data can reconstruct the local spectrum adequately. As the frequency domain estimates are integral representations of the signals in the time domain, the reconstruction errors in the frequency domain can be averaged out and become smaller than the errors encountered in the time domain. A study of the errors in the time domain is presented for the reconstruction, considering the mean posterior estimate.

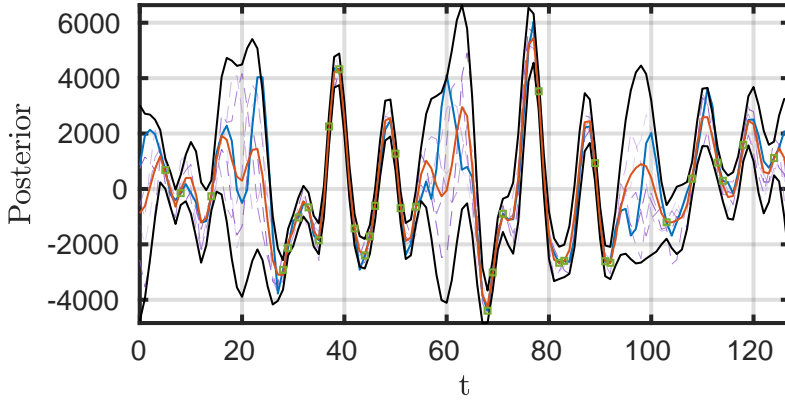
Two different criteria are chosen to evaluate the performance of the reconstruction: one is the error in the CGP mean reconstruction, and the other is the error in the CGP mean but only at the places where the observations/ measurements are available. This error analysis is performed for CGP reconstruction in the time domain. The performance is not studied in the frequency domain because the objective of the reconstruction in the frequency domain was to reconstruct the local spectrum and not the true spectrum. The error chosen is the relative Root Mean Square Error (rRMSE) in the percentage scale and is given by:

$$\text{rRMSE} = \sqrt{\frac{1}{N} \left( \sum_i \left( \frac{\hat{z}(i) - z(i)}{z(i)} \right)^2 \right)} \times 100 (\%). \quad (4.24)$$

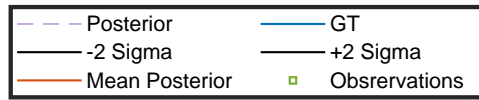
For this analysis, the number of samples in the original sequence is  $N_{\text{gt}} = 128$



(a)



(b)



(c)

Figure 4.2: Time domain reconstruction for real part of the signal **a** 12.5% data, **b** 25% data, **c** legend for the figures.

(can be considered ground truth). The analysis is carried out with respect to the samples considered in the measurements  $N$  at a constant normalized mean Doppler frequency  $\mu_{fn} = 0$  and normalized spectral width  $\sigma_{fn} = 0.04$ . The results are shown in Fig. 4.5. The number of Monte Carlo runs for this analysis is 128. The errors decrease with an increase in the number of data points.



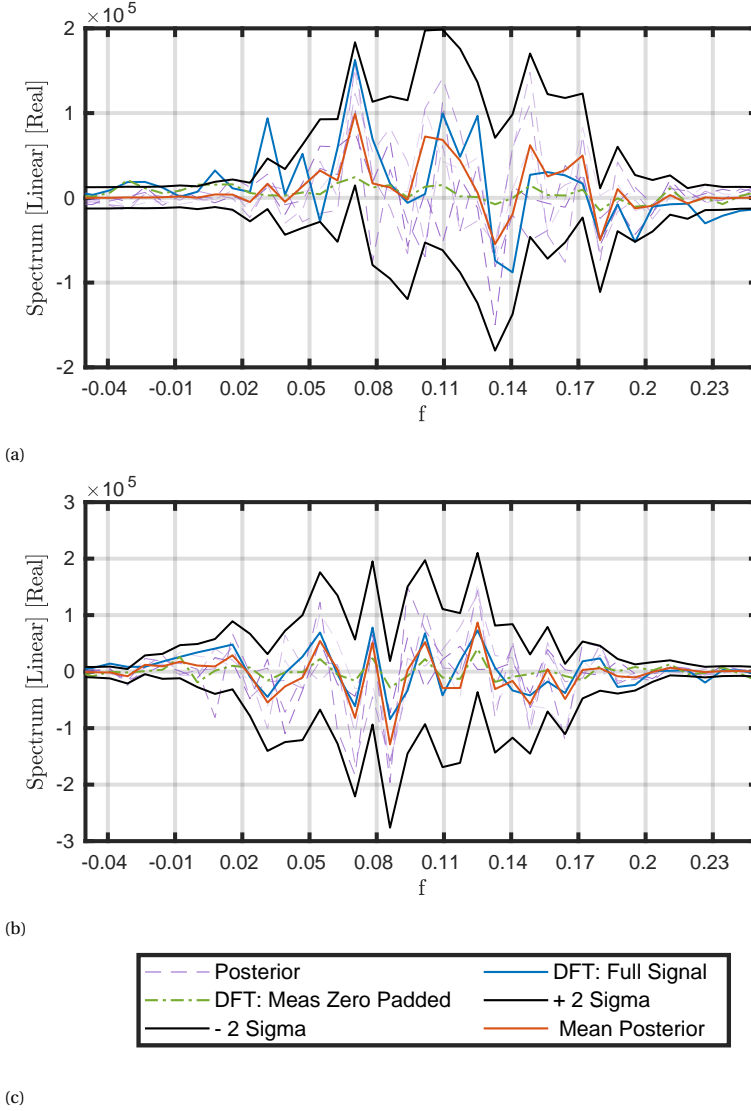


Figure 4.3: Real part of the frequency domain reconstruction **a** 12.5% data, **b** 25% data, **c** legend for the figures. “Meas” stands for measurements.

## 4.8. APPLICATION TO REAL RADAR DATA

The Doppler spectrum reconstruction is performed with data collected from a rain event on May 9, 2023 from the X-band in FMCW MESEWI radar (from the horizontal polarization “HH” channel) at the Delft University of Technology, Netherlands. The radar parameters are shown in Table 3.1. The sampled intermediate frequency data is processed as follows. After DC compensation, range processing is carried out

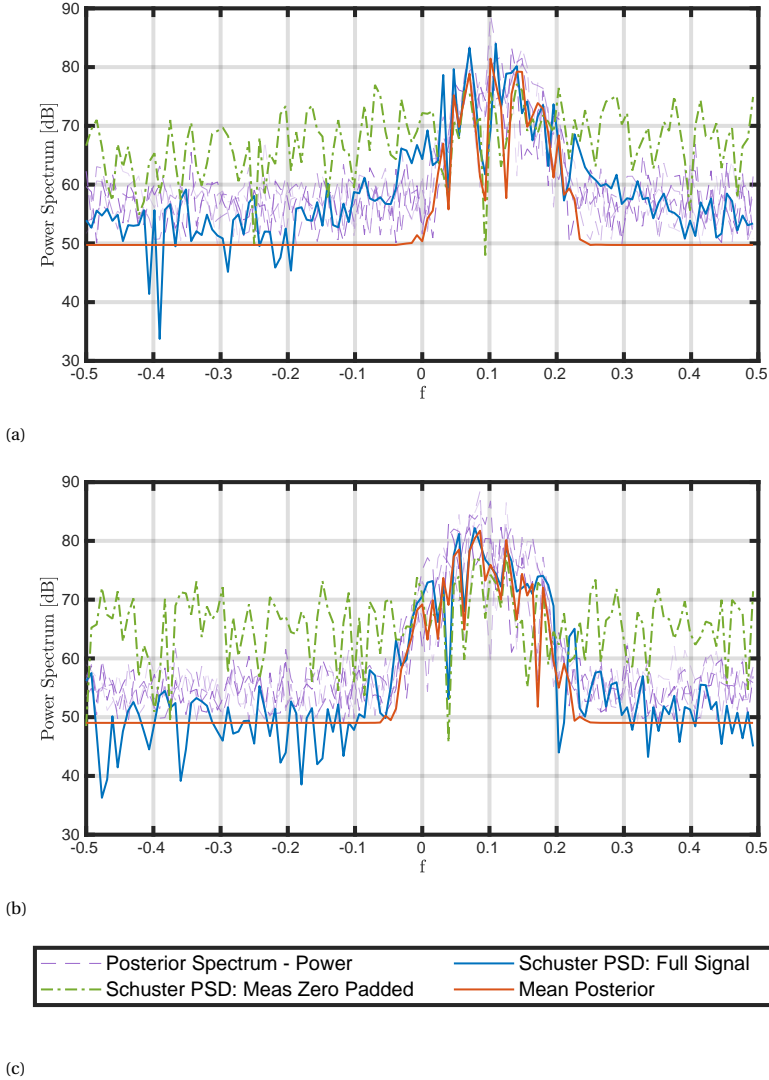


Figure 4.4: PSD reconstruction **a** 12.5% data, **b** 25% data, **c** legend for the figures. “Meas” stands for measurements.

by an FFT in the fast-time domain. The mean is subtracted from each slow time sequence to remove the effect of the clutter. The Doppler processing is carried out in each range-azimuth cell. However, in this chapter, the reconstruction of the Doppler spectrum at one resolution cell that had a range of 1.5 km from the radar and at an azimuth of  $277^\circ$  in a clockwise direction from the geographical north is shown. The elevation at which this data was acquired was  $30^\circ$ .

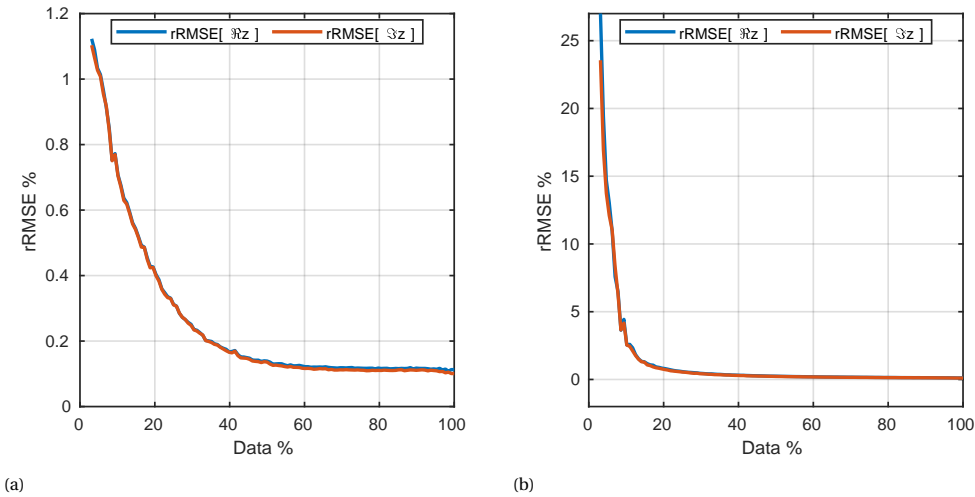


Figure 4.5: PSD reconstruction **a** rRMSE error in the full mean reconstruction, **b** rRMSE error in the mean reconstruction only at the observation points.

The radar scan speed was one rotation per minute 1 rpm with 512 echo samples available from each resolution cell for Doppler processing. The first 128 samples are considered for the study and these samples are considered as the ground truth in the time domain. To simulate a condition where only a few samples are available, random samples from this sequence as measurements are chosen to be used for the reconstruction. A few random samples are chosen for this research to show that the proposed approach can reconstruct the Doppler spectrum of extended weather targets with only a few aperiodically spaced measurements.

The hyper-parameter estimation is shown in Table 4.2. The time domain reconstruction of the real part of the echo samples is shown in Fig. 4.6. Similar conclusions can be drawn here, as in the case of simulated signal reconstruction. The reconstruction is better with an increase in the data points. In the figures, “GT” stands for the ground truth, which incorporates all the 128 samples in the sequence. Of these measurements, only a few are used for the reconstruction.

Table 4.2: Hyper-parameter (Doppler moments) estimation

Parameter	Percentage of data	Estimated (m/s)
$\mu_v$	12.5	-6.96
$\sigma_v$	12.5	0.50
$\mu_v$	25	-7.07
$\sigma_v$	25	0.63

The real parts of the reconstructed posterior spectrum (posterior mean with some realizations sampled from the posterior distribution) with the observations and

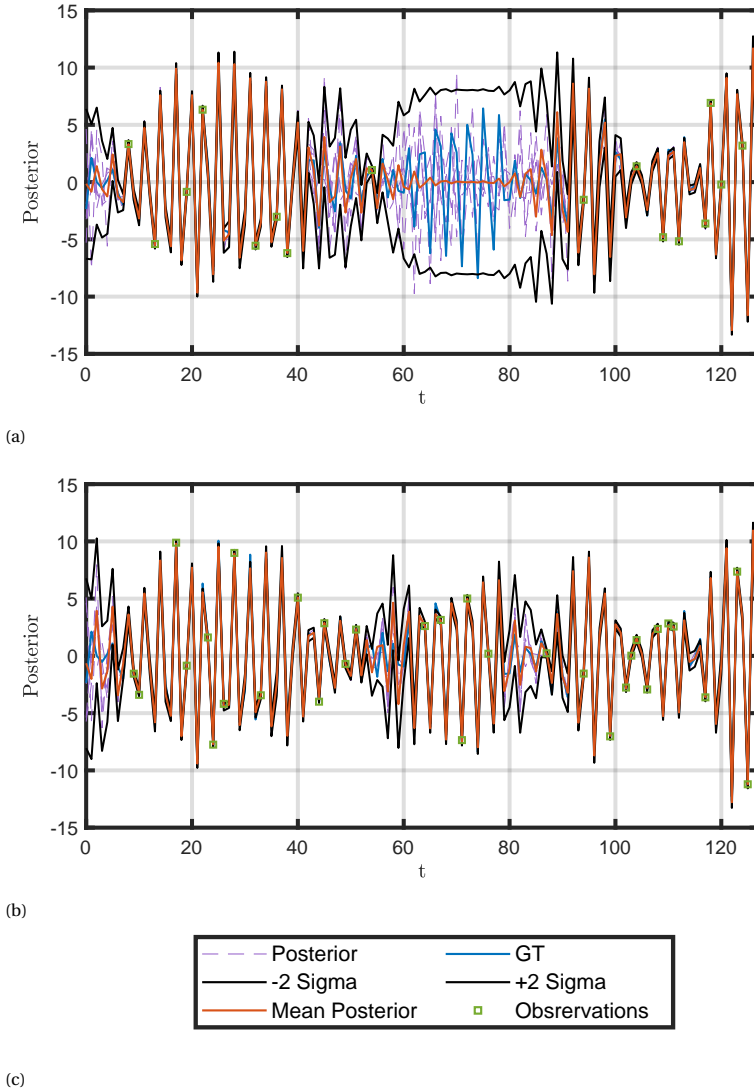
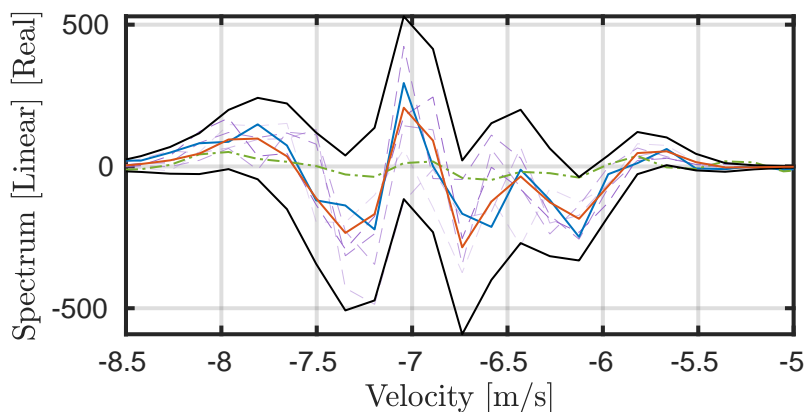
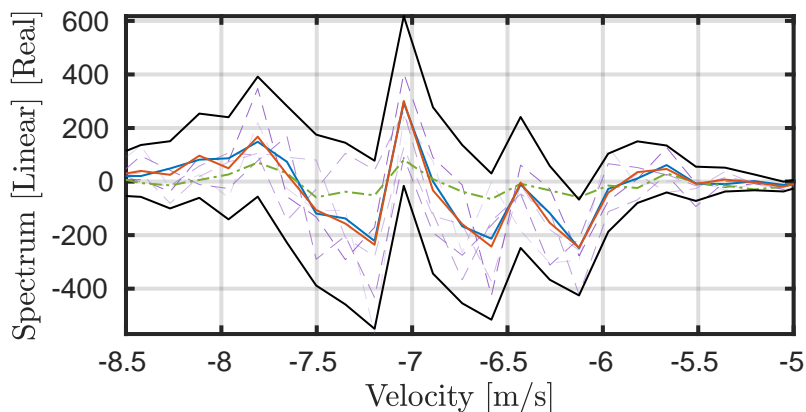


Figure 4.6: Time domain reconstruction for real part of the signal **a** 12.5% data, **b** 25% data, **c** legend for the figures.

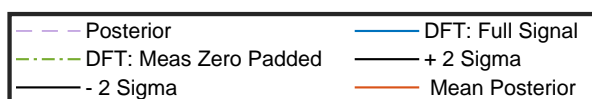
Schuster periodogram (DFT power spectrum) are shown in Fig. 4.7. The plots are zoomed in to show the useful part of the spectrum. The PSD reconstruction is shown in Fig. 4.8. Similar conclusions can be drawn for the reconstruction as they were drawn from the simulation analysis. The performance is superior to the Schuster periodogram constructed with zero-padded measurements. The reconstruction with only a few data points can match the trends of Schuster's periodogram constructed



(a)



(b)



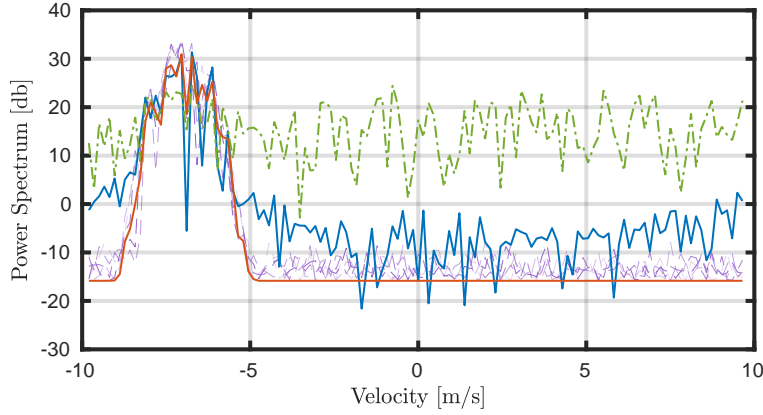
(c)

Figure 4.7: Real part of the frequency domain reconstruction **a** 12.5% data, **b** 25% data, **c** legend for the figures. “Meas” stands for measurements.

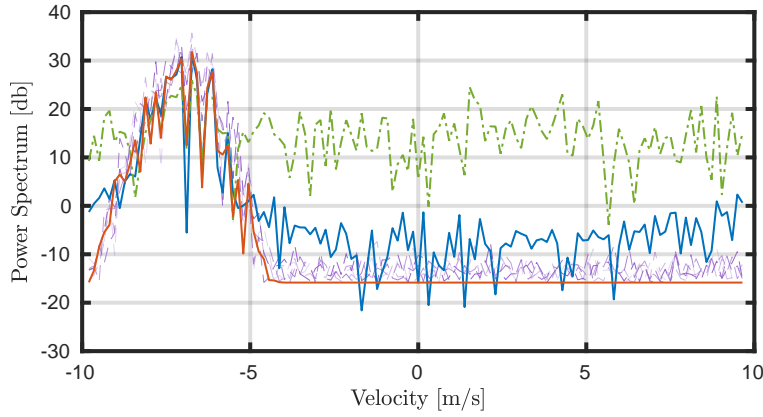
with the full signal.

## 4.9. CONCLUSIONS

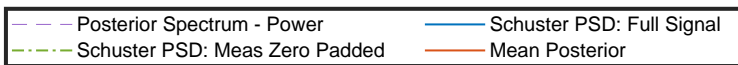
A time-domain approach to Doppler spectrum reconstruction is explored in this contribution. The signal in the time domain is assumed to be a stochastic complex Gaussian Process (CGP) with zero (**0**) mean and a complex covariance structure (**C**).



(a)



(b)



(c)

Figure 4.8: PSD reconstruction **a** 12.5% data, **b** 25% data, **c** legend for the figures. “Meas” stands for measurements.

The covariance  $\mathbf{C}$  is parameterized with physical parameters of interest related to the rain ( $\Theta$ ). In GP literature, these parameters are known as the hyper-parameters. For simplicity, the hyper-parameters are considered the same as in the previous chapter, i.e., the Doppler spectral moments.

Complex Gaussian process regression (CGP-R) is applied to reconstruct the Doppler spectrum. Firstly, the marginal log-likelihood for the hyper-parameters is

maximized to estimate the hyper-parameters ( $\hat{\Theta}$ ). Using the estimated parameters  $\hat{\Theta}$ , the signal and spectrum can be reconstructed using the CGP posterior. Unlike popular GP literature, this work tries to reconstruct the spectrum directly using a CGP posterior in the frequency domain. The CGP-R is a Bayesian technique. Therefore, uncertainty in the estimates is also computed in addition to the predicted signal mean in the time and frequency domain. To the author's knowledge, it is the first time a direct frequency domain posterior is formulated and applied to the weather radar echoes to reconstruct the Doppler spectrum for precipitation, making it novel.

The hyper-parameter estimation performance is assessed by the bias and variance in the estimates and compared with the non-parametric techniques, such as DFT and PP, and the parametric technique PSE proposed in the chapter 3 for equispaced echo samples for a fair comparison. The proposed CGP approach outperforms the other methods in terms of bias and variance. It matches the performance of PSE.

This approach has been applied to simulated radar echoes and real radar data acquired from MESEWI radar at TU Delft at specific resolution cells to reconstruct the Doppler spectrum with the CGP posterior. It has been shown that the CGP-R in the frequency domain can reconstruct the Doppler spectrum with only 12.5% of the echo samples. The posterior mean with 12.5% of the echo samples has excellent agreement with the DFT Doppler spectrum (using all the echo samples acquired during the observation). From the simulation analysis, it is concluded that the reconstruction rRMSE error in the time domain is only 1% when only 5% data is available for a normalized spectral width of  $\sigma_{fn} = 0.04$ . The uncertainty estimates are also computed. The frequency domain posterior is calculated directly using the time domain measurements, posing no additional computational burden.

To sum up, the novel time domain CGP-R approach is effective and accurate for the Doppler spectrum reconstruction with only a few echo samples, preferably un-uniformly spaced in time. The only drawback is the comparatively higher computational resources required than the PSE for the hyper-parameter estimation as it involves matrix inverse operations (as it uses both real and imaginary signal parts in the time domain).

# 5

## COUNTER-ALIASING OF DOPPLER SPECTRUM

*This chapter proposes an integrative approach to counter the effect of aliasing in the Doppler spectrum for precipitation. The previous chapter demonstrated that PSE surpasses state-of-the-art techniques for spectral width estimation, even with aliased spectra, but did not address the aliasing/ambiguity issue for the mean Doppler velocity estimation. PSE is limited to periodically sampled echo sequences. Here, an aperiodic sampling strategy is introduced, with parameter estimation formulated in the time domain using Complex Gaussian Process Regression (CGP-R). Unlike PSE, which uses PSDs of the echo sequence, CGP utilizes both real and imaginary parts, providing complete information. Besides Doppler moment estimation, a high-resolution local stochastic spectrum reconstruction using a direct CGP posterior in the frequency domain is proposed. This counter-aliasing approach is superior to other techniques, including the staggered pulse repetition time (PRT) de-aliasing approach, offering significant advancements in accurate and reliable Doppler spectrum analysis.*

---

Parts of this chapter have been published in:

T. Dash, H. Driessen, O. A. Krasnov, and A. Yarovoy, "Counter-Aliasing Is Better Than De-Aliasing: Application to Doppler Weather Radar With Aperiodic Pulse Train," *IEEE Transactions on Geoscience and Remote Sensing*, vol. 62, pp. 1–17, 2024,

S.A.K Syed Mohamed, T. Dash, O. A. Krasnov, J. Bout, R. v. d. Meer, and A. G. Yarovoy, "Application of non-uniform sampling to avoid aliasing in the precipitation Doppler spectrum," *2024 International Radar Symposium (IRS)*, pp. 216–221, 2024



## 5.1. INTRODUCTION

Aliasing is caused by the sensor configuration, which limits the reconstructed velocities/ frequencies to the Nyquist unambiguous velocity/ frequency limit. Aliasing causes ambiguity when the targets of interest move with higher velocities than this limit.

Doppler spectrum aliasing is not a new problem. It can also be found in other radar-related applications, such as automotive and millimeter wave applications [104], [105], [106], and synthetic aperture radar (SAR) remote sensing [107], [108], [109]. Doppler aliasing is also observed in studies other than radar, such as in ultrasound and ultrasonography sensing [110], [111], [112]. In this chapter, however, the focus is on the aliasing impact on the parameter retrievals and Doppler spectrum reconstruction for precipitation only.

The parameter that is heavily affected by aliasing is the mean Doppler velocity. It is further used to compute the vertical raindrop speed (also known as the terminal fall velocity) and the horizontal wind field as a function of space and time [9], [23], [24], [25], [26], [27], [28]. Some of the de-aliasing techniques are addressed in the post-processing phase to locate the mean Doppler velocity correctly by using information from other sources (also sometimes non-radar sources). These methods detect sharp mean Doppler velocity transitions across resolution volumes, assuming smooth and homogeneous wind fields. In these post-processing de-aliasing algorithms, challenges include missing or corrupted mean Doppler velocity retrievals, addressed by advanced tools like [113] and [114, Ch. 5] (model-based optimization technique). Some techniques incorporate temporal reflectivity and mean Doppler velocity variability to relax the assumption of a homogeneous wind field [115], albeit at increased computational cost. In addition, these temporal approaches may still rely on assumptions like reflectivity conservation [116] (often associated with fluid flow).

Aliasing in many existing sensor systems is inevitable due to one crucial system design related to the transmitted radar pulse train: the fixed interval between two successive transmitted signals (also known as the pulse repetition time, PRT). This type of signal sampling is known as periodic sampling. Therefore, the apparent strategy that has been tried to avoid aliasing is an aperiodic way of sampling the signal. Despite numerous efforts to realize optimized sampling strategies and parameter estimation techniques, aliasing remains an issue due to the lack of an appropriate frequency domain conversion technique (leading to much higher ambiguous lobe levels). One such sampling strategy is known as the staggered sampling sequence, where the sequence alternates between two periodically sampled sequences [19], [117]. Although the de-aliasing scheme presented with staggered sequences is computationally efficient, they are susceptible to errors introduced by the individual velocity estimates of the constituent sampling sequences. External inputs are often used to mitigate such errors, like spatial and temporal continuity of Doppler moments [19], [18].

To address the aliasing issues, one needs to broaden the research horizon, investigate the problem of ambiguity from various perspectives, and combine the outcomes of these investigations in one generic approach.

This chapter constructs a generic, novel, and integrative approach that exploits an aperiodic sampling sequence. An integrative approach means that complementary knowledge from different research areas has been brought together to address the problem of ambiguity (the word “integrative” is emphasized to show that it is not just a combination of techniques).

The various research areas which contribute to the integrative approach proposed are the following:

1. The Nyquist limit for aperiodically sampled signals.
2. Radar signal processing approaches to deal with aperiodically sampled signals in the frequency domain.
3. Frequency domain conversion techniques specifically designed for aperiodic sequences.
4. Model-based parameter estimation and reconstruction of Doppler frequency spectrum.

Each topic mentioned above in the literature considers several aspects of aliasing but ignores certain others. Hence, the significant contribution of this chapter is a novel integrative approach for radar-based weather monitoring that addresses the research gaps among all the areas mentioned above.

The proposed approach is based on Complex Gaussian Process (CGP) regression on aperiodically sampled signals. It is a parametric technique where parameter estimation is performed first, followed by spectrum estimation. Apart from the novel integrative approach to address the gaps and the advantages of each research area, an intuitive study of the Doppler parameter estimation performance analysis using the proposed technique is presented. This study presents the benefits of the integrative approach and shows the physical limiting conditions for accurately estimating Doppler velocity/ frequency parameters unambiguously. The parameter estimation is compared with the state-of-the-art Doppler moment estimators, such as the Discrete Fourier Transform (DFT), Pulse Pair (PP), the Parametric Spectrum Estimator (PSE) [56], and a staggered sampling approach [19]. The performance of the parameter estimation is also studied with respect to the non-linearity in the sampling sequence. Furthermore, the Doppler spectrum is reconstructed in the frequency domain directly using the CGP posterior [98] and compared with the non-uniform DFT-based periodogram (non-uniform Schuster periodogram). The integrative approach proposed in this chapter is classified as a counter-aliasing technique (and not a de-aliasing technique), where the Doppler velocities and the spectrum are estimated directly from an aperiodically sampled sequence. It does not involve any de-aliasing scheme where true velocities are estimated based on some pre-estimated velocities (e.g., staggered sampling) or extra information (e.g., Unfold Radar Velocity algorithm or UNRAVEL [113]).

The main body of the chapter is structured as follows. The §5.2 presents a broad overview of the state of the art and the rationale behind the proposed approach. The §5.3 explains the signal and the covariance model for typical precipitation events.

The §5.4 is devoted to estimating hyper-parameters in the CGP covariance model (parameters of the Doppler spectrum) and the local spectrum reconstruction. The §5.5 presents hyper-parameter estimation performance analysis results and Doppler spectrum reconstruction with simulated radar echoes. Finally, §5.6 concludes the chapter.

## 5.2. STATE OF THE ART AND THE RATIONALE BEHIND THE PROPOSED APPROACH

In this section, a comprehensive analysis of all the fields of study introduced in the Introduction §5.1 to understand better the issue of aliasing from different perspectives is presented. The missing analysis and research gaps in all these areas of study are delineated. Finally, the rationale behind the proposed integrative approach and its operation is presented.

### 5.2.1. THE NYQUIST LIMIT FOR APERIODICALLY SAMPLED SIGNALS

For any frequency domain interpretation, defining the maximum observable frequency allowed (also called the Nyquist limit) due to the measurement setup is essential. The Nyquist frequency limit is the maximum frequency observable as a result of digitally sampling a signal. The Nyquist limit is very well defined when the signal is sampled periodically ( $f_{\text{NY,per}} = 1/(2T_{k,\text{per}})$ ), where  $T_{k,\text{per}}$  is the periodic sampling interval. However, the Nyquist limit for aperiodically sampled sequences is very ill-defined in the literature. A definition is given in [118], [119], [120] for any sampling sequence (note the  $\leq$ ):

$$f_{\text{NY}} \leq \frac{1}{2} 10^d \text{Hz}, \quad (5.1)$$

where  $d$  is the decimal point precision. For example, if we consider a time sequence where we can measure time with six decimal point precision, the maximum Nyquist limit can be as large as 0.5 MHz if the sequence is aperiodic in nature. This property of breaking the periodicity of the sampling sequence is beneficial in avoiding ambiguity or aliasing. The corresponding velocity parameters are related to the frequency as  $v = f\lambda/2$ , where  $\lambda$  is the radar central wavelength. Therefore, the maximum unambiguous velocity of any sampling sequence as  $V_a$  is given by:

$$V_a \leq \frac{\lambda}{4} 10^d \text{Hz}. \quad (5.2)$$

Throughout the chapter, the subscript “per” is used for periodic sequences, “ap” for aperiodic sequences, and “st” for staggered sequences for clarity. A similar conclusion can be drawn from the literature describing staggered sampling sequences. A staggered sampling sequence is a sampling sequence that switches among several periodic sampling sequences. In [19] and [117], the staggered sequence is made with two periodic sampling sequences whose ratio of sampling intervals is denoted as  $m/n$ , where  $m$  and  $n$  are integers. If the sampling intervals are  $T_{\text{st},1}$  and  $T_{\text{st},2}$ , the underlying sampling interval that satisfies both should

be the greatest common divisor of  $T_{st,1}$  and  $T_{st,2}$ . If this underlying sampling interval is denoted as  $T_u$ , the intervals  $T_{st,1}$  and  $T_{st,2}$  are integer multiples of  $T_u$  ( $T_{st,1} = mT_u, T_{st,2} = nT_u$ ). This underlying sampling sequence decides the Nyquist frequency of the staggered sequence, i.e.,  $f_{NY,st} = 1/(2T_u)$  Hz. If  $m$  and  $n$  are relatively prime, the largest time interval of which  $T_{st,1}$  and  $T_{st,2}$  are integer multiples is  $10^{-d}$  s. The Nyquist frequency in this case is  $f_{NY,st} = 1/2 \times 10^d$  Hz. Therefore, the expression in (5.1) is justified for any sampling sequence. To sum up, in any aperiodic sequence in which there is no obvious greatest common divisor for all sampling intervals in the sequence, one can safely consider that there is still an underlying periodic structure (grid) of which all the sampling intervals are integer multiples, and it is  $T_u = 10^{-d}$  s.

Several methods exist to create an aperiodic sampling sequence, such as linearly increasing chirp sampling, random sampling based on a Gaussian distribution, sinusoidal sampling, etc [121], [122], [123]. However, choosing one for the required application of interest can be challenging. In this chapter, only the log-periodic sampling sequence is used and compared with the conventional periodic and staggered sampling cases. Firstly, a log-periodic sampling is chosen because it is inherently irrational, and the user can define the precision based on the desired decimal point accuracy (an equality sign can be realized for this sampling in (5.1) and (5.2)). The requirement for a certain number of decimal point accuracy can arise from hardware constraints for measuring the sample instances. Secondly, the parameters of the sampling rule can be tuned to ensure the minimum sampling interval doesn't subceed a threshold; hence, it allows for a fair comparison with a corresponding periodic sampling sequence. Thirdly, its performance in the case of point frequency response has been studied, and its performance is the best among all the other non-uniform sampling strategies in terms of the sidelobe levels [121]. A detailed explanation of the sampling rule with the log-periodic sampling strategy has been presented in the numerical simulation §5.5.

The application of log-periodic sampling can be found in the field of antenna array design [124] (here, the sampling refers to the physical placement of antennas in space), and Doppler processing [121]. In these studies, the effect of the log-periodic sampling is studied in the case where the signal consists of one sinusoid in the presence of white Gaussian noise. However, these analyses do not study the performance when the frequency spectrum of the target response is continuous and extended, like a typical precipitation-like Doppler spectrum.

### 5.2.2. RADAR SIGNAL PROCESSING APPROACHES TO DEAL WITH APERIODICALLY SAMPLED SIGNALS IN THE FREQUENCY DOMAIN

As the raw radar echoes are collected in the physical time domain, extra processing is often applied to visualize it in the frequency domain. Let's consider the unambiguous velocity interval being  $[-V_{a,per}, V_{a,per}]$  for a traditional periodic sampling case.

Let's assume that the majority of the scatterers (raindrops, in our case, in one big radar volume) are moving with an average velocity of  $v = 1.5V_{a,per}$  in reality. If we construct the Doppler power spectrum with a traditional frequency domain technique, we will find that the majority of the scatterers are moving with

$(-V_{a,\text{per}} + 0.5 \times V_{a,\text{per}})$ , meaning that the excess from  $V_{a,\text{per}}$  is circularly shifted and added in the opposite direction (at  $-V_{a,\text{per}}$ ). If we construct the power spectrum for velocities  $[-pV_{a,\text{per}}, pV_{a,\text{per}}]$ ,  $p > 1, p \in \mathbb{Z}^+$  in the hope of finding the true mean velocity at  $1.5 \times V_{a,\text{per}}$  with the maximum power level, to our surprise, we will find that the power levels of all radial velocities that are of the form  $v \pm 2pV_{a,\text{per}}$  are the same; causing ambiguity (these lobes in the frequency domain are called as “grating lobes” or “ambiguous lobes.”). As discussed in the previous subsection 5.2.1, in principle, with a proper frequency domain conversion technique, an aperiodic sequence should decrease these higher ambiguous lobe levels, making it unambiguous.

However, there are three missing pieces in the radar literature related to this issue. First, a suitable frequency domain conversion technique is unavailable to realize an unambiguous frequency spectrum for aperiodically sampled signals. Many studies use a Discrete Fourier Transform (DFT) based periodogram approach (Schuster periodogram [125]) to construct the frequency spectrum for aperiodically sampled signals.

5

However, using a simple DFT on aperiodically sampled signals is inefficient as the DFT approach inherently constructs the resonant peaks based on the sampling intervals. If the sampling interval is aperiodic, the DFT response becomes noise-like. Although the ambiguous lobe levels can be reduced, they are not considerably suppressed. These partly suppressed ambiguous lobes that create noisy artifacts in the spectrum will be referred to as “ambiguous artifacts” further in the text. The term “ambiguous locations” is used to refer to the locations in frequency where ambiguous lobes are expected. For example, aperiodic sampling has been used for Doppler frequency response for time series [121]. However, the analysis is restricted to point targets, and the frequency response is studied only with the Schuster periodogram, resulting in higher levels of ambiguous artifacts. Another example can be found in spatial aperiodic sampling, which is deliberately used in antenna array design for communication and radar applications for two main purposes. The first purpose is to increase the aperture size with fewer antenna elements than if designed periodically to have a larger gain and suppression of the ambiguous lobes to avoid confusion regarding the angle of arrival (radiation pattern). However, the radiation patterns of these antenna arrays in these studies are usually computed with a Schuster periodogram, resulting in higher levels in the ambiguous artifacts. Some extra processing is usually applied to suppress the artifacts further [126], [127].

Secondly, the Nyquist limit of such aperiodic sampling strategies is not well discussed. Thirdly, the effect of aliasing on continuous and extended frequency responses (like that from precipitation-like Doppler spectrum) is not discussed. For continuous and extended frequency response, by the application of the Schuster periodogram, ambiguity remains a problem when the normalized spectral width of the target crosses a threshold, even with an aperiodically sampled sequence. It is demonstrated in the simulation §5.5. Usage of Schuster periodogram can be found in [128] for log-periodic sampling for weather Doppler radar data. As this periodogram produced higher levels of ambiguous artifacts (especially deteriorating the frequency response as the spectral width increases), it suggests the use of techniques like

the iterative adaptive approach (IAA) proposed in [129] to suppress the artifacts further. The frequency grid chosen for this analysis can be very large; therefore, the computational complexity grows as a function of the number of iterations in the IAA algorithm. If used incorrectly, the useful spectra levels can also get suppressed along with the artifacts. Therefore, special care must be taken when applying these techniques.

A useful de-aliasing algorithm has been presented for the mean Doppler frequency in the study of the staggered sampling sequence of [19]. However, the algorithm is highly sensitive to errors in the individual estimates of the mean Doppler frequency by the two constituent periodic sampling sequences. Statistical performance analysis of the estimate of the mean Doppler frequency is not presented with respect to the spectral width in [19]. Therefore, the numerical analysis §5.5 of this chapter presents the performance of the Doppler moments estimation with a staggered sampling sequence with a staggered sampling ratio  $m/n \approx 2/3$  and is compared with the proposed log-periodic sampling sequence.

### 5.2.3. FREQUENCY DOMAIN CONVERSION TECHNIQUES SPECIFICALLY DESIGNED FOR APERIODIC SAMPLED SIGNALS.

After discussing the problem in the radar domain, the analysis is extended to the spectral estimation domain. Therefore, the literature based on spectrum estimation explicitly theorized for aperiodically sampled signals [130], [131] is explored. These techniques are typically found in the radio astronomy literature, where the received signal is usually not acquired at periodic intervals.

The Lomb-Scargle periodogram mentioned in [130], [131] is based on a least square fit of the observations with a Fourier-like basis, having discrete frequencies but different amplitudes for the real and imaginary parts. The study drawn from a Bayesian periodogram analyzed by [132] shows that the Lomb-Scargle periodogram is the optimal periodogram for aperiodic sequences, assuming that the signal is resonant with one sinusoid in the presence of white Gaussian noise. The Bayesian formalism of the generalized Lomb-Scargle periodogram is given in [131], [133].

The exponentiation of the generalized Lomb-Scargle periodogram for sinusoids with white Gaussian noise explained in [131], acts like a spectral window where the idea is to suppress the sidelobes and ambiguous artifacts significantly while retaining the shape of the main lobe; however, exponentiation should be performed carefully [118].

Although the nuances of such approaches are discussed, derivation of the power spectrum with a generalized Lomb-Scargle periodogram [134] for a complex signal (with real and imaginary parts of the signal acquired at the same instant with no decay factor in the model), demonstrates no difference from the classical Schuster periodogram. On the other hand, there is also a minimal difference in the sidelobe levels, even for real-valued signals. These techniques are also often designed for a Dirac comb-like frequency response (a combination of pointed frequencies placed at sparse locations in the frequency domain). The issues related to extended frequency responses still remain.

The staggered sampling of [19], is used in [117] to construct the Autocorrelation

Spectral Density (ASD). This technique is useful in separating clutter from precipitation. Although it shows the ASD preserves the spectral response of the clutter near the zero frequency and the sidelobe levels are adequate enough in the frequency range  $f < f_{NY}/5$  for a staggered sampling ratio of  $m/n = 2/3$ , it does not show the power levels at the ambiguous locations. Therefore, it is difficult to judge the ambiguous artifacts in the construction of ASD.

The approach proposed in this chapter is compared with the aperiodic Schuster periodogram in the numerical simulation §5.5, because the radar echoes in slow time, are also complex-valued, and the real and imaginary parts of the signal are received at the same time instant.

#### 5.2.4. MODEL-BASED PARAMETER ESTIMATION AND RECONSTRUCTION OF DOPPLER FREQUENCY SPECTRUM.

Using model-based techniques, some crucial parameters of the Doppler spectrum can be estimated first before reconstructing the spectrum. The literature on Gaussian processes (GP) addresses this issue. The covariance of the signal is modeled with these parameters. These parameters of the GP are estimated by performing the maximum likelihood estimation (MLE) on the marginal log-likelihood.

There are a few missing points in all these studies. The literature that studies the signal reconstruction in its original domain (for example, in this case, the time domain) often ignores the rebuilding of the frequency domain [135]. The literature that deepens into the frequency domain reconstruction often avoids the aliasing issue and complex signals and only deals with real-valued signals [101]. The ones that study complex signals with complex Gaussian processes (CGP) and study the frequency domain reconstruction [98] do not study the ambiguity issues in detail. In all the GP literature, the spectrum/ signal reconstruction is often assumed to be non-parametric. Still, in reality, the covariance of the signal is modeled with some parameters. These parameters are known as hyper-parameters, and the signal/ spectrum reconstruction is highly dependent on the estimated counterparts of these parameters.

The periodic covariance models (or periodic kernel functions) of the GP literature often have a quantity that can characterize an extended target (the spectral width explained earlier in the Introduction §5.1) and a quantity that characterizes the target's location (the mean Doppler frequency explained earlier).

For correlating the meaning of these parameters with normalized weather Doppler parameters mentioned in the Introduction §5.1, it is advised to check the literature:  $\gamma_q$ , and  $\theta_q$  of [101, eq. (15)] is similar as  $2\pi^2\sigma_{fn}^2$ , and  $\mu_{fn}$  of (4.23), respectively. However, as these studies focus on reconstructing the signal, they often do not present a performance analysis of the estimation of the hyper-parameters. For example, the focus of [136] is finding a global maximum in the log-likelihood containing these parameters. It is understood that they try to find the global maxima in an attempt to reach the true location of the target(s) by avoiding getting stuck at the ambiguous lobes (the local maxima). However, the performance of such hyper-parameter estimations has not been appropriately studied for extended targets (by varying the normalized spectral width).



It is also plausible that for certain values of normalized spectral widths, the global maxima for the location parameter (mean Doppler) becomes highly sensitive to the measurements, and the solution becomes truly ambiguous. These techniques are also often applied to signals with missing observations, but they do not often study the aliasing phenomenon and aperiodic sequences.

For the application discussed in this chapter, the hyper-parameters directly relate to physical phenomena in the atmosphere and are highly important for wind and turbulence predictions. As described in [69] and [56], modern fast-scanning weather radars do not have enough time on the extended target volumes due to their fast scanning nature. The “CGP” approach is often preferred, especially when the number of data points is small. Therefore, this chapter presents an estimation of these parameters with a few data points mimicking fast scanning radars.

### 5.2.5. RATIONALE BEHIND THE PROPOSED APPROACH

In this subsection, the proposed integrative approach for counter-aliasing is presented. A log-periodic sampling is adopted for this study as it has a good frequency response for point-like targets [121]. The explanation is given in the subsection 5.2.1. After that, the signal is modeled as a CGP with a covariance function that combines components containing three parameters (their strength, location, and width).

In this chapter, hyper-parameter estimation is conducted to assess the applicability of the proposed log-periodic sampling, focusing on the spectral width's impact on the performance. The spectral width, also a hyper-parameter, reflects the Doppler power spectrum's “flatness”. Larger spectral widths make unambiguous mean Doppler frequency detection more challenging. The study compares hyper-parameter estimation performance with classical Doppler moment estimators like DFT-based and Pulse Pair (PP) algorithms and a parametric spectrum estimation approach [56] (referred to as PSE). The novelty lies in examining how parameter estimations are influenced by this spectral width, addressing the question of “How wide is too wide”? The word “wide” is used to dictate a larger spectral width; typical spectrum width values for severe storms are discussed in [137]. Next, the chapter discusses the physical limitations of accurately estimating parameters. By enhancing the Nyquist unambiguous limit with the chosen sampling strategy, the study avoids global maxima estimation, favoring Newton-based gradient descent optimization from random starting points.

The performance analysis of such estimations is presented in terms of the bias and variance in the estimation (by performing a Monte Carlo simulation). The theoretical variances of such parameter estimation are also derived and compared with the numerical variances obtained from the simulations.

The power spectrum reconstruction is carried out directly in an extended frequency domain (avoiding the reconstruction in the time domain) using CGP posterior to reduce computational complexity [98], [101]. Furthermore, a realistic simulation of weather radar echoes is performed, having three extended targets (one clutter and two extended precipitation-like targets), and the reconstruction is shown using the proposed integrative approach.



### 5.3. SIGNAL AND COVARIANCE MODEL

The echo sequence model with time is given in (3.3), and measurement model with noise in (3.6). The signal at each instant of time is an ensemble of the backscattered signals from each scatterer in the radar resolution volume. The signal is assumed to be stationary (meaning that the frequency content remains constant over a short period). The noise in the measurement model is assumed to be zero mean complex white Gaussian. The measurement model is given as:

$$\mathbf{z} = \mathbf{s} + \mathbf{n}, \quad \{n_k\}_{k=0}^{N-1} \stackrel{i.i.d}{\sim} \mathcal{CN}(0, \sigma_n^2) \quad (5.3)$$

where  $\mathbf{z} = [z(0), z(1), \dots, z(N-1)]^T$  is the complex measurement vector with  $N$  echo samples,  $\mathbf{s}$  is the signal vector, and  $\mathbf{n}$  is the noise vector with noise variance  $\sigma_n^2$ . The signal is assumed to be a circularly symmetric complex Gaussian process (proper CGP) [98]. Proper CGPs have the following properties:

$$\mathbb{E}[z(t_a)z(t_b)^*] = C(t_a, t_b) = C(t_a - t_b) \quad (5.4)$$

$$\mathbb{E}[z(t_a)z(t_b)] = 0, \quad (5.5)$$

where  $C$  is the covariance of the echo samples and only a function of the time difference between the echoes ( $t_a - t_b$ ), and the asterisk (\*) refers to the complex conjugate. The expression in (5.5) is the pseudo covariance, 0 for a proper CGP. The pseudo covariance of Doppler weather radar echoes is 0 because the signal model [56, eq. (3), eq. (4)] assumes that the initial positions of the scatterers are uniformly distributed in the resolution volume. The covariance is modeled as a mixture of periodic kernels with Gaussian envelopes:

$$C(\tau) = \sum_{q=1}^Q R_q \exp(-2\pi^2 \sigma_{q,fn}^2 \tau^2) \exp(j2\pi \mu_{q,fn} \tau), \quad (5.6)$$

where  $Q$  is the number of Gaussian components in the mixture model,  $R_q$  is the total power,  $\mu_{q,fn} = \mu_{q,v}/(2V_{a,per})$  is the normalized mean Doppler frequency, and  $\sigma_{q,fn} = \sigma_{q,v}/(2V_{a,per})$  is the normalized Doppler spectrum width of the  $q$ th component in the mixture. The term  $j$  refers to the imaginary unit  $\sqrt{-1}$ . The  $V_{a,per}$  is the maximum unambiguous velocity for a periodic sampling case, and the parameters are normalized with  $2V_{a,per}$  to make the performance comparison and analysis easier. For velocity estimates, these normalized quantities can be scaled with  $2V_{a,per}$ . The periodic sequence considered here is a sequence having a sampling interval similar to or lesser than the minimum sampling interval of the aperiodic sequence. The details of the sampling sequences that are used in this chapter for performance analysis are given in the §5.5.1.

The motivation for modeling the weather radar signal covariance as a combination of multiple periodic Gaussian kernels is the following:

1. If the radar volume is considerably large and spans multiple altitudes in the atmosphere, there is a chance that the wind field is not constant in the volume and can have different mean velocities in the response.

2. Convective rain and vortices can contain multiple extended components in the Doppler response [138] [139].
3. Due to several types of clutter, an extended target response can be observed at the zero Doppler [140], [141], [142].

The approach developed in this chapter is also applicable to persistent stratiform rain events. The stratiform rain Doppler spectrum is usually modeled as one Gaussian-shaped continuous and extended spectrum. However, as mentioned earlier, if the radar volume is large and covers several altitudes, it can also contain multiple Gaussian-shaped spectra at different mean Doppler velocity locations (due to inhomogeneity in the wind field as a function of height), and the  $Q$  value can be adjusted in that case.

As the proposed approach can also handle a small amount of echo samples, the change in the Doppler velocity parameters can be tracked in time, which is beneficial for applications like hydrology. In this chapter, the Doppler covariance is modeled with mean velocity and spectral width. However, applications like hydrology may need more atmospheric parameters like the Drop Size Distribution (DSD) parameters or the DSD-derived parameters such as the rainfall rate and the terminal fall velocity of raindrops. The covariance can also be modeled with these parameters and considered in the future.

The signal  $z$  can then be considered a zero mean proper CGP:

$$\mathbf{z} \sim \mathcal{CGP}(\mathbf{0}, \mathbf{C}_{\text{CN}}, \mathbf{0}), \quad (5.7)$$

where the first entry is the mean, the second is the covariance, and the third is the pseudo-covariance. The covariance  $\mathbf{C}_{\text{CN}}$  is nothing but the complex covariance  $\mathbf{C}$  with added covariance of the zero mean complex white Gaussian noise  $\mathbf{C}_{\text{CN}} = \mathbf{C} + \sigma_n^2 \mathbf{1}_N$ .

## 5.4. HYPER-PARAMETER ESTIMATION AND SPECTRUM RECONSTRUCTION

The hyper-parameters are estimated by maximizing the log-likelihood (4.9): A constrained quasi-Newton optimization strategy is applied to optimize it. It uses active-set and the Limited Memory Broyden–Fletcher–Goldfarb–Shanno (L-BFGS) algorithms [93]. The algorithm 1 is used for the optimization similarly as in chapter 4. The parameter space for the normalized mean Doppler velocity is chosen as several multiples of the Nyquist interval of the equivalent periodic sequence.

Several other strategies can also be applied for global maxima optimization, like the Markov Chain Monte Carlo (MCMC) sampling methods [143]; these techniques are avoided as they are computationally expensive. For the hyper-parameter estimation performance analysis in §5.5.2, only one of these components ( $Q = 1$ ) is studied to make an intuitive comparison among the different approaches. The total power  $P$ , and the noise variance  $\sigma_n^2$  are considered known quantities for this analysis.

In the spectrum reconstruction §5.5.6, three components are considered: two for two extended weather targets and one for clutter ( $Q = 3$ ). In this case, the number

of unknown hyper-parameters is 8. The mean frequency of the clutter and the noise variance are considered known in this case. The unknown parameters are then the total powers of all the components, the mean frequencies of the extended targets, and the spectral widths of extended targets and clutter. The information on the number of components is assumed to be a known quantity. Closely spaced multiple extended weather targets are not studied in this chapter. If the number of components is unknown, it can also be used as a parameter to be estimated. There are several techniques to address the estimation of  $Q$ . It can be separately estimated using the Akaike Information Criterion (AIC), and the Bayesian Information Criterion (BIC) [144]. It can also be estimated jointly with the other parameters if a reversible jump Markov Chain Monte Carlo Parameter estimation strategy is adopted [97].

For very closely spaced extended targets with velocities modeled with a mixture model, it is a difficult problem and requires many data points. Even with many data points, the parameter estimation is difficult in practice for several other factors and requires dedicated attention [145]. The local spectrum reconstruction is performed using the theory explained in §4.4.

## 5

## 5.5. NUMERICAL SIMULATION

This section presents the performance analysis of the hyper-parameter estimation with  $Q = 1$ . The performance metrics are the bias and the variance.

### 5.5.1. SAMPLING STRATEGY

The specifications of the log-periodic sampling are given below. The following rule gives the sample time instances of the sampling strategy:

$$t_{k,\text{ap}} = \frac{d_1}{d_2} [\exp(d_2 k) - 1], \quad k = 0, 1, 2, \dots, N_{\text{ap}} - 1. \quad (5.8)$$

The parameter  $d_2$  is the exponential growth rate of the sequence. If  $d_2$  approaches 0, the sequence resembles a periodic sequence because  $\lim_{d_2 \rightarrow 0} [\exp(d_2 k) - 1] / d_2 = k$ . The larger the  $d_2$ , the more non-uniform the sequence becomes.

Let's define a periodic sampling sequence suitable enough for a fair comparison. The parameter  $d_1$  is chosen such that the minimum sampling interval of  $T_{k,\text{ap}}$  (i.e.,  $T_{k,\text{ap},\text{min}}$ ) remains greater or equal to the sampling interval of the periodic sampling  $t_{k,\text{per}}$  (i.e.,  $T_{k,\text{per}}$ ).

$$d_1 \approx T_{k,\text{per}}. \quad (5.9)$$

Firstly, this is deliberately posed in this chapter to compare the performance fairly. By imposing this, the number of samples in the aperiodic case is not greater than the periodic one. The spectral quantities, like the Doppler moments, are normalized to the Nyquist unambiguous velocity interval  $2V_{a,\text{per}}$  associated with this periodic sampling sequence for intuitive performance analysis.

Secondly, for practical applications involving FMCW radars, this fixed minimum interval between sweeps ensures a desired maximum range and avoids the issues related to the range overlaid signals. In practice, only the maximum unambiguous

range corresponding to this minimum sampling interval can be studied. A practical suggestion regarding the realization of the proposed aperiodic sampling sequence is presented in subsection 5.5.7. The study of the impact of overlaid signals is not explored. To ensure the same dwell time  $T_{\text{Dwell}}$ , the number of samples in the periodic sequence is typically larger than that of the aperiodic one.

$$\begin{aligned} t_{k,\text{per}} &= kT_{k,\text{per}}, \quad k = 0, 1, 2, \dots, N_{\text{per}} - 1, \\ N_{\text{per}} &= \left\lceil \frac{T_{\text{Dwell}}}{T_{k,\text{per}}} \right\rceil + 1 > N_{\text{ap}}, \quad \forall d_2 > 0 \end{aligned} \quad (5.10)$$

A sequence of  $N_{\text{per}} = 82$  samples for the periodic case and  $N_{\text{ap}} = 64$  samples for the aperiodic case is shown in Fig. 5.1 with  $d_1 = 1$  and  $d_2 = 0.0074$ . The decimal point precision in this sampling example is restricted to  $d = 3$  for the aperiodic sequence for the performance analysis.

Let's define a staggered sampling sequence as well for comparison. To make a fair comparison, the minimum spacing between the samples is chosen to be greater than  $T_{k,\text{per}}$ . To create a staggered sampling sequence with an underlying periodic sequence (with an interval of  $10^{-d}T_{k,\text{per}}$ ), the value of  $m = 1001$  and  $n = 1502$  are considered. The sampling sequence for the staggered case is, therefore,

$$\mathbf{t}_{\text{st}} = [0, 1.001, 2.503, 3.504, \dots]^T \times T_{k,\text{per}}. \quad (5.11)$$

It can be observed from (5.11) that the staggered sampling sequence has a minimum sampling interval greater than  $T_{k,\text{per}}$ , has a decimal point precision of  $d = 3$ , and a staggered sampling ratio  $T_{1,\text{st}}/T_{2,\text{st}} = m/n = 1001/1502 \approx 2/3$ . The constituent sampling intervals in this staggered sequence are  $T_{1,\text{st}} = 1.001T_{k,\text{per}}$ , and  $T_{2,\text{st}} = 1.502T_{k,\text{per}}$ . The theoretical unambiguous velocity for this sequence is:

$$V_{a,\text{ap}} = \frac{\lambda m}{4T_{1,\text{st}}} = \frac{\lambda n}{4T_{2,\text{st}}} \approx \frac{10^d}{2T_{k,\text{per}}} = 10^d V_{a,\text{per}}. \quad (5.12)$$

The mean Doppler frequency in the case of staggered sampling is estimated using the velocity difference transfer function approach given in [19]. Although the performance shown in [19] is as expected for smaller values of  $m$ , and  $n$  (typically  $< 100$ ), higher values for  $m$  and  $n$  ( $> 1000$ ) are chosen to test the performance when the theoretical maximum unambiguous velocity is much higher than the maximum unambiguous velocity of each constituent sampling sequence.

In the following sections 5.5.2 and 5.5.3, the performance analysis of the parameter estimations is studied with the normalized spectral width parameter  $\sigma_{fn}$  and  $d_2$ , respectively.

The performance analysis contains the bias and the standard deviation (square root of the variance) for the estimated parameters  $\hat{\Theta}$  ((3.17), (3.18)). The theoretical variances have been implemented and plotted for the CGP approach. The details are in Appendix B. The inverse of this Fisher information matrix should not be confused with the unbiased CRB in this case, as the retrievals are not entirely unbiased.

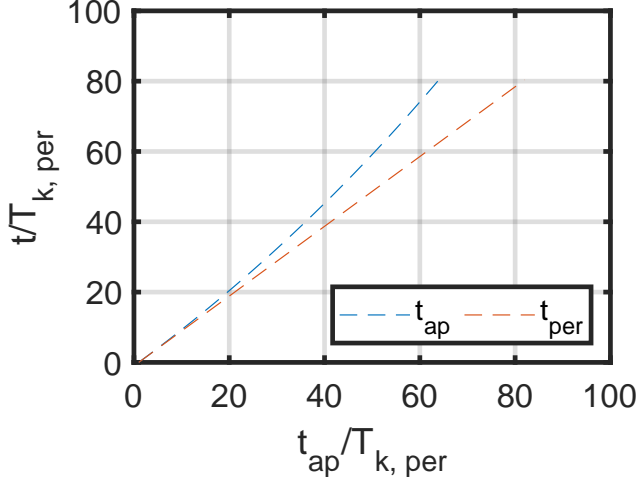


Figure 5.1: Sampling sequences; periodic and aperiodic cases.

However, these theoretical variances converge to the unbiased CRB for an infinite number of echo samples  $N \rightarrow \infty$  as the estimates are asymptotically unbiased. The biased-CRB limits can also be inferred by studying the bias gradient of the estimator, as shown in [91]. However, this is out of the scope of this chapter because a functional form of the bias gradient is harder to achieve.

### 5.5.2. PERFORMANCE ANALYSIS OF HYPER-PARAMETER ESTIMATION WITH $\sigma_{fn}$

In this sub-section, the bias and standard deviation for the hyper-parameters (Doppler moments) are studied with respect to the normalized spectral width  $\sigma_{fn}$  at a fixed  $d_2 = 0.0074$ . The normalization here is performed with the unambiguous interval for the periodic case ( $\mu_{fn} = \mu_v / (2V_{a,per})$ ,  $\sigma_{fn} = \sigma_v / (2V_{a,per})$ , where  $\mu_v$ , and  $\sigma_v$  are the denormalized Doppler velocity moments). The total power and the noise standard deviation are considered known quantities in these simulations. As both DFT and PSE use PSD for the estimation, an extended normalized frequency axis is used for a fair comparison. The bias and standard deviation in the estimation of the mean Doppler and Doppler spectrum width are presented in Fig. 5.2. The number of Monte Carlo simulations performed in this case is 128. The optimization parameters listed in the §3.5 are set to the following values:

$$\begin{aligned} [\mu_{fn,l}, \mu_{fn,u}] &= [-3, 3], \\ [\sigma_{fn,l}, \sigma_{fn,u}] &= [0, 0.5], \\ U &= 512, \end{aligned} \tag{5.13}$$

where  $U$  is the number of iterations in the optimization process explained in algorithm 1. In the examples of this chapter, the parameter space for normalized

mean Doppler velocity is chosen as three times the Nyquist unambiguous interval for the periodic counterpart.

#### ALGORITHMS PERFORMED ON THE PERIODICALLY SAMPLED DATA

The estimators presented for periodically sampled sequences are DFT, PSE of [56], and the PP algorithm.

The DFT approach of Doppler moment estimation is non-parametric and uses Schuster's periodogram as measurement. It is non-parametric because it assumes no parametric structure of the signal or its Schuster periodogram. The formula mentioned in [71, eq. (9)] is used to compute the mean Doppler frequency (similarly, the square root of the second central moment is computed) for the DFT approach with a known noise variance. For a fair comparison, first, the peak location (frequency at which the power is maximum) of the Schuster periodogram is detected, and one Nyquist unambiguous interval is chosen by keeping this location at the center.

The PSE algorithm is a parametric moment estimator using a semianalytical model for the expected Doppler PSD. The PSE is used on the PSD of a periodic sequence because the semianalytical model of the PSD [56, eq. (10)] has a lower bias when dealing with periodic sequences (because it considers the time on target in the model of the PSD as well). The performance analysis in [56] shows that the PSE is more accurate than Levin's approach (which uses a closed form of the Doppler PSD [80] without the time on target). Therefore, the performance using Levin's approach is not studied.

The PP estimates of the Doppler moments are based on the signal's autocorrelation with integer time lags. It is used on a periodic sequence where contiguous pairs can be found. The estimation of mean Doppler with the PP approach is used from [71, eq. (16)]. For the Doppler spectrum width (PP R0/R1), the formula [95, eq. (6.17)] is used as this estimator is asymptotically unbiased.

#### ALGORITHMS PERFORMED ON THE APERIODICALLY SAMPLED DATA

A DFT moment estimator is implemented on the Schuster periodogram computed for the aperiodically sampled data with log-periodic sampling. A similar approach with the peak location detection is performed for a fair comparison, as in the periodic case. The moments are computed using this as the frequency window with the DFT approach. The proposed CGP approach has also been implemented on the aperiodically sampled data with log-periodic sampling.

Two ways to compute the Doppler moments for the staggered sampling case are presented. First, the de-aliasing approach based on the velocity difference transfer function is used to compute the mean Doppler frequency [19]. To compute the de-aliased mean Doppler frequency, the individual mean Doppler frequencies corresponding to the two constituent periodic sampling sequences must first be estimated. These mean frequencies [73, Eq. (5.a), Eq. (5.b)] are estimated by the PP approach, but the one-lag autocorrelation can only be performed on independent pairs [73, Eq. (3), Eq. (4)] (contiguous pairs are not available in the case of a staggered sampling sequence). With this approach, the Doppler spectrum width is computed using only one constituent sampling (the smaller one) [73, Eq. (6)] using

the PP technique. The second technique applied to the staggered sampling case is the CGP technique proposed in this chapter, which can also be found in [17].

The true normalized mean Doppler frequency with which the simulation of the signals is carried out is  $\mu_{fn} = -1.2$ . The noise is added with an input SNR of 12 dB [90].

### PERFORMANCE ANALYSIS

It can be observed that the “DFT aperiodic” technique for the mean Doppler estimation has a small bias for extremely small normalized spectral widths. This validates the results in the literature for the periodogram techniques because a very small normalized spectral width is analogous to having one sinusoid in the signal. The non-uniform Schuster periodogram peak detection becomes increasingly ambiguous with increased spectral width.

The periodic counterparts, including the PP algorithm, also show biased results because of aliasing. In contrast to all these approaches, the proposed CGP approach has a much smaller bias in the normalized mean Doppler frequency estimates for normalized spectral widths less than 0.2. For larger normalized spectral widths, the estimates become increasingly biased because the optimized mean Doppler frequency becomes truly ambiguous and becomes highly sensitive to the measurement.

The normalized spectral width estimates follow a similar trend in terms of bias for the proposed CGP approach. The PP approach has a smaller bias in the higher normalized spectral width regions. The PSE has the smallest bias across all normalized spectral widths. It has also been showed in chapter 3.

The standard deviation for normalized spectral width of  $\sigma_{fn} > 0.3$  is not shown as the results of all estimators are increasingly biased. For the normalized mean Doppler frequency, the proposed approach has lower standard deviations than all the other approaches except for the PP below a normalized spectral width of less than 0.16. PP has the smallest standard deviation because it doesn't consider an extended frequency axis. Therefore, the estimation result is always near the fixed aliased frequency inside the bound  $[-0.5, 0.5]$ . The periodic approaches of DFT and PSE have a more significant standard deviation.

All the methods work similarly to the estimation of normalized spectral width except the DFT aperiodic approach. The theoretical variances for CGP are smaller than the numerical ones for the mean Doppler  $\mu_{fn}$ . The theoretical variance for the spectral width  $\sigma_{fn}$  is higher than the numerical one if  $\sigma_{fn} > 0.14$ . The principles of biased CRB can explain the differences between the numerical and theoretical variances. However, as explained earlier in this section, the biased CRBs are not computed.

The staggered sampling technique also suffers from a large bias for the normalized mean Doppler frequency. The reason for the large bias can be attributed to the fact that the values of  $m$  and  $n$  are large, although the ratio  $m/n \approx 2/3$ . It shows the limitation of the staggered sampling technique when the desired theoretical Nyquist unambiguous velocity is much larger than the Nyquist unambiguous velocity of the individual constituent periodic sequences. For large

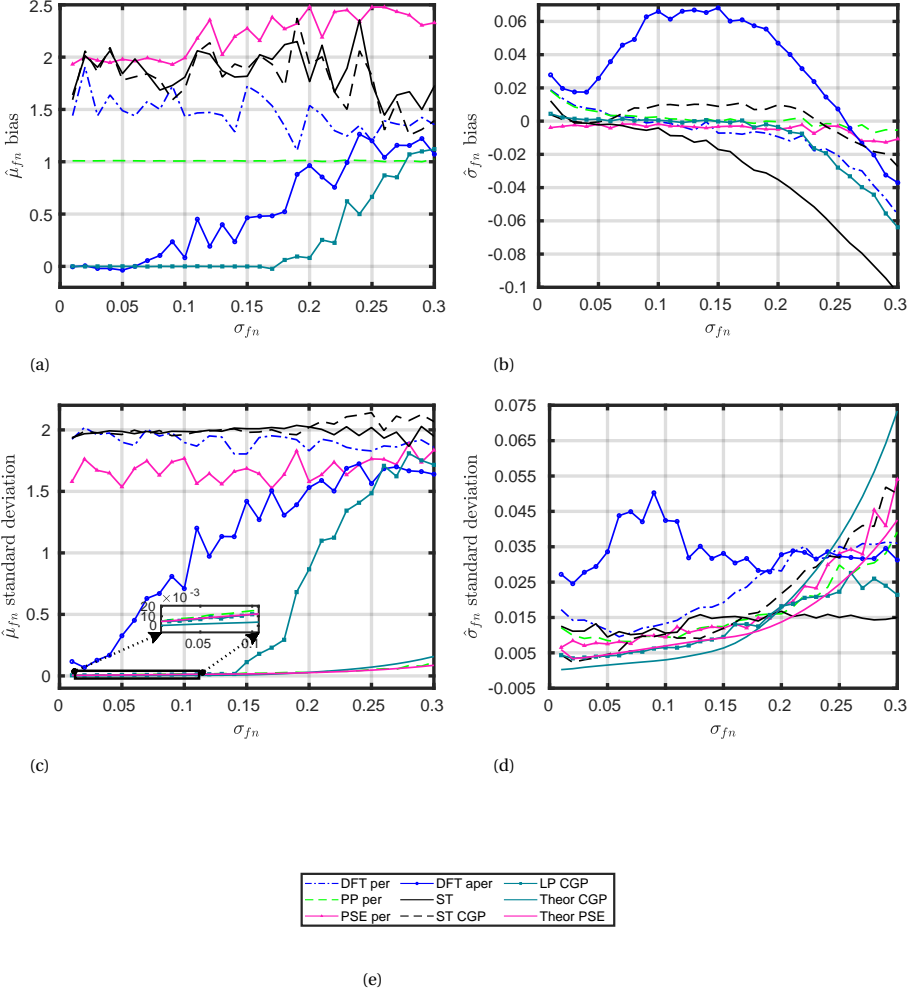


Figure 5.2: Estimation and performance of the Doppler moments with respect to  $\sigma_{fn}$ . For the periodic case, the number of samples is 82, whereas for the aperiodic case, it is 64. Bias in estimating **a** the mean normalized Doppler frequency  $\hat{\mu}_{fn}$ . **b** normalized Doppler frequency width  $\hat{\sigma}_{fn}$ . Standard deviation in estimating **c** the normalized mean Doppler frequency  $\hat{\mu}_{fn}$ . **d** the normalized Doppler spectrum width normalized  $\hat{\sigma}_{fn}$ . The abbreviation “per” refers to the periodic sampling, “aper” refers to the aperiodic one, “ST” refers to staggered sampling (“ST” for velocity difference transfer function and “ST CGP” for CGP applied to staggered sequence), “LP” for the log-periodic sampling, and “Theor” refers to the theoretical plots. **e** Legend for the plots.

values of  $m$  and  $n$  ( $> 1000$ ), to avoid errors, there are recommendations suggested in [19]. However, these suggestions need manual intervention and additional information based on continuity in space and time. Therefore, not all the suggestions for such a configuration are implemented in this chapter. However, it is noticed that the algorithms implemented on the staggered sequence successfully estimate the



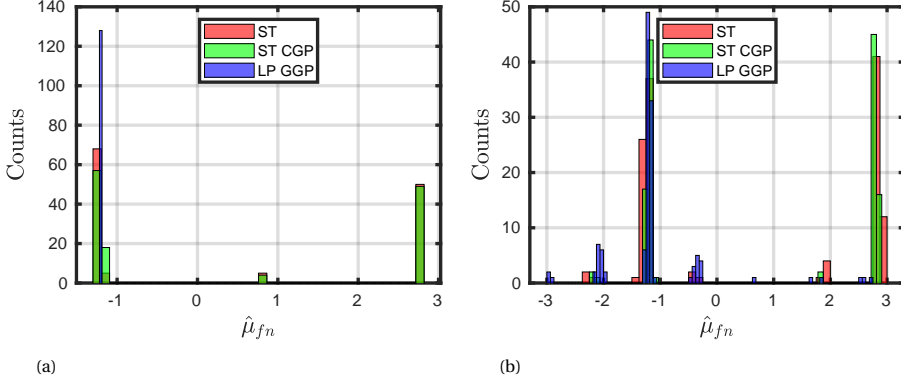


Figure 5.3: Histogram of parameter estimates  $\hat{\mu}_{fn}$  for staggered (“ST” for velocity difference transfer function and “ST CGP” for CGP applied to staggered sequence) and the proposed CGP (“LP” stands for the log-periodic sequence) approach at **a**  $\sigma_{fn} = 0.01$ , and **b**  $\sigma_{fn} = 0.2$ . True mean Doppler velocity is  $\mu_{fn} = -1.2$ .

5

true Doppler velocity almost half of the time across the Monte Carlo simulations. Therefore, instead of only bias and standard deviations in the estimates, the distribution (in terms of histograms) of the estimated normalized mean Doppler frequency by both the staggered sampling technique (both using velocity difference transfer function [19] and the CGP approach [17]) and the proposed CGP technique on the log-periodic sampling at normalized Doppler spectrum widths of  $\sigma_{fn}$  of 0.01 and 0.2 is shown in Fig. 5.3. The comparison with the staggered sampling approach shows that the proposed CGP approach is robust against different realizations of the measurements.

The histograms suggest that the proposed CGP approach is distributed around the true normalized mean Doppler frequency, and the width of this distribution increases with an increase in the normalized spectral width. However, the mean of this distribution is closer to the true normalized mean Doppler frequency. In the case of staggered sampling, the distribution is more discrete, and only around half of the estimates are around the true value. Therefore, the mean of all the estimates is far away from the true value, causing a larger bias in the estimates. For the Doppler spectrum width, however, the absolute bias is below 0.02 for smaller normalized spectral widths  $\sigma_{fn} < 0.16$ , indicating good performance. However, overall, the bias of the proposed CGP approach is smaller than that of the staggered PRT approach.

### 5.5.3. PERFORMANCE ANALYSIS OF HYPER-PARAMETER ESTIMATION WITH $d_2$ FOR THE APERIODICALLY SAMPLED SEQUENCE

This section presents the performance analysis results of the hyper-parameter estimation with the normalized spectral width  $\sigma_{fn}$  and the non-linearity in the aperiodic sampling sequence  $d_2$ . The value of  $d_1$  is 1 and number of samples  $N_{ap}$  is 33 for this analysis. The DFT-aperiodic approach is chosen for the comparison. The results are shown in Fig. 5.4 for the normalized mean Doppler frequency. The

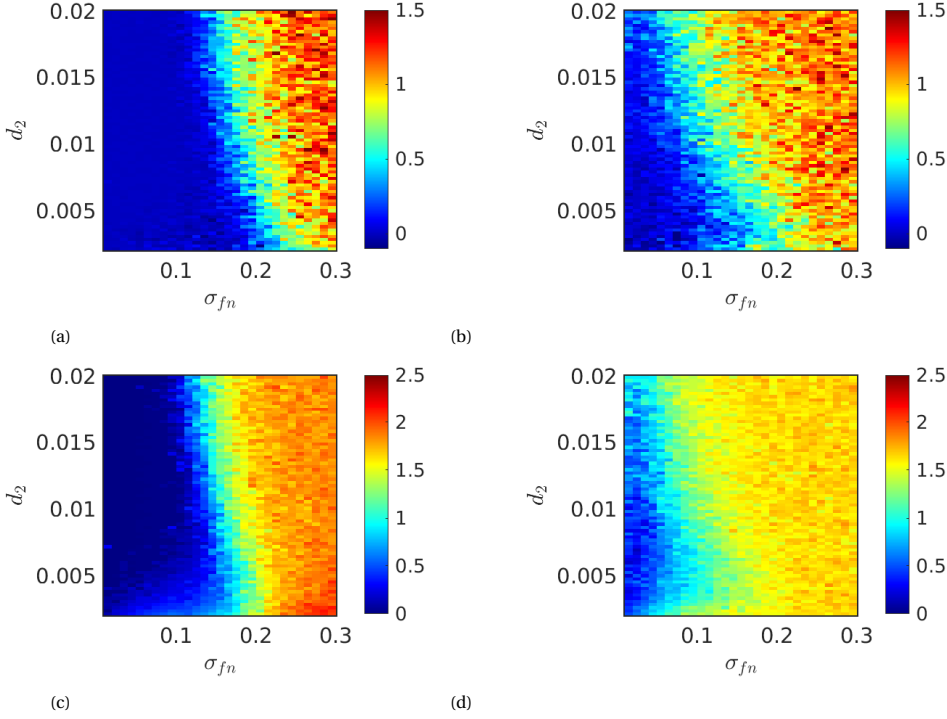


Figure 5.4: Estimation and performance of the normalized mean Doppler frequency  $\hat{\mu}_{fn}$  with respect to  $\sigma_{fn}$  and  $d_2$ . The number of samples is 33. Bias in estimating the mean normalized Doppler frequency  $\hat{\mu}_{fn}$ . a CGP, b DFT aperiodic. Standard deviation in estimating the mean normalized Doppler frequency  $\hat{\mu}_{fn}$ . c CGP, d DFT aperiodic.

optimization configuration, in this case, is different than the previous section. The parameter space for the normalized mean Doppler frequency has been reduced in this experiment to avoid outliers in the estimates. The configuration in this study is given below:

$$\begin{aligned} [\mu_{fn,l}, \mu_{fn,u}] &= [-3, 3], \\ [\sigma_{fn,l}, \sigma_{fn,u}] &= [0, 0.5], \\ U &= 256. \end{aligned} \tag{5.14}$$

It can be observed that the bias of  $\hat{\mu}_{fn}$  decreases with increasing non-linearity  $d_2$  for smaller spectral widths. It can also be observed that the spectral width at which the absolute bias starts to rise for CGP decreases with an increase in  $d_2$ . This implies a trade-off between the spectral width at which  $\hat{\mu}_{fn}$  gets increasingly biased and the estimator's accuracy for smaller spectral widths. To demonstrate this, Fig. 5.5 shows the location of the  $\sigma_{fn}$  (represented as  $\sigma_{fn}^{(Th)}$ ) at which the bias of  $\hat{\mu}_{fn}$  reaches a threshold that is 20% of its true value. In this analysis, the true  $\mu_{fn} = -1.2$ ,

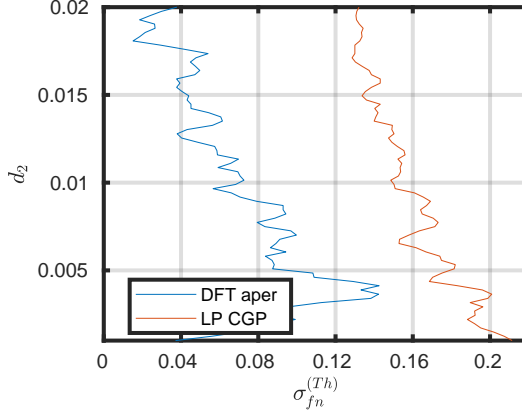


Figure 5.5: The spectral width at which  $|\mathbb{B}[\hat{\mu}_{fn}]| = 0.2|\mu_{fn}|$  as a function of the non-linearity in the sampling ( $d_2$ ).

5

and the threshold for the absolute bias is  $|\mathbb{B}[\hat{\mu}_{fn}]| = 0.2|\mu_{fn}|$ . It can be observed that the  $\sigma_{fn}^{(Th)}$  is decreasing with increasing  $d_2$ . Particularly,  $\sigma_{fn}^{(Th)}$  is nearly 0.2 till  $d_2$  is close to 0.004, nearly 0.16 till  $d_2$  is close to 0.01 and it converges to 0.12 for higher values of  $d_2$  (till 0.02). The values of  $\sigma_{fn}^{(Th)}$  for the DFT aperiodic approach are much smaller than the proposed CGP approach, indicating the superiority of CGP for applications involving extended targets.

The standard deviation for  $\hat{\mu}_{fn}$  of the CGP aperiodic approach has smaller values than the DFT approach for  $\sigma_{fn} < 0.12$ . The standard deviations of DFT and CGP have comparable values for  $\sigma_{fn} > 0.12$ , but the DFT aperiodic approach has slightly smaller values than the CGP approach because of its rigid, biased nature (because it uses a smaller frequency space for moment estimation: explained more in §5.5.2). Overall, for  $\sigma_{fn} < 0.12$ ,  $\forall d_2 < 0.02$ , the standard deviation of the CGP approach is superior to that of the DFT aperiodic one.

The performance analysis for the normalized Doppler spectrum width is shown in Fig. 5.6. For the spectral width estimation, the bias of the proposed CGP approach is nearly zero for  $\sigma_{fn} < 0.16$  for all values of  $d_2$ . The proposed approach is superior and less biased than the DFT aperiodic approach. The standard deviation of the CGP approach for  $\hat{\sigma}_{fn}$  is smaller than that of the DFT-aperiodic approach with increasing  $d_2$ . For  $\sigma_{fn} > 0.16$ , with increasing  $d_2$ , the standard deviation of CGP is smaller than that of the DFT aperiodic approach.

#### 5.5.4. RECOMMENDATION FOR MINIMUM PULSE REPETITION INTERVAL

With the abovementioned analysis, it can be concluded that for a normalized spectral width less than 0.16, the proposed approach produces unambiguous Doppler moments for a precipitation-like extended target (for  $d_2 < 0.01$ ). Therefore, it is recommended to use the log-periodic sampling with a minimum sampling interval ( $T_{ap,min}$ ), which satisfies the following relationship:

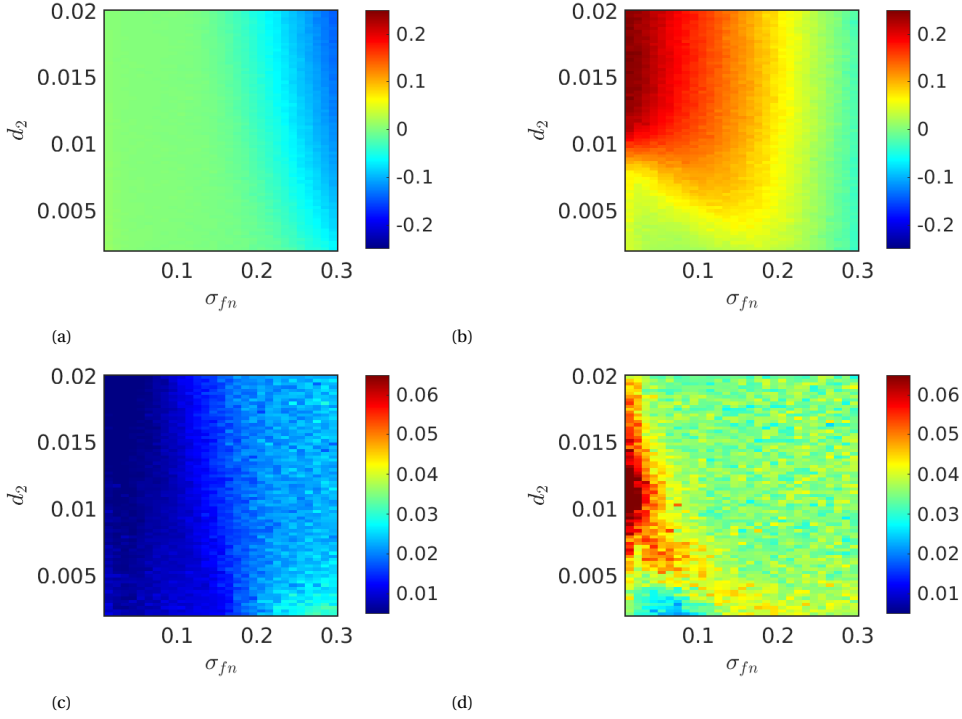


Figure 5.6: Estimation and performance of the normalized Doppler spectrum width  $\hat{\mu}_{fn}$  with respect to  $\sigma_{fn}$  and  $d_2$ . The number of samples is 33. Bias in estimating the normalized Doppler spectrum width  $\hat{\sigma}_{fn}$ . a CGP, b DFT aperiodic. Standard deviation in estimating the normalized Doppler spectrum width  $\hat{\sigma}_{fn}$ . c CGP, d DFT aperiodic.

$$\frac{\lambda}{2T_{\text{ap},\min}} \geq 6\sigma_v, \quad \forall d_2 < 0.01 \quad (5.15)$$

which implies:

$$T_{\text{ap},\min} \leq \frac{\lambda}{12\sigma_v}, \quad \forall d_2 < 0.01. \quad (5.16)$$

Here,  $\lambda$  is the radar central wavelength, and  $\sigma_v$  is the extended target's absolute, denormalized Doppler spectral width. The choice of  $\sigma_v$  depends on the application. It should be noted that this recommendation is specific to an acceptable bias of  $0.1|\mu_{fn}|$ , and with a non-linearity in the sampling  $d_2 < 0.01$ . However, for other user-defined requirements for the bias, variance of the parameters, and lower and upper bounds parameter space for the optimization, the simulation can be performed again to obtain similar recommendations as (5.16). The recommended minimum sampling interval reduces with a reduction in the acceptable bias or variance requirement for the mean Doppler velocity (for a given spectral width).

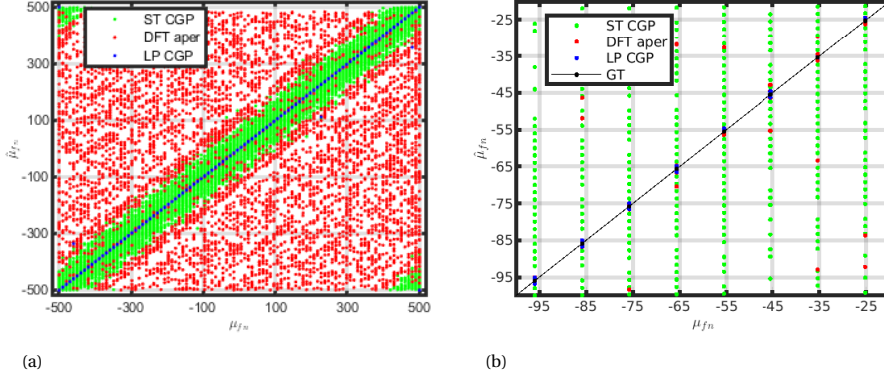


Figure 5.7: Estimation probability of  $\hat{\mu}_f$  with true  $\mu_f$ : **a** for  $\mu_{fn} \in [-500, 500]$  **b** for  $\mu_{fn} \in [-100, -20]$  (zoomed in). “GT”, “ST”, and “LP” stand for “Ground Truth”, “Staggered” and “Log-Periodic”, respectively.

## 5

### 5.5.5. PERFORMANCE ANALYSIS WITH VARYING $\mu_{fn}$

In the previous subsections, the performance has been assessed as a function of the normalized spectral width  $\sigma_{fn}$  at a fixed normalized mean frequency  $\mu_{fn}$ . In this subsection, the performance analysis of the proposed CGP approach with log-periodic sampling is presented at a constant normalized spectral width  $\sigma_{fn} = 0.06$ . The parameter space is chosen to be the complete theoretical Nyquist interval; in this case, at a decimal point precision of  $d = 3$  is  $2f_{NY} = 1000$ , which is much larger than the Nyquist interval of an equivalent periodic sequence having the sampling interval equal to the minimum sampling interval of the aperiodic one ( $2f_{NY,per} = 1$ ). This parameter space can be reduced if prior information on the mean  $\mu_{fn}$  is available. However, in this subsection, the entire parameter space is used to observe if there are outliers in the estimation for some realizations of the signals. At the same time, the number of starting points in the optimization has also been increased to  $U = 2048$  to reduce the number of outliers. The optimization configuration is therefore:

$$\begin{aligned} [\mu_{fn,l}, \mu_{fn,u}] &= [-500, 500], \\ [\sigma_{fn,l}, \sigma_{fn,u}] &= [0, 0.5], \\ U &= 2048. \end{aligned} \tag{5.17}$$

The scatter plot of  $\hat{\mu}_{fn}$  with the DFT aperiodic approach (with the log-periodic sampling), the CGP approach with both staggered sampling, and the proposed log-periodic sampling sequences with 128 Monte Carlo simulations are shown in Fig. 5.7a. A zoomed-in version is shown in Fig. 5.7b. It can be observed that  $\hat{\mu}_{fn}$  estimated with the proposed approach is localized at the true value. However, the variance between the staggered sampling and the DFT approach on the log-periodic sampling is much higher than the proposed approach.

To assess the quality of the estimates, a probability measure is also considered. The probability of  $\hat{\mu}_{fn}$ , i.e.,  $p(\hat{\mu}_{fn})$  given that the estimates are close to the true

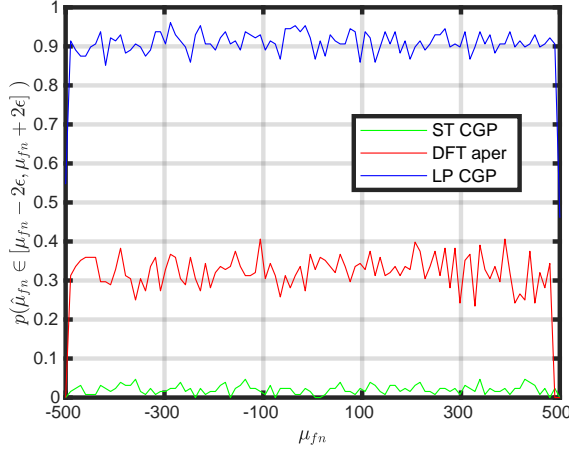


Figure 5.8: Estimation probability of  $p(\hat{\mu}_{fn} \in [\mu_{fn} - 2\epsilon, \mu_{fn} + 2\epsilon])$  (given in (5.18)). “ST”, and “LP” stand for “Staggered” and “Log-Periodic”, respectively. The approach “DFT aper” is applied on the log-periodic sampling sequence.

value (quantified by predefined thresholds) is computed. The thresholds are decided based on  $\sigma_{fn}$  and  $N$ :

$$p(\hat{\mu}_{fn} \in [\mu_{fn} - 2\epsilon, \mu_{fn} + 2\epsilon]) = \frac{|\{\hat{\mu}_{fn,i} : \mu_{fn} - 2\epsilon \leq \hat{\mu}_{fn,i} \leq \mu_{fn} + 2\epsilon, i = 1, \dots, N_{MC}\}|}{N_{MC}}, \quad (5.18)$$

$$\epsilon = \sqrt{\frac{\sigma_{fn}^2}{N}},$$

where the operator  $||$  is the cardinality, and  $N_{MC}$  is the number of Monte Carlo simulations used. This probability of (5.18) is computed with 128 Monte Carlo simulations. The thresholds here are equivalent to two standard deviation bounds around the true  $\mu_{fn}$ , where one standard deviation is  $\epsilon$ . This probability is shown in Fig. 5.8. It can be seen that the estimation probability is very high near the true  $\mu_{fn}$  (with a probability more than 0.91). Some outliers are detected for some realizations, but the probability is extremely small (below 0.1). Due to aliasing, the outlier probability increases as the true mean frequency approaches the  $f_{NY}$  (close to 500 or  $-500$ ). It is also observed that the proposed CGP approach with the log-periodic sampling sequence is superior to both the CGP approach with the staggered sampling sequence and the DFT aperiodic approach with the log-periodic sampling sequence. From this analysis, it can be concluded that the proposed approach with log-periodic sampling can enhance the maximum unambiguous frequency interval up to 1000 times that of an equivalent periodic sequence having a sampling interval the same as the minimum sampling interval of the log-periodic one.

Table 5.1: Hyper-parameter estimation for the three-extended-targets scenario of §5.5.6

Parameter	True	Estimated
$\mu_{1,fn}$	1	1.002
$\mu_{2,fn}$	0.6	0.6053
$\sigma_{1,fn}$	0.09	0.0881
$\sigma_{2,fn}$	0.06	0.0513
$\sigma_{3,fn}$	0.02	0.0161
$R_1$	10000	10120
$R_2$	10000	99424
$R_3$	1000	700

### 5.5.6. SIMULATION STUDY OF THE SPECTRUM RECONSTRUCTION

Three extended targets are used to simulate the radar echoes in time. Two of these extended targets mimic two precipitation-like targets. The mean locations of these two targets are kept outside the Nyquist unambiguous interval of the periodic sampling case purposefully to evaluate the retrieval and reconstruction. The third extended target is a clutter whose mean location is  $\mu_{3,fn} = 0$ , which is assumed to be a known quantity. The unknown hyper-parameters are  $\Theta = [\mu_{1,fn}, \mu_{2,fn}, \sigma_{1,fn}, \sigma_{2,fn}, \sigma_{3,fn}, R_1, R_2, R_3]$ . The number of echo samples for the periodic case is  $N_{\text{per}} = 213$ , and for the aperiodic case is  $N_{\text{ap}} = 128$ . The parameters for the aperiodic sequence are  $d_1 = 1$ , and  $d_2 = 0.0074$ . The hyper-parameter estimation is shown in Table 5.1. The spectrum reconstruction is then followed using the principles mentioned in the §4.4.

As it is a Bayesian approach, several different realizations of the power spectrum are presented in Fig. 5.9 by first sampling from the posterior distributions of its real and imaginary parts, respectively.

It can be concluded that the proposed CGP-based reconstruction avoids the ambiguous responses of the extended targets in the extended frequency domain by the counter-aliasing strategy. The reconstruction in the frequency domain is performed using the measurements in the time domain, posing no additional computational burden. The Schuster periodogram with the periodic sequence has produced an aliased Doppler spectrum in the extended frequency domain, making it uninformative. Likewise, the Schuster periodogram with the aperiodic sequence (same as the generalized Lomb-Scargle periodogram) has produced very high levels of artifacts (comparable with the power of the real targets), making it ambiguous. However, the CGP posterior avoids these ambiguous artifacts and has smaller sidelobe levels (around 35 dB) in this case. Therefore, there is an improvement of around 20 dB over the other approaches as far as the ambiguous artifact levels are concerned.

### 5.5.7. RECOMMENDATIONS FOR REAL RADAR APPLICATION

An application to real radar measurements with this proposed setting should be studied. Changing the reset time  $T_k^{(\text{reset})}$  aperiodically by applying the sampling rules for a Frequency Modulated Continuous Wave (FCMW) radar can be beneficial in

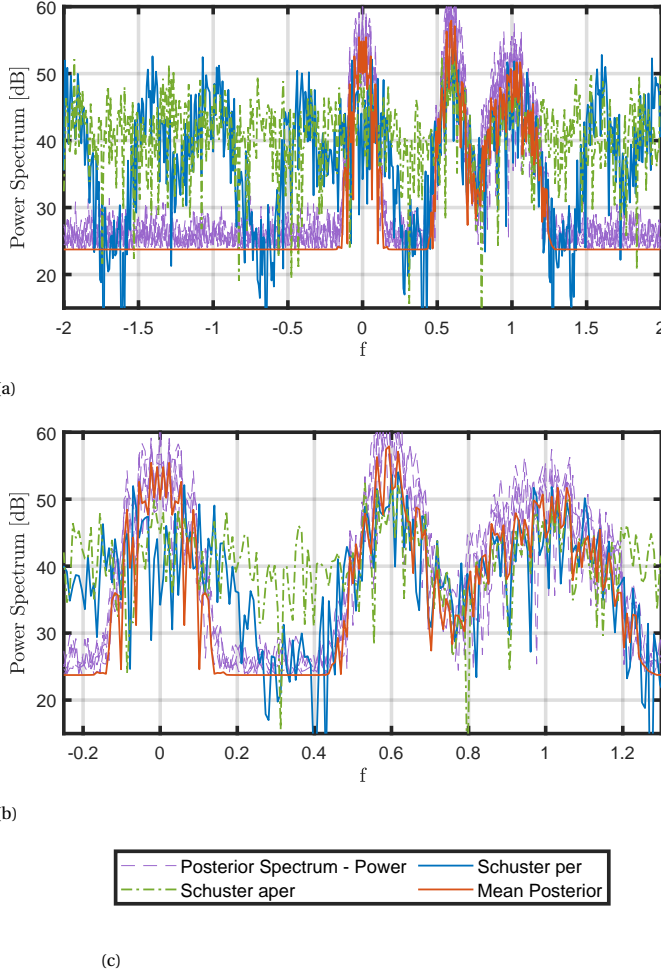


Figure 5.9: Spectrum Reconstruction: **a** Power spectrum **b** Power spectrum zoomed in **c** Legend for the plots. The posterior spectrum contains five realizations of the power spectrum.

realizing such a configuration. The reset time is the time difference between the end of one chirp and the start of the next. The chirp duration  $T^{(\text{chirp})}$  is constant and is very less than  $T_{k,\text{per}}$ . The reset time is given by:

$$\begin{aligned} T_k^{(\text{reset})} &= t_k(T_{k,\text{per}}, d_1, d_2) - t_{k-1}(T_{k,\text{per}}, d_1, d_2) - T^{(\text{chirp})}, \\ T^{(\text{chirp})} &<< T_{k,\text{per}}, \end{aligned} \quad (5.19)$$

and a constant reset time (when  $t_k(T_{k,\text{per}}, d_1, d_2) - t_{k-1}(T_{k,\text{per}}, d_1, d_2) = T_{k,\text{per}}$ ) will redirect the radar to the periodic pulse repetition mode.



## 5.6. CONCLUSIONS

In the previous chapter 3, the crucial contribution is the accurate estimation of the Doppler spectral width, which typically characterizes the turbulence in the rain. As this parameter is heavily affected by the Doppler resolution, the previous contributions attempted to estimate it accurately with poor Doppler resolution by modeling the signal PSD. It has been shown that even when the mean Doppler velocity is closer to the Nyquist unambiguous velocity, the PSE can accurately estimate the Doppler spectral width.

Although PSE is well suited for Doppler spectral width estimation, a serious problem remains in the accurate estimation of the mean Doppler velocity when the velocities of raindrops are higher than the maximum Nyquist unambiguous velocity permissible by the radar. The velocities are usually aliased into the permissible Nyquist interval, and the mean Doppler velocity estimate becomes ambiguous. This limitation comes because the samples are typically equispaced, making a periodic sequence.

This contribution explored what one could achieve using an aperiodic pulse train instead. The literature regarding aperiodic pulse trains to avoid the aliasing problem is vast. However, many research gaps were found by examining the issue of aliasing/ambiguity from several perspectives (research domain including non-radar domains). This contribution is novel, and an integrative signal processing approach is proposed to address the research gaps from all the research domains. A detailed literature review of all these research areas is presented, and the limitations are explained.

A novel sampling approach in the time domain is proposed for the aperiodic pulse train (with a log-periodic sampling sequence). The theoretical Nyquist unambiguous velocity limit for such aperiodic sequences is discussed in detail. The minimum sampling interval of the aperiodic sequence is kept higher than a threshold to make a fair performance comparison with a periodic sampling sequence having a pulse repetition interval the same as the minimum sampling interval of the aperiodic sequence. The Doppler moments are normalized with the Nyquist unambiguous interval of this equivalent periodic sampling sequence.

The CGP-R is chosen to estimate the Doppler moments as the signal is sampled aperiodically. The Doppler moment estimation is compared with the state-of-the-art methods for both aperiodic and equivalent periodic sampling sequences. Although some of the state-of-the-art moments estimation techniques perform as expected with aperiodically sampled sequences for pointed targets immersed in white Gaussian noise, the limitations of such methods to estimate the Doppler moments for extended targets have been demonstrated. It has been shown that the proposed approach outperforms the other methods for the normalized mean Doppler moment estimation (when the true normalized Doppler spectrum width remains smaller than 0.16; i.e.,  $\sigma_{fn} < 0.16$ ). An application-centric recommendation has been presented for the minimum sampling interval.

The performance of the proposed approach has been assessed by changing the parameter in the proposed sampling sequence, which is responsible for the non-linearity. It is concluded that the accuracy in the normalized mean Doppler velocity estimates improves with increasing non-linearity. Still, the spectral width at

which the bias in the estimate starts to increase decreases with an increase in the non-linearity in the sampling sequence, indicating a trade-off.

A novel criterion is proposed for designing a log-periodic sampling sequence with a minimum sampling interval lower than  $\lambda/(12 \times \sigma_v)$  (where the spectral width  $\sigma_v$  is related to the storm's severity) for an unambiguous retrieval of the mean Doppler velocity. The more severe the storm in terms of spectral width (which can result from strong turbulence, vortices, and convective storms), the smaller the minimum sampling interval needed.

In addition, the chapter presents a Bayesian inference (CGP-R) approach to reconstructing the Doppler spectrum with an extended velocity domain by directly using the aperiodically sampled echoes in the time domain. The reconstruction poses no additional computational burden. As it is a Bayesian technique, several different realizations of the power spectrum are realized. To the authors' knowledge, this is the first-ever implementation of the direct frequency domain CGP posterior on aperiodically sampled sequences for extended targets, making it novel. The mean estimate of the power spectrum converges to the true spectrum. It is shown that the posterior spectrum of the proposed reconstruction outperforms the conventional periodogram techniques capable of handling aperiodic signals, such as the aperiodic Schuster periodogram, in terms of accuracy. The problem of higher ambiguous artifacts is avoided using the proposed approach. It has been shown in Fig. 5.9 that there is at least 20 dB improvement in the ambiguous artifact levels.

This study does not include the impact of such a pulse train on estimating the target's range. However, as with the log-periodic sampling technique, the minimum sampling interval in the slow time can be maintained at a desired level, which can decide the maximum unambiguous range to which the mean Doppler velocity and Doppler spectrum width can be recovered.



# 6

## FITTING OF PRECIPITATION DOPPLER SPECTRUM WITH WIND AND RAIN DSD PARAMETERS

*A computationally efficient novel semi-analytical expected Doppler Power Spectral Density (PSD) model has been proposed as a function of the DSD, wind parameters, and the finite observation interval. A maximum likelihood estimation is proposed where the measurements are the stochastic Doppler PSD realizations. Although the proposed approach performs better than the existing approximate approaches, it is shown that the estimation of DSD parameters, in general, is very challenging because the log-likelihood (cost function with radar retrieved measurements) is not very sensitive to the DSD parameters. Nonetheless, even though estimates of DSD parameters are biased, the Doppler spectrum's fitting is sufficient for determining derived parameters such as the terminal fall velocity and median diameter of the raindrops.*

---

Parts of this chapter have been submitted to:

T. K. Dash, H. Driessen, O. A. Krasnov, and A. Yarovoy, "Joint Estimation of Raindrop Size Distribution and Radial Wind Velocity Parameters Using a Fast Scanning Weather Doppler Radar," *Journal of Atmospheric and Oceanic Technology*, 2025

## 6.1. INTRODUCTION

Although the DSD and wind parameter estimation are familiar problems and have been widely discussed in the literature, several challenges still exist. Suppose we consider the problem of DSD parameter estimation without considering the wind ones. In that case, the popularly followed methodologies can be categorized into polarimetry-based and Doppler Power Spectral Density (PSD)-based approaches. Although the polarimetry-based approaches provide reliable and informative estimates of the DSD parameters, measuring them correctly is challenging due to several issues, including calibration [147]. In this chapter, the focus is on the Doppler PSD-based approaches instead.

The state-of-the-art Doppler PSD-based DSD and wind parameter retrieval approaches do not address a joint estimation of these parameters. The ones that address a quasi-joint estimation have strong assumptions and are often equipped with one more radar system (sensitive to clear air but not precipitation) to have the information on the wind exclusive of the DSD ones [148], [149], [150], [151]. In addition, signal processing with such approaches requires much longer observation intervals. The stochastic Doppler PSD becomes smoother with increasing coherent observation interval, and the cost functions defined in these studies do not contain spectral variability [30]. However, if we consider the aviation application, the modern phased array (in elevation) X-band weather radars at airports are often required to scan quickly in the azimuthal direction to detect and track point-like targets (birds, drones, etc.), limiting the time on target per scan. Therefore, there is a need to use incoherent sets of Doppler PSDs from several fast radar scans as measurements and spectral variability in the cost function.

Furthermore, the Doppler PSD-based approaches are based on optimization, which requires computing the PSD several times. The existing model of the Doppler PSD involves the computation of an intractable integral in the Fourier domain, posing additional computational issues.

Joint estimation of the complete set of parameters for 3D wind field and rain DSD from Doppler PSD is not studied in the literature (except for [30]). The usual practice is to retrieve the wind parameters separately from the rain DSD and clear air reflections. Typically, radar facilities operating at different frequencies are used for separate retrieving Doppler velocities of clear air returns and precipitation. A long observation interval is required for good sensitivity and high Doppler resolution. Retrieval error minimization within the joint parameter estimation problem requires derivations and detailed analysis of numerical and theoretical variances, which are yet unavailable in the literature.

Considering the abovementioned issues, the challenge of jointly estimating these parameters with a fast-scanning X-band radar addressed in this chapter is unique. A novel formulation and approach is proposed to jointly estimate the wind and DSD parameter estimation by only using the Doppler PSDs as the measurements. The proposed approach has the following features addressing all the issues mentioned in the paragraphs above:

1. contains a novel and computationally efficient model of the Doppler PSD with

- wind, DSD parameters, and the limited observation interval,
2. proposes a joint wind and DSD parameters estimation algorithm from the Doppler PSD with limited observation interval,
  3. makes use of the PSD observations from the incoherent sequence of fast radar scans,
  4. provides the estimation of parameters and their analysis in terms of their theoretical variances, the CRB, and numerical biases (with Monte Carlo simulations).

The main body of the chapter is organized as follows. §6.2 discusses the classical approaches to estimate the DSD and wind parameters in detail. §6.3 discusses the signal model as a function of the parameters of interest. §6.4 explains the modeling of the Doppler PSD using the signal model of 6.3. §6.5 explains the optimization goals and how the inverse problem is solved. §6.6 presents the estimator's results using simulated data along with the computational aspects. Application of the joint estimation algorithm to the real radar data is described in §6.7. The conclusions are drawn in §6.8. The appendix C shows the decay study for the covariance of the reflectivity-weighted fall velocity spectrum. The appendix D presents the derivation of the theoretical variance of the estimator along with the CRB.

## 6.2. CLASSICAL DSD AND WIND PARAMETER ESTIMATIONS AND THE RATIONALE BEHIND THE PROPOSED APPROACH

The three-parameter gamma raindrop DSD model is the most popular in the literature [3] and is also considered in this chapter. It is given by:

$$N(D) = N_0 D^\eta \exp(-\Lambda D), \quad (6.1)$$

where  $N_0(\text{m}^{-3}\text{mm}^{-1-\eta})$  is the number of raindrops per unit volume per unit size interval,  $\eta$  is the shape parameter, and  $\Lambda(\text{mm}^{-1})$  is the rate parameter<sup>1</sup>. The DSD also can be represented with the scale parameter instead of the rate parameter, where the scale parameter is inversely proportional to the rate parameter ( $D_0 \propto 1/\Lambda(\text{mm})$ ), where  $D_0$  has the physical meaning of the median diameter of the raindrops in the resolution volume).

Estimating the DSD parameters from radar data has been studied extensively in the existing literature, and it is not a trivial problem. There are several challenges involved because radars do not measure these parameters directly. The radar observables that are typically used for DSD parameter estimation are the reflectivity( $Z$ ), Doppler spectrum, differential reflectivity( $Z_{\text{dr}}$ ), the linear depolarization ratio( $L_{\text{dr}}$ ), differential phase( $\phi_{\text{dp}}$ ), and its derivative with respect to range( $k_{\text{dp}}$ ). The observables  $Z_{\text{dr}}$ ,  $L_{\text{dr}}$ ,  $\phi_{\text{dp}}$ , and  $k_{\text{dp}}$  are available if the radar is

<sup>1</sup>In literature, the shape parameter is often denoted as  $\mu$ . However, to have consistency with [56](chapter 3),  $\mu$  is chosen for the radial mean wind velocity and  $\eta$  for the shape parameter of the DSD (which is also followed in some other literature, such as, [2]).

polarimetric [62], [152]. The DSD parameter estimates based on polarimetry are more reliable because they provide extra information about the ensemble of raindrops. However, measuring them poses additional difficulties due to inaccuracies caused by calibration issues. With the polarimetric observations, a sensitivity analysis can also be found in [147]. This chapter focuses more on the DSD parameter estimation with the help of received echoes with one polarization only. Therefore, the techniques based on reflectivity and Doppler spectrum become relevant for comparison and analysis.

The Doppler spectrum-based estimation techniques can further be categorized based on the type of radar system. The techniques listed in [148], [149], [150], [151], [30], [153], use a model of the Doppler PSD that is a sum of clear sky echo spectrum usually spread around zero Doppler velocity and a convoluted spectrum between the clear sky spectrum and the vertical fall spectrum (also called as the rain spectrum). Due to the convolution with the clear air spectrum, the rain spectrum is usually broader than expected. However, as these radar systems (consisting of one or two radars) are sensitive to the clear air spectrum independent of the fall spectrum, it is convenient to estimate the clear air parameters (also referred to as wind parameters) such as the mean wind field and wind spectral width (usually associated with turbulence) independently of the DSD parameters. The DSD parameters can then be estimated by deconvolving the rain spectrum using the estimated wind parameters. It is also noteworthy that the clear sky spectrum model in all the studies mentioned above is considered around the zero Doppler, assuming that the radars always point upwards (Vertically Pointing Radar (VPR)).

However, modern Doppler weather radars operate in the X-band and are usually not very sensitive to clear sky reflections. Therefore, the Doppler PSD does not separately contain the clear sky spectrum and is always convolved with the fall spectrum. Furthermore, these radars also scan the azimuth and don't always have to be pointed vertically. Estimating the DSD and wind parameters jointly from this convolved Doppler PSD becomes challenging.

The existing estimators do not perform this estimation jointly and, therefore, have multiple steps. For example, the DSD parameter estimation from the statistical moments of the fall PSD [2], [65], using VPRs, assume that the contribution of the wind spectra in the Doppler PSD comes from vertical air motion only. The mean terminal fall velocity of the scatterers  $V_T$  is computed by subtracting the air velocity  $V_{\text{wind}}$  from the mean velocity calculated from the Doppler PSD ( $V_T = \mu_r - V_{\text{wind}}$ ), where  $\mu_r$  is the mean radial velocity measured from Doppler PSD). The spectral width caused only due to the vertical fall ( $\sigma_p$ ) can be computed by subtracting the variances ( $\sigma_p^2 = \sigma_r^2 - \sigma_{\text{wind}}^2$ ), where  $\sigma_r$  is the radial spectral width measured from Doppler PSD). The DSD parameters are estimated using functional empirical relationships of  $V_T$  and  $\sigma_p$  with respect to the parameters [2].

These Doppler moment-based estimators have several problems. Firstly, the estimators rely on the spectral moments estimated from the observed PSDs. In the case of scanning radars, the moment estimates are usually biased, especially the spectral width, due to comparatively lower observation interval [56], [69]. With wind profilers and VPRs, for example, the coherent acquisition times for Doppler

processing is in the order of several minutes [148], [149] for an accurate DSD parameter estimation. Secondly, the approximate empirical models correlating the spectral widths of the fall spectrum and the air (wind) spectrum are biased because the fall spectrum can not be characterized only with two spectral moments (because the drop size distribution is not symmetric). A very small error in the computation of the spectral moments can heavily affect the DSD parameter estimation. Thirdly, if we do not use VPRs, the wind spectra will not produce a near-zero mean radial velocity response, causing the radial mean Doppler velocity to be a function of the projection of both the terminal fall velocity and the 3D wind velocity in the radial direction.

This chapter focuses only on one X-band radar that scans the azimuth very fast, resulting in very low observation time for Doppler processing. The modeling of the PSD with the DSD and wind parameters is presented in this chapter using (6.1) and the principles presented in [56] to incorporate the observation interval in the model. The PSD model includes two different covariance functions with respect to time. The first one is the covariance function of the complex time domain signal, assuming that the radar only observes the wind, and the second one assumes that the radar only observes the fall velocity of raindrops. As the second covariance function involves an intractable integral over the diameters of the raindrops, a novel approximate formulation of the covariance function related to the fall speed (which depends on the DSD parameters) is presented to reduce the computation time.

A maximum likelihood estimator is proposed in which the log-likelihood considers the spectral variability of stochastic signals. The estimator's performance is assessed by the numerical bias, variance (computed with a Monte Carlo simulation), and theoretical variance.

### 6.3. SIGNAL MODEL

This section explains the modeling of the radar echo samples in time from a precipitation event from one range-resolution volume. Considering a volume filled with  $M$  scatterers (raindrops), the radar echoes at each instant  $t_k$ , a superposition of backscattered signals from all the scatterers.

$$s(t_k) = \sum_{m=1}^M A_m \exp \left[ j \left( \frac{4\pi}{\lambda} v_{m,r} t_k + \beta_m \right) \right] \quad (6.2)$$

In (6.2),  $A_m$  is the amplitude caused by the  $m$ th scatterer,  $\lambda$  is the radar central wavelength,  $v_{m,r}$  is the radial velocity of the  $m$ th scatterer,  $\beta_m$  is the initial phase of the  $m$ th scatterer that is a function of its initial position, and  $j$  is the imaginary unit ( $j = \sqrt{-1}$ ) [56]. Unlike in [56], where the amplitudes of each scatterer were considered the same, in this chapter, it is assumed that these amplitudes depend on their respective diameters  $D_m$ . In the Rayleigh scattering regime, the power received from the scatterers is proportional to the sixth order of the diameter. Therefore, the amplitude for each scatterer is proportional to the third order of the diameter.

$$A_m \propto D_m^3 \quad (6.3)$$



The radial velocities of the scatterers  $v_r$  can be modeled as a scalar sum of the projection of the 3D wind velocity and the fall velocity in the radial direction. The radial velocity is given by:

$$\begin{aligned} v_r = & V_{\text{wind}} \left[ \cos(\psi_0) \cos(\psi) \cos(\phi - \phi_0) \right. \\ & \left. + \sin(\psi_0) \sin(\psi) \right] \\ & + V_T \sin(\psi), \end{aligned} \quad (6.4)$$

where  $(\psi, \phi)$  are the observation angles in elevation and azimuth, and  $(\psi_0, \phi_0)$  is the wind direction. For simplicity, this model assumes that the wind direction is stationary without any local variations. However, for more complex wind fields, the wind velocity  $V_{\text{wind}}$  and the direction can be modeled as functions of space. The  $V_T$  is the vertical fall velocity of raindrops. Many models of the fall velocity of raindrops as a function of their diameters are available in the literature. An exponential model is used for the velocities as given below [154], [155]:

$$V_T(D) = -(c_1 - c_2 \exp(-c_3 D)), \quad (6.5)$$

where  $c_1 = 9.65$  m/s,  $c_2 = 10.34$  m/s, and  $c_3 = 0.6$  mm<sup>-1</sup>. This model is used for simplicity, but more complex power law models can also be used with extra atmospheric physical parameters (such as Reynold's and Davies' numbers, atmospheric pressure at different altitudes, etc.) [39], [38], [37], [43], [156], [41], [157]. The expression of (6.4) can be rewritten as:

$$v_r = V + V_T \psi, \quad (6.6)$$

where the trigonometric expressions in the projections are included in the velocities ( $V = V_{\text{wind}} [\cos(\psi_0) \cos(\psi) \cos(\phi - \phi_0) + \sin(\psi_0) \sin(\psi)]$ , and  $V_T \psi = V_T \sin(\psi)$ ). The diameters of the raindrops are assumed to be independent and identically distributed according to a gamma distribution:

$$\begin{aligned} \{D_m\}_{m=1}^M & \stackrel{i.i.d.}{\sim} \text{Gamma}(\eta + 1, \Lambda), \\ p(D) & = \frac{\Lambda^{\eta+1}}{\Gamma(\eta + 1)} D^\eta \exp(-\Lambda D), \end{aligned} \quad (6.7)$$

where the parameters of this gamma distribution are explained in (6.1), and  $\Gamma$  is the gamma function. The concentration term  $N_0$  is related to the normalization constant of the probability distribution as  $N_0 = M \times \frac{\Lambda^{\eta+1}}{\Gamma(\eta+1)}$  [158]. In the existing literature,  $M$  is often represented as  $N_T$  (in m<sup>-3</sup>). The initial phases of the scatterers  $\beta_m$  are assumed to be independent and identically distributed according to a uniform distribution:

$$\{\beta_m\}_{m=1}^M \stackrel{i.i.d.}{\sim} \mathcal{U}[-\pi, +\pi]. \quad (6.8)$$

The radial wind velocity associated with the scatterers is assumed to be independent and identically distributed according to a Gaussian distribution:

$$\{V_m\}_{m=1}^M \stackrel{i.i.d.}{\sim} \mathcal{N}(\mu_v, \sigma_v^2) \quad (6.9)$$

where  $\mu_v$  is the radial mean wind velocity, and  $\sigma_v$  is the spectral width related to the radial wind (also known as the velocity dispersion parameter). The measurement model of the time series presented in (6.2) is the signal added with zero mean white complex Gaussian noise with variance  $\sigma_n^2$ :

$$\mathbf{z} = \mathbf{s} + \mathbf{n}, \quad \{n_k\}_{k=0}^{N-1} \stackrel{i.i.d.}{\sim} \mathcal{CN}(0, \sigma_n^2), \quad (6.10)$$

where  $N$  is the number of coherent echo samples.

## 6.4. SEMI-ANALYTICAL FORM OF THE EXPECTED PSD AND FORMULATION OF THE COVARIANCE RELATED TO VERTICAL FALL

The semi-analytical form of the PSD, considering the number of coherent echo samples ( $N$ ), can be given as (a generalized form of [56, eq. (10)]):

$$\begin{aligned} F(v) = R & \left[ 1 + \sum_{q=1}^{N-1} \left( 1 - \frac{q}{N} \right) \right. \\ & \times \left[ Y(q)G(q) \exp \left( -j \frac{4\pi T}{\lambda} v \right) \right. \\ & \left. \left. + Y(-q)G(-q) \exp \left( j \frac{4\pi T}{\lambda} v \right) \right] \right], \end{aligned} \quad (6.11)$$

where  $Y(q)$  is the normalized covariance function of the signal related to the radial wind only, and  $G(q)$  is the normalized covariance function of the signal related to the fall velocity only,  $T$  is the pulse repetition time, and  $R$  is the total power (reflectivity). Usually, the reflectivity is denoted as  $Z$  in the literature. However, to make the analysis consistent with estimation theory,  $Z$  is used to represent measurement PSDs and, therefore, chose  $R$  as reflectivity.

The difference between [56, eq. (10)] and (6.11) is that the earlier only considered a Gaussian-shaped Doppler PSD, and therefore the term inside the summation is much simplified. Equation (6.11) is the more generic form of [56, eq. (10)], which considers the covariance function of the signal inside the summation ( $Y(q) \times G(q)$ ). The covariance function of the signal is a multiplication of two different covariance functions because the radial velocity of the scatterer is a scalar sum of the projections of the wind and the vertical fall velocity of the scatterers onto the radial direction. To realize this, a similar derivation can be performed as in [56, Appendix. A] by replacing  $v_r$  as  $V + V_{T\psi}$  and using two different probability distributions for  $V$  and  $V_{T\psi}$ .

These covariance functions can also be represented as the expectation of the signal multiplied by its complex conjugate. It is assumed that the initial positions of the scatterers in the resolution volume follow a uniform distribution; the covariance function becomes a function of only the time difference (or delay  $q$ ). A detailed formulation can be found in [98], [56, Eq. 9]. To perfectly characterize a complex sequence, a pseudo-covariance is often formulated along with the

covariance. However, with the same assumption of uniformly distributed scatterers, the pseudo-covariance is zero [98]. The complex-valued random processes with zero pseudo-covariance are known as *circularly symmetric Complex Gaussian Processes* (CGP) or *Proper Gaussian Processes* [135]. The covariance related to the radial wind component is given by:

$$Y(q) = \int_{-\infty}^{+\infty} p(V) \exp(jVq) dV \quad (6.12)$$

$$= \exp\left(-\frac{1}{2} \left(\frac{4\pi T}{\lambda}\right)^2 \sigma_v^2\right) \exp\left(j \frac{4\pi T}{\lambda} \mu_v\right).$$

The covariance function of the reflectivity weighed fall velocity spectrum  $G(q)$  is given by:

$$G(q) = \int_0^\infty \frac{N(D)D^6}{R} \frac{dD}{dV_{T\psi}} \exp(jV_{T\psi}q) dV_{T\psi}, \quad (6.13)$$

where  $R$  is given by:

$$R = \int_0^\infty N(D)D^6 dD = M \frac{\Gamma(\eta+7)}{\Gamma(\eta+1)\Lambda^6}. \quad (6.14)$$

The above-mentioned integral (6.13) can be simplified to the following:

$$G(q) = \frac{M \exp(jqC_1)}{R} \frac{\Lambda^{\eta+1}}{\Gamma(\eta+1)} \times \int_0^\infty D^{\eta+6} \exp(-\Lambda D) \exp(-jqC_2 \exp(-c_3 D)) dD, \quad (6.15)$$

where  $C_1 = c_1 \frac{4\pi T}{\lambda} \sin(\psi)$ , and  $C_2 = c_2 \frac{4\pi T}{\lambda} \sin(\psi)$ . With a change of parametrization  $y = D\Lambda$ , we have:

$$G(q) = \frac{\exp(jqC_1)}{\Gamma(\eta+7)} \int_0^\infty y^{\eta+6} \exp(-y) f(y) dy, \quad (6.16)$$

where  $f(y) = \exp(-jqC_2 \exp(-\frac{c_3}{\Lambda} y))$ . Using generalized Gauss-Laguerre quadrature [159] on the integral in (6.16), the expression for  $G(q)$  can be rewritten as:

$$G(q) = \exp(jqC_1) \sum_{i=1}^n w_i f(y_i), \quad (6.17)$$

where  $y_i$  are the zeros of the generalized Gauss-Laguerre polynomial  $L_n^{\eta+6}(y)$ , and the weights  $w_i$  are:

$$w_i = \frac{\Gamma(n+\eta+7)y_i}{n!(n+1)^2 \left[L_{n+1}^{\eta+6}(y_i)\right]^2}. \quad (6.18)$$

In this case, the choice of  $n$  depends on the delay  $q$ ; the larger the  $q$ , the larger should be  $n$  to achieve smaller errors. To decide a universal value of  $n$  for this application, the decay of  $G(q)$  should be studied with respect to  $q$ . For an accurate estimation of the parameters of a random process with a decaying covariance

function, it is essential to have enough samples to capture a considerably correlated part of the signal. In this study,  $n = 64$  is chosen. A detailed analysis of the decay of  $G(q)$  and the choice of  $n$  is presented in the Appendix C.

The power spectral density of a stochastic random process is assumed to be exponentially distributed [56], [80], [81]. The parameters  $\Theta$  are estimated by maximizing the log-likelihood given below:

$$\begin{aligned} \log(p(\mathbf{Z}|\Theta)) \\ = - \sum_{i=1}^N \left[ L \log(\pi(F(v_i, \Theta) + \sigma_n^2)) + \frac{\sum_{l=1}^L Z_l(v_i)}{F(v_i, \Theta) + \sigma_n^2} \right]. \end{aligned} \quad (6.19)$$

The noise variance  $\sigma_n^2$  is assumed to be a known quantity,  $Z_l$  are the PSD measurements, and  $L$  is the number of such PSD measurements. These PSD observations need not be coherent. The inverse problem can be represented as:

$$\hat{\Theta} = \max_{\Theta} \log(p(\mathbf{Z}|\Theta)). \quad (6.20)$$

## 6.5. OPTIMIZATION GOALS

A quasi-Newton-based gradient descent optimization with the Limited Memory Broyden–Fletcher–Goldfarb–Shanno (L-BFGS) algorithm [93] is chosen for faster computation. To avoid local optima, the optimization is performed from distinct starting points in the parameter space. The optimization algorithm with different starting points can be found in [102, Algorithm. 1]. The lower bound (lb) and upper bounds (ub) for the parameters in the simulations and also in the real data are:

$$\begin{aligned} [\mu_v^{\text{lb}}, \mu_v^{\text{ub}}] &= [-V_a, V_a], \\ [\sigma_v^{\text{lb}}, \sigma_v^{\text{ub}}] &= [0, \hat{\sigma}^{(\text{PP})}], \\ [\eta^{\text{lb}}, \eta^{\text{ub}}] &= [-1, 20], \\ [\Lambda^{\text{lb}}, \Lambda^{\text{ub}}] &= [0.1, 20], \end{aligned} \quad (6.21)$$

where,  $V_a$  is the maximum unambiguous velocity of the radar and  $\hat{\sigma}^{(\text{PP})}$  is the estimated Doppler spectral width estimated with the Pulse Pair (PP) approach.

## 6.6. NUMERICAL SIMULATION

For the numerical simulation study, the radar echoes are generated with the signal model of (6.2). The drop sizes are sampled from a gamma distribution (6.7). No truncation has been applied to limit the maximum drop size in these simulations. The estimation of the parameters is first studied with an increase in the radial wind-related spectral width  $\sigma_v$ . This parameter explains the contribution of the radial wind in the Doppler spectrum; it is essential to understand the bias and uncertainty in the estimates of the DSD parameter retrievals based on it. The simulation parameters are set according to Table 6.1. The proposed approach is called the “WiDSE” (Wind and DSD Estimator).

Table 6.1: Parameters for the analysis

Parameter	Value
$L$	32
$N$	64
$M$	100000
$V_a$	18.75 m/s
$\psi$	45°

The bias and standard deviations are obtained with a Monte Carlo simulation of 128 different realizations of the measurements. The standard deviations are studied with respect to the theoretical ones of (D.11). For the DSD parameter retrieval, the approach of [2] is used as a reference. The approach of [2] is referred to as “Chen’s approach” in the analysis, and a superscript of “Chen” is used on top of the variables whenever relevant. An assumption has been considered: prior knowledge of the radial wind-related parameters  $\mu_v$  and  $\sigma_v$ . As the existing Doppler PSD methods of DSD parameter retrieval assume that the radial wind parameters are known beforehand precisely (from the measurements of another radar sensitive to clear sky reflections, for example), the performance of one such method is assessed, but with imposed uncertainty in the estimations of  $\mu_v^{(\text{Chen})}$  and  $\sigma_v^{(\text{Chen})}$ .

The uncertainty in these parameters is imposed across the Monte Carlo simulations. The  $\hat{\mu}_v^{(\text{Chen})}$  is sampled from a Gaussian distribution (with mean as the true  $\mu_v$ ), and  $\hat{\sigma}_v^{2(\text{Chen})}$  is sampled from a gamma distribution.

$$\hat{\mu}_v^{(\text{Chen})} \stackrel{i.i.d.}{\sim} \mathcal{N}\left(\mu_v^{(\text{True})}, \left[\frac{2V_a}{5N}\right]^2\right) \quad (6.22)$$

$$\hat{\sigma}_v^{2(\text{Chen})} \stackrel{i.i.d.}{\sim} \text{Gamma}(100 \times \sigma_v^{2(\text{True})} + 1, 100) \quad (6.23)$$

A hat on the parameters refers to the fact that they are estimated quantities. For the DSD parameter estimation, the following are used:

$$\hat{\Lambda}^{(\text{Chen})} = c_3 \left( \frac{\Omega - 1}{1 - 2\Omega} \right), \quad (6.24)$$

$$\hat{\eta}^{(\text{Chen})} = \frac{\log \left[ \frac{c_{2\psi}}{c_{1\psi} - \hat{V}_{T\psi}} \right]}{\log \left[ 1 + \frac{c_3}{\hat{\Lambda}^{(\text{Chen})}} \right]} - 7, \quad (6.25)$$

where  $\Omega$  is given by:

$$\Omega = \frac{\log \frac{c_{1\psi} - \hat{V}_{T\psi}}{c_{2\psi}}}{\log \left[ \left( \frac{\hat{\sigma}_{p\psi}^2}{c_{2\psi}^2} \right) + \left( \frac{c_{1\psi} - \hat{V}_{T\psi}}{c_{2\psi}} \right)^2 \right]}. \quad (6.26)$$

These equations are used from [2, eq. (12, 13, 14)]. In these equations,  $\hat{V}_{T\psi}$  and  $\hat{\sigma}_{p\psi}$  are used as  $\hat{V}_{T\psi} = \mu_r - \hat{\mu}_v^{(\text{Chen})}$  and  $\hat{\sigma}_{p\psi}^2 = \sigma_r^2 - \hat{\sigma}_v^{2(\text{Chen})}$  (The  $\psi$  subscript

refers to the fact that the variables include the elevation angle  $\psi$ :  $\hat{V}_{T\psi} = \hat{V}_T \sin(\psi)$ ,  $\hat{\sigma}_{p\psi} = \hat{\sigma}_p \sin(\psi)$ ,  $c_{1\psi} = c_1 \sin(\psi)$ ,  $c_{2\psi} = c_2 \sin(\psi)$ . Here,  $\mu_r$  and  $\sigma_r$  are the mean and spectrum widths computed from the incoherent average of  $L$  Doppler PSDs, each having  $N$  coherent echoes integrated.

The assertion that Chen's approach, as described in [2], does not aim to estimate the DSD parameters accurately may not fully capture the intent and methodology presented in the study. In the research, a combination of retrievals from radar and a disdrometer (with empirical second-order relationship between  $\eta$  and  $\Lambda$ ) is studied to treat the estimation of these parameters accurately. As the focus is only on radar retrievals and not disdrometer ones, the analysis is restricted to the above-mentioned equations (6.24), (6.25), and (6.26).

The approach is not compared with the other Doppler-based approaches such as [30] because, in these studies, only one realization of the Doppler PSD is used with very high Doppler resolution. Furthermore, the optimization procedure in [30] is iterative, where one parameter is estimated at once exclusive of the others in each iteration, increasing the computational cost.

The bias is the difference between the expected value of the estimated quantity and the true value.

$$\mathbb{B}[\hat{\Theta}] = \mathbb{E}[\hat{\Theta}] - \Theta. \quad (6.27)$$

Here, the expectation of the estimated quantity is computed by doing a Monte Carlo simulation and taking the average. Therefore, a positive bias refers to an overestimation, and a negative bias refers to an underestimation. The following expression computes the numerical variance in the parameters:

$$\mathbb{V}[\hat{\Theta}] = \mathbb{E}[(\hat{\Theta} - \mathbb{E}[\hat{\Theta}])^2]. \quad (6.28)$$

The standard deviation in the estimates is computed by taking the square root of  $\mathbb{V}[\hat{\Theta}]$ .

The theoretical variances are computed by taking the inverse of the Fisher information matrix, and the detailed derivation is shown in Appendix D. The Fisher information matrix (in this case, it is a  $4 \times 4$  because there are four parameters) is derived by taking the expectation of the second derivative of the log-likelihood. For the discussion on theoretical variance (and how it is different than the unbiased-CRB), unbiased CRB, and biased CRB, refer to §3.5.

The biases of parameters are dependent on each other. In this case, it is a  $4 \times 4$  matrix. The identity matrix is  $\mathbf{1}$ , and the Fisher information matrix is  $\mathbf{I}$  (all having the same dimension of  $4 \times 4$ ). The bias gradients  $\nabla_{\theta}$  are computed with respect to the parameters themselves. The estimation bias is caused by many factors, such as insufficient echo sample size ( $N$ ), optimization process inaccuracies, parameter space constraints, etc. Therefore, the functional forms of the bias-gradients are harder to achieve [160] and are not a part of this chapter.

At  $N \rightarrow \infty$  and  $L \rightarrow \infty$ , the theoretical standard deviations converge to the CRB as the estimator becomes unbiased. Chen's approach produces very low standard deviations because of its biased nature. The estimation variance of WiDSE is inversely proportional to  $L$  and can be verified by (D.1), (D.2), and (D.11).

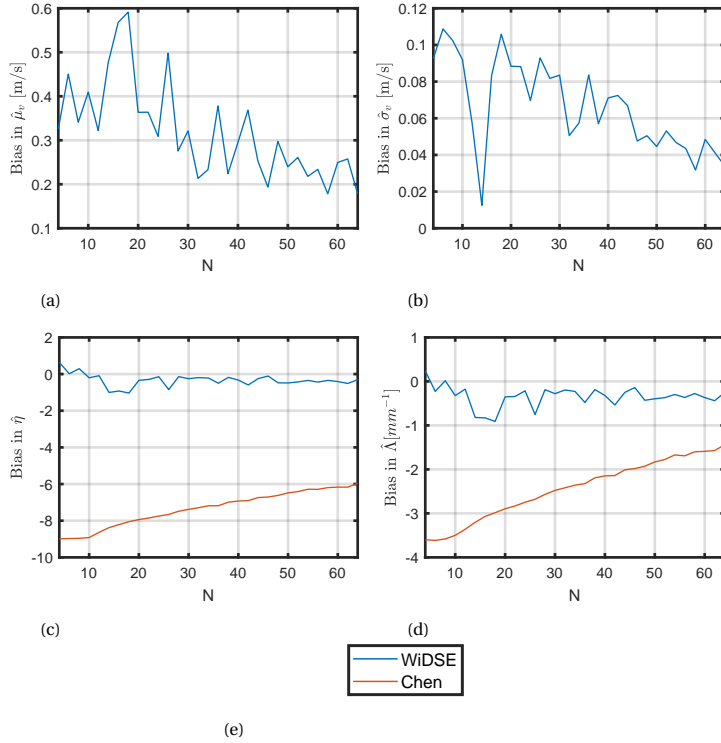


Figure 6.1: Bias in the estimation of: a  $\hat{\mu}_v$  m/s b  $\hat{\sigma}_v$  m/s c  $\hat{\eta}$  d  $\hat{\Lambda}$  mm<sup>-1</sup> at  $\mu_v = 3.53$  m/s,  $\sigma_v = 0.6$  m/s,  $\eta = 2.07$ ,  $\Lambda = 3.48$  mm<sup>-1</sup>, and  $L = 32$  with the number of coherent echo samples  $N$ . e Legend for the figures.

### 6.6.1. DEPENDENCE ON THE NUMBER OF COHERENT ECHO SAMPLES $N$

The performance with the number of coherent echo samples  $N$  is presented in Fig. 6.1 and 6.2. The parameter values chosen are:  $\mu_v = 3.53$  m/s,  $\sigma_v = 0.6$  m/s,  $\eta = 2.07$ ,  $\Lambda = 3.48$  mm<sup>-1</sup>, and number of realizations is  $L = 32$ .

With an increasing number of samples, the estimates are converging. The proposed WiDSE approach is superior to Chen's approach in terms of bias in the estimates. The numerical standard deviations follow the same trend as the theoretical ones. The variance analysis is carried out after  $N = 23$  to avoid numerical errors in the integrals in the formulae in the Fisher information matrix.

### 6.6.2. DEPENDENCE ON THE RADIAL WIND SPECTRAL WIDTH ( $\sigma_v$ )

The bias and standard deviation in the estimates are shown in Fig. 6.3 and 6.4, respectively. It can be seen that the bias of the DSD parameters increases with an increase in the contribution of the radial wind spectral width. The contribution of the radial wind component in the Doppler spectrum rises with an increase in the spectral width; as a result, the DSD parameters suffer from larger biases.

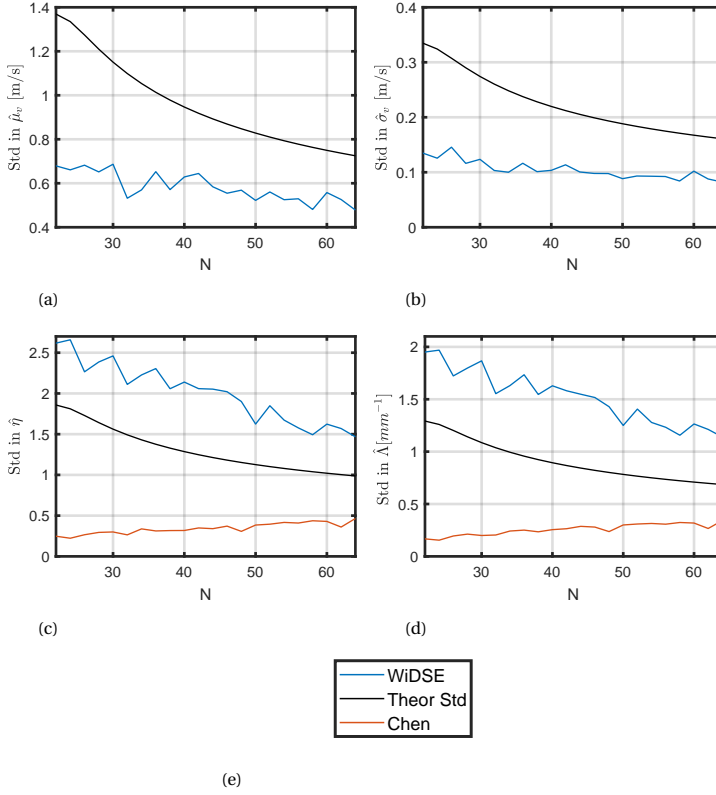


Figure 6.2: Standard deviation in the estimation of: **a**  $\hat{\mu}_v$  m/s **b**  $\hat{\sigma}_v$  m/s **c**  $\hat{\eta}$  **d**  $\hat{\Lambda}$  mm<sup>-1</sup> at  $\mu_v = 3.53$  m/s,  $\sigma_v = 0.6$  m/s,  $\eta = 2.07$ ,  $\Lambda = 3.48$  mm<sup>-1</sup>, and  $L = 32$  with the number of coherent echo samples  $N$ . The expression “Theor” refers to theoretical plots, **e** Legend for the figures.

Nonetheless, the bias of WiDSE is smaller than Chen’s approximation.

The numerical estimation variance of mean Doppler velocity, spectrum width, and the DSD parameters (for spectral widths  $> \sigma_v = 1.1$  m/s) for  $\eta = 1.5$  do not follow the trend of the theoretical variance. It can be attributed to the fact that for larger spectral widths and larger  $\eta > 0$ , the biases in the estimates affect the numerical variance. The numerical and theoretical variances for smaller  $\eta$  values follow similar trends for smaller spectral widths.

### 6.6.3. DEPENDENCE ON THE DSD PARAMETERS

The performance with the parameter  $\eta$  at fixed  $\mu_v$ , and  $\sigma_v$  are presented in Fig. 6.5 and 6.6. The  $\Lambda$  parameter is also varied with  $\eta$  based on a quadratic relationship proposed in [161, eq. (18)]. This relationship is used for the parameter sweep to assess the performance. The estimation of  $\eta$  and  $\Lambda$  are still done independently. The parameters  $\mu_v$ ,  $\sigma_v$  are set to 3.53 m/s, and 0.6 m/s, respectively. The number of echoes  $N = 64$ , and the number of realizations are  $L = 32$ .



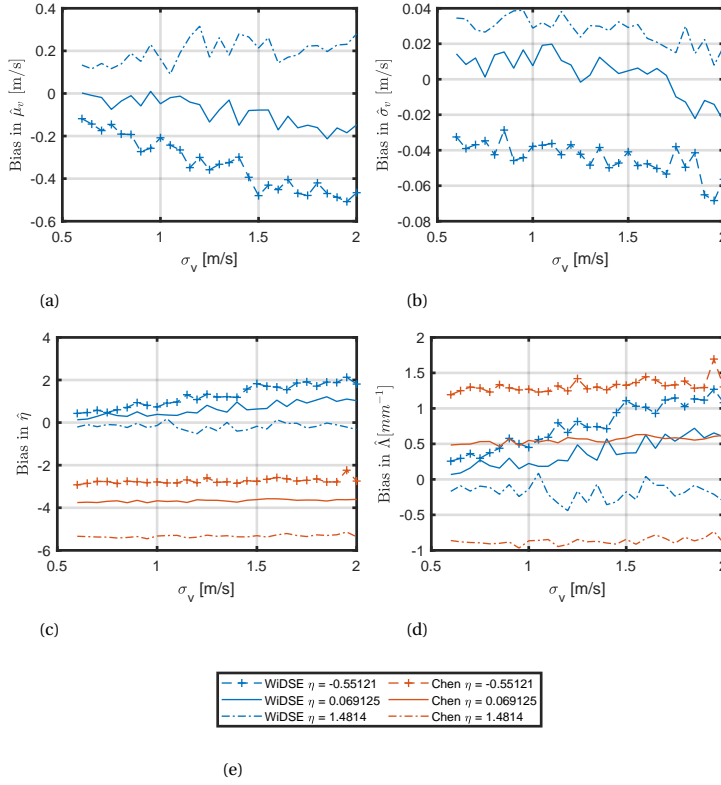


Figure 6.3: Bias in the estimation of: a  $\hat{\mu}_v$  m/s b  $\hat{\sigma}_v$  m/s c  $\hat{\eta}$  d  $\hat{\Lambda}$   $\text{mm}^{-1}$ , with the radial wind spectral width  $\sigma_v$  at  $N = 64$ , and  $L = 32$ . e Legend for the figures.

It can be observed that the bias of the proposed WiDSE technique is much smaller than that of the Doppler moment based on Chen's approximate formulae. Even though WiDSE performs better than the Doppler moments-based approach, it can be observed that the bias degrades with an increase in  $\eta$  and  $\Lambda$ .

The standard deviations in the estimates of the DSD parameters tend to increase with an increase in  $\eta$  or  $\Lambda$ . The theoretical plots are in good agreement with the numerical ones. Their biased nature can explain the difference between the theoretical and numerical standard deviations.

#### 6.6.4. DEPENDENCE ON $L$ WITH KNOWN AND UNKNOWN CONCENTRATION

A crude assumption of a previously known concentration parameter (which affects the reflectivity) has been applied in all the above performance analyses. However, in real measurements, this assumption may not hold because of the lack of knowledge about the concentration parameter of the Gamma DSD ( $N_0$ ). As  $N_0$  is a parameter typically multiplied in the reflectivity model, a slight change in this parameter can

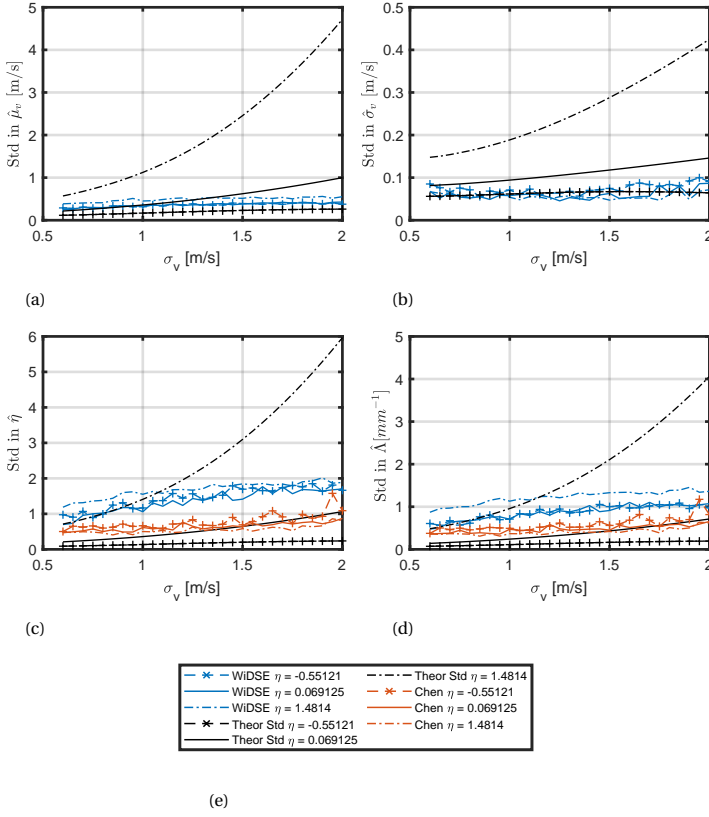


Figure 6.4: Standard deviation in the estimation of: a  $\hat{\mu}_v$  m/s b  $\hat{\sigma}_v$  m/s c  $\hat{\eta}$  d  $\hat{\Lambda}$  mm<sup>-1</sup>, with the radial wind spectral width  $\sigma_v$  at  $N=64$ , and  $L=32$ . The expression “Theor” refers to theoretical plots e Legend for the figures.

heavily affect the relative change in the reflectivity. Here, the performance of WiDSE is presented with respect to  $L$  (number of PSD measurements) with and without the knowledge of the reflectivity. In the known  $N_0$  case, as in the previous parameter sweeps, the reflectivity is estimated as shown in (6.14). In the unknown case, the reflectivity is estimated as the average power in the signal. The averaging of  $L$  sequences is done incoherently:

$$\hat{R} = \frac{1}{L} \sum_{l=1}^L \frac{1}{N} \sum_{k=0}^{N-1} |z_{l,k}|^2. \quad (6.29)$$

It can also be estimated in the frequency domain by computing the integral power in the PSD. The bias and standard deviations in the estimates are presented in Fig. 6.7 and Fig. 6.8, respectively, for WiDSE with respect to  $L$  (with  $N=64$ ). The values of the other parameters are  $\mu_v = 3.53$  m/s,  $\sigma_v = 0.6$  m/s,  $\eta = 2.07$ , and  $\Lambda = 3.48$  mm<sup>-1</sup>.

The bias in the estimates increases when the value of  $N_0$  is not known perfectly.

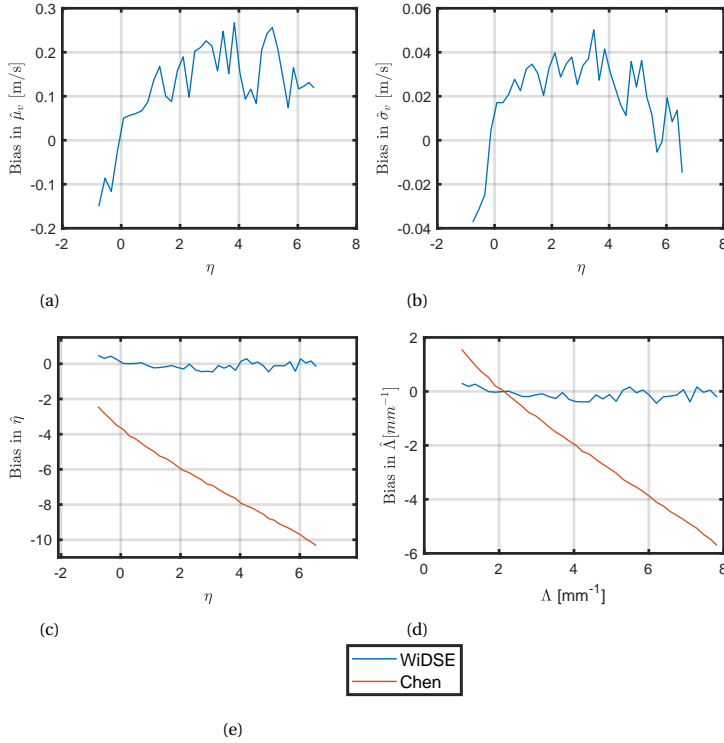


Figure 6.5: Bias in the estimation of: a  $\hat{\mu}_v$  m/s b  $\hat{\sigma}_v$  m/s c  $\hat{\eta}$  d  $\hat{\Lambda}$  mm<sup>-1</sup> with the DSD parameters at  $\sigma_v = 0.6$  m/s,  $N = 64$ , and  $L = 32$ . e Legend for the figures.

The radial wind parameters suffer from underestimation when  $N_0$  is not known perfectly. With an increasing  $L$ , the standard deviations decrease and follow similar trends as the theoretical ones. Therefore, the knowledge of  $N_0$  is crucial for accurately estimating the DSD parameters.

### 6.6.5. DISCUSSION ON DSD-DERIVED QUANTITIES

In the previous subsections 6.6.1, 6.6.2, 6.6.3, and 6.6.4, the limitations in the parameter estimation with the proposed technique are evident in some instances; such as the lack of knowledge regarding  $N_0$ , for higher radial wind spectral widths  $\sigma_v$  and higher shape parameter  $\eta$  (often associated with light rain events).

It is known that weather radars are usually not very sensitive to larger  $\eta$  values because of their significant-resolution volumes spanning several cubic meters in dimension. Radar retrievals are generally sensitive to larger diameters, usually at the DSD's tail.

Although the DSD parameters are biased when computed with the proposed approach, an excellent fit for the Doppler spectrum can still be achieved. To demonstrate this, the log-likelihood is shown with respect to  $\Lambda$  and  $\eta$  parameter

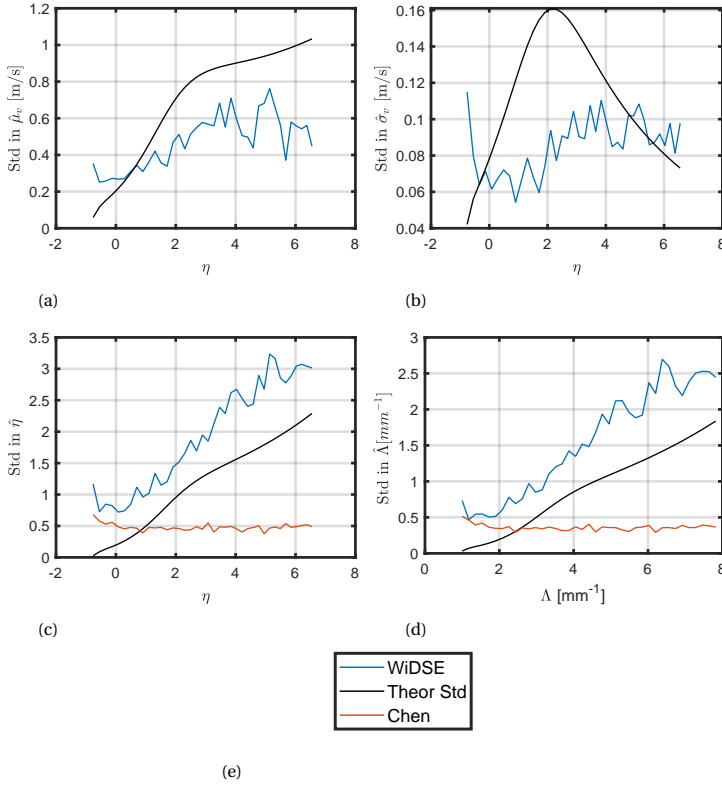


Figure 6.6: Standard deviation in the estimation of: a  $\hat{\mu}_v$  m/s b  $\hat{\sigma}_v$  m/s c  $\hat{\eta}$  d  $\hat{\Lambda}$  mm<sup>-1</sup> with the DSD parameters at  $\sigma_v = 0.6$  m/s,  $N = 64$ , and  $L = 32$ . The expression “Theor” refers to theoretical plots, e Legend for the figures.

space, assuming that  $\mu_v$ ,  $\sigma_v$ , and  $N_0$  are known perfectly. The log-likelihood is shown in Fig. 6.9 for  $\eta = 1.2$  and  $\Lambda = 3$ .

Firstly, it can be observed that the range of values the log-likelihood contains is very limited. Secondly, although it has a maximum in the log-likelihood, the profile is exceptionally smooth. The final estimate, therefore, can be very sensitive to the starting point in the optimization routine. Consequently, the optimization is started from several randomly selected starting points. Any estimate on the bright line on this plot can still fit the Doppler spectrum adequately.

For practical applications, if the objective is to separate the contribution of the radial wind from the fall velocity spectrum, the proposed approach can be proven extremely valuable because of its computational efficiency. A spatial distribution profile of fall and radial wind velocity spectra can be achieved efficiently.

The reconstructed Doppler spectrum is presented for a particular case to show the fit with the simulated Doppler spectrum. The test case chosen for this analysis is taken from the analysis shown in Fig. 6.7 and 6.8 at  $L = 64$ . Three sets of estimated

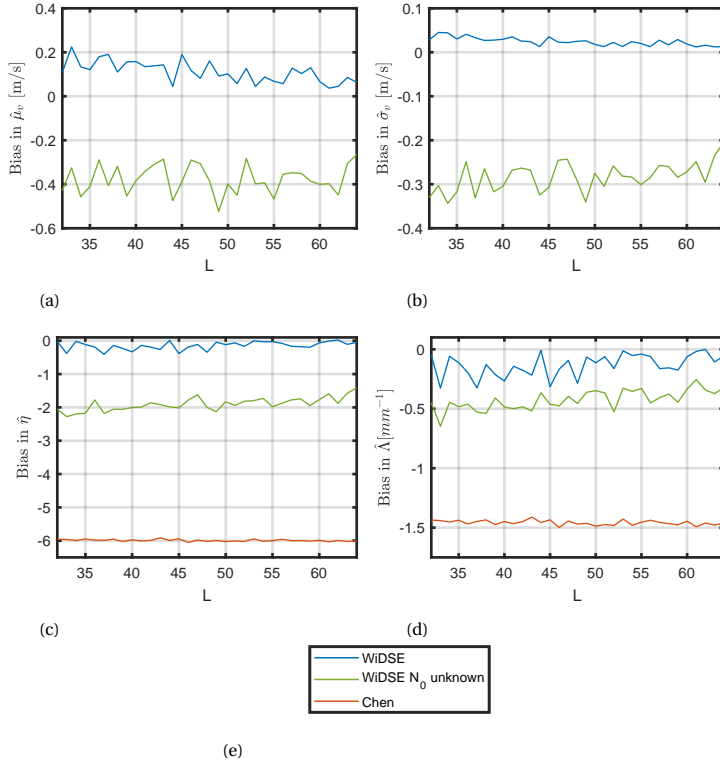


Figure 6.7: Bias in the estimation of: a  $\hat{\mu}_v$  m/s b  $\hat{\sigma}_v$  m/s c  $\hat{\eta}$  d  $\hat{\Lambda}$  mm<sup>-1</sup> with  $L$  at  $\sigma_v = 0.6$  m/s,  $N = 64$ ,  $\eta = 2.07$ ,  $\Lambda = 3.48$  mm<sup>-1</sup>. The expression “Theor” refers to theoretical plots, e Legend for the figures.

parameters are chosen, and they are:

1. Statistical average obtained from the Monte Carlo runs  $\mathbb{E}[\Theta]$ .
2. Two standard deviation bounds on either side of the average estimate,  $\mathbb{E}[\Theta] \pm 2\sqrt{\mathbb{V}[\Theta]}$ .

The Fig. 6.10 shows the Doppler spectrum reconstruction by replacing the estimated parameters in the PSD model of (6.11).

The mean terminal fall velocity ( $\bar{V}_T$ ) derived with [2, Eq. (4)] is presented in Fig. 6.11a. The statistical retrievals with DSD parameter sweep in the subsection 6.6.3 are used for this analysis. The proposed approach is in good agreement with the real mean terminal fall velocity. The median volume drop diameter ( $D_0$ ) [3, Eq. (5)] is presented in Fig. 6.11b. The retrievals of  $D_0$  also have good agreement with the ground truth.

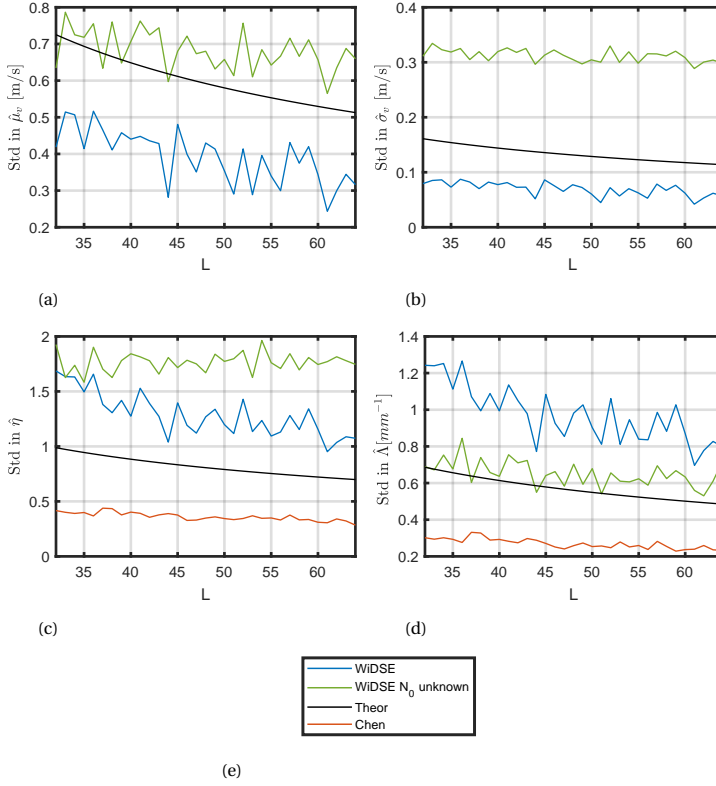


Figure 6.8: Standard deviation in the estimation of: **a**  $\hat{\mu}_v$  m/s **b**  $\hat{\sigma}_v$  m/s **c**  $\hat{\eta}$  **d**  $\hat{\Lambda}$  mm<sup>-1</sup> with  $L$  at  $\sigma_v = 0.6$  m/s,  $N = 64$ ,  $\eta = 2.07$ ,  $\Lambda = 3.48$  mm<sup>-1</sup>. The expression “Theor” refers to theoretical plots, **e** Legend for the figures.

### 6.6.6. COMPUTATIONAL RESOURCE CONSIDERATIONS

The computational time required for the parameter estimation is proportional to the number of iterations needed for the optimization procedure. Each iteration involves the computation of the log-likelihood multiple times. Hence, the time required for the entire process is proportional to the time needed to compute the log-likelihood. It has been observed that with the same computer, the computation of the correlation function  $G(q)$  requires around one decisecond (for  $N = 64$ ) when the internal form (6.16), whereas the approximate solution proposed in this chapter (6.17) requires only a few milliseconds resulting in a very fast computation. Furthermore, the log-likelihood is based only on the PSD, so it is computationally more efficient than the covariance-based parameter estimation approaches (because the covariance-based approaches require the computation of the inverse covariance, which is computation-heavy).

With a Linux operating system (Red Hat Linux, 256 GB random access memory) and MATLAB environment, a typical optimization execution at parameters with the

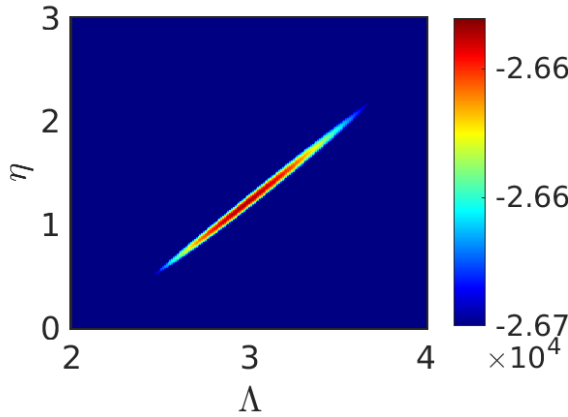


Figure 6.9: Log-likelihood (6.19)  $\log(p(Z|\Theta))$  with  $\eta$ , and  $\Lambda$  at  $N = 64$ ,  $L = 32$  at fixed values of  $\mu_v$  and  $\sigma_v$ . True values of  $\eta$  and  $\Lambda$  are 1.2 and 3 respectively.

WiDSE approach takes, on average, around 55 ms. Here, the average is computed with 512 runs of the optimizer with distinct starting points of the parameters (chosen randomly from a uniform distribution inside the parameter space). The total time for the optimization increases with an increase in the number of distinct starting points one wants to use for the optimization. If the hardware allows parallel computing, retrievals for several resolution volumes can be performed at the same time.

## 6.7. APPLICATION TO REAL RADAR OBSERVATIONS

### 6.7.1. DESCRIPTION OF THE EXPERIMENT

The proposed approach has been applied to real radar data recorded from the X-band fully polarimetric (9.4 GHz) MESEWI radar at the Delft University of Technology in the Netherlands. The horizontal (HH) polarization data has been used in the experiment presented in this chapter. The radar specifications are shown in Table 6.2.

Table 6.2: MESEWI radar specifications

Parameter	Value
Center Frequency ( $f_c$ )	9.4 GHz
PRI ( $T$ )	813.2 $\mu$ s
Beamwidth in Azimuth ( $d\phi$ )	2.5°
Beamwidth in Elevation ( $d\psi$ )	2°
Elevation Angle ( $\psi$ )	30°
ADC Sampling $f_s$	4.92 MHz
$V_a$	9.8 m/s

The data that is used in this experiment is from 32 fast scans (azimuthal scanning

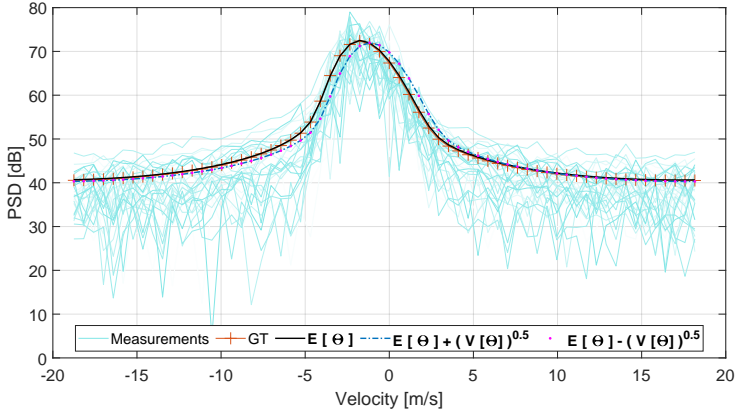


Figure 6.10: Doppler spectrum reconstruction at three sets of estimated parameters. “GT” stands for Ground Truth. In the legend, the  $\mathbb{E}[\Theta]$ ,  $\mathbb{V}[\Theta]$  are expected value and variance of the radial wind and the DSD parameters. The Doppler spectrum is then computed using (6.11) with the parameter values mentioned in the legend.

6

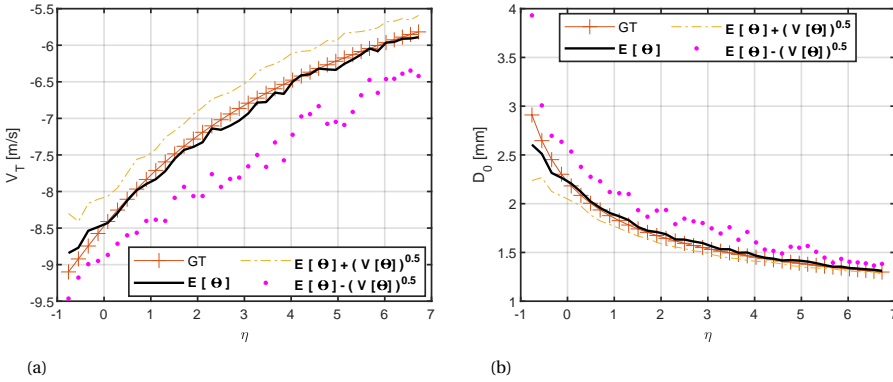


Figure 6.11: **a** Terminal fall velocity retrieval  $\hat{V}_T$  m/s. “GT” stands for Ground Truth. In the legend, the  $\mathbb{E}[\Theta]$ ,  $\mathbb{V}[\Theta]$  are expected value and variance of the DSD parameters. The terminal fall velocity is then computed using [2, Eq. (4)] with the parameter values mentioned in the legend, **b** Median volume diameter  $\hat{D}_0$  mm. In the legend, the  $\mathbb{E}[\Theta]$ ,  $\mathbb{V}[\Theta]$  are expected value and variance of the DSD parameters. The median volume drop diameter is then computed using [3, Eq. (5)] with the parameter values mentioned in the legend.



speed of  $\Omega = 5$  rotations per minute, rpm). The date of observation was May 9, 2023. The range processing and clutter treatment for this configuration are explained in §3.7.

The number of radar echoes (in slow-time for Doppler processing) per resolution volume is 100. The number of scans integrated using the proposed WiDSE algorithm is  $N_{\text{scan}} = 32$ . The total number of echo samples per resolution volume is  $32 \times 100$ , which is arranged with  $L \times N = 64 \times 50$ , meaning that there are 64 observations (realizations) for Doppler processing with each observation containing 50 echo samples each.

For the retrieval with WiDSE, some prior information is used for the concentration parameter  $N_0$  and the attenuation of reflectivity in the rain for the X-band as a function of the range  $\epsilon(r)$ . This prior information is used to model the reflectivity to avoid underestimation of the spectral width (radial turbulence) parameter  $\sigma_v$ , as demonstrated in sub-section 6.6.4 (with unknown  $N_0$ ).

For  $N_0$ , an average estimate (during the time of radar observation) is used by analyzing the data of a disdrometer located at the Green Village (at the Delft University of Technology) at around a range of 475m at an azimuthal angle of  $\phi = 130^\circ$  from the MESEWI radar location (The azimuth is considered clockwise;  $0^\circ$  is towards the north). The disdrometer provides the values for the concentration parameter  $N_0$  once per minute. An average concentration of  $N_0 = 3829 \text{ mm}^{-1} \text{ m}^{-3}$  is used for the experiment in this chapter. For the attenuation, an approximate empirical model has been used from [13, Ch. 5, Tab. 5.2] (in  $\text{dB km}^{-1}$ ) at a temperature of  $10^\circ\text{C}$ . This attenuation model is a function of the rain rate (in  $\text{mmh}^{-1}$ ). Ideally, for each range cell, the rain rate should be modeled with an integral over the DSD (is proportional to an integral involving the third power of the diameters and the DSD). However, this chapter uses an average rain rate of  $2 \text{ mmh}^{-1}$  (light rain) by analyzing the disdrometer data. The reflectivity is modeled by the following relationship:

$$R(r) = N_0 \frac{\mathcal{V}}{10^{\epsilon(r)/10} \times r} \frac{\Gamma(\eta + 7)}{\Lambda^{\eta+7}}, \quad (6.30)$$

where  $r$  is the range of the target (in km) and  $\mathcal{V}$  is the volume of the range cell  $\mathcal{V} = r^2 \cos(\psi) dr d\psi d\phi$ . The measured signal already considers the radar constant, which includes a correction related to the range of the targets, gains of the antenna systems (both the transmitter and receiver), attenuation correction in the receiver, and a calibration correction. Therefore, (6.30) is suitable enough as a model for the measured reflectivity.

The  $L$  measurement PSDs are computed, and for the retrieval process, four PSD values around the zero velocity are not considered to avoid the clutter region. Ideally, the clutter (without the clutter treatment in the pre-processing step) should be modeled along with precipitation, which is avoided in this chapter for simplicity.

The results of the mean Doppler velocity (using the PP approach) and the averaged reflectivity are shown in Fig. 6.12.

It can be seen from Fig. 6.12a that the reflectivity corresponds to a light rain event. It also shows a bright band ring of strong reflection around a range of 4.5 km. It is the melting layer in the atmosphere where the precipitation forms

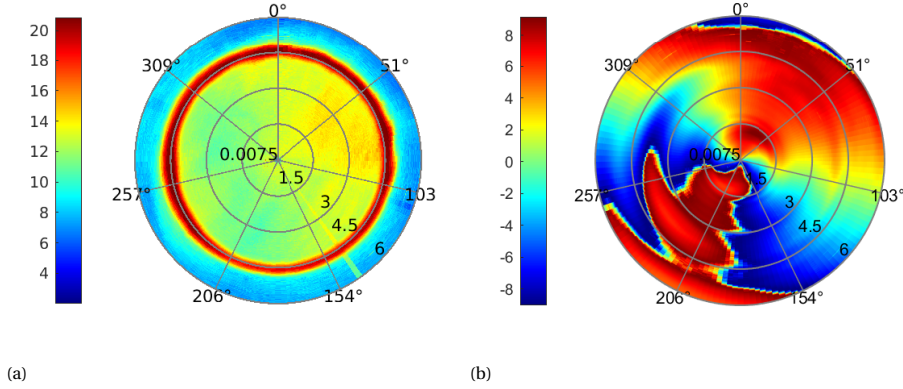


Figure 6.12: **a** Average reflectivity (dbZ) using  $L = 64$  PSDs, **b** Average mean Doppler velocity (m/s) using  $L = 64$  different mean Doppler velocities computed in each resolution volume using the PP approach.

[96]. The WiDSE processing is carried out for resolution volumes with reflectivity of more than 10 dBZ. It can be seen from the mean Doppler velocity (Fig. 6.12b) that the precipitation moving direction is towards  $\phi = 15^\circ$  (as the mean Doppler velocity is tapered with a cosine function (6.4) across the azimuth and at  $\phi = 15^\circ$  it has a maximum). Therefore, the mean Doppler velocity is close to zero at  $\phi = 135^\circ$ , and  $\phi = 315^\circ$  as these directions are perpendicular to the moving direction ( $\phi - \phi_{(\max)} \approx 90^\circ$ ). Around these azimuthal angles, the precipitation Doppler spectrum comes closer to the clutter region. As in this experiment clutter removal has been used and for the application of the WiDSE approach, the clutter Doppler frequencies are not considered in the PSD measurements, the estimation accuracy degrades (more on this in subsection 6.7.2).

The retrievals of the radial wind and DSD parameters with the proposed WiDSE approach are presented in the following sub-section 6.7.2. In all the retrievals, a crude assumption of signal stationarity (for 6.4 minutes) has been considered. The WiDSE approach can be extended in the future to accommodate a rapidly changing atmosphere where the parameters of interest change over time. However, for this chapter, for demonstration purposes only, this crude assumption is considered.

### 6.7.2. APPLICATION OF WiDSE ON REAL RADAR DATA

The retrievals of radial wind, DSD parameters, along with the derived mean terminal fall velocity ( $\hat{V}_{T\psi}/\sin\psi$ ) of raindrops and the median volume raindrop size ( $D_0$ ), are shown in Fig. 6.13. The scatter plot of the estimated DSD parameters till a range 2.24 km with the WiDSE approach, highlighted scatter plot of the estimated DSD parameters around the Green Village ( $\pm 75m$  of where the disdrometer is located), and the estimated DSD parameters with both higher order and lower order method of moments approaches [4] applied on the disdrometer data is shown in Fig. 6.14. The fitting to the Doppler spectrum at some specific resolution volumes is shown in Fig. 6.15. The log-likelihood of (6.19) is shown in Fig. 6.16.

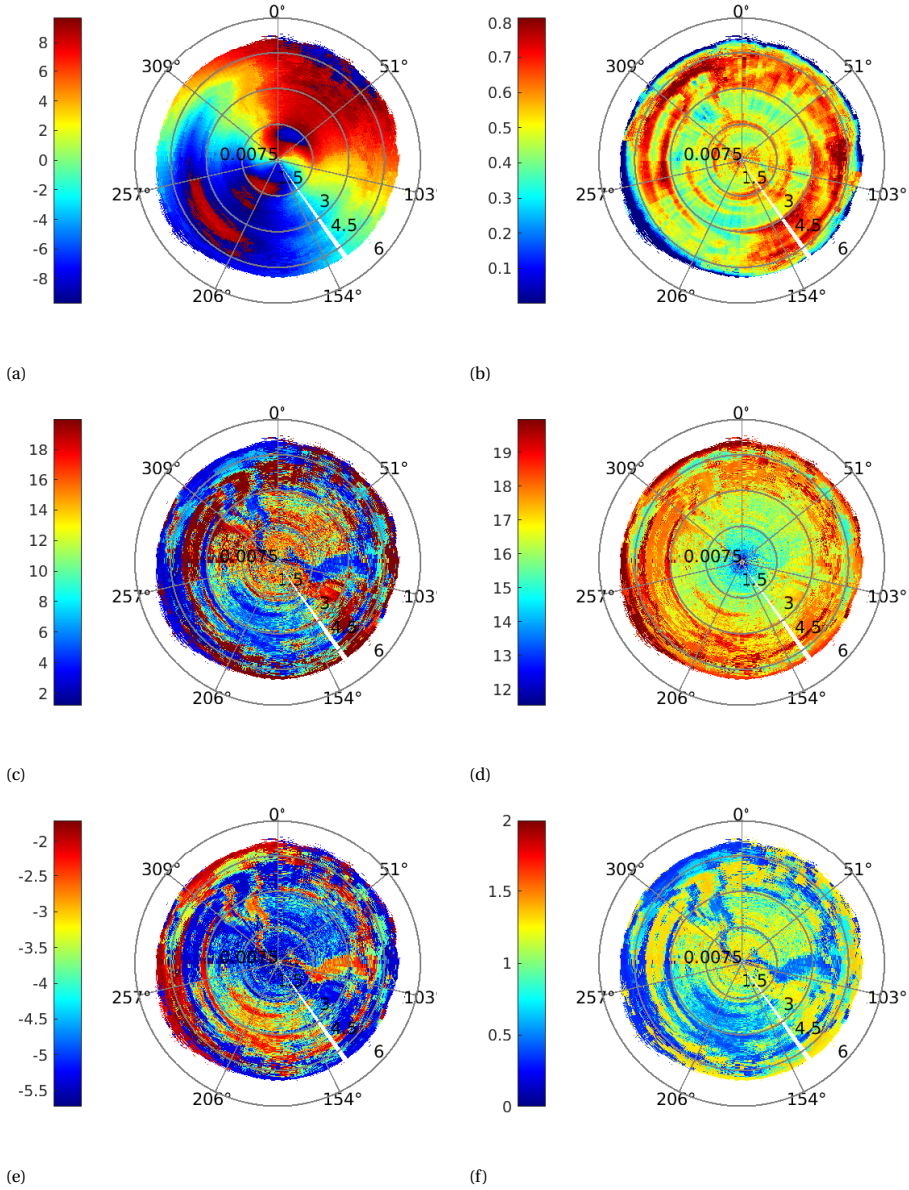


Figure 6.13: Plan Position Indicator (PPI) plots after applying WiDSE algorithm, **a** mean radial wind velocity  $\bar{\mu}_v$  m/s, **b** mean radial velocity width  $\bar{\sigma}_v$  m/s, **c** DSD shape parameter  $\hat{\eta}$ , **d** DSD rate parameter  $\hat{\Lambda}$  mm<sup>-1</sup>, and derived parameters, **e** mean terminal fall velocity  $\bar{V}_{T\psi}/\sin(\psi)$  m/s, **f** median diameter  $\hat{D}_0 = (3.67 + \hat{\eta}) / \hat{\Lambda}$  mm.

Some key findings are made from these results (Fig. 6.13-Fig. 6.16) and are listed below.

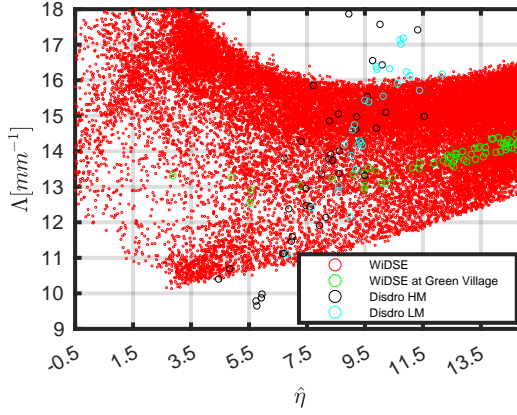


Figure 6.14: Scatter plot of the estimated DSD parameters  $\hat{\eta}$  and  $\hat{\Lambda} \text{ mm}^{-1}$ . “HM” stands for the higher order method of moments, “LM” stands for the lower order method of moments [4], and “Disdro” stands for disdrometer.

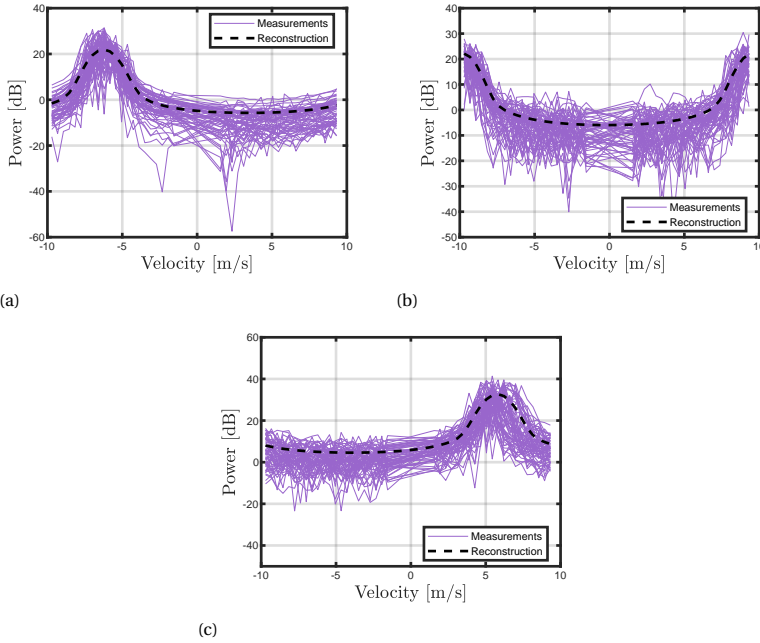


Figure 6.15: Doppler spectrum reconstruction at specific resolution volumes, **a** at the Green Village;  $r = 472 \text{ m}$ ,  $\phi = 128^\circ$ , **b** at a radar volume where the mean Doppler velocity is aliased (Fig. 6.12b),  $r = 1.829 \text{ km}$ ,  $\phi = 257^\circ$ , **c** at the melting layer,  $r = 4.662 \text{ km}$ ,  $\phi = 73^\circ$ .

1. In the mean Doppler velocity retrieval (Fig. 6.12b) and the retrieved mean radial wind with WiDSE approach (Fig. 6.13a), it can be observed that the

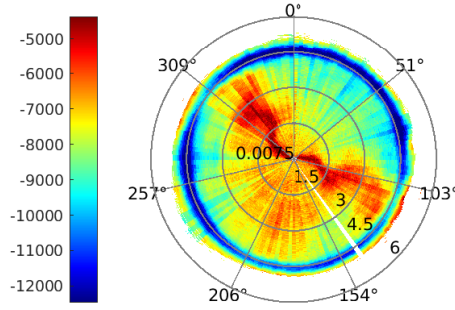


Figure 6.16: Optimal log-likelihood using (6.19) at the estimated parameter values  $\hat{\Theta}$ . The melting layer (around  $r = 4.5$  km) is adequately filtered out because it has very small log-likelihood values than the other regions.

6

- aliased velocity region of Fig. 6.12b is not symmetric and only appears in the negative radial velocity regions (around  $\phi = 170^\circ$  till  $\phi = 260^\circ$ ). However, as WiDSE tries to decouple the radial wind contribution by eliminating the mean terminal fall velocity (as a function of the retrieved DSD parameters), the aliased regions of the mean radial wind velocity retrieval are more symmetric than the mean Doppler velocity.
2. With increasing range, the radar volumes become bigger, introducing a broadening in the Doppler spectrum. Therefore, the radial velocity width  $\hat{\sigma}_v$  values are usually higher at higher ranges. A similar trend is also observed for  $\hat{\eta}$  and  $\hat{\Lambda}$ .
  3. At the zero mean Doppler velocity regions (around  $\phi = 135^\circ$ , and  $\phi = 315^\circ$ ), and the mean Doppler aliased regions (around  $\phi = 170^\circ$  till  $\phi = 260^\circ$ ), the estimated  $\hat{\eta}$ , the absolute value of the derived  $|\hat{V}_{T\psi}/(\sin\psi)|$ , and the median volume drop diameters  $D_0$  are underestimated. This underestimation can be attributed to the lack of useful spectrum for zero Doppler regions (clutter region is eliminated in the retrievals) and Doppler aliasing at the aliased regions. These regions are below the melting layer.
  4. Except for the above-mentioned regions, below the melting layer, the mean terminal fall velocity estimate is very uniform and around  $-4.5$  m/s to  $-5.5$  m/s. Similarly, the estimated median volume diameters are between  $0.8$  mm to  $1.4$  mm indicating observation of a light rain event. These estimated mean terminal fall velocities correspond to the estimated drop sizes for stratiform rain ([154, Fig. 3]).
  5. From Fig. 6.14, it can be seen that the range of values of the estimated DSD parameters from WiDSE coincides with the ones from the disdrometer. Radar and disdrometer are instruments with different sensitivities. Therefore, the estimated parameters from both sensors can exhibit different variances.

Radar volumes are several cubic meters, and radar is sensitive to larger drops, whereas the disdrometer is sensitive to the smaller ones as well. Radar signals are received from the atmosphere from a certain height, whereas a disdrometer measures the drop sizes in close proximity to the ground.

6. These large values of the DSD parameters  $\hat{\eta}$  and  $\hat{\Lambda}$  correspond to light rain and can be verified from the statistical analysis of [162, Fig. 4(a)]. The outliers with smaller  $\eta$  values come from the zero mean Doppler and aliased mean Doppler regions.
7. As explained in detail in the simulation study in the section 3.6, the DSD parameters can be very biased with the WiDSE approach. However, the derived parameters, such as the mean terminal fall velocity of the raindrops  $\hat{V}_{T\psi}/(\sin\psi)$  and the median volume drop size  $D_0$ , can be very accurate and more trustworthy. The WiDSE approach efficiently distinguishes the contribution of radial wind and mean terminal fall velocity from the Doppler spectrum.
8. When it comes to the melting layer, as the processes are dynamic, the Doppler spectrum does not remain stationary during the time of observation. Therefore, the parameter retrievals are not very stable. From Fig. 6.15c, it can be observed that the measured Doppler spectral content is not stable (from scan-to-scan), and therefore, the reconstructed Doppler spectrum with the WiDSE approach has a wider spectral width to account for the broadening.
9. Fig. 6.15a and Fig. 6.15b shows the Doppler spectrum reconstruction at the Green Village area and a volume where the Doppler spectrum is aliased, respectively. From a visual inspection, it can be seen that the fitting is sufficient for these locations.
10. From the log-likelihood computed at the optimal parameter values Fig. 6.16, it can be observed that the zero mean Doppler regions have a higher log-likelihood. However, a higher log-likelihood in this case is not necessarily due to an adequate fit but is associated with the fact that the useful spectra (around zero Doppler) are not taken as measurements. Another key observation drawn from the log-likelihood is that the high-reflectivity regions of the melting layer (near  $r = 4.5$  km) are sufficiently filtered out with very low log-likelihood values, suggesting that the stationary Doppler spectrum assumption with time is violated.

## 6.8. CONCLUSIONS

In this chapter, a maximum likelihood approach for a joint DSD and radial wind parameter estimation using fast-scanning weather radar Doppler PSD measurements is proposed. The proposed model of the PSD is a function of the DSD, radial wind parameters, and the finite observation time.

It has been shown that the proposed approach directly estimates all of the radial wind and DSD parameters, unlike the existing approaches where the DSD parameters

are estimated from either the Doppler moments of a vertically pointed radar or by using prior information on the wind parameters (from a wind profiler radar). With the proposed approach, the Doppler spectrum can be fit jointly and efficiently with rain DSD and radial wind parameters from the point of view of measurement and computation times. Furthermore, it does not require the radar to be only vertically pointed. Therefore, the proposed approach can benefit aviation safety and air traffic control applications, which require the spatial distribution (spatial coverage with high temporal resolution) of the mean terminal fall velocity of raindrops (a function of the rain DSD) and radial wind fields.

The performance of the parameter estimation has been studied extensively by Monte Carlo simulations for several parameter sweeps, such as number of coherent samples  $N$ , radial wind spectral width  $\sigma_v$ , the DSD parameters ( $\eta$  and  $\Lambda$ ), and number of PSD realizations  $L$ . The proposed estimator (WiDSE) is compared with Chen's approximate formulae for the DSD parameter retrieval from Doppler moments of the fall velocity spectrum. It has been shown that the proposed estimator has a smaller bias than Chen's approximate formulae.

The DSD parameter estimates bias and standard deviation increase with increased radial wind velocity dispersion (radial wind spectral width or turbulence in the radial wind) and shape parameter of the DSD. It is shown that the prior information on the concentration parameter  $N_0$  is essential for the DSD parameter retrieval.

The theoretical variances in estimating the parameters are derived and plotted along with the numerical variances. The theoretical variances are computed by using the Fisher information matrix. As the estimator is biased, the numerical variances do not always follow the theoretical ones. The biased Crámer Rao lower bound (CRB) for this biased estimator can also be derived by studying the bias gradients in the future. However, with an increase in the number of coherent samples  $N$  and the number of PSD realizations  $L$ , the theoretical variances converge to the unbiased CRBs as the estimator is asymptotically unbiased.

The novel approximate model proposed in this chapter for the computation of the correlation function of the reflectivity-weighted fall velocity spectrum ( $G(q)$ ) helps in very efficient and fast parameter estimation.

The proposed approach can use several incoherent PSD measurements from multiple radar scans. A practical application of such a scenario can be observed in the case of fast azimuthal scanning radars where the time on target per scan per resolution volume is small.

The fit of the Doppler spectrum is shown for one particular test case, and the derived mean terminal fall velocity retrieval is presented as a function of the DSD parameters. The proposed approach can adequately fit the Doppler spectrum. The retrieved mean terminal fall velocity with the proposed approach also agrees with the ground truth despite the estimated DSD parameters suffering from larger bias and variance with an increase in the shape DSD parameter  $\eta$ .

Although the model of the Doppler PSD as a function of gamma DSD parameters is presented, it does not include the concentration parameter  $N_0$ . Estimating this parameter requires additional complexity because it is a parameter that is simply a multiplier in the reflectivity.



In addition, this chapter does not consider any relationship between the  $\eta$  and  $\Lambda$  parameters. However, a relationship can be considered in the future as explained in [163] for reducing the complexity of the parameter estimation.

The proposed approach has been applied to real radar data acquired from the MESEWI radar of the Delft University of Technology on a day with light rain. Although there are some variations in the estimated DSD parameters with the WiDSE approach applied to the real radar data, the derived parameters, such as the median volume drop size and the mean terminal fall velocity of raindrops, are stable. The log-likelihood performed in this chapter shows the potential to distinguish the melting layer region with very high reflectivity from the regions with precipitation. The results are sufficiently explained by a validation performed with the data from a disdrometer. For modeling the reflectivity for the acquired data, an average value of the  $N_0$  parameter is used that was acquired from the disdrometer.

In the future, this  $N_0$  parameter can be used as an estimation parameter for the radar. The rain-related attenuation can also be modeled with the DSD parameters in the future to make the study complete. Furthermore, at X-band frequencies, a pure Rayleigh scattering approximation does not hold (for raindrops having diameters bigger than 2.3 mm [13, Tab. 5.1]). A mixture of Rayleigh and Mie scattering principles should be used for the DSD retrieval.





# 7

## CONCLUSIONS AND RECOMMENDATIONS

The Doppler processing for radar sensing of extended targets like precipitation has been further developed in this work. The atmospheric parameters that are the focus of the thesis are the mean Doppler velocity, which is a scalar sum of the projections of mean wind and mean vertical velocity of the raindrops, the spectral width, which is a measure of the turbulence in the rain, and the raindrop size distribution (DSD) parameters. In each chapter of the thesis, new measurement and estimation techniques are developed, several distinct atmospheric parameters of interest are studied, and recommendations for estimating those accurately and efficiently are presented.

The major contributions of the thesis are the following:

1. **NOVEL DOPPLER MOMENT ESTIMATION APPROACH NAMED THE PARAMETRIC SPECTRUM ESTIMATOR (PSE) FOR FAST AZIMUTHALLY SCANNING RADARS USING INCOHERENT OBSERVATIONS FROM SEVERAL SCANS: (CHAPTER 3)**

A Doppler power spectral density (PSD) model for the precipitation-like target is proposed as a function of the Doppler moments and the observation interval. A log-likelihood is then formulated by assuming that the spectral power is distributed exponentially at each velocity/ frequency. This log-likelihood function can deal with multiple such PSDs. Multiple PSDs can be acquired from several radar scans for a typical scanning radar. A maximum likelihood estimation is performed on the log-likelihood to estimate the Doppler moments. The proposed PSE approach is applied to real scanning radar data acquired from the MESEWI radar at TU Delft. It has been shown that the PSE approach is superior to the other methods. The spectrum reconstruction is also presented with all the methods, and the fitting with PSE outperforms. The PSE approach needs comparatively smaller dwell time than the other methods,

which shows its applicability for fast scanning radars. A scanning strategy is proposed as a function of the velocity dispersion parameter (a measure of the turbulence in the atmosphere).

## 2. NOVEL LOCAL DOPPLER SPECTRUM RECONSTRUCTION WITH A SHORT TIME ON TARGET BY USING COMPLEX GAUSSIAN PROCESS REGRESSION (CGP-R): (CHAPTER 4)

Complex Gaussian process regression (CGP-R) is applied to reconstruct the Doppler spectrum. Firstly, the marginal log-likelihood of the hyperparameters given the time domain radar echoes is maximized to estimate the hyperparameters  $\Theta$ . Using the estimated parameter  $\Theta$ , the signal and spectrum can be reconstructed using the CGP posterior. As the CGP regression is a Bayesian technique, uncertainty in the estimates is also computed in addition to the predicted signal mean in the time and frequency domain. To the author's knowledge, it is the first time a direct frequency domain posterior is formulated and applied to the weather radar echoes to reconstruct the Doppler spectrum for precipitation, making it novel. The hyper-parameter estimation performance is assessed by the bias and variance in the estimates and compared with the DFT and PP nonparametric techniques for equispaced echo samples for a fair comparison. The proposed CGP approach outperforms the other methods regarding bias and variance for true normalized spectral widths  $\sigma_{fn} < 0.2$  for the normalized spectral width estimation. This approach has been applied to the real radar data acquired from MESEWI radar at TU Delft at specific resolution cells to reconstruct the Doppler spectrum with the CGP posterior. It has been shown that the CGP-R in the frequency domain can reconstruct the Doppler spectrum with only 12.5% of the echo samples. The posterior mean with 12.5% of the echo samples has excellent agreement with the DFT Doppler spectrum (using all the echo samples acquired during the observation). The uncertainty estimates are also computed. The frequency domain posterior is calculated directly using the time domain measurements, posing no additional computational burden.

## 3. A NOVEL INTEGRATIVE APPROACH FOR RECONSTRUCTION OF THE PRECIPITATION DOPPLER SPECTRUM BY AVOIDING ALIASING IN THE DOPPLER SPECTRUM BY EXPLOITING AN APERIODIC PULSE TRAIN (CHAPTER 5)

A novel sampling approach in the time domain is proposed for the aperiodic pulse train (with a log-periodic sampling sequence). The theoretical Nyquist unambiguous velocity limit for such aperiodic sequences is discussed in detail. The minimum sampling interval of the aperiodic sequence is kept higher than a threshold to make a fair performance comparison with a periodic sampling sequence having a pulse repetition interval the same as the minimum sampling interval of the aperiodic sequence. The Doppler moments are normalized with the Nyquist unambiguous interval of this equivalent periodic sampling sequence. The CGP-R is chosen to estimate the Doppler moments as the

signal is sampled aperiodically. The Doppler moment estimation is compared with the state-of-the-art methods for both aperiodic and equivalent periodic sampling sequences. Although some of the state-of-the-art moments estimation techniques perform as expected with aperiodically sampled sequences for pointed targets immersed in white Gaussian noise, the limitations of such methods to estimate the Doppler moments for extended targets have been demonstrated. It has been shown that the proposed approach outperforms the other methods for the normalized mean Doppler moment estimation (when the true normalized Doppler spectrum width remains smaller than 0.16, i.e.,  $\sigma_{fn} < 0.16$ ). An application-centric recommendation has been presented for the minimum sampling interval. Furthermore, CGP-R has been used to reconstruct the Doppler spectrum for simulated realistic radar signals. Unlike the previous contributions, the simulated radar signals are generated by considering three extended targets, two precipitation-like and one clutter-like (at zero frequency). This signal model mimics severe weather conditions like multilayered precipitation or precipitation with wake vortices. The reconstruction of the Doppler spectrum is compared with the periodic and aperiodic Schuster's periodogram. It is shown that the proposed CGP-R outperforms, and the Doppler spectrum is reconstructed unambiguously. The normalized mean Doppler velocity for each extended target is estimated unambiguously.

#### 4. A NOVEL APPROACH OF FITTING THE DOPPLER SPECTRUM EFFICIENTLY WITH DSD AND WIND VELOCITY PARAMETERS TO GET REAL-TIME ACCURATE AND HIGH-RESOLUTION INFORMATION ABOUT HORIZONTAL WIND AND VERTICAL FALL VELOCITY OF RAINDROPS (CHAPTER 6)

Assuming that the radial wind field of raindrops forms a Gaussian distribution and the diameters of raindrops form a Gamma raindrop size distribution (DSD), a novel Doppler power spectrum model is derived. The shape of such a spectrum is not a perfect Gaussian but has a skewness because of the DSD. The contribution of the DSD on the Doppler spectrum increases with increasing elevation angle. The proposed model of the Doppler spectrum involves an intractable integral. A novel approximation using Gauss-Laguerre polynomials has been proposed for the intractable integral to reduce the computational time. The PSD model in this study is a more generic form of the PSD proposed for the Doppler moment estimation in Chapter 3. Estimating the DSD's shape and rate parameters, the mean wind velocity, and the wind spectral width is performed with a maximum likelihood estimation. Several parameter sweeps have been shown with all the parameters, including the number of echo samples and radar scans. The proposed approach is much more efficient than the state-of-the-art techniques when it comes to the computational resources required. However, the estimated parameters, especially the DSD parameters, can be heavily biased. The theoretical variances in estimating the parameters are derived and compared with the numerical ones computed from Monte Carlo simulations. Although the abovementioned limitations exist for

DSD parameter estimation, the proposed approach is powerful in efficiently fitting the Doppler spectrum. Estimating the derived parameters, such as the terminal fall velocity and the median diameter of the raindrops in a resolution volume, have a smaller and acceptable bias. Therefore, the proposed technique efficiently separates the contribution of wind from the vertical velocity of the raindrops for each radar resolution volume. The proposed technique is an essential and efficient tool for high-resolution wind field estimation.

The research contributions presented in the thesis transition from specific to generic formulations of Doppler spectrum parameter estimation, presenting novel methodologies that enhance the accuracy and efficiency of fast-scanning modern radars. The research proposed in this thesis shows a correlation between the physical parameters of interest and the measurement strategy, which includes radar parameters such as the azimuthal scan speed, non-linearity in the pulse repetition interval, and so on.

The thesis outcome is useful in the formulation of measurement techniques for radars and serves as a precursor for adaptive measurement strategies and high-resolution wind field estimation, significantly advancing radar meteorology and making the thesis a novel, holistic, and generic study.

## FUTURE RESEARCH DIRECTIONS

While several novel approaches that deal with fitting the Doppler spectrum from precipitation efficiently and accurately for fast scanning weather radars have been proposed in this thesis, this study has also catalyzed further research for the future. The following directions can be considered in the future:

1. Parameter estimation for complex weather phenomena such as multi-layer precipitation, presence of vortices, rapidly changing wind fields, wind updrafts, etc: this study will demonstrate the limitations of the existing techniques and instruments for such convoluted estimation problems.
2. A direct 3D wind field estimation using advanced techniques in combination with the ones presented in this thesis: these methods can be validated with real data acquired from a radar having a phased array of antennas for the elevation. This study will help predict wind fields with high spatial and temporal resolution.
3. Classification of different types of hydrometeors, such as rain, snow, hail, ice, etc, using radars: this study will enhance the identification of various hydrometeors in radar images, improving the effectiveness of radar echo processing.
4. Adequate modeling of the dynamics of various hydrometeor types within the melting layer, along with the retrieval of their physical parameters using radar echoes, is of critical importance. Such a study will provide significant insights into the melting processes and their alterations due to climate change, thereby enhancing our understanding of these complex phenomena.

# A

## EXPECTED VALUE OF THE POWER SPECTRUM

The expectation of the square of the modulus of the spectrum function (taken from (3.9)) is presented in this Appendix. Here, for the derivation, we do not use the normalization  $(1/N)$ . A change of parametrization from velocity to angular frequency ( $\omega = \frac{4\pi T}{\lambda} v$ ) is used in the derivation for mathematical simplicity.

$$\mathbb{E}[|S(\omega)|^2] = A^2 \mathbb{E} \left[ \sum_{m=1}^M \frac{\sin^2 \left( N \frac{(\omega_{m,r} - \omega)}{2} \right)}{\sin^2 \left( \frac{\omega_{m,r} - \omega}{2} \right)} \right] \quad (\text{A.1})$$

As the velocities of the raindrops are assumed independent and identically distributed, the right-hand side of (A.1) can be approximated to the following integral:

$$\mathbb{E}[|S(\omega)|^2] = A^2 M \int_{-\infty}^{+\infty} \frac{\sin^2 \left( N \frac{(x - \omega)}{2} \right)}{\sin^2 \left( \frac{x - \omega}{2} \right)} p(x) dx, \quad (\text{A.2})$$

where the  $p(x)$  is the probability density function of the frequencies which is assumed to be Gaussian in this case. The integral is then:

$$\mathbb{E}[|S(\omega)|^2] = A^2 M \int_{-\infty}^{+\infty} \frac{\sin^2 \left( N \frac{(x - \omega)}{2} \right)}{\sin^2 \left( \frac{x - \omega}{2} \right)} \frac{1}{\sqrt{2\pi\sigma_\omega^2}} \times \exp \left( -\frac{(x - \mu_\omega)^2}{2\sigma_\omega^2} \right) dx, \quad (\text{A.3})$$

where,  $\mu_\omega$  and  $\sigma_\omega$  are normalized angular frequency equivalents of the normalized Doppler frequencies. It can be further simplified as:

$$\begin{aligned} \mathbb{E}[|S(\omega)|^2] &= A^2 M \int_{-\infty}^{+\infty} \exp(-j(N-1)(x - \omega)) \\ &\times \left( \frac{\exp(jN(x - \omega)) - 1}{\exp(j(x - \omega)) - 1} \right)^2 \frac{1}{\sqrt{2\pi\sigma_\omega^2}} \times \exp \left( -\frac{(x - \mu_\omega)^2}{2\sigma_\omega^2} \right) dx. \end{aligned} \quad (\text{A.4})$$

A

If a parametrization  $\zeta = \exp(j(x-\omega))$  is applied,  $\exp(-j(N-1)(x-\omega)) \times \left( \frac{\exp(jN(x-\omega))-1}{\exp(j(x-\omega))-1} \right)^2$  takes the following form:

$$I(\zeta) = \zeta^{-(N-1)} \left( \frac{\zeta^N - 1}{\zeta - 1} \right)^2, \quad (\text{A.5})$$

where the expression  $\frac{\zeta^N - 1}{\zeta - 1}$  is equal to a finite length (N term) sum of a geometric progression with starting point 1 and a common factor of  $\zeta$

$$I(\zeta) = \zeta^{-(N-1)} \left( \sum_{n=0}^{N-1} \zeta^n \right)^2 \quad (\text{A.6})$$

The expression  $(\sum_{n=0}^{N-1} \zeta^n)^2$  can be expanded using the principles of multinomial expansion, which then can be generalized by the following expression:

$$I(\zeta) = N + \sum_{n=1}^{N-1} n (\zeta^{n-N} + \zeta^{N-n}). \quad (\text{A.7})$$

Replacing  $\zeta$  as the function of  $x$ , we have:

$$I(x) = N + \sum_{n=1}^{N-1} n \left( \exp(j(x-\omega)(n-N)) + \exp(j(x-\omega)(N-n)) \right). \quad (\text{A.8})$$

This can be rewritten by a change in parametrization  $n = N - q$ ,

$$I(x) = N + \sum_{q=1}^{N-1} (N-q) \left( \exp(j(x-\omega)q) + \exp(-j(x-\omega)q) \right) \quad (\text{A.9})$$

Hence, the original integral (A.1) can be written as:

$$\mathbb{E}[|S(\omega)|^2] = A^2 M \int_{-\infty}^{+\infty} \frac{1}{\sqrt{2\pi\sigma_\omega^2}} \exp\left(-\frac{(x-\mu_\omega)^2}{2\sigma_\omega^2}\right) I(x) dx. \quad (\text{A.10})$$

The integral of a complex exponential function multiplied with a Gaussian function is generalized by the following relation:

$$\int_{-\infty}^{+\infty} \frac{1}{\sqrt{2\pi\sigma^2}} \exp\left(-\frac{(x-\mu)^2}{2\sigma^2}\right) \exp(j\eta x) dx = \exp\left(-\frac{\sigma^2 \eta^2}{2}\right) \exp(j\eta \mu). \quad (\text{A.11})$$

Using (A.11), we can rewrite (A.10) as

$$\begin{aligned} \mathbb{E}[|S(\omega)|^2] &= A^2 M \left( N + \sum_{q=1}^{N-1} (N-q) \times \left[ \exp\left(-\frac{\sigma_\omega^2 q^2}{2}\right) \right. \right. \\ &\quad \left. \left. \times \left( \exp(jq(\mu_\omega - \omega)) + \exp(-jq(\mu_\omega - \omega)) \right) \right] \right), \end{aligned} \quad (\text{A.12})$$

which then simplifies to:

$$\begin{aligned} &\mathbb{E}[|S(\omega)|^2] \\ &= A^2 M \left( N + 2 \sum_{q=1}^{N-1} (N-q) \times \left[ \exp\left(-\frac{\sigma_\omega^2 q^2}{2}\right) \times \cos(q(\mu_\omega - \omega)) \right] \right). \end{aligned} \quad (\text{A.13})$$

Changing the parametrization from angular frequency to velocity, and normalizing it with the number of samples  $N$ , we have the following final expression for the PSD:

$$\mathbb{E}[\frac{1}{N}|S(\nu)|^2] = A^2 M \left( 1 + 2 \sum_{q=1}^{N-1} \left( 1 - \frac{q}{N} \right) \times \left[ \exp \left( - \left( \frac{4\pi T}{\lambda} \right)^2 \frac{\sigma_v^2 q^2}{2} \right) \times \cos \left( \frac{4\pi T}{\lambda} q (\mu_\nu - \nu) \right) \right] \right). \quad (\text{A.14})$$





# B

## THEORETICAL VARIANCE AND THE CRB OF PSE AND CGP

### B.1. PSE

The log-likelihood of (3.14) is used to compute the theoretical variance. Here, as there are two parameters (here we consider the normalized frequency parameters)  $\Theta = [\theta_a, \theta_b] = [\mu_\nu, \sigma_\nu]$ , the Fisher matrix is of dimension  $(2 \times 2)$ . The entries of the Fisher matrix are given by:

$$I_{a,b} = -\mathbb{E} \left[ \frac{\partial^2 \log(p(\mathbf{Z}|\Theta))}{\partial \theta_a \partial \theta_b} \right]. \quad (\text{B.1})$$

The derivative of (3.14) with respect to any one of the parameters ( $\theta_a$  or  $\theta_b$ ) is given by:

$$\begin{aligned} & \frac{\partial \log(p(\mathbf{Z}|\Theta))}{\partial \theta_a} \\ &= - \sum_{i=1}^N \left[ \frac{L}{F(v_i, \Theta) + \sigma_n^2} \frac{\partial F(v_i, \Theta)}{\partial \theta_a} - \frac{\sum_{l=1}^L Z_l(v_i)}{(F(v_i, \Theta) + \sigma_n^2)^2} \frac{\partial F(v_i, \Theta)}{\partial \theta_a} \right]. \end{aligned} \quad (\text{B.2})$$

The derivative of the above expression with respect to the other parameter ( $\theta_a$  or  $\theta_b$ ) is therefore given by (Using only  $F$  instead of  $F(v_i, \Theta)$  and  $Z_l$  instead of  $Z_l(v_i)$  for convenience):

$$\begin{aligned} & \frac{\partial^2 \log(p(\mathbf{Z}|\Theta))}{\partial \theta_a \partial \theta_b} \\ &= - \sum_{i=1}^N \left[ \frac{-L(F + \sigma_n^2) + 2 \sum_{l=1}^L Z_l}{(F(v_i, \Theta) + \sigma_n^2)^3} \left( \frac{\partial F}{\partial \theta_a} \right) \left( \frac{\partial F}{\partial \theta_b} \right) + \frac{L(F + \sigma_n^2) - \sum_{l=1}^L Z_l}{(F(v_i, \Theta) + \sigma_n^2)^2} \frac{\partial^2 F}{\partial \theta_a \partial \theta_b} \right]. \end{aligned} \quad (\text{B.3})$$

The expectation of the expression above is given by (using the fact that  $\mathbb{E}[Z] = F + \sigma_n^2$ ):

$$\mathbb{E} \left[ \frac{\partial^2 \log(p(\mathbf{Z}|\Theta))}{\partial \theta_a \partial \theta_b} \right] = - \sum_{i=1}^N \left[ \frac{L}{(F(v_i, \Theta) + \sigma_n^2)^2} \left( \frac{\partial F}{\partial \theta_a} \right) \left( \frac{\partial F}{\partial \theta_b} \right) \right]. \quad (\text{B.4})$$

For normalized velocity parameters ( $\lambda/(2T) = 2V_a$ ), the function  $F$  can be written as:

$$\begin{aligned} & F(f, \mu_{fn}, \sigma_{fn}) \\ &= M \times \left[ 1 + 2 \cdot \sum_{q=1}^{N-1} \left( 1 - \frac{q}{N} \right) \times \exp \left( -2\pi^2 \sigma_{fn}^2 q^2 \right) \times \cos \left( 2\pi q (\mu_{fn} - f) \right) \right]. \end{aligned} \quad (\text{B.5})$$

The derivatives of the above expression are given below:

$$\frac{\partial F}{\partial \mu_{fn}} = -4\pi \cdot M \cdot \sum_{q=1}^{N-1} q \left( 1 - \frac{q}{N} \right) \times \exp \left( -2\pi^2 \sigma_{fn}^2 q^2 \right) \sin(2\pi q (\mu_{fn} - f)). \quad (\text{B.6})$$

$$\frac{\partial F}{\partial \sigma_{fn}} = -8\pi^2 M \times \sum_{q=1}^{N-1} q^2 \left( 1 - \frac{q}{N} \right) \exp \left( -2\pi^2 \sigma_{fn}^2 q^2 \right) \times \cos(2\pi q (\mu_{fn} - f)) \quad (\text{B.7})$$

Therefore, the theoretical variance is given by:

$$\mathbb{V}^{\text{Theor}}[\hat{\theta}_a] \geq \mathbf{I}_{a,a}^{-1}. \quad (\text{B.8})$$

It is also known as the square of the reciprocal of the sensitivity [80, eq. (4)]. As the estimator is unbiased for both the parameters for  $N \rightarrow \infty$ , (B.8) can be used at  $N \rightarrow \infty$  to compute the unbiased CRB.

$$\mathbb{V}[\hat{\theta}_a] \geq \mathbf{I}_{a,a}^{-1}|_{N \rightarrow \infty}. \quad (\text{B.9})$$

A closed form of the unbiased CRB is out of the scope of this thesis.

## B.2. CGP

The log-likelihood of (4.9) is used to compute the theoretical variance of the hyper-parameters of the CGP. The inverse Fisher information matrix is computed for the CGP likelihood (with real-valued covariance), and the diagonal entries of its inverse are considered. The entries of the Fisher information matrix are:

$$\mathbf{I}_{a,b} = -\mathbb{E} \left[ \frac{\partial^2 \log(p(\mathbf{z}|\Theta))}{\partial \theta_a \partial \theta_b} \right] = \frac{1}{2} \text{Tr} \left( \mathbf{C}_R^{-1}(\Theta) \frac{\partial \mathbf{C}_R(\Theta)}{\partial \theta_a} \mathbf{C}_R^{-1}(\Theta) \frac{\partial \mathbf{C}_R(\Theta)}{\partial \theta_b} \right), \quad (\text{B.10})$$

where the operator “Tr” refers to the matrix trace. The theoretical variance is therefore:

$$\mathbb{V}^{\text{Theor}}[\hat{\theta}_a] = (\mathbf{I}^{-1})_{a,a}. \quad (\text{B.11})$$

# C

## DECAY STUDY OF $G(q)$ : AUTO-CORRELATION FUNCTION RELATED TO THE VERTICAL FALL VELOCITY

Firstly, it can be observed that in (6.17), the weights are a function of the  $\eta$  DSD parameter, and the function  $f$  is a function of the other DSD parameter  $\Lambda$ . Implementing (6.17) is made efficient by having a matrix of the weights  $w_i$  for several  $\eta$  values saved in the computer. For the implementation, we saved the weights  $w_i$  for  $\eta = -2(0.001)20$ ; an array between  $-2$  and  $20$  is considered with a step of  $0.001$ . The accuracy of the Gauss-Laguerre depends on the choice of the order  $n$  and the value of the function  $f(y_i)$  for a given set of parameters  $\eta, \Lambda$ .

For a Gaussian-shaped power spectrum (with a periodic decaying Gaussian covariance like  $Y(q)$ ), it is recommended to have at least  $N = 1/\sigma_{fn}$  ( $\sigma_{fn} = \sigma_v/(2V_a)$ ) is the normalized spectral width with  $V_a$  being the unambiguous velocity interval) samples for an accurate estimation of the parameters with  $\sigma_{fn} < 0.2$  [56]. As  $G(q)$  does not have a closed form expression with respect to  $q$ , a functional description of the decay for all possible combinations of  $\eta$  and  $\Lambda$  is challenging to achieve.

The  $G(q)$  does not follow a quadratic Gaussian periodic decay; it is unfair to fit it with one. The approximate expressions of the second spectral moment of the fall PSD given in [2] can give us an idea about the decay rate of the covariance  $G(q)$ . However, it does not provide all the decay characteristics because of its non-Gaussian nature. In this section, we compare the mean lifetime and halftime of the decay based on the spectral width formulation of [2], with a numerical study using the integral form of  $G(q)$  given in (6.16).

We use the theoretical formula of [2] for the spectral width ( $\sigma_W$ ) to plot  $N_{\text{lifetime}} = 1/(\sqrt{2\pi^2}\sigma_{fWn})$ , where  $\sigma_{fWn} = \sigma_W/(2V_a)$  is the normalized fall spectrum

width. To consider only vertical fall, the elevation is  $\psi = 90^\circ$ . The radar unambiguous velocity is 37.5 m/s, more than three times the fall velocity of a hypothetical drop with infinite diameter (can be checked by (6.5)). For the estimation problem, the maximum unambiguous velocity interval does not matter significantly because the PSD model also considers the aliasing of the PSD by considering the finite observation interval ( $N$ ). To validate the theoretical approximation, we also compute the integral (6.16) numerically and find  $N_{\text{lifetime, numerical}} = q|_{G(q)=\exp(-1)}$ . For the half-life,  $N_{\text{half-life}} = \sqrt{\log(2)}/(\sqrt{2\pi^2}\sigma_{fWn})$  and  $N_{\text{half-life, numerical}} = q|_{G(q)=0.5}$ .

The purpose of studying the lifetime and half-life of the decay is not to prove that  $G(q)$  does not fit a Gaussian decay but to study the number of echo samples needed to adequately cover the correlated part of the sequence. It helps us decide on a suitable value of  $n$  for the Gauss-Laguerre quadrature (see (6.17)) for realistic values of  $\eta$  and  $\Lambda$ .

The period of the covariance is often associated with the mean vertical fall velocity of the scatterers. For raindrops, if we examine (6.5), we know that the maximum velocity of raindrops can reach  $c_1 = 9.65$  m/s for a hypothetical drop of size infinite.

The difference between the half-lives and lifetimes of the numerical one and the model of [2] is presented in Fig. C.1c and C.1d as a function of  $\eta$  and  $\Lambda$  in dB scale. It can be immediately observed that the difference in the lifetime is larger than the half-life, especially for smaller  $\Lambda$  values (which is an indicator of larger raindrops in the volume). This analysis shows that the  $G(q)$  decays slower than a quadratic Gaussian decay. Nonetheless, we can observe that the time samples required for realistic median drop sizes are less than 20 (if we consider the median drop size roughly  $(3.67 + \eta)/\Lambda$  [3] and a maximum drop size of 4mm [164]). It can be observed from the Fig. C.1a, and C.1b in dB scale.

Fig. C.2 shows  $G(q)$  (both real and imaginary parts) using the integral form of (6.16) and the approximate form of (6.17) with  $n = 64$  for  $\eta = 10$ , and  $\Lambda = 4$ . This configuration is chosen as it is the worst case in terms of decay, meaning that the one lifetime with this configuration is comparatively larger than other DSD parameter combinations. The approximate form of 6.17 follows the integral form for a considerable time of decay. After around  $q = 70$ , the approximate form accumulates errors.

Although we have kept  $n = 64$ , it can be changed based on the application using a logic similar to that in this Appendix. In addition, the decay of the covariance function  $Y(q)$  should also be considered along with  $G(q)$ . If the number of samples required to capture the covariance of  $Y(q)$  adequately is larger than 64, the  $n$  should be increased. For rigorous consideration of the convergence of the Gauss-Laguerre quadrature, [165] can be followed. A quick look into Uspensky's formulae [166] suggests that the convergence in our case should depend on a relation between  $\eta$  and the function  $f$  which depends on the parameter  $\Lambda$ .

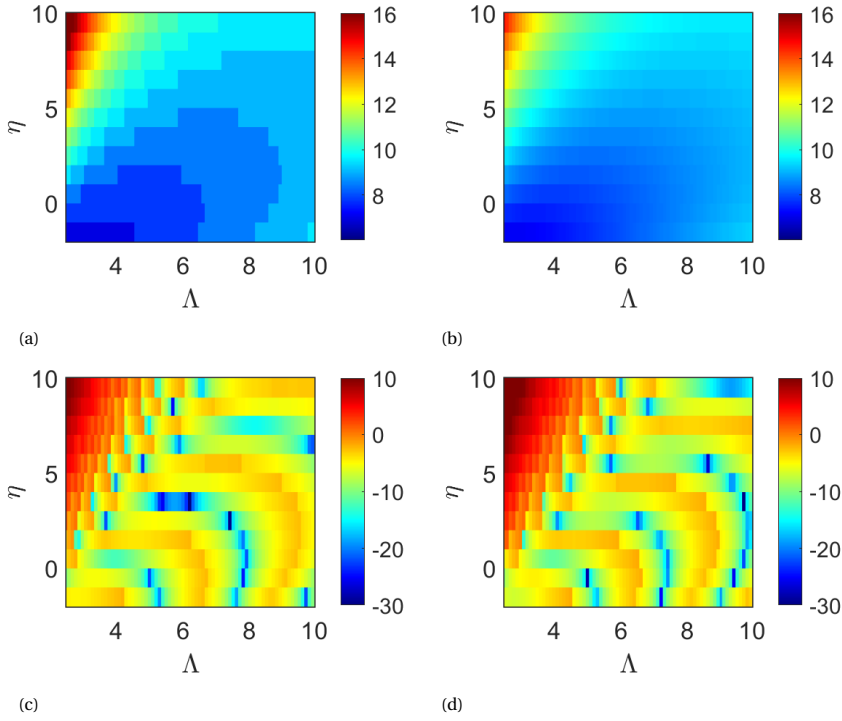


Figure C.1: Decay study for  $G(q)$  with  $\eta$ , and  $\Lambda$  **a** Lifetime computed numerically **b** Analytical lifetime based on [2] **c** Difference of halftimes between the numerical and the analytical methods. **d** Difference of lifetimes between the numerical and the analytical methods. The times are converted to dB scale for better visualization.

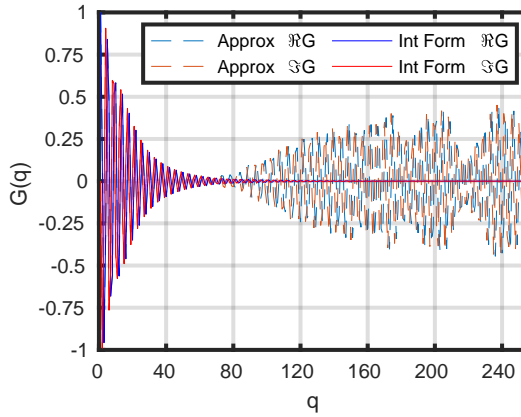


Figure C.2:  $G(q)$ . "Int form" is the original integral of (6.16), and "Approx" is the approximation of (6.17).



# D

## THEORETICAL VARIANCE AND THE CRAMER RAO LOWER BOUND (CRB) OF WIDSE

The elements of the Fisher matrix with any two parameters are given by:

$$I_{a,b} = -\mathbb{E} \left[ \frac{\partial^2 \log(p(\mathbf{Z}|\Theta))}{\partial \theta_a \partial \theta_b} \right]. \quad (\text{D.1})$$

The expectation term above is given by ( $\mathbb{E}[Z] = F + \sigma_n^2$ ): [56, eq. 34]

$$\mathbb{E} \left[ \frac{\partial^2 \log(p(\mathbf{Z}|\Theta))}{\partial \theta_a \partial \theta_b} \right] = - \sum_{i=1}^N \left[ \frac{L}{(F(\nu_i, \Theta) + \sigma_n^2)^2} \left( \frac{\partial F}{\partial \theta_a} \right) \left( \frac{\partial F}{\partial \theta_b} \right) \right]. \quad (\text{D.2})$$

$$\frac{\partial F}{\partial \mu_\nu} = R \sum_{q=1}^{N-1} q \left( 1 - \frac{q}{N} \right) \left[ \exp(-j \frac{4\pi T}{\lambda} \nu) \frac{\partial Y(q)}{\partial \mu_\nu} G(q) + \exp(j \frac{4\pi T}{\lambda} \nu) \frac{\partial Y(-q)}{\partial \mu_\nu} G(-q) \right], \quad (\text{D.3})$$

where:

$$\begin{aligned} \frac{\partial Y(q)}{\partial \mu_\nu} &= j \frac{4\pi T}{\lambda} q Y(q) \\ \frac{\partial Y(-q)}{\partial \mu_\nu} &= -j \frac{4\pi T}{\lambda} q Y(-q). \end{aligned} \quad (\text{D.4})$$

The derivative with respect to  $\sigma_\nu$  is given by:

$$\frac{\partial F}{\partial \sigma_\nu} = R \sum_{q=1}^{N-1} q \left( 1 - \frac{q}{N} \right) \left[ \exp(-j \frac{4\pi T}{\lambda} \nu) \frac{\partial Y(q)}{\partial \sigma_\nu} G(q) + \exp(j \frac{4\pi T}{\lambda} \nu) \frac{\partial Y(-q)}{\partial \sigma_\nu} G(-q) \right], \quad (\text{D.5})$$



where:

$$\begin{aligned}\frac{\partial Y(q)}{\partial \sigma_v} &= -q^2 \left( \frac{4\pi T}{\lambda} \right)^2 \sigma_v Y(q) \\ \frac{\partial Y(-q)}{\partial \sigma_v} &= -q^2 \left( \frac{4\pi T}{\lambda} \right)^2 \sigma_v Y(-q).\end{aligned}\tag{D.6}$$

The derivative with respect to  $\eta$  is given by:

$$\begin{aligned}\frac{\partial F}{\partial \eta} &= R \sum_{q=1}^{N-1} q \left( 1 - \frac{q}{N} \right) \left[ \exp(-j \frac{4\pi T}{\lambda} \nu) Y(q) \frac{\partial G(q)}{\partial \eta} + \exp(j \frac{4\pi T}{\lambda} \nu) Y(-q) \frac{\partial G(-q)}{\partial \eta} \right] \\ &+ \frac{\partial R}{\partial \eta} \frac{F}{R},\end{aligned}\tag{D.7}$$

where:

$$\begin{aligned}\frac{\partial G(q)}{\partial \eta} &= \frac{\exp(j C_1 q)}{\Gamma(\eta + 7)} \int_0^1 \left( \frac{\Lambda}{c_3} \right)^{\eta+7} u^{\frac{\Lambda}{c_3}-1} \exp(-j C_2 q u) \\ &\times (\log(u^{-1}))^{\eta+6} \left[ \log\left(\frac{\Lambda}{c_3}\right) + \log(\log(u^{-1})) - \psi^{(0)}(\eta + 7) \right] du \\ \frac{\partial G(-q)}{\partial \eta} &= \frac{\exp(-j C_1 q)}{\Gamma(\eta + 7)} \int_0^1 \left( \frac{\Lambda}{c_3} \right)^{\eta+7} u^{\frac{\Lambda}{c_3}-1} \exp(j C_2 q u) \\ &\times (\log(u^{-1}))^{\eta+6} \left[ \log\left(\frac{\Lambda}{c_3}\right) + \log(\log(u^{-1})) - \psi^{(0)}(\eta + 7) \right] du \\ \frac{\partial R}{\partial \eta} &= R \times (\psi^{(0)}(\eta + 7) - \psi^{(0)}(\eta + 1)).\end{aligned}\tag{D.8}$$

The original integral of  $G(q)$  in (6.15) is from 0 to  $\infty$ . However, in the above expressions for (D.8), the definite integral limits have been changed from 0 to 1 by using a transformed variable  $u = \exp(-\Lambda D)$  to have numerical stability in the implementation. Here,  $\psi^{(0)}(x)$  is the digamma function  $\psi^{(0)}(x) = \Gamma'(x)/\Gamma(x)$ .

The derivative with respect to  $\Lambda$  is given by:

$$\begin{aligned}\frac{\partial F}{\partial \Lambda} &= R \sum_{q=1}^{N-1} q \left( 1 - \frac{q}{N} \right) \left[ \exp(-j \frac{4\pi T}{\lambda} \nu) Y(q) \frac{\partial G(q)}{\partial \Lambda} + \exp(j \frac{4\pi T}{\lambda} \nu) Y(-q) \frac{\partial G(-q)}{\partial \Lambda} \right] \\ &+ \frac{\partial R}{\partial \Lambda} \frac{F}{R},\end{aligned}\tag{D.9}$$

where:

$$\begin{aligned}
 \frac{\partial G(q)}{\partial \Lambda} &= \frac{\exp(jC_1 q)}{\Gamma(\eta+7)} \int_0^1 \left(\frac{\Lambda}{c_3}\right)^{\eta+7} u^{\frac{\Lambda}{c_3}-1} \exp(-jC_2 q u) \\
 &\quad \times (\log(u^{-1}))^{\eta+6} \left[ \frac{\eta+7}{\Lambda} + \frac{1}{c_3} \log(u) \right] du \\
 \frac{\partial G(-q)}{\partial \Lambda} &= \frac{\exp(-jC_1 q)}{\Gamma(\eta+7)} \int_0^1 \left(\frac{\Lambda}{c_3}\right)^{\eta+7} u^{\frac{\Lambda}{c_3}-1} \exp(jC_2 q u) \\
 &\quad \times (\log(u^{-1}))^{\eta+6} \left[ \frac{\eta+7}{\Lambda} + \frac{1}{c_3} \log(u) \right] du \\
 \frac{\partial R}{\partial \Lambda} &= -6M \frac{\Gamma(\eta+7)}{\Gamma(\eta+1)} \Lambda^{-7}.
 \end{aligned} \tag{D.10}$$

The theoretical variances (also known as the square of the reciprocal of the sensitivity [80, eq. (4)]) is computed as:

$$\mathbb{V}^{\text{Theor}}[\hat{\theta}_a] \geq \mathbf{I}_{a,a}^{-1}. \tag{D.11}$$

The estimator is unbiased when  $N \rightarrow \infty$ , (D.11) can be used at  $N \rightarrow \infty$  to compute the unbiased CRB.

$$\mathbb{V}[\hat{\theta}_a] \geq \mathbf{I}_{a,a}^{-1}|_{N \rightarrow \infty}. \tag{D.12}$$

No closed form of this unbiased CRB is given in this thesis.



# BIBLIOGRAPHY

- [1] T. Oguchi, "Scattering from hydrometeors: A survey," *Radio Science*, vol. 16, no. 5, pp. 691–730, 1981.
- [2] C. H. Chen, C. L. Su, J. H. Chen, and Y. H. Chu, "Vertical wind effect on slope and shape parameters of gamma drop size distribution," *Journal of Atmospheric and Oceanic Technology*, vol. 37, no. 2, pp. 243–262, 2020.
- [3] C. W. Ulbrich, "Natural Variations in the Analytical Form of the Raindrop Size Distribution," *Journal of Applied Meteorology and Climatology*, vol. 22, no. 10, p. 1764–1775, 1983.
- [4] Y. H. Chu and C. L. Su, "An investigation of the slope-shape relation for gamma raindrop size distribution," *Journal of Applied Meteorology and Climatology*, vol. 47, no. 10, pp. 2531–2544, 2008.
- [5] T. Dash, O. A. Krasnov, and A. G. Yarovoy, "Performance Analysis of the Wind Field Estimation for a Very Fast Scanning Weather Radar," in *2022 23rd International Radar Symposium (IRS)*, pp. 420–425, IEEE, 9 2022.
- [6] R. Penrose, *Shadows of the Mind: A Search for the Missing Science of Consciousness*. Oxford University Press, 1994.
- [7] A. C. Best, "The size distribution of raindrops," *Quarterly Journal of the Royal Meteorological Society*, vol. 76, no. 327, pp. 16–36, 1950.
- [8] R. Doviak and D. S. Zrnica, *Doppler Radar and Weather Observations*, vol. 36. 1993.
- [9] K. Browning and R. Wexler, "The Determination of Kinematic Properties of a Wind Field Using Doppler Radar," *Journal of Applied Meteorology and Climatology*, vol. 7, pp. 105–113, 1968.
- [10] K. A. Scharfenberg, D. J. Miller, T. J. Schuur, P. T. Schlatter, S. E. Giangrande, V. M. Melnikov, D. W. Burgess, D. L. Andra, M. P. Foster, and J. M. Krause, "The Joint Polarization Experiment: Polarimetric Radar in Forecasting and Warning Decision Making," *Weather and Forecasting*, vol. 20, pp. 775–788, 10 2005.
- [11] D. Atlas, ed., *Radar in Meteorology*. Boston, MA: American Meteorological Society, 1990.
- [12] P. L. Heinselman and S. M. Torres, "High-temporal-resolution capabilities of the National Weather Radar Testbed Phased-Array Radar," *Journal of Applied Meteorology and Climatology*, vol. 50, no. 3, pp. 579–593, 2011.

- [13] Zrnic Dusan and Ryzhkov Alexander, *Radar Polarimetry for Weather Observations*.
- [14] E. Yoshikawa, T. Ushio, Z. Kawasaki, S. Yoshida, T. Morimoto, F. Mizutani, and M. Wada, "MMSE beam forming on fast-scanning phased array weather radar," *IEEE Transactions on Geoscience and Remote Sensing*, vol. 51, no. 5, pp. 3077–3088, 2013.
- [15] E. Gorgucci and V. Chandrasekar, "Evaluation of attenuation correction methodology for dual-polarization radars: Application to X-band systems," *Journal of Atmospheric and Oceanic Technology*, vol. 22, no. 8, pp. 1195–1206, 2005.
- [16] T. Oguchi, "Electromagnetic Wave Propagation and Scattering in Rain and Other Hydrometeors," *Proceedings of the IEEE*, vol. 71, no. 9, pp. 1029–1078, 1983.
- [17] D. N. Moiseev, C. M. Nguyen, and V. Chandrasekar, "Clutter suppression for staggered PRT waveforms," *Journal of Atmospheric and Oceanic Technology*, vol. 25, no. 12, pp. 2209–2218, 2008.
- [18] D. Schwartzman and R. D. Palmer, "Doppler Velocity Recovery and Dealiasing Algorithm for Multi-PRT Scans in Weather Radars," *IEEE Transactions on Geoscience and Remote Sensing*, vol. 62, 2024.
- [19] S. M. Torres, Y. F. Dubel, and D. S. Zrnić, "Design, implementation, and demonstration of a staggered PRT algorithm for the WSR-88D," *Journal of Atmospheric and Oceanic Technology*, vol. 21, no. 9, pp. 1389–1399, 2004.
- [20] D. A. Warde and S. M. Torres, "Range Overlaid Staggered PRT," in *25th Conference on International Interactive Information and Processing Systems (IIPS) for Meteorology, Oceanography, and Hydrology*, pp. 1–23, 2009.
- [21] M. Sachidananda and D. S. Zrnić, "Clutter filtering and spectral moment estimation for Doppler weather radars using staggered pulse repetition time (PRT)," *Journal of Atmospheric and Oceanic Technology*, vol. 17, no. 3, pp. 323–331, 2000.
- [22] A. Oude Nijhuis, *Radar remote sensing of wind vector and turbulence intensity fields from raindrop backscattering*. PhD thesis, TU Delft, 2019.
- [23] C. Qiu and Q. Xu, "A Simple Adjoint Method of Wind Analysis for Single-Doppler Data," *Journal of Atmospheric and Oceanic Technology*, vol. 9, no. 5, pp. 588–598, 1992.
- [24] A. Shapiro, S. Ellis, and J. Shaw, "Single-Doppler Velocity Retrievals with Phoenix II Data: Clear Air and Microburst Wind Retrievals in the Planetary Boundary Layer," *Journal of the Atmospheric Sciences*, vol. 52, no. 9, pp. 1265–1287, 1995.

- [25] C. Qiu and Q. Xu, "Least Squares Retrieval of Microburst Winds from Single-Doppler Radar Data," *Monthly Weather Review*, vol. 124, no. 6, pp. 1132–1144, 1996.
- [26] Y. C. Liou, "An explanation of the wind speed underestimation obtained from a least squares type single-Doppler radar velocity retrieval method," *Journal of Applied Meteorology*, vol. 41, no. 7, pp. 811–823, 2002.
- [27] C. J. Qiu, A. M. Shao, S. Liu, and Q. Xu, "A two-step variational method for three-dimensional wind retrieval from single Doppler radar," *Meteorology and Atmospheric Physics*, vol. 91, no. 1-4, pp. 1–8, 2006.
- [28] Y. C. Liou, H. B. Bluestein, M. M. French, and Z. B. Wienhoff, "Single-Doppler velocity retrieval of the wind field in a tornadic supercell using mobile, phased-array, Doppler radar data," *Journal of Atmospheric and Oceanic Technology*, vol. 35, no. 8, pp. 1649–1663, 2018.
- [29] Y.-C. Liou, T.-C. Chen Wang, and P.-Y. Huang, "The Inland Eyewall Reintensification of Typhoon Fanapi (2010) Documented from an Observational Perspective Using Multiple-Doppler Radar and Surface Measurements," *Monthly Weather Review*, vol. 144, pp. 241–261, 1 2016.
- [30] C. Unal, "High-resolution raindrop size distribution retrieval based on the doppler spectrum in the case of slant profiling radar," *Journal of Atmospheric and Oceanic Technology*, vol. 32, no. 6, pp. 1191–1208, 2015.
- [31] "Robin Radar Systems full 3D Advanced Bird Detection Radar - MAX3D."
- [32] F. F. Abraham, "Functional Dependence of Drag Coefficient of a Sphere on Reynolds Number," *Physics of Fluids*, vol. 13, no. 8, 1970.
- [33] C. Davies, "Particle-fluid interaction," *Journal of Aerosol Science*, vol. 10, 9 1979.
- [34] R. Osborne, "XXIX. An experimental investigation of the circumstances which determine whether the motion of water shall be direct or sinuous, and of the law of resistance in parallel channels," *Philosophical Transactions of the Royal Society of London*, vol. 174, 12 1883.
- [35] R. Osborne, "IV. On the dynamical theory of incompressible viscous fluids and the determination of the criterion," *Philosophical Transactions of the Royal Society of London. (A.)*, vol. 186, 12 1895.
- [36] J. E. McDonald, "THE SHAPE AND AERODYNAMICS OF LARGE RAINDROPS," *Journal of Meteorology*, vol. 11, 12 1954.
- [37] K. V. Beard, "The Effects of Altitude and Electrical Force on the Terminal Velocity of Hydrometeors," *Journal of the Atmospheric Sciences*, vol. 37, 6 1980.
- [38] D. L. Mitchell, "Use of Mass- and Area-Dimensional Power Laws for Determining Precipitation Particle Terminal Velocities," *Journal of the Atmospheric Sciences*, vol. 53, 6 1996.

- [39] H. P. Böhm, "A General Equation for the Terminal Fall Speed of Solid Hydrometeors," *Journal of the Atmospheric Sciences*, vol. 46, 8 1989.
- [40] J. P. Böhm, "A general hydrodynamic theory for mixed-phase microphysics. Part I: drag and fall speed of hydrometeors," *Atmospheric Research*, vol. 27, 2 1992.
- [41] A. J. Heymsfield and J. Iaquinta, "Cirrus Crystal Terminal Velocities," *Journal of the Atmospheric Sciences*, vol. 57, 4 2000.
- [42] H. Pruppacher and J. Klett, *Microphysics of Clouds and Precipitation*, vol. 18. Dordrecht: Springer Netherlands, 2010.
- [43] V. I. Khvorostyanov and J. A. Curry, "Terminal Velocities of Droplets and Crystals: Power Laws with Continuous Parameters over the Size Spectrum," *Journal of the Atmospheric Sciences*, vol. 59, pp. 1872–1884, 6 2002.
- [44] D. L. Mitchell and A. J. Heymsfield, "Refinements in the Treatment of Ice Particle Terminal Velocities, Highlighting Aggregates," *Journal of the Atmospheric Sciences*, vol. 62, 5 2005.
- [45] V. I. Khvorostyanov and J. A. Curry, "Fall Velocities of Hydrometeors in the Atmosphere: Refinements to a Continuous Analytical Power Law," *Journal of the Atmospheric Sciences*, vol. 62, 12 2005.
- [46] D. Atlas, S. Y. Matrosov, A. J. Heymsfield, M.-D. Chou, and D. B. Wolff, "Radar and Radiation Properties of Ice Clouds," *Journal of Applied Meteorology*, vol. 34, 11 1995.
- [47] S. Y. Matrosov, R. F. Reinking, R. A. Kropfli, and B. W. Bartram, "Estimation of Ice Hydrometeor Types and Shapes from Radar Polarization Measurements," *Journal of Atmospheric and Oceanic Technology*, vol. 13, 2 1996.
- [48] S. Y. Matrosov, "A Dual-Wavelength Radar Method to Measure Snowfall Rate," *Journal of Applied Meteorology*, vol. 37, 11 1998.
- [49] S. Y. Matrosov, "Retrievals of vertical profiles of ice cloud microphysics from radar and IR measurements using tuned regressions between reflectivity and cloud parameters," *Journal of Geophysical Research: Atmospheres*, vol. 104, pp. 16741 – 16753, 7 1999.
- [50] S. Y. Matrosov and A. J. Heymsfield, "Use of Doppler radar to assess ice cloud particle fall velocity-size relations for remote sensing and climate studies," *Journal of Geophysical Research: Atmospheres*, vol. 105, pp. 22427 – 22436, 9 2000.
- [51] H. Russchenberg, L. Spek, D. Moisseev, C. Unal, Y. Dufournet, and C. Venkatachalam, "On the use of spectral polarimetry to observe ice cloud microphysics with radar," in *Precipitation: Advances in Measurement, Estimation and Prediction*, Berlin, Heidelberg: Springer Berlin Heidelberg, 2008.

- [52] A. Ryzhkov, M. Pinsky, A. Pokrovsky, and A. Khain, "Polarimetric Radar Observation Operator for a Cloud Model with Spectral Microphysics," *Journal of Applied Meteorology and Climatology*, vol. 50, 4 2011.
- [53] A. N. Kolmogorov, "Dissipation of energy in the locally isotropic turbulence," *Proceedings of the Royal Society of London. Series A: Mathematical and Physical Sciences*, vol. 434, 7 1991.
- [54] F. Yanovsky, H. Russchenberg, and C. Unal, "Retrieval of information about turbulence in rain by using Doppler-polarimetric Radar," *IEEE Transactions on Microwave Theory and Techniques*, vol. 53, 2 2005.
- [55] A. O. Nijhuis, "Zephyros v0 . 2 ( Software package for wind / EDR simulation and retrieval )," vol. 2, 2014.
- [56] T. Dash, H. Driessen, O. Krasnov, and A. Yarovoy, "Doppler Spectrum Parameter Estimation for Weather Radar Echoes Using a Parametric Semi-analytical Model," *IEEE Transactions on Geoscience and Remote Sensing*, vol. 62, pp. 1–18, 2024.
- [57] T. Dash, H. Driessen, O. A. Krasnov, and A. Yarovoy, "Incoherent Doppler Processing for Doppler Moment and Noise Estimation for Precipitation," in *Proceedings of the 4th URSI Atlantic RadioScience Conference – AT-RASC 2024*, no. May, (Meloneras, Spain), pp. 1–4, URSI – International Union of Radio Science, 2024.
- [58] F. Yanovsky, H. Russchenberg, L. Ligthart, and Y. Aver'yanova, "Model of drop canting in microwave remote sensing of rain," in *Fourth International Kharkov Symposium 'Physics and Engineering of Millimeter and Sub-Millimeter Waves'. Symposium Proceedings (Cat. No.01EX429)*, pp. 471–473, IEEE, 2001.
- [59] F. Yanovsky, I. Prokopenko, K. Prokopenko, H. Russchenberg, and L. Ligthart, "Radar estimation of turbulence eddy dissipation rate in rain," in *IEEE International Geoscience and Remote Sensing Symposium*, IEEE, 2002.
- [60] P. Borque, E. Luke, and P. Kollias, "On the unified estimation of turbulence eddy dissipation rate using Doppler cloud radars and lidars," *Journal of Geophysical Research: Atmospheres Research*, vol. 121, no. 10, pp. 5091–6129, 2016.
- [61] B. E. Sheppard, "Measurement of Raindrop Size Distributions Using a Small Doppler Radar," *Journal of Atmospheric and Oceanic Technology*, vol. 7, no. 2, pp. 255–268, 1990.
- [62] H. W. J. Russchenberg, "Doppler Polarimetric Radar Measurements of the Gamma Drop Size Distribution of Rain," vol. 32, no. 12, pp. 1815–1825, 1993.
- [63] K. S. Gage and C. R. Williams, "Recent developments in the use of Doppler radar profilers for the remote sensing of precipitating clouds," *Microwave Remote Sensing of the Atmosphere and Environment III*, vol. 4894, no. May, p. 293, 2003.



- [64] Y. L. Kogan, Z. N. Kogan, and D. B. Mechem, "Assessing the errors of cloud liquid water and precipitation flux retrievals in marine stratocumulus based on Doppler radar parameters," *Journal of Hydrometeorology*, vol. 8, no. 4, pp. 665–677, 2007.
- [65] W. Klaassen, "Determination of Rain Intensity from Doppler Spectra of Vertically Scanning Radar," *Journal of Atmospheric and Oceanic Technology*, vol. 6, no. 4, pp. 552–562, 1989.
- [66] J. Campbell, K. J. Hutchison, and E. Karpinski, "Variation of Doppler Ultrasound Spectral Width In The Post-Stenotic Velocity Field," vol. 15, no. 6, pp. 535–539, 1989.
- [67] T. Thompson and H. Moore, "A Model for Doppler Radar Echoes from Mars," *Lunar and Planetary Science Conference*, no. Mar. 14-18, 1988, Proceedings (A89-36486 15-91), pp. 409–422, 1989.
- [68] G. J. Black, "Planetary Radar Astronomy," *Single-Dish Radio Astronomy: Techniques and Applications, ASP Conference Proceedings*, vol. Vol. 278, pp. 271–290, 2002.
- [69] T. Dash, O. A. Krasnov, and A. G. Yarovoy, "Performance Analysis of the Wind Field Estimation for a Very Fast Scanning Weather Radar," *Proceedings International Radar Symposium*, vol. 2022-Septe, pp. 420–425, 2022.
- [70] D. S. Zrnic and R. J. Doviak, "System requirements for phased array weather radar," tech. rep., 2005.
- [71] D. Sirmans and B. Bumgarner, "Numerical Comparison of Five Mean Frequency Estimators," *Journal of Applied Meteorology*, vol. 14, pp. 991–1003, 9 1975.
- [72] P. R. Mahapatra and D. S. Zrnić, "Practical Algorithms for Mean Velocity Estimation in Pulse Doppler Weather Radars Using a Small Number of Samples," *IEEE Transactions on Geoscience and Remote Sensing*, vol. GE-21, no. 4, pp. 491–501, 1983.
- [73] D. S. Zrnic, "Spectral Moment Estimates from Correlated Pulse Pairs," *IEEE Transactions on Aerospace and Electronic Systems*, vol. AES-13, no. 4, pp. 344–354, 1977.
- [74] D. Warde, D. Schwartzman, and C. D. Curtis, "Generalized Multi-Lag Estimators (GMLE) for Polarimetric Weather Radar Observations," *IEEE Transactions on Geoscience and Remote Sensing*, vol. 61, pp. 1–12, 2023.
- [75] G. Meymaris, J. K. Williams, and J. C. Hubbert, "Performance of a Proposed Hybrid Spectrum Width Estimator for the NEXRAD ORDA," *25th Conference on International Interactive Information and Processing Systems for Meteorology, Oceanography and Hydrology*, pp. 1–9, 2009.

- [76] R. Doviak and D. Zrnić, *Doppler Radar and Weather Observations*. 2nd ed., 1993.
- [77] J. Lee, "Poly-pulse pair estimation in a Doppler weather radar," *IEEE Antennas and Propagation Society, AP-S International Symposium (Digest)*, vol. 4, pp. 1968–1971, 2000.
- [78] J. M. Dias, "Nonparametric estimation of mean Doppler and spectral width," *IEEE Transactions on Geoscience and Remote Sensing*, vol. 38, no. 1, pp. 271–282, 2000.
- [79] R. Palmer, J. Cruz, and D. Zrnić, "Enhanced autoregressive moving average spectral estimation applied to the measurement of Doppler spectral width," *IEEE Transactions on Geoscience and Remote Sensing*, vol. 29, no. 5, 1991.
- [80] M. J. Levin, "Power Spectrum Parameter Estimation," *IEEE Transactions on Information Theory*, vol. 11, no. 1, pp. 100–107, 1965.
- [81] J. M. Dias and J. M. Leitão, "Maximum likelihood estimation of spectral moments at low signal to noise ratios," *ICASSP, IEEE International Conference on Acoustics, Speech and Signal Processing - Proceedings*, vol. 4, pp. 149–152, 1993.
- [82] J. Klostermeyer, "Maximum entropy estimation of Doppler shift and spectral width of VHF radar signals," vol. 24, no. 1, pp. 47–63, 1989.
- [83] P. Waldteufel, "An analysis of weather spectra variance in a tornadic storm," *NOAA Tech. Memo ERL NSSL*, no. 76, 1976.
- [84] B. L. Cheong, R. D. Palmer, and M. Xue, "A time series weather radar simulator based on high-resolution atmospheric models," *Journal of Atmospheric and Oceanic Technology*, vol. 25, no. 2, pp. 230–243, 2008.
- [85] P. T. May and R. G. Strauch, "An Examination of Wind Profiler Signal Processing Algorithms," *Journal of Atmospheric and Oceanic Technology*, vol. 6, no. 4, pp. 731–735, 1989.
- [86] W. Rudin, *Principles of Mathematical Analysis*. third ed., 1953.
- [87] T. Puhakka, V. Chandrasekar, and P. V. S. Puhakka, "Evaluation of FM pulse compression for weather radars," in *33rd Conference on Radar Meteorology*, pp. 1–12, 2007.
- [88] S. M. Torres and D. S. Zrnić, "Whitening in Range to Improve Weather Radar Spectral Moment Estimates. Part I: Formulation and Simulation," *Journal of Atmospheric and Oceanic Technology*, vol. 20, pp. 1433–1448, 11 2003.
- [89] I. R. Ivić, D. S. Zrnić, and S. M. Torres, "Whitening in range to improve weather radar spectral moment estimates. Part II: Experimental evaluation," *Journal of Atmospheric and Oceanic Technology*, vol. 20, no. 11, pp. 1449–1459, 2003.

- [90] D. S. Zrnić, "Simulation of Weatherlike Doppler Spectra and Signals," *Journal of Applied Meteorology*, vol. 14, pp. 619–620, 6 1975.
- [91] C. L. Matson and A. Haji, "Biased Cramér-Rao lower bound calculations for inequality-constrained estimators," *Journal of the Optical Society of America A*, vol. 23, no. 11, pp. 2702–2713, 2006.
- [92] P. Stoica and R. Moses, *Spectral Analysis of Signals*, vol. 24. 2008.
- [93] T. Liu and D. Li, "Convergence of the BFGS-SQP method for degenerate problems," *Numerical Functional Analysis and Optimization*, vol. 28, no. 7-8, pp. 927–944, 2007.
- [94] C. G. Broyden, "The convergence of a class of double-rank minimization algorithms 1. General considerations," *IMA Journal of Applied Mathematics (Institute of Mathematics and Its Applications)*, vol. 6, no. 1, pp. 76–90, 1970.
- [95] E. G. Baxa and J. Lee, "The Pulse-Pair Algorithm as a Robust Estimator of Turbulent Weather Spectral Parameters Using Airborne Pulse Doppler Radar," tech. rep., 1991.
- [96] H. W. Russchenberg and L. P. Ligthart, "Backscattering by and propagation through the melting layer of precipitation: a new Polarimetric Model," *IEEE Transactions on Geoscience and Remote Sensing*, vol. 34, no. 1, pp. 3–14, 1996.
- [97] C. Andrieu and A. Doucet, "Joint bayesian model selection and estimation of noisy sinusoids via reversible jump MCMC," *IEEE Transactions on Signal Processing*, vol. 61, no. 14, pp. 3653–3655, 1999.
- [98] T. K. Dash, H. Driessen, O. A. Krasnov, and A. Yarovoy, "Precipitation Doppler Spectrum Reconstruction with Gaussian Process Prior," *2023 IEEE Conference on Antenna Measurements and Applications (CAMA)*, pp. 909–914, 2023.
- [99] R. Boloix-Tortosa, J. J. Murillo-Fuentes, F. J. Payan-Somet, and F. Perez-Cruz, "Complex Gaussian Processes for Regression," *IEEE Transactions on Neural Networks and Learning Systems*, vol. 29, no. 11, pp. 5499–5511, 2018.
- [100] C. E. Rasmussen and C. K. Williams, *Gaussian Processes for Machine Learning*, vol. 7. 2000.
- [101] F. Tobar, "Bayesian nonparametric spectral estimation," *Advances in Neural Information Processing Systems*, vol. 2018-Decem, no. NeurIPS, pp. 10127–10137, 2018.
- [102] T. Dash, H. Driessen, O. A. Krasnov, and A. Yarovoy, "Counter-Aliasing Is Better Than De-Aliasing: Application to Doppler Weather Radar With Aperiodic Pulse Train," *IEEE Transactions on Geoscience and Remote Sensing*, vol. 62, pp. 1–17, 2024.

- [103] S.A.K Syed Mohamed, T. Dash, O. A. Krasnov, J. Bout, R. v. d. Meer, and A. G. Yarovoy, "Application of non-uniform sampling to avoid aliasing in the precipitation Doppler spectrum," *2024 International Radar Symposium (IRS)*, pp. 216–221, 2024.
- [104] S. Yuan, P. Aubry, F. Fioranelli, and A. G. Yarovoy, "A Novel Approach to Unambiguous Doppler Beam Sharpening for Forward-Looking MIMO Radar," *IEEE Sensors Journal*, vol. 22, no. 23, pp. 23494–23506, 2022.
- [105] S. Yuan, F. Fioranelli, and A. G. Yarovoy, "3DRUDAT : 3D Robust Unambiguous Doppler Beam Sharpening Using Adaptive Threshold for Forward-Looking Region," *IEEE Transactions on Radar Systems*, vol. 2, pp. 138–153, 2024.
- [106] B. Yang, S. Liu, H. Zhang, and Y. Zhou, "A Velocity Ambiguity Resolution Algorithm Based on Improved Hypothetical Phase Compensation for TDM-MIMO Radar Traffic Target Imaging," *IEEE Journal of Selected Topics in Applied Earth Observations and Remote Sensing*, vol. 17, pp. 3409–3424, 2024.
- [107] S. Chen, Y. Yuan, S. Zhang, H. Zhao, and Y. Chen, "A New Imaging Algorithm for Forward-Looking Missile-Borne Bistatic SAR," *IEEE Journal of Selected Topics in Applied Earth Observations and Remote Sensing*, vol. 9, no. 4, pp. 1543–1552, 2016.
- [108] M. Zhang, G. Liao, X. He, and S. Zhu, "Unambiguous Forward-Looking SAR Imaging on HSV-R Using Frequency Diverse Array," *Sensors*, vol. 20, p. 1169, 2020.
- [109] Y. Zhang, D. Mao, Y. Zhang, Y. Huang, and J. Yang, "Multi-Beam Doppler beam sharpening approach for airborne forward-looking radar imaging," in *2017 IEEE International Geoscience and Remote Sensing Symposium (IGARSS)*, pp. 6142–6145, 2017.
- [110] S. Muth, S. Dort, I. A. Sebag, M.-J. Blais, and D. Garcia, "Unsupervised dealiasing and denoising of color-Doppler data," *Medical Image Analysis*, vol. 15, pp. 577–588, 8 2011.
- [111] H. Nahas, J. S. Au, T. Ishii, B. Y. S. Yiu, A. J. Y. Chee, and A. C. H. Yu, "A Deep Learning Approach to Resolve Aliasing Artifacts in Ultrasound Color Flow Imaging," *IEEE Transactions on Ultrasonics, Ferroelectrics, and Frequency Control*, vol. 67, pp. 2615–2628, 12 2020.
- [112] A. Oglat, M. Matjafri, N. Suardi, M. Oqlat, M. Abdelrahman, and A. Oqlat, "A review of medical doppler ultrasonography of blood flow in general and especially in common carotid artery," *Journal of Medical Ultrasound*, vol. 26, no. 1, p. 3, 2018.
- [113] V. Louf, A. Protat, R. C. Jackson, S. M. Collis, and J. Helmus, "Unravel: A robust modular velocity dealiasing technique for doppler radar," *Journal of Atmospheric and Oceanic Technology*, vol. 37, no. 5, pp. 741–758, 2020.

- [114] W. Lu, "User-centric signal processing of high-resolution meteorological phased array radar," tech. rep., Delft University of Technology, 2023.
- [115] C. N. James and J. Houze, "A real-time four-dimensional Doppler dealiasing scheme," *Journal of Atmospheric and Oceanic Technology*, vol. 18, no. 10, pp. 1674–1683, 2001.
- [116] Q. Xu and C. Qiu, "Adjoint-Method Retrievals of Low-Altitude Wind Fields from Single-Doppler Reflectivity and Radial-Wind Data," *Journal of Atmospheric and Oceanic Technology*, vol. 12, no. 5, pp. 1111–1119, 1995.
- [117] S. M. Torres and D. A. Warde, "Staggered-PRT Sequences for Doppler Weather Radars. Part I: Spectral Analysis Using the Autocorrelation Spectral Density," *Journal of Atmospheric and Oceanic Technology*, vol. 34, pp. 51–63, 1 2017.
- [118] J. T. VanderPlas, "Understanding the Lomb–Scargle Periodogram," *The Astrophysical Journal Supplement Series*, vol. 236, no. 1, p. 16, 2018.
- [119] G. L. Bretthorst, "Frequency Estimation and Generalized Lomb-Scargle Periodograms," *Statistical Challenges in Astronomy*, pp. 309–329, 2006.
- [120] C. Koen, "The Nyquist frequency for irregularly spaced time-series: A calculation formula," *Monthly Notices of the Royal Astronomical Society*, vol. 371, no. 3, pp. 1390–1394, 2006.
- [121] A. W. Doerry, "Radar Doppler processing with nonuniform PRF," Tech. Rep. SAND2017-7851, Sandia National Laboratories Albuquerque, Albuquerque, New Mexico, 2017.
- [122] F. Particke, A. Schmidt, C. Rugheimer, and T. Mahr, "Additive random sampling for radar signal processing," *2017 IEEE-APS Topical Conference on Antennas and Propagation in Wireless Communications, APWC 2017*, vol. 2017-Janua, pp. 93–96, 2017.
- [123] M. W. Maciejewski, H. Z. Qui, I. Rujan, M. Mobli, and J. C. Hoch, "Nonuniform sampling and spectral aliasing," *Journal of Magnetic Resonance*, vol. 199, pp. 88–93, 7 2009.
- [124] C. J. Ryan, W. L. Beardell, J. Murakowski, D. D. Ross, G. J. Schneider, and D. W. Prather, "Log-periodic temporal apertures for grating lobe suppression in k-space tomography," *Optics Express*, vol. 28, no. 11, pp. 15969–15983, 2020.
- [125] A. Schuster, "On the investigation of hidden periodicities with application to a supposed 26 day period of meteorological phenomena," *Terrestrial Magnetism*, vol. 3, pp. 13–41, 1898.
- [126] Y. Aslan, "Optimization of virtually aperiodic linear sparse arrays," *Microwave and Optical Technology Letters*, vol. 64, no. 2, pp. 318–324, 2022.

- [127] M. Xu, C. Zhang, H. Qiao, Q. Zhang, C. Deng, and W. Yu, "Sparse Antenna Array With Flat-Top and Sharp," *IEEE Transactions on Antennas and Propagation*, vol. 71, no. 6, pp. 4695–4703, 2023.
- [128] S. A. Kader, "De-aliasing of Doppler Spectrum for a Fast Scanning Phased Array Radar Thesis Report De-aliasing of Doppler Spectrum for a Fast Scanning Phased Array Radar," tech. rep., Delft University of Technology, Delft, 2023.
- [129] T. Yardibi, J. Li, P. Stoica, M. Xue, and A. B. Baggeroer, "Source Localization and Sensing : A Nonparametric Iterative Adaptive Approach Based on Weighted Least Squares," *IEEE Transactions on Aerospace and Electronic Systems*, vol. 46, no. 1, pp. 425–443, 2010.
- [130] P. Stoica, E. G. Larsson, and J. Li, "Adaptive Filter-bank Approach to Restoration and Spectral Analysis of Gapped Data," *The Astronomical Journal*, vol. 120, pp. 2163–2173, 10 2000.
- [131] A. Mortier, J. P. Faria, C. M. Correia, A. Santerne, and N. C. Santos, "BGLS : A Bayesian formalism for the generalised Lomb-Scargle periodogram," *Astronomy & Astrophysics*, vol. 573, no. 24908, pp. 1–6, 2015.
- [132] E. T. Jaynes and G. L. Bretthorst, *Probability Theory: The Logic of Science*. Cambridge: Cambridge Univ. Press, 2003.
- [133] N. J. Bartlett, C. Renton, and A. G. Wills, "An Improved Random Matrix Prediction Model for Manoeuvring Extended Targets," no. 1, pp. 1–13, 2021.
- [134] G. L. Bretthorst, "Generalizing the Lomb-Scargle periodogram—the nonsinusoidal case," in *AIP Conference Proceedings*, vol. 568, pp. 246–251, AIP, 2001.
- [135] R. Boloix-Tortosa, F. J. Payán-Somet, E. Arias-de Reyna, and J. J. Murillo-Fuentes, "Proper Complex Gaussian Processes for Regression," pp. 1–15, 2015.
- [136] Y. Wang, R. Khardon, and P. Protopapas, "Nonparametric Bayesian Estimation of Periodic Light Curves," *The Astrophysical Journal*, 756, vol. 67, pp. 1–12, 2012.
- [137] M. Fang, R. J. Doviak, and V. Melnikov, "Spectrum width measured by WSR-88D: Error sources and statistics of various weather phenomena," *Journal of Atmospheric and Oceanic Technology*, vol. 21, no. 6, pp. 888–904, 2004.
- [138] D. S. Zrnic and R. J. Doviak, "Velocity Spectra of Vortices Scanned with a Pulse-Doppler Radar," *Journal of Applied Meteorology*, vol. 14, pp. 1531–1539, 12 1975.
- [139] P. Kollias, B. A. Albrecht, and F. D. Marks, "Cloud radar observations of vertical drafts and microphysics in convective rain," *Journal of Geophysical Research: Atmospheres*, vol. 108, no. D2, pp. 1–12, 2003.

- [140] C. Unal, "Spectral polarimetric radar clutter suppression to enhance atmospheric echoes," *Journal of Atmospheric and Oceanic Technology*, vol. 26, no. 9, pp. 1781–1797, 2009.
- [141] A. Djafri, "Mapping of weather radar ground clutter using the digital elevation model (SRTM)," *Signal & Image Processing : An International Journal*, vol. 3, pp. 135–151, 8 2012.
- [142] M.-H. Golbon-Haghighi, G. Zhang, Y. Li, and R. Doviak, "Detection of Ground Clutter from Weather Radar Using a Dual-Polarization and Dual-Scan Method," *Atmosphere*, vol. 7, p. 83, 6 2016.
- [143] J. Hensman, N. Durrande, and A. Solin, "Variational fourier features for Gaussian processes," *Journal of Machine Learning Research*, vol. 18, pp. 1–52, 2018.
- [144] P. Stoica and Y. Selen, "Model-order selection: a review of information criterion rules," *IEEE Signal Processing Magazine*, vol. 21, pp. 36–47, 7 2004.
- [145] S. E. Finder, E. Treister, and O. Freifeld, "Effective Learning of a GMRF Mixture Model," *IEEE Access*, vol. 10, pp. 7289–7299, 2022.
- [146] T. K. Dash, H. Driessen, O. A. Krasnov, and A. Yarovoy, "Joint Estimation of Raindrop Size Distribution and Radial Wind Velocity Parameters Using a Fast Scanning Weather Doppler Radar," *Journal of Atmospheric and Oceanic Technology*, 2025.
- [147] C. Gatidis, M. Schleiss, and C. Unal, "Sensitivity analysis of DSD retrievals from polarimetric radar in stratiform rain based on the  $\mu$ - $\Lambda$  relationship," *Atmospheric Measurement Techniques*, vol. 15, no. 16, pp. 4951–4969, 2022.
- [148] K. Wakasugi, A. Mizutani, M. Matsuo, S. Fukao, and S. Kato, "A Direct Method for Deriving Drop-Size Distribution and Vertical Air Velocities from VHF Doppler Radar Spectra," *Journal of Atmospheric and Oceanic Technology*, vol. 3, no. 4, pp. 623–629, 1986.
- [149] D. K. Rajopadhyaya, P. T. May, and R. A. Vincent, "Measuring Drop-Size Distributions in Clouds with a Clear-Air-Sensing Doppler Radar," *Journal of Atmospheric and Oceanic Technology*, vol. 10, no. 5, pp. 710–717, 1993.
- [150] E. E. Gossard, "Measuring Drop-Size Distributions in Clouds with a Clear-Air-Sensing Doppler Radar," *Journal of Atmospheric and Oceanic Technology*, vol. 5, no. 5, pp. 640–649, 1988.
- [151] C. R. Williams and K. S. Gage, "Raindrop size distribution variability estimated using ensemble statistics," *Annales Geophysicae*, vol. 27, no. 2, pp. 555–567, 2009.

- [152] E. A. Brandes, G. Zhang, and J. Vivekanandan, "Comparison of polarimetric radar drop size distribution retrieval algorithms," *Journal of Atmospheric and Oceanic Technology*, vol. 21, no. 4, pp. 584–598, 2004.
- [153] P. Currier, S. Avery, B. Balsley, K. Gage, and W. Ecklund, "Combined use of 50 MHz and 915 MHz wind profilers in the estimation of raindrop size distributions," vol. 19, no. 10, pp. 1017–1020, 1992.
- [154] D. Atlas, R. C. Srivastava, and R. S. Sekhon, "Doppler radar characteristics of precipitation at vertical incidence," *Reviews of Geophysics*, vol. 11, no. 1, pp. 1–35, 1973.
- [155] R. Gunn and Gilbert D. Kinzer, "The Terminal Velocity of Fall for Water Droplets in Stagnant Air," *Journal of the Atmospheric Sciences*, vol. 6, no. 4, pp. 243–248, 1949.
- [156] A. Kokhanovsky, "Optical properties of terrestrial clouds," *Earth-Science Reviews*, vol. 64, no. 3-4, pp. 189–241, 2004.
- [157] A. J. Heymsfield, S. Lewis, A. Bansemer, J. Iaquinta, L. M. Miloshevich, M. Kajikawa, C. Twohy, and M. R. Poellot, "A General Approach for Deriving the Properties of Cirrus and Stratiform Ice Cloud Particles," *Journal of the Atmospheric Sciences*, vol. 59, 1 2002.
- [158] C. L. Su, Y. H. Chu, and I. Y. Lo, "Negative correlation between terminal velocity and VHF radar reflectivity: Observation and plausible explanation," *Annales Geophysicae*, vol. 27, no. 4, pp. 1631–1642, 2009.
- [159] E. W. Weisstein, "Laguerre-Gauss Quadrature."
- [160] J. A. Fessler and A. O. Hero, "Cramer-Rao lower bounds for biased image reconstruction," *Midwest Symposium on Circuits and Systems*, vol. 1, no. d, pp. 253–256, 1993.
- [161] G. Zhang, J. Vivekanandan, and E. Brandes, "A method for estimating rain rate and drop size distribution from polarimetric radar measurements," *IEEE Transactions on Geoscience and Remote Sensing*, vol. 39, no. 4, pp. 830–841, 2001.
- [162] C. Gatidis, M. Schleiss, and C. Unal, "A new power-law model for  $\mu$ - $\Lambda$  relationships in convective and stratiform rainfall," *Atmospheric Measurement Techniques*, vol. 17, no. 1, pp. 235–245, 2024.
- [163] C. Gatidis, M. Schleiss, and C. Unal, "A new power-law model for  $\mu$  – $\Lambda$  relationships in convective and stratiform rainfall," *Atmospheric Measurement Techniques*, vol. 17, pp. 235–245, 1 2024.
- [164] L. D. Carey and W. A. Petersen, "Sensitivity of C-Band Polarimetric Radar-Based Drop Size Estimates to Maximum Diameter," *Journal of Applied Meteorology and Climatology*, vol. 54, pp. 1352–1371, 6 2015.



- [165] G. Mastroianni and G. Monegato, "Error Estimates for Gauss-Laguerre and Gauss-Hermite Quadrature Formulas," in *Approximation and Computation: A Festschrift in Honor of Walter Gautschi*, pp. 421–434, Boston, MA: Birkhäuser Boston, 1994.
- [166] J. V. Uspensky, "On the Convergence of Quadrature Formulas Related to an Infinite Interval," *Transactions of the American Mathematical Society*, vol. 30, no. 3, p. 542, 1928.

## EPILOGUE

In bringing this thesis to closure, I envisage that the conclusions presented in the thesis may change with the advent of a deeper understanding of the underlying physical and mathematical principles. The instruments that measure the weather dynamics like the one discussed in this thesis can be upgraded to accommodate the novel understanding of the dynamics of the hydrometeors and scattering mechanisms exploited by the instruments. Although the future insights remain uncertain, I believe that an amalgamation of adequate physical models with precise enough mathematical ideas will illuminate new dimensions to our inquiry into the unprecedented.



# ACKNOWLEDGEMENTS

The outcome of any research depends on many factors, such as daily Dutch weather conditions or the evolution of the stock market. The result can be very highly unpredictable, but at least one thing we can be very sure of is that all these factors have contributed to the outcome, one way or the other. I am thankful for all these factors, although I can never be aware of some of them in my lifetime. However, one factor I can acknowledge is the support I received from many people, directly or indirectly.

I sincerely thank Prof. DSc. Alexander Yarovoy for his continuous support during the most difficult times during the PhD. His profound interest in various fields of study, combined with his compassion toward the researchers, fuels innovation and growth in the research group. I am grateful for all his prompt remarks and feedback, which made my PhD trajectory smooth and exciting. I have learned a lot regarding the right approach and attitude towards research. Needless to say, he is an excellent teacher and coach.

I sincerely thank Dr. Oleg Krasnov for supervising me throughout the duration. His expertise in atmospheric sciences and radar system design has helped me garner the essentials to advance my research. Furthermore, his critical thinking and evaluation at each step of the way came as a blessing that only made me a better researcher.

Of course, I would like to acknowledge the supervision of Dr. Hans Driessen when I needed it the most. I have learned the “try, fail, learn, and repeat” approach to research from him. In the most difficult times, he has helped me gather my thoughts and manage my tasks efficiently by focusing on one task at a time.

I would like to thank “Airport Technology Lab” at the Rotterdam The Hague Innovation Airport (RHIA) for supporting and funding my research. I would like to acknowledge F. van der Zwan for his support during the experiments that I have used in this thesis. I also want to thank prof. dr. Felix Yanovsky and the team at SkyEcho for their valuable inputs for the real radar data acquisition.

I would like to thank my doctoral committee for carefully reading and appreciating my thesis: Prof. dr. ir. H.W.J. Russchenberg, Prof. dr. ir. B. De Schutter, Prof. dr. ir. R. Uijlenhoet, Prof. dr. D. Moiseev, and Prof. dr. ir. F.M.J. Willems. In addition, I would like to thank dr. M.A. Schleiss for attending my “Go/ No Go” meeting and giving me very valuable feedback. I would like to thank my supervisor for my master’s thesis, dr. David Prinsloo, for being a mentor and listening to my ideas during the initial difficult times in the PhD.

Special thanks to the support staff of the MS3 group, Esther de Klerk and Minke van der Put, for organizing fun events that helped me take off the stress in the research. I also want to acknowledge ir. Pascal Aubry for his support during my master’s program.

I especially like to acknowledge the beautiful friendships I have with my current and former fellow office mates: Dr. Utku Kumbul, Dr. Sen Yuan, Dr. Dingyang Wang, and “to be Dr.” Feza Celik, with special mention to the amazing friendship I have made with Costanza Vecchi. The activity that I enjoyed the most during my PhD was supervising master students for their theses. It was the constant learning process that I specifically enjoyed a lot. I would like to acknowledge Ir. Alexandru Girdianu, Ir. Sultan Abdul and Ir. Wenyi Lu for doing their master’s thesis work with my supervision. In addition, I would also like to thank the interns I have supervised: Ahmed Benkhadra, Taha El Hassouni, Malo Spinner, and Erwan Carrere. I also want to thank the external researchers and former master students I have interacted with: Ignacio Esteban, Luis A. López, Dr. ing. Vincenzo Carotenuto, Antonin Locatelli, Nicolas Van de Kreeke, Thomas Epailly, Ir. Srikar Chaganti, Ir. Surya Subramani.

I also like to thank all the former and current colleagues at MS3: Dr. Max Schope, Dr. Ronny Gundel, Dr. Wietse Bouwmeester, Dr. Jainping Wang, Dr. Francesco Fioranelli, Dr. ir. Bert-Jan Kooij, Dr. Ignacio Roldan, Peter Svenningsson, Nicolas Kruse, Berk Onat, Simmy Zhu, Romain Vergez, Mujtaba Hassan, Aitor Correias, Simon Hehenberger, Rutkay Guneri, Apostolos Pappas, Nakorn Kumchaiseemak, Stefano Chioccarello, Changxu Zhao, Viktor Vozar, Mareike Wendelmuth, Kuitong Lou, Adrian Lamoral, Mate Ivanyi, Jonas Heylen, Nick Cancrinus, and Peiyu Zhang.

I would like to extend my heartfelt gratitude to my incredible support system—the remarkable friends I have been fortunate to make during my master’s and PhD journey. Ir. Ashish Dhiman, Ir. Agney Bhakre, Ir. Soham Dharieswar, Ir. (soon to be “Dr.”) Rishikesh Joshi, Shagun Dogra, Ir. Nikhil Shriyan, Ir. Parinita Nitnaware, Hrishikesh Deshpande, Ir. Hrishikesh Sivanandan, Ir. (soon to be “Dr.”) Antony Pelekanidis, Merel Verhoef, Ir. Arjav Amur, and Ir. Saravana Nagesh—thank you for always being there for me and for patiently enduring my rants during the tough times. Your unwavering support has meant the world to me. I also want to thank my friends back in India, Amlan Patnaik, Anshuman Pati, Anubhav Routray, and Rohit Patra, for always being there: special mention to my senior colleague Priyambada Choudhury.

I thank my teachers, Mamata Mishra and Aruna Tripathy, Abinaya Paremeswaran, and Ruthvika Angadi, who shaped who I am today. I want to especially mention the late Basu Lenka, who, when I was just 10 years old, transformed my struggles with mathematics into a strong foundation, marking a pivotal turning point in my academic journey. Furthermore, I thank my extended family, including aunts, uncles, and cousins.

I thank my late grandfather (1942-2013), Ganeshwar Tripathy, for supporting me in every way possible. Furthermore, I express my deepest gratitude to my parents, Sasmita Tripathy and Dr. Gobinda C. Dash, and my brother, Tadit Kumar Dash, for their irreplaceable support and the uncountable sacrifices they have made for me. Thank you for teaching me about the priceless life values that go far beyond money, fame, or material achievements.

# CURRICULUM VITÆ

## Tworit Kumar Dash

### BIOGRAPHY

Tworit Dash was born in Nayagarh, Odisha, India, in 1994. He received the B.Tech. (Bachelor of Technology) degree from the Department of Instrumentation and Electronics Engineering, College of Engineering and Technology, Bhubaneswar, India, in 2016, and the M.Sc. degree (*cum laude*) in electrical engineering, telecommunication, and sensing systems track from the Delft University of Technology, Delft, The Netherlands, in 2020. Before doing the master, he worked at Robert Bosch India (2016-2018) as an engine calibration engineer. In September 2020, he joined the Microwave, Sensing, Signals, and Systems (MS3) Group at Delft University of Technology as a Ph.D. student.



**Date of Birth:** 10-07-1994, Nayagarh, India

**Education:**

2005–2009 **N.A.C High School, Nayagarh, Odisha, India**

Degree: Matriculation

Percentage: 90.16%

2009–2011 **Nayagarh Junior College, Nayagarh, Odisha, India**

Degree: High School/Junior College

Percentage: 89%

2012–2016 **College of Engineering and Technology, Odisha, India**

Degree: Bachelor of Technology (B-Tech)

Track: Instrumentation and Electronics

C-GPA: 8.94/10

2018–2020 **Delft University of Technology, The Netherlands**

Degree: Master of Science (MSc)

Track: Telecommunications and Sensing Systems

Thesis: “*Computationally Efficient Horn Antenna Design*”

Thesis Grade: 9 (cum laude)

Supervisor: Prof. DSc. Alexander Yarovoy

**Work Experience:**

2016–2018 **Robert Bosch India**

Designation: Engine Calibration Engineer

Work Package: On-board diagnostics (OBD-I & OBD-II)

**Awards:**

2016 Alumni Merit Award (Best Student) for the batch: 2012–2016

# LIST OF PUBLICATIONS

## JOURNAL ARTICLES

3. **T. K. Dash**, H. Driessen, O. A. Krasnov, and A. Yarovoy, "Joint Estimation of Raindrop Size Distribution and Radial Wind Velocity Parameters Using a Fast Scanning Weather Doppler Radar," *J. Atmos. Ocean. Technol.*, 2025. [Submitted]
2. **T. Dash**, H. Driessen, O. A. Krasnov and A. Yarovoy, "Counter-Aliasing Is Better Than De-Aliasing: Application to Doppler Weather Radar With Aperiodic Pulse Train," in *IEEE Transactions on Geoscience and Remote Sensing*, vol. 62, pp. 1-17, 2024, Art no. 5109017, doi: 10.1109/TGRS.2024.3438567.
1. **T. Dash**, H. Driessen, O. Krasnov, and A. Yarovoy, "Doppler Spectrum Parameter Estimation for Weather Radar Echoes Using a Parametric Semi-analytical Model," *IEEE Trans. Geosci. Remote Sens.*, vol. 62, pp. 1–18, 2024, doi: 10.1109/TGRS.2023.3338233.

## CONFERENCE PAPERS

6. **T. Dash**, W. Lu, O. Krasnov and A. Yarovoy, "Detection of Precipitation Using Scanning Radars with Strong Sectorial Interferences," *IGARSS 2024 - 2024 IEEE International Geoscience and Remote Sensing Symposium*, Athens, Greece, 2024, pp. 515-519, doi: 10.1109/IGARSS53475.2024.10642725.
5. S.A.K Syed Mohamed, **T. Dash**, O. A. Krasnov, J. Bout, R. van der Meer, and A. G. Yarovoy, "Application of non-uniform sampling to avoid aliasing in the precipitation Doppler spectrum," *2024 Int. Radar Symp.*, pp. 216–221, 2024.
4. **T. Dash**, H. Driessen, O. A. Krasnov and A. Yarovoy, "Incoherent Doppler Processing for Doppler Moment and Noise Estimation for Precipitation," *2024 4th URSI Atlantic Radio Science Meeting (AT-RASC)*, Meloneras, Spain, 2024, pp. 1-4, doi: 10.46620/URSIATRASC24/GTAX4119.
3. **T. K. Dash**, H. Driessen, O. Krasnov and A. Yarovoy, "Precipitation Doppler Spectrum Reconstruction with Gaussian Process Prior," *2023 IEEE Conference on Antenna Measurements and Applications (CAMA)*, Genoa, Italy, 2023, pp. 909-914, doi: 10.1109/CAMA57522.2023.10352683.
2. **T. Dash**, A. Girdianu, O. A. Krasnov, and A. G. Yarovoy, "Beamforming for a Fast Scanning Phased Array Weather Radar," in *Proceedings of the 20th European Radar Conference*, 2023, pp. 290–293, doi: 10.23919/eurad58043.2023.10289351.
1. **T. Dash**, O. A. Krasnov, and A. G. Yarovoy, "Performance Analysis of the Wind Field Estimation for a Very Fast Scanning Weather Radar," in *Proceedings International Radar Symposium*, 2022, vol. 2022-Septe, pp. 420–425.



## DATASETS

2. **T. Dash**, F. Van Der Zwan, S. A. K. Syed Mohamed, H. Driessen, O. Krasnov, and A. Yarovoy, "Real Weather Radar Data Doppler Moments Processing using Parametric Spectrum Estimator (PSE)." 4TU.ResearchData, Aug. 21, 2024, doi: 10.4121/5D20FB09-7803-4400-908E-06EC7364BEA3.V1.
1. **T. Dash**, H. Driessen, O. Krasnov, and A. Yarovoy, "Parametric Spectrum Estimator (PSE) to estimate the Doppler Moments of precipitation Doppler Spectrum." 4TU.ResearchData, Aug. 19, 2024, doi: 10.4121/E6921114-10D4-48EC-96B6-DA7714647275.V1.

## PAPERS OUTSIDE THE SCOPE OF THIS THESIS

1. **T. K. Dash**, D. Prinsloo and A. Yarovoy, "Radiation from the Open-ended Over-moded Cylindrical Waveguide," 2024 4th URSI Atlantic Radio Science Meeting (AT-RASC), Meloneras, Spain, 2024, pp. 1-4, doi: 10.46620/URSIATRASC24/QEUT4611.